

**APPLIED
COMPUTATIONAL
ELECTROMAGNETICS
SOCIETY
JOURNAL**

July 2018
Vol. 33 No. 7
ISSN 1054-4887

The ACES Journal is abstracted in INSPEC, in Engineering Index, DTIC, Science Citation Index Expanded, the Research Alert, and to Current Contents/Engineering, Computing & Technology.

The illustrations on the front cover have been obtained from the research groups at the Department of Electrical Engineering, The University of Mississippi.

THE APPLIED COMPUTATIONAL ELECTROMAGNETICS SOCIETY

<http://aces-society.org>

EDITORS-IN-CHIEF

Atef Elsherbeni

Colorado School of Mines, EE Dept.
Golden, CO 80401, USA

Sami Barmada

University of Pisa, ESE Dept.
56122 Pisa, Italy

ASSOCIATE EDITORS-IN-CHIEF: REGULAR PAPERS

Mohammed Hadi

Kuwait University, EE Dept.
Safat, Kuwait

Antonio Musolino

University of Pisa
56126 Pisa, Italy

Marco Arjona López

La Laguna Institute of Technology
Torreon, Coahuila 27266, Mexico

Alistair Duffy

De Montfort University
Leicester, UK

Abdul A. Arkadan

Colorado School of Mines, EE Dept.
Golden, CO 80401, USA

Paolo Mezzanotte

University of Perugia
I-06125 Perugia, Italy

Wenxing Li

Harbin Engineering University
Harbin 150001, China

Salvatore Campione

Sandia National Laboratories
Albuquerque, NM 87185, USA

Luca Di Rienzo

Politecnico di Milano
20133 Milano, Italy

Maokun Li

Tsinghua University
Beijing 100084, China

Wei-Chung Weng

National Chi Nan University, EE Dept.
Puli, Nantou 54561, Taiwan

Rocco Rizzo

University of Pisa
56123 Pisa, Italy

Mauro Parise

University Campus Bio-Medico of Rome
00128 Rome, Italy

Alessandro Formisano

Seconda Università di Napoli
81031 CE, Italy

Sima Noghianian

University of North Dakota
Grand Forks, ND 58202, USA

Piotr Gas

AGH University of Science and Technology
30-059 Krakow, Poland

ASSOCIATE EDITORS-IN-CHIEF: EXPRESS PAPERS

Lijun Jiang

University of Hong Kong, EEE Dept.
Hong, Kong

Steve J. Weiss

US Army Research Laboratory
Adelphi Laboratory Center (RDRL-SER-M)
Adelphi, MD 20783, USA

Amedeo Capozzoli

Univerita di Napoli Federico II, DIETI
I-80125 Napoli, Italy

Shinichiro Ohnuki

Nihon University
Tokyo, Japan

William O'Keefe Coburn

US Army Research Laboratory
Adelphi Laboratory Center (RDRL-SER-M)
Adelphi, MD 20783, USA

Yu Mao Wu

Fudan University
Shanghai 200433, China

Kubilay Sertel

The Ohio State University
Columbus, OH 43210, USA

Jiming Song

Iowa State University, ECE Dept.
Ames, IA 50011, USA

Maokun Li

Tsinghua University, EE Dept.
Beijing 100084, China

EDITORIAL ASSISTANTS

Matthew J. Inman

University of Mississippi, EE Dept.
University, MS 38677, USA

Shanell Lopez

Colorado School of Mines, EE Dept.
Golden, CO 80401, USA

EMERITUS EDITORS-IN-CHIEF

Duncan C. Baker

EE Dept. U. of Pretoria
0002 Pretoria, South Africa

Allen Glisson

University of Mississippi, EE Dept.
University, MS 38677, USA

Ahmed Kishk

Concordia University, ECS Dept.
Montreal, QC H3G 1M8, Canada

Robert M. Bevensee

Box 812
Alamo, CA 94507-0516, USA

Ozlem Kilic

Catholic University of America
Washington, DC 20064, USA

David E. Stein

USAF Scientific Advisory Board
Washington, DC 20330, USA

EMERITUS ASSOCIATE EDITORS-IN-CHIEF

Yasushi Kanai

Niigata Inst. of Technology
Kashiwazaki, Japan

Levent Gurel

Bilkent University
Ankara, Turkey

Erdem Topsakal

Mississippi State University, EE Dept.
Mississippi State, MS 39762, USA

Mohamed Abouzahra

MIT Lincoln Laboratory
Lexington, MA, USA

Sami Barmada

University of Pisa, ESE Dept.
56122 Pisa, Italy

Alexander Yakovlev

University of Mississippi, EE Dept.
University, MS 38677, USA

Ozlem Kilic

Catholic University of America
Washington, DC 20064, USA

Fan Yang

Tsinghua University, EE Dept.
Beijing 100084, China

EMERITUS EDITORIAL ASSISTANTS

Khaled ElMaghoub

Trimble Navigation/MIT
Boston, MA 02125, USA

Anne Graham

University of Mississippi, EE Dept.
University, MS 38677, USA

Christina Bonnington

University of Mississippi, EE Dept.
University, MS 38677, USA

Mohamed Al Sharkawy

Arab Academy for Science and Technology, ECE Dept.
Alexandria, Egypt

JULY 2018 REVIEWERS: REGULAR PAPERS

Sajjad Abazari Aghdam

Tamizh Arasu S.

Mehdi Bahadorzadeh

Sami Barmada

Ozlem Coskun

Angela Covas

Alistair Duffy

Jun Fan

Sulmer Fernandez Gutierrez

Anwar Hassan Ibrahim

Gui Chao Huang

He Huang

Yong Mao Huang

Jiangtao Huangfu

Milan Ilic

Ulrich Jakobus

Zhu Jun

William Kefauver

Saad Kiani

Sarat Kotamraju

Jin Li

Kai Li

Lianlin Li

Miaolan Li

Yixin Li

Omid Manoochehri

Ronald Marhefka

Rashid Mirzavand

Adam Mock

Osama Mohamed

Sima Noghalian

Antonio Orlandi

Hakan Partal

Milos Pavlovic

Andrew Peterson

Javad Pourahmadazar

Dhanapal R.

Luis Ramirez

C.J. Reddy

Sebastien Rondineau

Rachid Saadane

Angamuthu Sabanayagam

Siva Sankari S.A.

Yan Shi

Guo Shuai

Jan Sikora

Kwok Kan So

Sellakkutti Suganthi

Yi Sui

Guilin Sun

Aathmanesan T.

Yuvaraja T.

Shifei Tao

Yogesh Thakare

Wouter Tierens

Zhaofeng Wu

Shaoqiu Xiao

Fang Xiaoxing

Honglei Xu

John Young

Wenhua Yu

Kirill Zeyde

Hong-Xing Zheng

Lijia Zhu

JULY 2018 REVIEWERS: EXPRESS PAPERS

Vinh Dang

John Daniel

Grant Ellis

Ulrich Jakobus

Fatih Kaburcuk

Angelo Liseno

Seth McCormick

Ben Minnaert

Andrea Morabito

Ehsan Mostafapour

Ozlem Ozgun

Qiang Ren

Omar Saraereh

Yuvaraja T.

Ren Xingang

TABLE OF CONTENTS – REGULAR PAPERS

Domain Decomposition Scheme in Newmark-Beta-FDTD for Dispersive Grating Calculation Sheng-Bing Shi, Wei Shao, and Kai Wang.....	718
An Interpolation Scheme for Green’s Function and its Application in Method of Moment Yanlin Xu, Hu Yang, Xiang Liu, and Rongjun Shen.....	724
An Empirical Formula for Resonant Frequency Shift due to Jerusalem-Cross FSS with Substrate on One Side Hsing-Yi Chen and Shu-Huan Wen	730
The Human Body Modelled by Canonical Geometric Shapes for the Analysis of Scattered E-fields Giovanni Manfredi, Valentina Di Mattia, Paola Russo, Alfredo De Leo, and Graziano Cerri	741
Design and Implementation of Dual Band Microstrip Patch Antenna for WLAN Energy Harvesting System Osama Amjad, Syeda W. Munir, Şehabeddin T. İmeçi, and Ali Ö. Ercan	746
A Compact Tunable Triple Stop-Band Filter Based on Different Defected Microstrip Structures Yingsong Li, Shengyuan Luo, and Wenhua Yu.....	752
Mutual Coupling Reduction of a MIMO Antenna Array Using 3-D Novel Meta-material Structures Kai Yu, Yingsong Li, and Xiaoguang Liu	758
Wideband Multi-Port Network Integrated by 3-dB Branch-Line Couplers Nor Azimah Mohd Shukor, Norhudah Seman, and Tharek Abd Rahman.....	764
Efficient Design of Metamaterial Absorbers using Parametric Macromodels Giulio Antonini, Maria Denise Astorino, Francesco Ferranti, Fabrizio Frezza, and Nicola Tedeschi	772
Optimization of T-shaped Suspension Magnetic Ring for Vertical Axis Wind Turbine Zhu Jun, Song Dandan, Han Qiaoli, Wang Jinmei, Guanghua Li, and Li Shaolong	781

TABLE OF CONTENTS – EXPRESS PAPERS

Advanced Imaging for Down-Looking Contactless GPR Systems Davide Comite, Federica Murgia, Ilaria Catapano, Francesco Soldovieri, and Alessandro Galli	790
A High Resolution Algorithm for Null Broadening Beamforming Based on Subspace Projection and Virtual Antenna Array Wenxing Li, Hang Yang, and Yunlong Mao	794
On the Design and Simulation of Antennas on Ultra-thin Flexible Substrates Ahmed Kashkool, Samer Yahya, Hussain Al-Rizzo, Abbas Al-Wahhamy, and Ayman A. Issac.....	798
Modelling of Electromagnetic Scattering from Large and General Intakes on Complex Platforms Alessandro Mori, Stefano Bertini, Mirko Bercigli, Raffaele Scuderi, Paolo de Vita, and Stefano Sensani.....	802
A Finite Difference Frequency Domain Based Full Vectorial Transverse Modesolver for Anisotropic Waveguides with Arbitrary Permittivity and Permeability Tensors Varun Singh.....	806
Broadband Permittivity and Permeability Extraction of Ferrite Cores up to the GHz Range via Measurements and Simulations Christian Reinhold, Peter Scholz, and Ulrich Jumar.....	810
An HSS-Matrix-Based Fast Direct Solver with Randomized Algorithm Weikang Yu, Hu Yang, Shengguo Li, and Yanlin Xu	814
A Compact CPW-Fed MIMO Antenna with Band-Notched Characteristic for UWB System Li-Yan Chen, Jing-Song Hong, and Muhammad Amin.....	818

Domain Decomposition Scheme in Newmark-Beta-FDTD for Dispersive Grating Calculation

Sheng-Bing Shi, Wei Shao, and Kai Wang

School of Physics

University of Electronic Science and Technology of China, Chengdu, 610054, China
shengbing77@163.com, weishao@uestc.edu.cn, wkaiuestc2016@163.com

Abstract — In this work, an efficient domain decomposition scheme is introduced into the unconditionally stable finite-difference time-domain (FDTD) method based on the Newmark-Beta algorithm. The entire computational domain is decomposed into several subdomains, and thus the large sparse matrix equation produced by the implicit FDTD method can be divided into some independent small ones, resulting in a fast speed lower-upper decomposition and backward substitution. The domain decomposition scheme with different subdomain schemes and different subdomain numbers is studied. With a generalized auxiliary differential equation (ADE) technique, the extraordinary optical transmission through a periodic metallic grating with bumps and cuts is investigated with the domain decomposition Newmark-Beta-FDTD. Compared with the traditional ADE-FDTD method and the ADE-Newmark-Beta-FDTD method, the results from the proposed method show its accuracy and efficiency.

Index Terms — Domain decomposition, extraordinary optical transmission (EOT), Newmark-Beta-FDTD, surface plasmons.

I. INTRODUCTION

Enhanced transmission through subwavelength metallic openings has inspired great attention since the observation of extraordinary optical transmission (EOT) through a thick metal film perforated with a two-dimensional (2-D) array of subwavelength holes was reported [1]. Due to the vast potential applications of EOT, such as photolithography, optical data storage, organic light-emitting diodes, and photodetectors, many theoretical and experimental studies have been performed in understanding the interaction of light with metals in various subwavelength structures [2]-[4]. In general, the finite-difference time-domain (FDTD) method is used for the analysis of periodic metallic gratings. However, the surface plasmon polaritons (SPPs) are highly localized along the metal-dielectric interface. To simulate the effect of SPPs accurately, fine spatial

mesh should be used in this interface region. This result in an extremely small time step by the Courant-Friedrich-Levy (CFL) constraint [5], causing a long computing time. To remove this limitation in simulation, some unconditionally stable FDTD methods were introduced [6]-[9]. Recently, a new unconditionally stable FDTD method based on the Newmark-Beta algorithm has been proposed [10]. For large or multiscale problems with a tremendous number of unknowns, however, the calculation of its large and sparse linear equations leads to a heavy computation burden.

A promising solution for the calculation of large-scale matrices is the domain decomposition (DD) scheme [11-13]. In this paper, an efficient DD scheme is originally introduced into Newmark-Beta-FDTD for the analysis of two-dimensional (2-D) dispersive metallic gratings. As SPPs are highly localized near the metal-dielectric interfaces, graded grids with the fine spatial size are used for accuracy. A number of FDTD-based algorithms for the analysis of dispersive materials have already been proposed in literature, such as the auxiliary differential equation (ADE) method [5], the Z-transform method [14], and the method based on the discrete convolution of the dispersion relation [15]. Since the ADE method offers a more general representation for the dispersion relation, it is employed to simulate the dispersion effect caused by SPPs. The DD-Newmark-Beta-FDTD method decomposes the whole computational domain into several small subdomains. With the theory of Schur complement system, the solution of the large-scale matrix can be converted to the solutions of some small independent ones. With the reverse Cuthill-McKee (RCM) technique to preprocess the coefficient matrix in each subsystem before performing the lower-upper (LU) decomposition, the small linear systems can be solved efficiently. The EOT through a periodic metallic grating is investigated, and the results verify the efficiency and accuracy of the proposed method.

II. NUMERICAL FORMULATION

The formulation of the Newmark-Beta-FDTD

method based on the ADE technique has been presented in [16]. The dispersion relation of the Drude medium is given by:

$$\varepsilon(\omega) = 1 - \frac{\omega_p^2}{\omega(\omega + i\gamma)}, \quad (1)$$

where ω_p is the plasma frequency, γ is the absorption coefficient, and ω is the angular frequency of the wave.

Here, the implementation process of ADE-Newmark-Beta-FDTD in domain decomposition will be elaborated in detail. Without loss of generality, the whole computational domain is decomposed into four subdomains, marked as D_1 , D_2 , D_3 , and D_4 , and the interfaces between neighboring subdomains are named as Γ_{12} , Γ_{14} , Γ_{23} , and Γ_{34} , as shown in Fig. 1. For a specific simulated structure, different size grids can be adopted in different subdomains. For simplicity, the uniform mesh is used for all subdomains in Fig. 1, and the information in adjacent subdomains can be directly coupled by the interfaces.

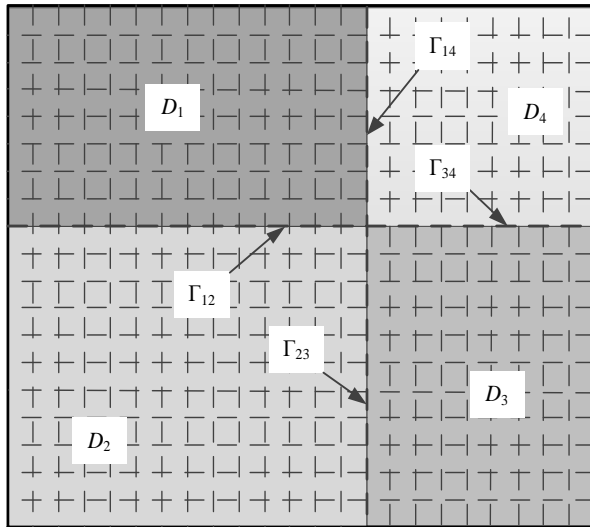


Fig. 1. Four subdomains in a 2-D computational domain.

For the original system, the implicit updated matrix equation in Newmark-Beta-FDTD can be written as:

$$\mathbf{A}\mathbf{H}_z^{n+1} = \mathbf{b}^n, \quad (2)$$

where \mathbf{A} is a large banded-sparse matrix. After the whole computational domain is divided into four subdomains, the unknowns, namely the magnetic field variables on the grids, are reordered starting with those in D_1 , followed by those in D_2 , D_3 , and D_4 , and ending with those on interfaces. We use n_i ($i = 1, 2, 3$, and 4) to represent the number of unknowns in each subdomain and n_Γ to represent the number of unknowns on the interfaces, where $\Gamma = \Gamma_{12} \cup \Gamma_{14} \cup \Gamma_{23} \cup \Gamma_{34}$. Thus, the new matrix system is written as:

$$\begin{bmatrix} \mathbf{A}_{11} & 0 & 0 & 0 & \mathbf{A}_{1\Gamma} \\ 0 & \mathbf{A}_{22} & 0 & 0 & \mathbf{A}_{2\Gamma} \\ 0 & 0 & \mathbf{A}_{33} & 0 & \mathbf{A}_{3\Gamma} \\ 0 & 0 & 0 & \mathbf{A}_{44} & \mathbf{A}_{4\Gamma} \\ \mathbf{A}_{\Gamma 1} & \mathbf{A}_{\Gamma 2} & \mathbf{A}_{\Gamma 3} & \mathbf{A}_{\Gamma 4} & \mathbf{A}_{\Gamma\Gamma} \end{bmatrix} \begin{bmatrix} \mathbf{H}_{z1} \\ \mathbf{H}_{z2} \\ \mathbf{H}_{z3} \\ \mathbf{H}_{z4} \\ \mathbf{H}_{z\Gamma} \end{bmatrix} = \begin{bmatrix} \mathbf{b}_1 \\ \mathbf{b}_2 \\ \mathbf{b}_3 \\ \mathbf{b}_4 \\ \mathbf{b}_\Gamma \end{bmatrix}, \quad (3)$$

where \mathbf{A}_{ii} corresponds to the interior-to-interior system, $\mathbf{A}_{i\Gamma}$ corresponds to the interior-to-interface coupling between D_i and Γ , $\mathbf{A}_{\Gamma i}$ corresponds to the interface-to-interior coupling between Γ and D_i , and $\mathbf{A}_{\Gamma\Gamma}$ corresponds to the interface-to-interface contribution. The vectors of \mathbf{H}_{z_i} and $\mathbf{H}_{z\Gamma}$ represent the magnetic field components corresponding to the subdomain D_i and interface Γ , respectively. And the vectors \mathbf{b}_i and \mathbf{b}_Γ are known terms in accordance with \mathbf{H}_{z_i} and $\mathbf{H}_{z\Gamma}$. The orders of \mathbf{A}_{ii} and $\mathbf{A}_{i\Gamma}$ are $n_i \times n_i$ and $n_i \times n_\Gamma$, respectively. To elaborate the matrix generation in each subdomain, the implicit updated equation of H_z in [16] is rewritten here:

$$\begin{aligned} & \left[\frac{\mu_0}{2\Delta t} + C \left(\frac{1}{2\Delta y^2} + \frac{1}{2\Delta x^2} \right) \right] H_z \Big|_{i+\frac{1}{2}, j+\frac{1}{2}}^{n+1} \\ & - \frac{C}{4\Delta y^2} \left(H_z \Big|_{i+\frac{1}{2}, j+\frac{3}{2}}^{n+1} + H_z \Big|_{i+\frac{1}{2}, j-\frac{1}{2}}^{n+1} \right) \\ & - \frac{C}{4\Delta x^2} \left(H_z \Big|_{i+\frac{3}{2}, j+\frac{1}{2}}^{n+1} + H_z \Big|_{i-\frac{1}{2}, j+\frac{1}{2}}^{n+1} \right) \\ & = \frac{\mu_0}{2\Delta t} H_z \Big|_{i+\frac{1}{2}, j+\frac{1}{2}}^{n-1} \\ & + \frac{C}{\Delta y} \left(\hat{E}_x \Big|_{i+\frac{1}{2}, j+1}^{n+1} - \hat{E}_x \Big|_{i+\frac{1}{2}, j}^{n+1} \right) - \frac{C}{\Delta x} \left(\hat{E}_y \Big|_{i+1, j+\frac{1}{2}}^{n+1} - \hat{E}_y \Big|_{i, j+\frac{1}{2}}^{n+1} \right) \\ & + \frac{1}{2\Delta y} \left(E_x \Big|_{i+\frac{1}{2}, j+1}^n - E_x \Big|_{i+\frac{1}{2}, j}^n \right) - \frac{1}{2\Delta x} \left(E_y \Big|_{i+1, j+\frac{1}{2}}^n - E_y \Big|_{i, j+\frac{1}{2}}^n \right) \\ & + \frac{1}{4\Delta y} \left(E_x \Big|_{i+\frac{1}{2}, j+1}^{n-1} - E_x \Big|_{i+\frac{1}{2}, j}^{n-1} \right) - \frac{1}{4\Delta x} \left(E_y \Big|_{i+1, j+\frac{1}{2}}^{n-1} - E_y \Big|_{i, j+\frac{1}{2}}^{n-1} \right) \end{aligned}, \quad (4)$$

where

$$C = \frac{2\Delta t + \gamma\Delta t^2}{4\varepsilon + 2\varepsilon\gamma\Delta t + \varepsilon_0\Delta t^2\omega_p^2}, \quad (5)$$

ε and ε_0 are the electric permittivity of the medium and free space, respectively, μ_0 is the magnetic permeability, γ is the absorption coefficient, and ω_p is the plasma frequency.

Since the magnetic field is updated in an implicit way, the interface between difference subdomains is placed on the location of H_z . Taking \mathbf{A}_{22} and $\mathbf{A}_{2\Gamma}$ in (3) for example, the interface Γ_{23} located at $x = i+5/2$ between D_2 and D_3 is placed on the middle of the grids due to the sample location of magnetic fields, as shown in Fig. 2. As we know, the central difference scheme is adopted in spatial derivatives. For the region $x \leq (i+1/2)$, the five magnetic fields in (4) are located in the interior

of D_2 and there is only interior-to-interior coupling between them. So the elements in A_{22} can be filled in the same way as the original implicit matrix. For the magnetic field component $H_z(i+3/2, j+1/2)$, from (4) and Fig. 2, its three neighboring components of $H_z(i+3/2, j-1/2)$, $H_z(i+3/2, j+3/2)$, and $H_z(i+1/2, j+1/2)$ are located in D_2 , and their coefficients are loaded in A_{22} normally. However, the component $H_z(i+5/2, j+1/2)$ is located on the interface of Γ_{23} , and its coefficient should be loaded in $A_{2\Gamma}$. The other sub-matrices can be filled in the same way. Moreover, there is no direct coupling between the interior unknowns of any two isolated subdomains due to the center difference scheme in space domain, so the elements in A_{ij} ($i \neq j$) are equal to zero. Besides, it is worth noting that $A_{\Gamma i} = A_{i\Gamma}^T$.

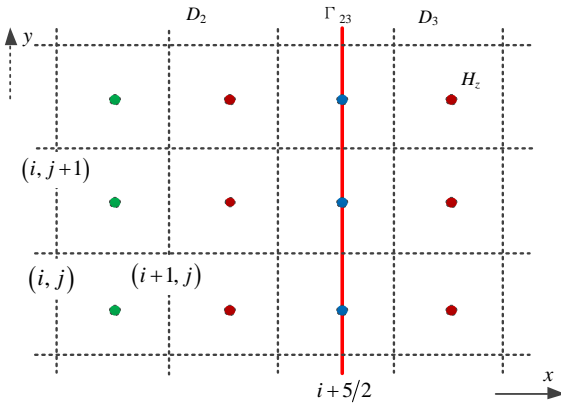


Fig. 2. Local mesh between D_2 and D_3 .

While the matrices are filled, we rewrite (3) into several small equations as:

$$A_{11}\mathbf{H}_{z1} + A_{1\Gamma}\mathbf{H}_{z\Gamma} = \mathbf{b}_1, \quad (6a)$$

$$A_{22}\mathbf{H}_{z2} + A_{2\Gamma}\mathbf{H}_{z\Gamma} = \mathbf{b}_2, \quad (6b)$$

$$A_{33}\mathbf{H}_{z3} + A_{3\Gamma}\mathbf{H}_{z\Gamma} = \mathbf{b}_3, \quad (6c)$$

$$A_{44}\mathbf{H}_{z4} + A_{4\Gamma}\mathbf{H}_{z\Gamma} = \mathbf{b}_4, \quad (6d)$$

$$A_{1\Gamma}^T\mathbf{H}_{z1} + A_{2\Gamma}^T\mathbf{H}_{z2} + A_{3\Gamma}^T\mathbf{H}_{z3} + A_{4\Gamma}^T\mathbf{H}_{z4} + A_{\Gamma\Gamma}\mathbf{H}_{z\Gamma} = \mathbf{b}_{\Gamma}. \quad (6e)$$

From (6a)-(6e), we obtain the updated equation of $\mathbf{H}_{z\Gamma}$ as:

$$\left(A_{\Gamma\Gamma} - \sum_{i=1}^4 A_{i\Gamma}^T A_{ii}^{-1} A_{i\Gamma} \right) \mathbf{H}_{z\Gamma} = \mathbf{b}_{\Gamma} - \sum_{i=1}^4 A_{i\Gamma}^T A_{ii}^{-1} \mathbf{b}_i. \quad (7)$$

It is called as the Schur complement system [17] and the coefficient matrix on the left side and the vector on the right side are known. Once the magnetic fields on the interface have been solved from (7), the other magnetic fields in the subdomains can be solved from (6a)-(6d).

It should be noted that (6a)-(6d) are independent from each other, and then, they can be solved in a parallel manner. In order to solve those equations efficiently, the RCM technique is used to reduce the bandwidth of the coefficient matrix, resulting in an efficient LU decomposition. More importantly, the LU decomposition

needs to be performed only once at the beginning of the calculation since the coefficient matrix keeps unchanged in the whole time-marching process.

When several small matrix equations are solved independently, much less time and memory are required than solving a large one. Furthermore, if the electromagnetic fields on an interface or in a subdomain are to be obtained, there is no need to solve all the subdomain systems.

III. NUMERICAL RESULTS AND DISCUSSION

To validate the accuracy and efficiency of the proposed DD-Newmark-Beta-FDTD method for solving the multiscale problem with dispersive materials, the transmission resonances of periodic metallic grating structures are investigated in the visible and near infrared regions in this section.

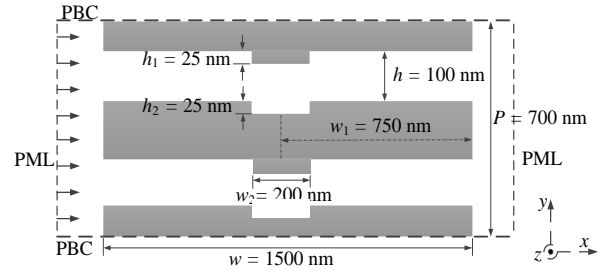


Fig. 3. Schematic of a unit cell of the periodic metallic grating with bumps and cuts.

The unit cell of the periodic metallic grating with bumps and cuts is investigated, as shown in Fig. 3. The computational domain is truncated by the perfectly matched layer (PML) on the left and right sides and periodic boundary condition (PBC) on the top and bottom. A modulated Gaussian pulse is used as the source excitation, and its time variation is given by:

$$F(t) = \sin(2\pi f_0 t) \cdot e^{-(t-t_0)^2/\tau^2}, \quad (8)$$

where the center frequency $f_0 = 215$ THz, $\tau = 1/(2f_0)$ and $t_0 = 3\tau$. The metal loaded on the grating is gold and the considered wavelength range is from 700 nm to 2500 nm. Hence, the corresponding parameters are $\omega_p = 1.37 \times 10^{16}$ rad/s and $\gamma = 4.08 \times 10^{13}$ rad/s [18]. To simulate the effect of SPPs around the bumps and cuts accurately, graded cells are used in both x - and y -directions. The minimum cell size is 1×0.1 nm² and the total cell number of the computational domain is 129×176 . The traditional FDTD method, the Newmark-Beta-FDTD method, and the proposed DD-Newmark-Beta-FDTD method are employed for this simulation, where $\Delta t_{\text{FDTD}} = 1.6667 \times 10^{-4}$ fs is chosen for FDTD according to the CFL constraint, while $\Delta t_{\text{Newmark}} = 1100 \Delta t_{\text{FDTD}} = 1.8333 \times 10^{-1}$ fs (CFLN = $\Delta t_{\text{Newmark}} / \Delta t_{\text{FDTD}} = 1100$) is chosen for Newmark-Beta-

FDTD and DD-Newmark-Beta-FDTD. Figure 4 shows that the results of the transmission and reflection spectrums of this grating structure from the three methods, in which the whole computational domain is decomposed into four subdomains for DD-Newmark-Beta-FDTD. From this figure, it can be seen that the results from DD-Newmark-Beta-FDTD are in good agreement with those from FDTD and Newmark-Beta-FDTD. In addition, the transmission spectrum shows the transmission peaks of four waveguide resonances which are associated with different standing wave modes of the slit acting as the Fabry-Pérot (F-P) cavity [19]. Furthermore, compared with the grating without bumps and cuts [16], the transmission peaks for the four resonance modes in the F-P cavity exhibit a red shift. This transmission behavior can be explained by the localized waveguide resonance mode [19]. The resonant wavelength of the F-P mode in a smooth slit array is given by $2kL_{FP} + \theta = 2N\pi$, where $k = 2n\pi/\lambda$ is the wave number (λ is the wavelength of the N th order mode, and n is the effective refractive index of the fundamental Bloch mode propagating in the slit), L_{FP} is the length of the cavity, and θ , an N -dependent value, is the total phase reflected at the ends of the slits. The loading of the perpendicular bumps and cuts enlarges the effective length of F-P cavity for both odd and even modes. Hence, the resonance wavelengths of all modes become large and show a red shift. This method can be used to minimize the volume of the light-wave devices.

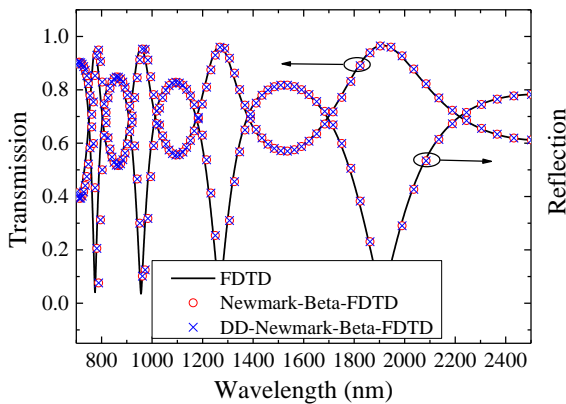


Fig. 4. Transmission and reflection spectrums of the grating with bumps and cuts from FDTD, Newmark-Beta-FDTD (CFLN = 1100), and DD-Newmark-Beta-FDTD (CFLN = 1100 and four subdomains).

In order to evaluate the computational accuracy of those methods, the mean absolute percentage error (MAPE) of the four resonance wavelengths is written as:

$$\text{MAPE} = \frac{1}{4} \sum_{n=1}^4 \left| \frac{\lambda_{\text{peak}} - \lambda_{\text{peak-FDTD}}}{\lambda_{\text{peak-FDTD}}} \right| \times 100\%, \quad (9)$$

where $\lambda_{\text{peak-FDTD}}$ is the transmission peaks from FDTD and it acts as the referenced result. Table 1 presents the computational efforts for the three methods, where CFLN = 1100 (MAPE < 1%) of Newmark-Beta-FDTD and DD-Newmark-Beta-FDTD is chosen to guarantee simulation precision. Since the time step of Newmark-Beta-FDTD is chosen 1100 times of FDTD, its CPU time can be reduced to about 1.18% of FDTD, but its memory requirement is about 4.68 times of FDTD. Applying the DD scheme to Newmark-Beta-FDTD with four subdomains, almost 40% of the CPU time and 65% of the memory requirement is saved.

Table 1: Comparison of the computational efforts for the three methods

Method	CFLN	MAPE	CPU Time (s)	Memory (Mb)
FDTD	1	-	51913	33.14
Newmark-Beta-FDTD	1100	0.90%	611	155.24
DD-Newmark-Beta-FDTD (4 subdomains)	1100	0.90%	381	54.64

Table 2: Comparison of the computational efforts for DD-Newmark-Beta-FDTD and Newmark-Beta-FDTD

Method	Domain Number	MAPE	CPU Time (s)	Memory (Mb)
Newmark-Beta-FDTD	1	0.90%	611.46	155.24
DD-Newmark-Beta-FDTD	2	0.90%	467.65	74.59
	3	0.90%	420.62	62.03
	4	0.90%	381.27	54.64
	5	0.90%	347.79	50.43
	6	0.90%	314.80	47.95

Furthermore, the whole computational domain is sequentially decomposed into two to six subdomains along the x -direction for DD-Newmark-Beta-FDTD simulations. With CFLN = 1100, the computational efforts of DD-Newmark-Beta-FDTD and Newmark-Beta-FDTD are compared in Table 2. From this Table, both the CPU time and memory requirement are reduced by using the domain decomposition scheme, and a larger subdomain number results in higher efficiency both in CPU time and memory requirement. The reason is that the LU decomposition of several small matrices costs much less time and memory than a huge one. In addition, it can also be seen from Table 2 that MAPE of DD-Newmark-Beta-FDTDs remains unchanged when the whole computational domain is divided into different subdomains. This is because the DD scheme based on the Schur complement system does not involve any approximation in the calculation process.

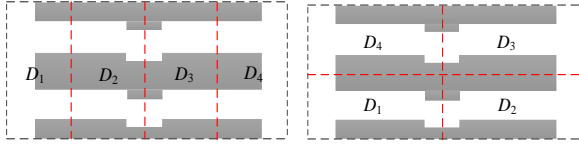


Fig. 5. Two different decomposition structures for four subdomains: (a) Case 1 and (b) Case 2.

Finally, the different spatial structures of the DD scheme are investigated. In the first case, the computational domain of the grating is decomposed into four subdomains with the same number of unknowns along the x -direction, as shown in Fig. 5 (a). In the second case, the whole domain is decomposed into four subdomains along the x - and y -directions, as shown in Fig. 5 (b). Table 3 shows that the computational accuracy and memory requirement of the two cases are the same. However, since the bandwidth of the matrix A_{iF} in Case 1 is smaller than that in Case 2, Case 1 costs less time in preconditioning coefficient matrices and solving equations.

Table 3: Comparison of the computational efforts for different decomposition structures

Case	Domain Number	MAPE	CPU Time (s)	Memory (Mb)
Case 1	4	0.90%	381.27	54.64
Case 2	4	0.90%	416.59	54.64

IV. CONCLUSION

This work introduces an efficient domain decomposition scheme to the unconditionally stable Newmark-Beta-FDTD method for periodic metallic grating analysis. Since the original computational domain can be decomposed into several small subdomains, the huge matrix equation can be transformed into several small independent ones. With the preconditioning RCM technique to the LU decomposition, which is executed only once at the beginning of the calculation, those small updated equations can be solved independently. The accuracy and efficiency of the proposed method are verified from the numerical example of the periodic metallic grating. The effects of different decomposition structures are also investigated. It has been proved that the DD-Newmark-Beta-FDTD method has high efficiency and low memory requirement while remaining high accuracy. This method is very suitable for the simulation in electrically large size structures involving multiscale grid division, such as photonic gratings, photonic crystals, microwave devices and antennas.

ACKNOWLEDGMENT

This work was supported by the National Natural Science Foundation of China (No. 61471105 and 6133107).

REFERENCES

- [1] T. W. Ebbesen, H. J. Lezec, H. F. Ghaemi, T. Thio, and P. A. Wolff, "Extraordinary optical transmission through sub-wavelength hole arrays," *Nature*, vol. 391, no. 6668, pp. 667-669, Feb. 1998.
- [2] C. Genet and T. W. Ebbesen, "Light in tiny holes," *Nature*, vol. 445, no. 7123, pp. 39-46, Jan. 2007.
- [3] J. A. Porto, F. J. Garcia-Vidal, and J. B. Pendry, "Transmission resonance on metallic gratings with very narrow slits," *Phy. Rev. Lett.*, vol. 83, no. 14, pp. 2845-2848, Oct. 1999.
- [4] H. J. Lezec and T. Thio, "Diffracted evanescent wave model for enhanced and suppressed optical transmission through subwavelength hole arrays," *Opt. Exp.*, vol. 12, no. 16, pp. 3629-3651, Aug. 2004.
- [5] A. Taflov and S.C. Hagness, *Computational Electrodynamics: The Finite-Difference Time-Domain Method*. Norwood, MA: Artech House, 2000.
- [6] T. Namiki, "A new FDTD algorithm based on alternating-direction implicit method," *IEEE Trans. Microw. Theory Techn.*, vol. 47, no. 10, pp. 2003-2007, Oct. 1999.
- [7] L. Gao, B. Zhang, and D. Liang, "The splitting finite difference time-domain methods for Maxwell's equations in two dimensions," *J. Comput. Appl. Math.*, vol. 205, no. 1, pp. 207-230, Aug. 2007.
- [8] E. L. Tan, "Unconditionally stable LOD-FDTD method for 3-D Maxwell's equations," *IEEE Microw. Wireless Compon. Lett.*, vol. 17, no. 2, pp. 85-87, Feb. 2007.
- [9] G. Sun and C. W. Truneman, "Efficient implementations of the Crank-Nicolson scheme for the finite-difference time-domain method," *IEEE Trans. Microw. Theory Techn.*, vol. 54, no. 5, pp. 2275-2284, May 2006.
- [10] S. B. Shi, W. Shao, X. K. Wei, X. S. Yang, and B. Z. Wang, "A new unconditionally stable FDTD method based on the Newmark-Beta algorithm," *IEEE Microw. Theory Techn.*, vol. 64, no. 12, pp. 4082-4090, Dec. 2016.
- [11] M. N. Vouvakis, Z. Cendes, and J. F. Lee, "A FEM domain decomposition method for photonic and electromagnetic band gap structures," *IEEE Trans. Antennas Propag.*, vol. 54, no. 2, pp. 721-733, Feb. 2006.
- [12] B. Z. Wang, R. Mittra, and W. Shao, "A domain decomposition finite-difference utilizing characteristic basis functions for solving electrostatic problems," *IEEE Trans. Electromagn. Compat.*, vol. 50, no. 4, pp. 946-952, Nov. 2008.
- [13] G. Q. He, W. Shao, X. H. Wang, and B. Z. Wang, "An efficient domain decomposition Laguerre-FDTD method for two-dimensional scattering

problems,” *IEEE Trans. Antennas Propag.*, vol. 64, no. 5, pp. 2639-2645, May 2013.

- [14] D. Sullivan, “Nonlinear FDTD formulations using Z transforms,” *IEEE Trans. Microw. Theory Techn.*, vol. 43, no. 3, pp. 676-682, Mar. 1995.
- [15] R. J. Luebbers and F. Hunsberger, “FDTD for Nth-order dispersive media,” *IEEE Trans. Antennas Propag.*, vol. 40, no. 11, pp. 1297-1301, Nov. 1992.
- [16] S. B. Shi, W. Shao, T. L. Liang, L. Y. Xiao, X. S. Yang, and H. Ou, “Efficient frequency-dependent Newmark-Beta-FDTD method for periodic grating calculation,” *IEEE Photonics J.*, vol. 8, no. 6, pp. 1-9, Dec. 2016.
- [17] T. N. Phillips, “Preconditioned iterative methods for elliptic problems on decomposed domains,” *Int. J. Comput. Math.*, vol. 44, pp. 5-18, 1992.
- [18] E. D. Palik, *Handbook of Optical Constants in Solids*. Academic, 1982.
- [19] A. P. Hibbins, M. J. Lockyear, and J. R. Sambles, “The resonant electromagnetic fields of an array of metallic slits acting as Fabry-Pérot cavities,” *J. Appl. Phys.*, vol. 99, no. 12, pp. 1-5, June 2006.



Sheng-Bing Shi was born in Hubei, China, in 1990. He received the B.S. degree in Physics from the Yangtze University, Jingzhou, China, in 2013. In 2015, he received the M.S. degree in Radio Physics at University of Electronic Science and Technology of China (UESTC). Currently, he is

working toward the Ph.D. degree in Radio Physics at UESTC.

His research interest is computational electromagnetics.



Wei Shao received the B.E. degree in Electrical Engineering, and the M.Sc. and Ph.D. degrees in Radio Physics from the University of Electronic Science and Technology of China (UESTC), Chengdu, in 1998, 2004, and 2006, respectively.

He joined the UESTC in 2007.

From 2010 to 2011, he was a Visiting Scholar with the Electromagnetic Communication Laboratory, Pennsylvania State University, State College, PA, USA. He is currently a Professor with UESTC.

His current research interests include computational electromagnetics and antenna design.



Kai Wang was born in Sichuan, China, in 1992. He received his B.E. degree in Electronic Information Science and Technology from the University of Electronic Science and Technology of China (UESTC) in 2015. He is working toward the M.S. degree in Radio Physics at

UESTC. His research interest is computational electromagnetics.

An Interpolation Scheme for Green's Function and its Application in Method of Moment

Yanlin Xu¹, Hu Yang¹, Xiang Liu², and Rongjun Shen¹

¹ College of Electronic Science
National University of Defense Technology, Changsha, 410073, China
13298656824@163.com, yanghu90@163.com, 271069796@qq.com

² College of Information and Communication Engineering
Hunan Institute of Science and Technology, Yueyang, 414000, China
1175235011@qq.com

Abstract — An interpolation scheme is put forward to accelerate the calculation of free space Green's function. Through theoretical analysis, a universal rule on how to build value lists for the phase item of Green's function is discussed. And this rule can guarantee accuracy of the interpolation scheme. Accuracy and efficiency of the scheme are verified in the calculation of impedance matrix for method of moment. Besides, this scheme can also be applied to other applications which contain the calculation of Green's functions and is especially useful for the analysis of large scale problems. Moreover, this scheme can be combined with other existing improved approaches of method of moment.

Index Terms — Green's function, impedance matrix, interpolation scheme, method of moment.

I. INTRODUCTION

Green's function of free space can be viewed as the electric field of ideal point source. Thus, it is the basis of electromagnetic problems and is frequently used in computational electromagnetics [1-4]. In this work, a typical application of Green's function in method of moment (MoM) is discussed.

MoM is a classic frequency-domain algorithm and was first applied to the analysis of electric field integral equation by Harrington in 1968 [5]. It transforms a vector integral equation into a scalar matrix equation by two processes called discretization and test.

The discretization process discretizes the unknown vector into a series of basic functions and the test process uses a series of test functions to make inner products. Usually, to ensure accuracy, a sampling rate of $\lambda/10$ is required. This makes MoM unsuitable for large scale problems due to the limitations on memory cost $O(N^2)$ and computational complexity $O(N^3)$.

To overcome or improve drawbacks of MoM and accelerate the calculation of its impedance matrix,

several approaches are proposed in the past decades. Among which, fast multi-pole method (FMM) and multi-level fast multi-pole method (MLFMM) [6-8] attracts most attention due to its excellent performance in efficiency and accuracy. Apart from FMM/MLFMM, other improved approaches such as multilevel matrix decomposition algorithm (MLMDA) [9], wavelet-based modelling method [10], improved impedance matrix localization method (IML) [11], triangular expansion method [12], synthetic basis functions method (SBFM) [13] and etc. also made great progresses. To summarize, these improved approaches accelerate the calculation of impedance matrix through mathematical operation.

Unlike the above, in this work, we put emphasis on the calculation of Green's functions. As is known to all, the calculation of Green's function takes a considerable part in the calculation of impedance matrix for MoM. Then, considering periodic properties of phase term of Green's function, an interpolation scheme is presented to improve the efficiency of the calculation of Green's function. This work first discusses the calculation of impedance matrix and analyzes the proportion of Green's function in the total calculation. Then, based on the periodic properties of Green's function, a value list for the phase term is built to accelerate the calculation process. Moreover, we theoretically analyze and prove the determination of the number of segments for the value list to acquire a constant accuracy. Efficiency and accuracy of the interpolation scheme are validated by numerical examples in the calculation of impedance matrix for MoM. Notably, this scheme can also be perfectly combined other applications those contain the calculation of Green's function as it is an independent process.

II. BASIC THEORY

For PEC bodies, MoM usually bases on the EFIE, which can be compactly written as:

$$\hat{n} \times L(\mathbf{J}) = \hat{n} \times \mathbf{E}_{inc}, \quad (1)$$

Where \mathbf{E}_{inc} represents the incident wave, \mathbf{J} is the surface current, L is the electric integral operator and defined as:

$$L(\mathbf{X}) = j\omega\mu \int_S \left[\mathbf{X} + \frac{1}{k^2} \nabla(\nabla \cdot \mathbf{X}) \right] g dS. \quad (2)$$

Usually, Rao-Wilton-Glisson (RWG) functions [14] are adopted to discretize (1) and transform it into a linear matrix equation:

$$\mathbf{Z}\mathbf{I} = \mathbf{V}, \quad (3)$$

Where $\mathbf{Z} = \{z_{mn}\}_{N \times N}$ is the impedance matrix, $\mathbf{V}_{N \times 1}$ is the exciting matrix, and $\mathbf{I}_{N \times 1}$ is the current coefficients

$$z_{mn} = \langle \mathbf{f}_m(\mathbf{r}), L(\mathbf{f}_n(\mathbf{r}')) \rangle = \int_S \mathbf{f}_m(\mathbf{r}) \cdot L(\mathbf{f}_n(\mathbf{r}')) ds = j\omega\mu \int_S \int_{S'} g(\mathbf{r} - \mathbf{r}') \left(\frac{\mathbf{f}_m(\mathbf{r}) \cdot \mathbf{f}_n(\mathbf{r}') - 1}{k^2} \nabla_s \cdot \mathbf{f}_m(\mathbf{r}) \nabla_{s'} \cdot \mathbf{f}_n(\mathbf{r}') \right) ds' ds, \quad (4)$$

$$\int_S \int_{S'} g(\mathbf{r} - \mathbf{r}') (\mathbf{f}_m(\mathbf{r}) \cdot \mathbf{f}_n(\mathbf{r}')) ds' ds = \left[\left(\int_{S_n^+} g(\mathbf{r}_{m,c}^+ - \mathbf{r}') \mathbf{f}_n(\mathbf{r}') ds' \right) \cdot (\mathbf{f}_m(\mathbf{r}_{m,c}^+) A_m^+) + \left(\int_{S_n^-} g(\mathbf{r}_{m,c}^- - \mathbf{r}') \mathbf{f}_n(\mathbf{r}') ds' \right) \cdot (\mathbf{f}_m(\mathbf{r}_{m,c}^-) A_m^-) \right]$$

$$= \frac{l_n l_m}{4} \left(\frac{1}{A_n^+} \int_{T_n^+} \rho_n^+ g(\mathbf{r}_{m,c}^+ - \mathbf{r}') ds' \cdot \rho_m^{c+} + \frac{1}{A_n^-} \int_{T_n^-} \rho_n^- g(\mathbf{r}_{m,c}^- - \mathbf{r}') ds' \cdot \rho_m^{c-} + \frac{1}{A_n^+} \int_{T_n^+} \rho_n^+ g(\mathbf{r}_{m,c}^- - \mathbf{r}') ds' \cdot \rho_m^{c-} + \frac{1}{A_n^-} \int_{T_n^-} \rho_n^- g(\mathbf{r}_{m,c}^+ - \mathbf{r}') ds' \cdot \rho_m^{c+} \right), \quad (5)$$

$$= \frac{l_n l_m}{4} \left(g(\mathbf{r}_{m,c}^+ - \mathbf{r}_{n,c}^+) \rho_n^+ \cdot \rho_m^{c+} + g(\mathbf{r}_{m,c}^+ - \mathbf{r}_{n,c}^-) \rho_n^- \cdot \rho_m^{c+} + g(\mathbf{r}_{m,c}^- - \mathbf{r}_{n,c}^+) \rho_n^+ \cdot \rho_m^{c-} + g(\mathbf{r}_{m,c}^- - \mathbf{r}_{n,c}^-) \rho_n^- \cdot \rho_m^{c-} \right)$$

$$\int_S \int_{S'} g(\mathbf{r} - \mathbf{r}') (\nabla_s \cdot \mathbf{f}_m(\mathbf{r}) \nabla_{s'} \cdot \mathbf{f}_n(\mathbf{r}')) ds' ds = l_m \left(\int_{S_n^+} \nabla_{s'} \cdot \mathbf{f}_n(\mathbf{r}') g(\mathbf{r}_{m,c}^+ - \mathbf{r}') ds' - \int_{S_n^-} \nabla_{s'} \cdot \mathbf{f}_n(\mathbf{r}') g(\mathbf{r}_{m,c}^- - \mathbf{r}') ds' \right)$$

$$= l_m l_n \left(\frac{1}{A_n^+} \int_{T_n^+} g(\mathbf{r}_{m,c}^+ - \mathbf{r}_{n,c}^+) ds' - \frac{1}{A_n^-} \int_{T_n^-} g(\mathbf{r}_{m,c}^+ - \mathbf{r}_{n,c}^-) ds' - \frac{1}{A_n^+} \int_{T_n^+} g(\mathbf{r}_{m,c}^- - \mathbf{r}_{n,c}^+) ds' + \frac{1}{A_n^-} \int_{T_n^-} g(\mathbf{r}_{m,c}^- - \mathbf{r}_{n,c}^-) ds' \right). \quad (6)$$

From (5) and (6) we can see that, the calculation of Green's function takes a considerable part of the total calculation. For each Z_{mn} , Green's function needs to be calculated 4 times. Thus, for a problem with N RWG functions, the scale of impedance matrix will be N^2 which means Green's function need to be calculated $4N^2$ times. Moreover, considering the singularity of Green's function, if nine-point approximation [14] is adopted, the calculation of Green's function will be $36N^2$ times. Besides, (5) and (6) indicate the calculation of Green's function is independent of the calculation of impedance matrix. Thus, we can obtain the values of Green's functions in advance.

Green's function is defined as:

$$g(R) = e^{-jkR} / 4\pi R. \quad (7)$$

For brevity, we ignore the constant coefficient of g and define $h=4\pi g$. h contains two parts: the magnitude item $1/R$ and the phase item e^{-jkR} . We plot the values of h changing with R , as shown in Fig. 1. From Fig. 1 we can see that values of h exhibit a periodic distribution around origin point with the decrease of R . And the periodic properties are caused by the phase item e^{-jkR} .

Considering trajectory of Green's function's phase item is a circle whose radius is 1. We can discretize the trajectory into numerous segments and build a value list for each segment, as shown in Fig. 2. With the value list, we no longer need to calculate the phase item and

matrix of RWG functions. The impedance matrix is calculated as (4).

Where $\mathbf{f}_m(\mathbf{r})$ is the m -th RWG function, g and k is the Green's function of free space and the wave number.

Equation (4) contains two parts which are computed in (5) and (6). Where ρ represents the vector in a couple of triangular patches T_n^\pm , l_n is the edge length of the common edge of T_n^\pm , A_n^\pm is the areas of T_n^\pm . These symbols are the basic definitions of RWG function, and we are not going to introduce them for the sake of simplicity.

we can get the value directly from the list according to kR . Accuracy of the value list is controlled by the total number of segments M . And the larger of M , the higher accuracy it will be. To determine the proper number of segments M , we do the derivation for h :

$$\frac{dh}{dR} = \left(-\frac{1}{R^2} - \frac{jk}{R} \right) e^{-jkR}. \quad (8)$$

Then,

$$|dh| = \sqrt{\frac{1}{R^4} + \frac{k^2}{R^2}} |dR|. \quad (9)$$

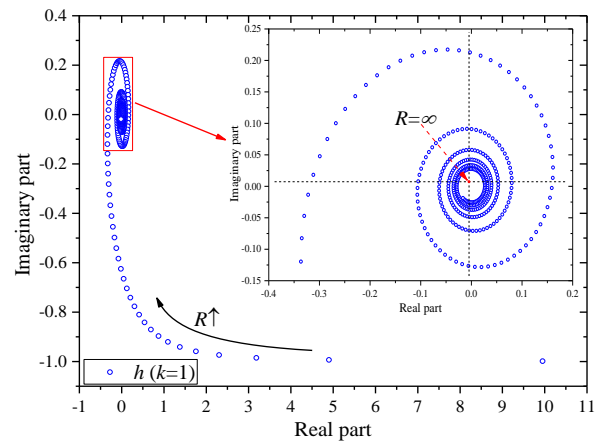


Fig. 1. Values of Green's function changing with R .

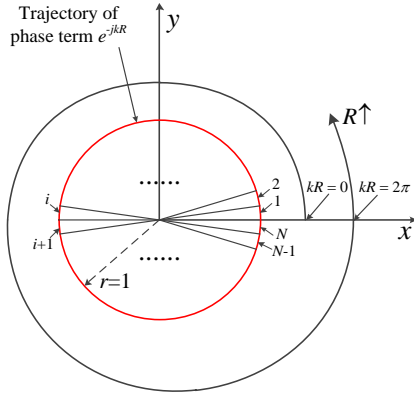


Fig. 2. Trajectory of Green's function phase item which is divided into N segments.

In fact, $|dh|$ represents the absolute error of h which is a circle around the real value as shown in Fig. 3 and accurate relationship between $|dh|$ and $|dR|$ is shown in Fig. 4.

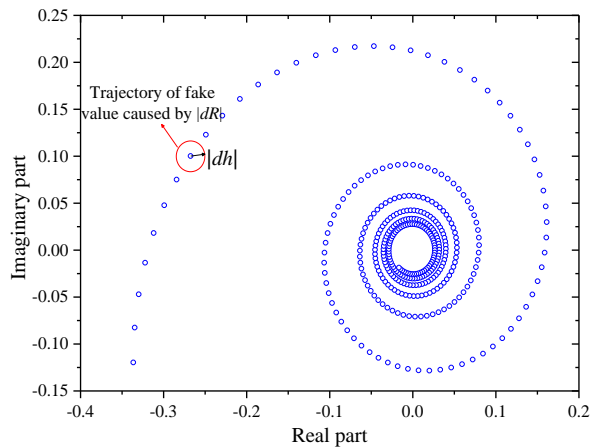


Fig. 3. Fake value trajectory of Green's function.

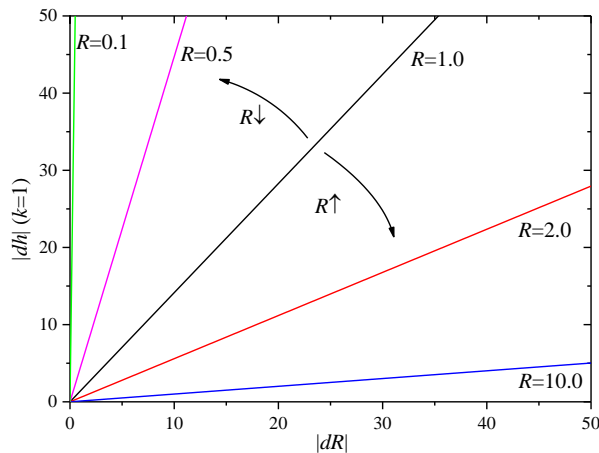


Fig. 4. Relationship between $|dh|$ and $|dR|$.

However, from (9) we see that $|dh|$ are determined by $|dR|$, k , and R . For a constant $|dR|$ and k , $|dh|$ increases with the decrease of R . Extremely, $|dh| \rightarrow |dR|/R^2$ ($R \rightarrow 0$). Thus, if we need a constant precision of δ , it will be:

$$|dh| \leq \delta \Rightarrow |dR| \leq \delta / \sqrt{\frac{1}{R^4} + \frac{k^2}{R^2}}. \quad (10)$$

Then, we can get the number of segments M by:

$$|dR| = \frac{2\pi}{kM} \leq \delta / \sqrt{\frac{1}{R^4} + \frac{k^2}{R^2}} \Rightarrow M \geq \frac{2\pi}{k\delta} \sqrt{\frac{1}{R^4} + \frac{k^2}{R^2}}. \quad (11)$$

In fact, (11) is unsolvable for if $R=0$, the number of segment $M=+\infty$ which is impossible in reality. However, in MoM, to avoid singularity of Green's function, nine-point approximation method is adopted which makes the minimum of R is determined by the minimum length of edges of triangular patches, as shown in Fig. 5. Here, we consider a generalized situation: in most occasions, a sampling rate of $\lambda/10$ is required to ensure the accuracy. It will be:

$$R_{\min} \approx \frac{l}{3} \leq \frac{\lambda}{30}. \quad (12)$$

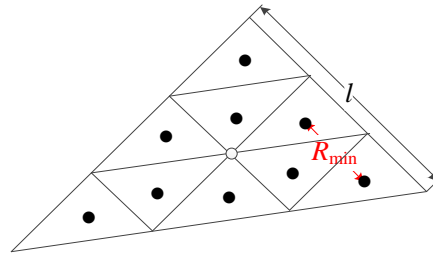


Fig. 5. Sketch map of nine-point approximation.

Substituting R_{\min} into (11), we can get the number of segments M . And in a specific application, R_{\min} can be obtained from the information of triangulations. More significantly, with (11), accuracy of the approach can be controlled which is the main contribution of this work. Having got the number of segments, we can build a value list of Green's function phase item for each segment as shown in Table 1.

Then, if we want to get the value of a specific Green's function, we no longer need to calculate the phase item and can directly get the phase item by searching the value list according to the index in (13) where operator $\text{mod}(\bullet)$ represents getting the remainder after division:

$$n = \text{mod}(kR / 2\pi). \quad (13)$$

If n locates in the i -th range of kR , we can directly assign $e^{jkR} \approx v_i$. More importantly, the value list is independent of the problems we are analyzing and is universal for all problems. Thus, we can compute and store it in advance; which is helpful for improving efficiency, especially for large scale problems. For example, in an electromagnetic problem, if there are

$N=10^4$ RWG functions, the size of impedance matrix will be $N^2=10^8$. For each couple of RWG functions, Green's functions between them need to be calculated 4

times. Moreover, if nine-point approximation is adopted to avoid singularity, there will be more than 36×10^8 time calculations of Green's functions.

Table 1: A value list for the phase item of Green's function (M_0 is the number of segments)

No.	1	2	...	i	...	M_0
Range of kR	$[0, 2\pi/M_0]$	$[2\pi/M_0, 4\pi/M_0]$...	$[2\pi(i-1)/M_0, 2\pi i/M_0]$...	$[2\pi(M_0-1)/M_0, 2\pi]$
Value	v_1	v_2	...	v_i	...	v_{M_0}

III. NUMERICAL RESULTS

To validate efficiency and accuracy of the approach, we compare the elapsed time and approximation errors between direct calculation method and the interpolation scheme with working frequency being $f=1$ GHz and the number of segments being $M_0=1.9 \times 10^7$, as shown in Fig. 6 and Fig. 7. And from the results we can see that, the elapsed time of direct calculation method is about 3.5 times of the interpolation scheme with approximation error of the interpolation scheme being less than 10^{-6} .

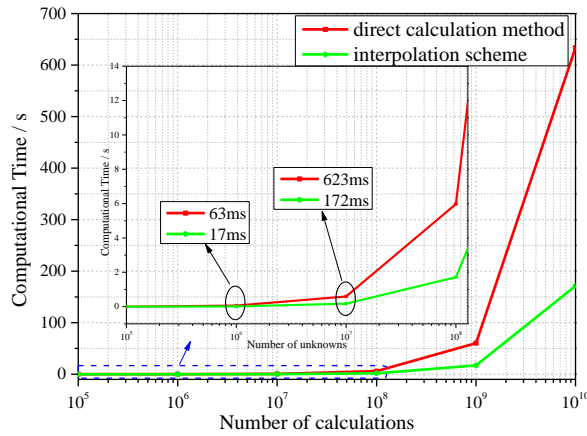


Fig. 6. Changing tendency of computational time varies with the number of calculations. Figures are obtained in a 64-bit personal computer whose dominant frequency is 3.2 GHz.

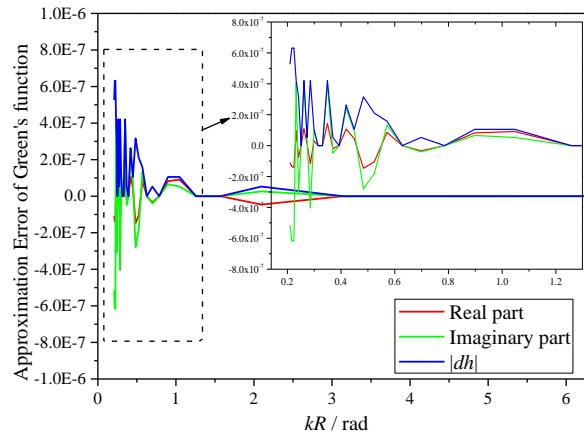


Fig. 7. Approximation error of the interpolation scheme in comparison to direct calculation method.

This demonstrates that the interpolation scheme not only can maintain accuracy but can also improve the efficiency to some extent. Especially, the advantages of the interpolation scheme become bigger with growth of computational scales and this is meaningful for the analysis of large scale problems. More appealing, since the value list of Green's function phase item is built on the basis of kR , it has taken working frequency into consideration which means the value list built for one case can be also reused for other applications. And if we want to get a higher accuracy, we only need to make the value of segments M bigger according to R_{\min} .

Then, to further demonstrate efficiency and accuracy of the proposed interpolation scheme, we calculate the elapsed time in filling impedance matrix for a sphere whose radius is 0.3m with working frequency ranging from 0.5 GHz to 2.0 GHz. Figure 8 shows the comparison between direct calculation method and the proposed interpolation scheme. Results exhibit advantages of the proposed interpolation scheme in improving efficiency. Specifically, for 2.0 GHz, the elapsed time of filling impedance matrix is improved about 15% compared to direct calculation method. This may seem not to be very appealing to us. But, it should be noted that, this improvement is obtained only on the calculation of Green's function. And this scheme can be combined with other fast calculation methods such as FMM to further speed up the solution of MoM matrix.

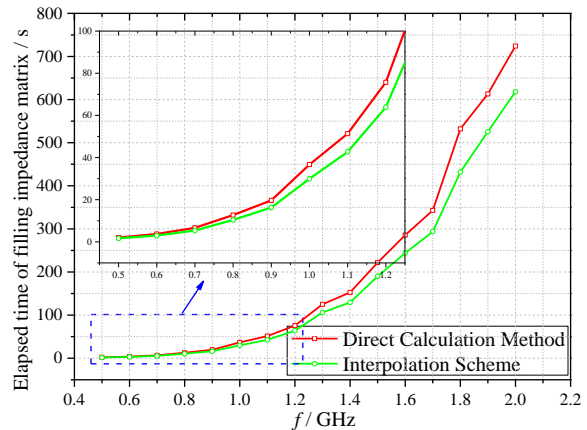


Fig. 8. Elapsed time of filling impedance matrix for a sphere whose radius is 0.3m with working frequency ranging from 0.5 GHz to 2.0 GHz. Sampling rate of triangulation is $\lambda/10$.

Moreover, we also compare the impedance matrices calculated by the proposed interpolation scheme and direct calculation method as shown in Fig. 9. From Fig. 9 we know that, in general, discrepancy between the interpolation scheme and direct calculation method is close to 0 dB which reflects that the proposed scheme has a satisfying accuracy.

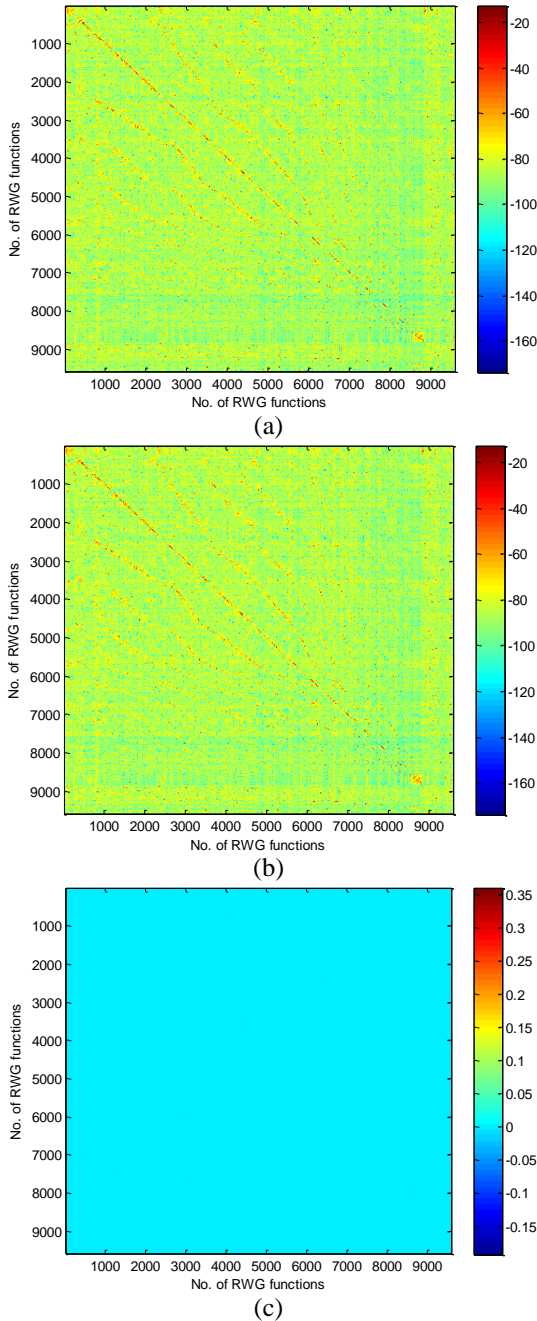


Fig. 9. Impedance matrix ($20\log_{10}|Z|$) of a sphere whose radius is 0.3m with working frequency being 1.25 GHz. (a) Direct calculation method; (b) the interpolation scheme; (c) discrepancy of (a) and (b): $20\log_{10}|Z_a/Z_b|$.

V. CONCLUSION

An interpolation scheme is proposed to accelerate the calculation of Green's function. Through theoretical analysis, we explore the method on how to build a universal value list to ensure a constant accuracy and this is the main contribution of this work. Finally, via numerical examples and the calculation of MoM matrix, accuracy and efficiency of the proposed interpolation scheme is fully validated. Moreover, the scheme is not only limited to the calculation of impedance matrix but also suits for all problems including the calculation of Green's functions.

REFERENCES

- [1] C. Tai, *Dyadic Green Functions in Electromagnetic Theory*. 2nd, IEEE Press, 1994.
- [2] V. I. Okhmatovski and A. C. Cangellaris, "A new technique for the derivation of closed-form electromagnetic Green's functions for unbounded planar layered media," *IEEE Trans. Antennas Propag.*, vol. 50, pp. 1005-1016, July 2002.
- [3] S. M. Jeffrey, J. C. Peter, J. H. Michael, and W. W. Aihua, "A Green's function approach to calculate scattering width for cylindrical cloaks," *Applied Computational Electromagnetics Society*, vol. 25, no. 2, Feb. 2010.
- [4] B. Honarbakhsh and A. Tavakoli, "A closed-form spatial Green's function for the thick microstrip substrate: The meshless interpolation approach," *Applied Computational Electromagnetics Society*, vol. 28, no. 2, Feb. 2013.
- [5] R. F. Harrington, *Field Computation by Moment Method*. New York: Macmillan, 1968.
- [6] N. Engheta, W. D. Murphy, V. Rokhlin, and M. S. Vassilion, "The fast multipole method (FMM) for electromagnetic scattering problems," *IEEE Trans. Antennas Propag.*, vol. 40, no. 6, pp. 634-644, June 1992.
- [7] J. M. Song and W. C. Chew, "Multilevel fast multipole algorithm for solving combined field integral equations of electromagnetic scattering," *Microwave Opt. Tech. Lett.*, vol. 10, no. 1, pp. 14-19, Sep. 1995.
- [8] J. M. Song, C. C. Lu, and W. C. Chew, "MLFMA for electromagnetic scattering from large complex objects," *IEEE Trans. Antennas Propag.*, vol. 45, pp. 1488-1493, Oct. 1997.
- [9] J. M. Rius, J. Parron, E. Ubada, et al., "Multilevel matrix decomposition algorithm for analysis of electrically large electromagnetic problems in 3-D," *Microwave Opt. Tech. Lett.*, vol. 22, no. 3, pp. 15-26, 1999.
- [10] K. F. Sabet, J. C. Cheng, and L. P. B. Katehi, "Efficient wavelet-based modeling of printed circuit antenna arrays," *IET Microwave, Antennas & Propagation*, vol. 146, pp. 289-304, 1999.

- [11] F. X. Canning, "Improved impedance matrix localization method," *IEEE Trans. Antennas Propag.*, vol. 41, no. 5, pp. 659-667, 1993.
- [12] H. H. Hu and Y. F. Sun, "A fast efficient method for computing impedance matrix," *Journal of Hefei University of Technology*, vol. 34, no. 4, Apr. 2011. (In Chinese).
- [13] Y. L. Xu, Y. Hu, et al., "Scattering analysis of periodic composite metallic and dielectric structures with synthetic basis functions," *Applied Computational Electromagnetics Society*, vol. 30, no. 10, Oct. 2015.
- [14] S. M. Rao, D. R. Wilton, and A. W. Glisson, "Electromagnetic scattering by surfaces of arbitrary shape," *IEEE Trans. Antennas Propag.*, vol. AP-30, pp. 409-418, May 1982.
- [15] Y. Kamen and L. Shirman, "Triangle rendering using adaptive subdivision," *IEEE Computer Graphics and Applications*, pp. 95-103, Mar.-Apr. 1998.



Xu Yanlin was born in Anhui, China, in 1990. He received the B.S. degree in Electronic Engineering from National University of Defense Technology, Changsha, China, in 2013, and is currently pursuing the M.S. degree in Electronic Science and Technology at National University of Defense Technology, Changsha, China.

His research interests include computational electromagnetic and its applications in scattering analysis.



Yang Hu was born in Anhui, China, in 1973. He received the Ph.D. degree in Electronic Science and Technology at National University of Defense Technology, Changsha, China, in 2007, and is currently a Professor of National University of Defense Technology.

Yang has been researching on time domain algorithm and its applications, waveguide slot array antenna, UWB antenna, microstrip antenna etc.



Liu Xiang was born in Hunan, China, in 1972. He received B.S. degree in Electronic Technology from National University of Defense Technology, Changsha, China, in 1994, and received M.S. degree in Electronic and Communication Engineering at National University of Defense Technology, Changsha, China, in 2006. He is currently an Associate Professor in Hunan Institute of Science and Technology, Changsha, China.

His research interests are electronic science and communication engineering.



Rongjun Shen was born in Anhui, China, in 1936. He is a Member of the Chinese Academy of Engineering, China. He is also a Professor with the College of Electronic Science and Engineering, National University of Defense Technology, Changsha, China. His current research interests include air survey and satellite communications.

An Empirical Formula for Resonant Frequency Shift due to Jerusalem-Cross FSS with Substrate on One Side

Hsing-Yi Chen and Shu-Huan Wen

Department of Communications Engineering
Yuan Ze University, Chung-Li, Taoyuan, 32003, Taiwan
eehychen@saturn.yzu.edu.tw, s1058603@mail.yzu.edu.tw

Abstract — An empirical formula for calculating the shifted resonant frequencies of Jerusalem-cross frequency selective surfaces (FSSs) with different substrates is derived based on extensive calculations made on widely varying in shifted dual resonant frequencies for substrates with different relative dielectric constants and thickness. The coefficients in the empirical formula were determined by using least-square curve fitting technique to fit 672 sets of shifted resonant frequencies obtained by the HFSS simulator. Numerical results of shifted resonant frequencies obtained from the empirical formula are generally in good agreement with those calculated by the HFSS simulator and measurement. The average error in the shifted resonant frequencies is less than 5 percent. The empirical formula thus provides a simple, inexpensive, and quick method for obtaining optimum geometrical parameters of a dual-band Jerusalem-cross FSS with a substrate consisting of different dielectric constants and thickness for arbitrarily specifying two resonant frequencies.

Index Terms — Empirical formula, Jerusalem-cross frequency selective surface, least-square curve fitting, shifted resonant frequencies.

I. INTRODUCTION

Frequency selective surface (FSS) has a wide variety of applications including design of antennas [1-14], realization of polarizers [15], improvement of transmission for signals through energy-saving glass [16-19], synthesis of artificial magnetic conductors (AMCs) and electromagnetic band-gap surfaces (EBGs) [20-23], design of spatial microwave and optical filters [24-36], invention of electromagnetic absorbers [37-42], and creation of planar metamaterials [43]. The FSS is usually formed by periodic arrays of metallic patches or slots of arbitrary geometries. For a patch FSS, it is designed where transmission is minimum but reflection is maximum in the neighborhood of the resonant frequency. Reverse situation happens to the slot FSS. Here transmission is maximum but reflection is minimum in the neighborhood of the resonant frequency.

Three numerical methods are often used to analyze different types of FSS parameters. They are method of moments (MoM) [24], finite-difference time-domain (FDTD) method [44-46], and finite-element method (FEM) [47]. However, these numerical methods can be costly and labor intensive due to the many electromagnetic equations governing FSS theory which should be solved. Alternatively, the equivalent circuit method [48-50] is much simpler than numerical methods for the design of FSS parameters. A limitation of the equivalent circuit method is that it can be used only for a FSS constructed without substrates. It is expected that the presence of the dielectric substrate will shift the resonant frequencies downwards [51-52]. For a Jerusalem-cross FSS with substrate on one side, resonant frequency will be shifted by a factor between unity and $[(\epsilon_r+1)/2]^{1/2}$ depending on the substrate thickness [25, 53], where ϵ_r is the relative dielectric constant of the substrate.

Based on equivalent circuit models [49], we proposed the least-square curve fitting technique [54] to quickly obtain optimum values of geometrical parameters of a dual-band Jerusalem-cross FSS without substrate for arbitrarily specifying any dual resonant frequencies [55]. The computational time of the proposed technique is less than 30 seconds for obtaining optimum parameters of a dual-band Jerusalem-cross FSS without substrate. However, the proposed technique has a limitation which is only available for a dual-band Jerusalem-cross FSS without substrate. In order to investigate the shift effect of resonant frequency on a dual-band Jerusalem-cross grid with different substrates, one higher resonant frequency and one lower resonant frequency were first arbitrarily specified. Then optimum geometrical parameters of the dual-band Jerusalem-cross FSS without substrate were quickly obtained by using our proposed technique [55] for the dual resonant frequency response. Based on the same optimum geometrical parameters, the shifted dual resonant frequencies of the Jerusalem-cross grid with different substrates on one side were studied by using the Ansoft high-frequency structure simulator (HFSS, Ansoft, Pittsburgh, PA). After further study on shift effects, we derived an empirical

formula for quickly obtaining optimum parameters of a dual-band Jerusalem-cross FSS with substrate for arbitrarily specifying any dual resonant frequencies. The empirical formula was derived based on extensive calculations made on widely varying in shifted dual resonant frequencies for substrates with different relative dielectric constants, conductivities, and thickness.

II. JERUSALEM-CROSS FSS WITHOUT SUBSTRATE

Figure 1 shows a Jerusalem-cross FSS without substrate. Its geometrical parameters p , w , s , h , and d are also shown in Fig. 1. Where p is the periodicity of a unit cell, w is the width of the conductive strip, s is the separation distance between adjacent units, h is the width of the end caps of the Jerusalem-cross, and d is the length of the end caps of the Jerusalem-cross. Based on Langley and Drinkwater's studies [49], for any array of thin, continuous, infinitely long, and perfectly conducting Jerusalem-cross FSSs, the Jerusalem-cross FSS can be replaced by an equivalent circuit model. This equivalent circuit can generate one lower resonant frequency f_{OL} (in reflection band), one higher resonant frequency f_{OH} (in reflection band), and a transmission band frequency f_t . For arbitrarily specifying any dual resonant frequencies, the optimum values of geometrical parameters of a dual-band Jerusalem-cross FSS without substrate can be quickly obtained by using our proposed technique [55]. The specified dual resonant frequencies will have a downward trend if the dual-band Jerusalem-cross FSS is constructed with substrate on one side [25], [51-53]. Therefore, it is worth studying further on the down-shifting effect of the dual resonant frequencies on Jerusalem-cross FSS with different substrates.

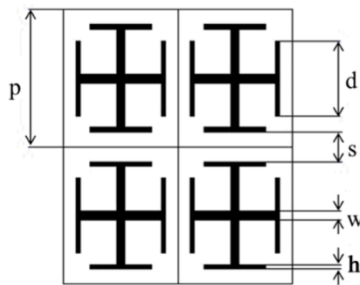


Fig. 1. Geometrical parameters of a FSS constructed with Jerusalem-Cross grids.

III. SUBSTRATE EFFECTS

The FSS is usually printed on a substrate for mechanical strength as shown in Fig. 2. Definitions of geometrical parameters p , w , s , h , and d shown in Fig. 2 are described in Section II. Geometrical parameters t and T are the thickness of the copper foil and the substrate, respectively. Using our proposed technique [55], optimum geometrical parameters ($p = 5.33$ mm, $w = 0.5195$ mm,

$s = 0.3897$ mm, $h = 0.4311$ mm, $d = 3.168$ mm) of a dual-band Jerusalem-cross FSS without substrate are easily obtained for arbitrarily specifying two resonant frequencies of 16.2 and 50.7 GHz. Based on the same optimum geometrical parameters and assuming $t = 0.1$ mm and $T = 0.0$ mm (in air), simulation results of transmission for the Jerusalem-cross FSS without substrate obtained by using the HFSS simulator are shown in Fig. 3. In the simulation, the relative dielectric constant $\epsilon_r = 1.0$ and conductivity $\sigma = 5.8 \times 10^7$ S/m of the copper foil were adopted. Obviously, the dual resonant frequencies f_{OL} and f_{OH} are found at 16.2 and 50.7 GHz, respectively. In the following studies, the optimum geometrical parameters ($p = 5.33$ mm, $w = 0.5195$ mm, $s = 0.3897$ mm, $h = 0.4311$ mm, $d = 3.168$ mm) and the thickness of copper foil $t = 0.1$ mm of the dual-band Jerusalem-cross FSS with substrate are always kept unchanged. However, one of the parameters T (thickness of the substrate), ϵ_r (relative dielectric constant of the substrate), and σ (conductivity of the substrate) is changed in each study. Figure 4 shows the comparison of frequency responses of transmission for the Jerusalem-cross FSS with and without substrate. In HFSS simulations, the relative dielectric constant of the substrate is changed from $\epsilon_r = 1.0$ to $\epsilon_r = 10.0$. The thickness and the conductivity of the substrate $T = 0.8$ mm and $\sigma = 1.3 \times 10^{-3}$ S/m are kept unchanged, respectively. The relative dielectric constant $\epsilon_r = 1.0$ means that the substrate is replaced by air. As shown in Fig. 4, the higher resonant frequency f_H decreases from 50.7 GHz to 23.6 GHz and the lower resonant frequency f_L decreases from 16.2 GHz to 7.5 GHz when the relative dielectric constant increases from $\epsilon_r = 1.0$ to $\epsilon_r = 10.0$, respectively. Figure 5 also shows the comparison of frequency responses for transmission of the Jerusalem-cross FSS with and without substrate. In Fig. 5, the thickness of the substrate is changed from $T = 0.0$ mm to 3.0 mm. The relative dielectric constant and the conductivity of the substrate $\epsilon_r = 3.0$ and $\sigma = 1.3 \times 10^{-3}$ S/m are kept unchanged, respectively. The thickness of the substrate $T = 0.0$ mm also means that the substrate is replaced by air. Figure 5 shows that the higher resonant frequency f_H decreases from 50.7 GHz to 34.6 GHz and the lower resonant frequency f_L decreases from 16.2 GHz to 11.5 GHz when the thickness of the substrate is changed from $T = 0.0$ mm to 3.0 mm, respectively. From the resonant frequency responses shown in Fig. 5, it is found that the shift of resonant frequency is a function of the substrate thickness. In terms of resonant wavelength, the variation of the thickness of the substrate is in the range of $0 - 0.2704 \lambda_{OH}$ and $0 - 0.0864 \lambda_{OL}$, where λ_{OH} and λ_{OL} are the higher and the lower resonant wavelengths of the FSS without substrate, respectively. The shifting factors of the higher and the lower resonant frequencies are found to be $1.0 - 0.682$ and $1.0 - 0.709$ for the thickness of the substrate

ranging from 0.0 to $0.2704 \lambda_{0H}$ and from 0.0 to $0.0864 \lambda_{0L}$, respectively. Figure 6 shows the frequency response of transmission for the Jerusalem-cross FSS with substrate. In Fig. 6, the conductivity of the substrate is changed from $\sigma = 1.0 \times 10^{-5}$ to 1.0×10^{-1} S/m. The relative dielectric constant $\epsilon_r = 3.0$ and the thickness of the substrate $T = 0.8$ mm are kept unchanged. In Fig. 6, it is found that the shift of resonant frequency resulting from the variation of the conductivity of the substrate is insignificant.

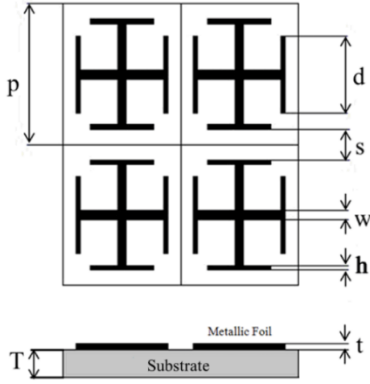


Fig. 2. A Jerusalem-cross FSS with a supporting substrate.

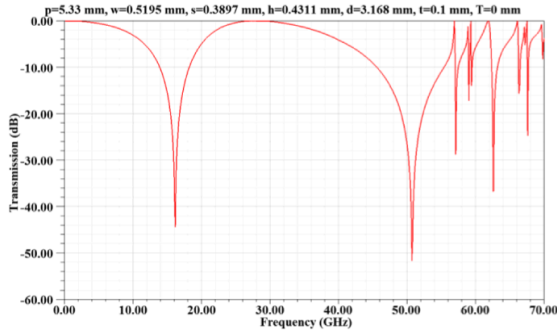


Fig. 3. The frequency responses of transmission of the Jerusalem-cross FSS without substrate.

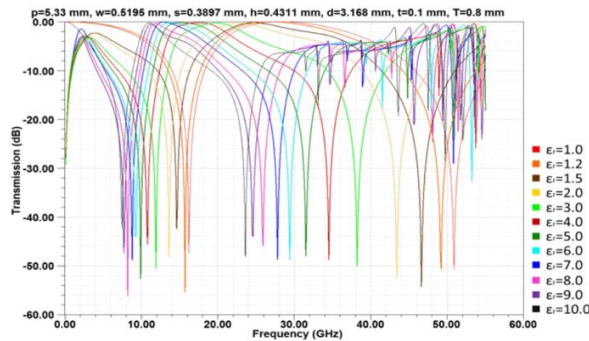


Fig. 4. Comparison of frequency responses of transmission for the Jerusalem-cross FSS with and without substrate. The thickness and the conductivity of the substrate $T = 0.8$ mm and $\sigma = 1.3 \times 10^{-3}$ S/m are kept unchanged, respectively.

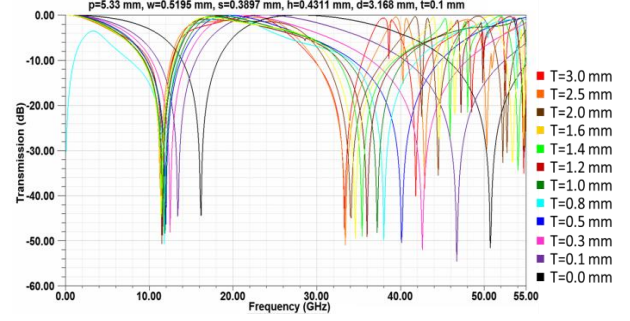


Fig. 5. Comparison of frequency responses of transmission for the Jerusalem-cross FSS with and without substrate. The relative dielectric constant and the conductivity of the substrate $\epsilon_r = 3.0$ and $\sigma = 1.3 \times 10^{-3}$ S/m are kept unchanged, respectively.

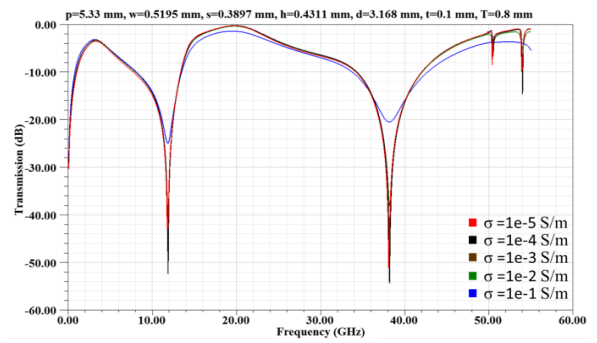


Fig. 6. Frequency responses of transmission for the Jerusalem-cross FSS with substrate. The relative dielectric constant and the thickness of the substrate $\epsilon_r = 3.0$ and $T = 0.8$ mm are kept unchanged, respectively.

IV. LEAST-SQUARE CURVE FITTING TECHNIQUE

Figure 7 and Fig. 8 show that the resonant frequencies of a Jerusalem-cross FSS with a substrate are shifted downwards due to increases in the relative dielectric constant of the substrate from 1.0 to 10 and to increases in the thickness of the substrate from 0.0 to 3.0 mm. Based on observation from Figs. 7 and 8, the following empirical formula (1) is proposed to calculate the dual-band resonant frequencies for a Jerusalem-cross FSS with different substrates:

$$f = \frac{A_5 f_0}{(\epsilon_r + A_1) A_2 \times (T + A_3) A_4}, \quad (1)$$

where f denotes the higher resonant frequency f_H or the lower resonant frequency f_L of a Jerusalem-cross FSS with different substrates. f_0 denotes the higher resonant frequency f_{0H} or the lower resonant frequency f_{0L} of a Jerusalem-cross FSS without substrate. ϵ_r and T (mm) are the relative dielectric constant and thickness of the substrate, respectively. A_1, A_2, A_3, A_4 , and A_5 are unknown coefficients to be solved for the empirical formula.

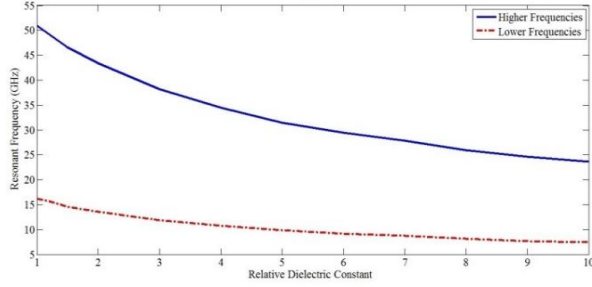


Fig. 7. Resonant frequencies of a Jerusalem-cross FSS with a substrate are shifted downwards due to increases in the relative dielectric constant of the substrate from 1.0 to 10. The thickness and the conductivity of the substrate are $T=0.8$ mm and $\sigma=1.3 \times 10^{-3}$ S/m, respectively. The geometrical parameters of the FSS are $p=5.33$ mm, $w=0.5195$ mm, $s=0.3897$ mm, $h=0.4311$ mm, $d=3.168$ mm, respectively.

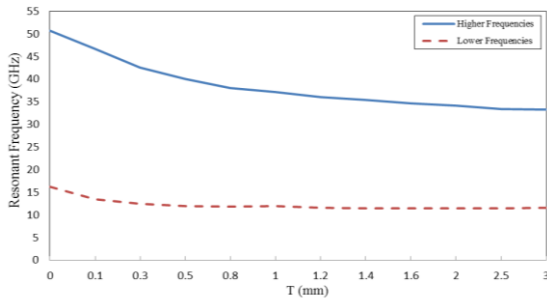


Fig. 8. Resonant frequencies of a Jerusalem-cross FSS with a substrate are shifted downwards due to increases in the thickness of the substrate from 0.0 to 3.0 mm. The relative dielectric constant and the conductivity of the substrate are $\epsilon_r=3.0$ and $\sigma=1.3 \times 10^{-3}$ S/m, respectively. The geometrical parameters of the FSS are $p=5.33$ mm, $w=0.5195$ mm, $s=0.3897$ mm, $h=0.4311$ mm, $d=3.168$ mm, respectively.

Basically, the resonant frequency f is a nonlinear function expressed by (1) in terms of the relative dielectric constant ϵ_r and thickness of the substrate T . The method of differential corrections, together with Newton's iterative method [54], can be used to fit the nonlinear function f . The differential corrections method approximates the nonlinear functions with a linear form that is more convenient to use for an iterative solution. By estimating approximate values of the unknown coefficients $A_1^{(0)}$, $A_2^{(0)}$, $A_3^{(0)}$, $A_4^{(0)}$, and $A_5^{(0)}$, and expanding (1) in a Taylor's series with only the first-order terms retained, we obtain:

$$f = f^{(0)} + \Delta A_1 \left(\frac{\partial f}{\partial A_1} \right)^{(0)} + \Delta A_2 \left(\frac{\partial f}{\partial A_2} \right)^{(0)} + \Delta A_3 \left(\frac{\partial f}{\partial A_3} \right)^{(0)} + \Delta A_4 \left(\frac{\partial f}{\partial A_4} \right)^{(0)} + \Delta A_5 \left(\frac{\partial f}{\partial A_5} \right)^{(0)}. \quad (2)$$

The superscript (0) is used to indicate values obtained after substituting the first guess ($A_1^{(0)}$, $A_2^{(0)}$, $A_3^{(0)}$, $A_4^{(0)}$, and $A_5^{(0)}$), for the unknown coefficients in (1). Equation (2)

is a linear function of the correction terms ΔA_1 , ΔA_2 , ΔA_3 , ΔA_4 , and ΔA_5 , and hence the least-square curve fitting method can be used directly to determine these correction terms. The correction terms, when added to the first guess, give an improved approximation of the unknown coefficients, i.e., $A_1^{(1)} = A_1^{(0)} + \Delta A_1$, $A_2^{(1)} = A_2^{(0)} + \Delta A_2$, $A_3^{(1)} = A_3^{(0)} + \Delta A_3$, $A_4^{(1)} = A_4^{(0)} + \Delta A_4$, and $A_5^{(1)} = A_5^{(0)} + \Delta A_5$. When the improved estimates $A_1^{(1)}$, $A_2^{(1)}$, $A_3^{(1)}$, $A_4^{(1)}$, and $A_5^{(1)}$ are subsequently substituted as new estimates of the unknown coefficients, the Taylor's series reduces to:

$$f = f^{(1)} + \Delta A_1 \left(\frac{\partial f}{\partial A_1} \right)^{(1)} + \Delta A_2 \left(\frac{\partial f}{\partial A_2} \right)^{(1)} + \Delta A_3 \left(\frac{\partial f}{\partial A_3} \right)^{(1)} + \Delta A_4 \left(\frac{\partial f}{\partial A_4} \right)^{(1)} + \Delta A_5 \left(\frac{\partial f}{\partial A_5} \right)^{(1)}, \quad (3)$$

where $f^{(1)}$ as well as its derivatives are obtained by substituting the values of $A_1^{(1)}$, $A_2^{(1)}$, $A_3^{(1)}$, $A_4^{(1)}$, and $A_5^{(1)}$ in (1), respectively. Again, the correction terms ΔA_1 , ΔA_2 , ΔA_3 , ΔA_4 , and ΔA_5 are determined using the least-square curve fitting method. The procedure is continued until the solution converges to within a specified accuracy.

The criterion of best fit of the technique of least-square curve fitting is that the sum of the squares of the errors be a minimum expressed by:

$$S = \sum_{i=1}^N \epsilon_i^2 = \text{minimum}, \quad (4)$$

where the term errors ϵ_i^2 means the difference between the measured (observed) values of the resonant frequencies $f_M(i)$ and computed values from (3) for the i^{th} case, respectively. N is the total number of cases. Substituting (3) into (4), the result yields:

$$S = \sum_{i=1}^N [f_M(i) - f(i)]^2. \quad (5)$$

A necessary condition that a minimum for the error function S exists is that the partial derivatives with respect to each of the correction terms ΔA_1 , ΔA_2 , ΔA_3 , ΔA_4 , and ΔA_5 be zero. For example, in the first iteration,

$$\begin{aligned} \frac{\partial S}{\partial (\Delta A_j)} = & -2 \sum_{i=1}^N \left(\frac{\partial f}{\partial A_j} \right)^{(0)} [f_M(i) - f_1^{(0)} - \Delta A_1 \left(\frac{\partial f}{\partial A_1} \right)^{(0)} - \Delta A_2 \left(\frac{\partial f}{\partial A_2} \right)^{(0)} \\ & - \Delta A_3 \left(\frac{\partial f}{\partial A_3} \right)^{(0)} - \Delta A_4 \left(\frac{\partial f}{\partial A_4} \right)^{(0)} - \Delta A_5 \left(\frac{\partial f}{\partial A_5} \right)^{(0)}] \\ = & 0, \end{aligned} \quad (6)$$

where $j=1, 2, 3, 4$, and 5 . Equation (6) can be expressed as a matrix equation:

$$\begin{bmatrix} \sum_{i=1}^N \left(\frac{\partial f}{\partial A_1} \right)^{(0)2} & \dots & \sum_{i=1}^N \left(\frac{\partial f}{\partial A_1} \right)^{(0)} \left(\frac{\partial f}{\partial A_5} \right)^{(0)} \\ \sum_{i=1}^N \left(\frac{\partial f}{\partial A_2} \right)^{(0)} \left(\frac{\partial f}{\partial A_1} \right)^{(0)} & \dots & \sum_{i=1}^N \left(\frac{\partial f}{\partial A_2} \right)^{(0)} \left(\frac{\partial f}{\partial A_5} \right)^{(0)} \\ \dots & \dots & \dots \\ \sum_{i=1}^N \left(\frac{\partial f}{\partial A_5} \right)^{(0)} \left(\frac{\partial f}{\partial A_1} \right)^{(0)} & \dots & \sum_{i=1}^N \left(\frac{\partial f}{\partial A_5} \right)^{(0)2} \end{bmatrix} \times \begin{bmatrix} \Delta A_1 \\ \Delta A_2 \\ \Delta A_3 \\ \Delta A_4 \\ \Delta A_5 \end{bmatrix} = \begin{bmatrix} \sum_{i=1}^N \left(\frac{\partial f}{\partial A_1} \right)^{(0)} [f_M(i) - f^{(0)}] \\ \sum_{i=1}^N \left(\frac{\partial f}{\partial A_2} \right)^{(0)} [f_M(i) - f^{(0)}] \\ \dots \\ \sum_{i=1}^N \left(\frac{\partial f}{\partial A_5} \right)^{(0)} [f_M(i) - f^{(0)}] \end{bmatrix}. \quad (7)$$

One can easily solve for the correction terms ΔA_1 , ΔA_2 , ΔA_3 , ΔA_4 , and ΔA_5 in (7) by Gaussian elimination method.

V. VALIDATION OF THE EMPIRICAL FORMULA

After curve-fitting 672 sets of shifted resonant frequencies calculated by the HFSS simulator, the coefficients $A_1 = 3.009$, $A_2 = 0.55$, $A_3 = 10.185$ (mm), $A_4 = 0.249$, and $A_5 = 3.66$ are obtained by the least-square curve fitting technique. In order to validate the empirical formula, we compared the shifted resonant frequencies calculated by the HFSS simulator with those obtained by the empirical formula for four different dual-band Jerusalem-cross FSSs with a substrate on one side. Comparisons of shifted resonant frequencies calculated by the HFSS simulator and the empirical formula are shown in Figs. 9-20. From Figs. 9-20, it is shown that numerical results of shifted resonant frequencies obtained from the empirical formula are generally in good agreement with those calculated by the HFSS simulator. The average error in the shifted resonant frequencies is less than 5 percent.

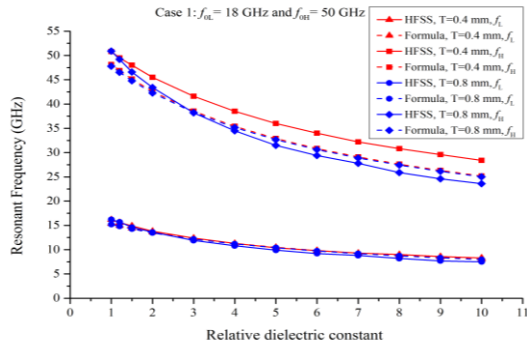


Fig. 9. Comparisons of shifted resonant frequencies calculated by the HFSS simulator and the empirical formula for case 1. The conductivity of the substrate is $\sigma = 1.3 \times 10^{-3}$ S/m ($p = 5.33$, $w = 0.5195$, $s = 0.3897$, $h = 0.4311$, $d = 3.168$, and $t = 0.1$. Unit: mm).

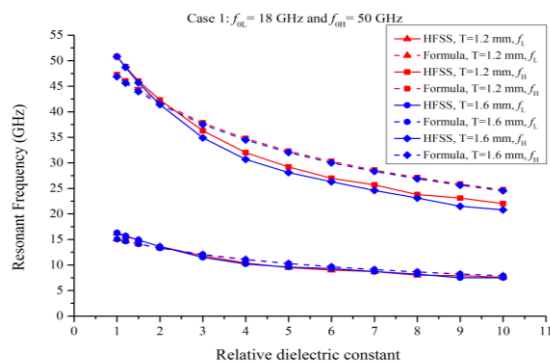


Fig. 10. Comparisons of shifted resonant frequencies calculated by the HFSS simulator and the empirical formula for case 1. The conductivity of the substrate is $\sigma = 1.3 \times 10^{-3}$ S/m ($p = 5.33$, $w = 0.5195$, $s = 0.3897$, $h = 0.4311$, $d = 3.168$, and $t = 0.1$. Unit: mm).

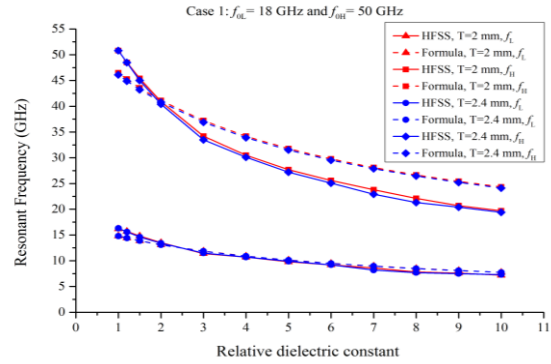


Fig. 11. Comparisons of shifted resonant frequencies calculated by the HFSS simulator and the empirical formula for case 1. The conductivity of the substrate is $\sigma = 1.3 \times 10^{-3}$ S/m ($p = 5.33$, $w = 0.5195$, $s = 0.3897$, $h = 0.4311$, $d = 3.168$, and $t = 0.1$. Unit: mm).

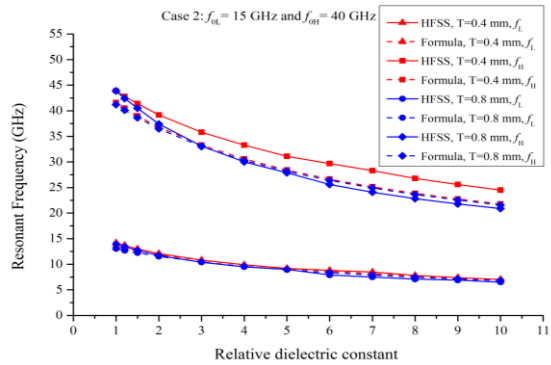


Fig. 12. Comparisons of shifted resonant frequencies calculated by the HFSS simulator and the empirical formula for case 2. The conductivity of the substrate is $\sigma = 1.3 \times 10^{-3}$ S/m ($p = 5.701$, $w = 0.5038$, $s = 0.5413$, $h = 0.4483$, $d = 3.895$, and $t = 0.1$. Unit: mm).

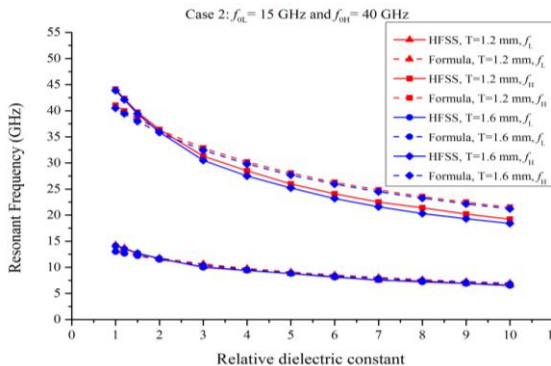


Fig. 13. Comparisons of shifted resonant frequencies calculated by the HFSS simulator and the empirical formula for case 2. The conductivity of the substrate is $\sigma = 1.3 \times 10^{-3}$ S/m ($p = 5.701$, $w = 0.5038$, $s = 0.5413$, $h = 0.4483$, $d = 3.895$, and $t = 0.1$. Unit: mm).

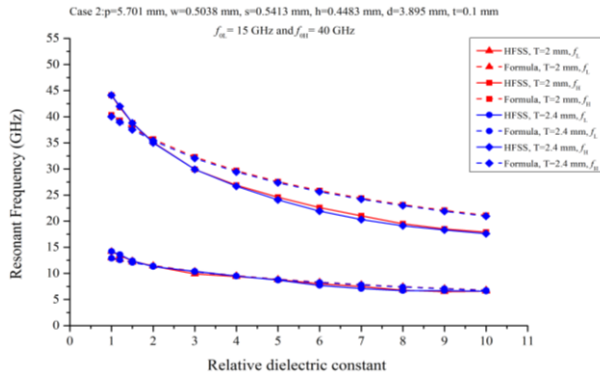


Fig. 14. Comparisons of shifted resonant frequencies calculated by the HFSS simulator and the empirical formula for case 2. The conductivity of the substrate is $\sigma = 1.3 \times 10^{-3}$ S/m ($p = 5.701$, $w = 0.5038$, $s = 0.5413$, $h = 0.4483$, $d = 3.895$, and $t = 0.1$. Unit: mm).

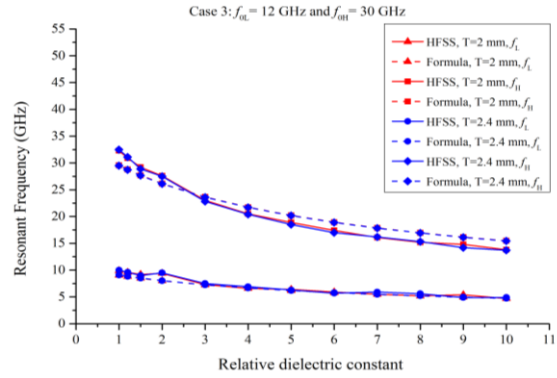


Fig. 17. Comparisons of shifted resonant frequencies calculated by the HFSS simulator and the empirical formula for case 3. The conductivity of the substrate is $\sigma = 1.3 \times 10^{-3}$ S/m ($p = 7.265$, $w = 0.7234$, $s = 0.7829$, $h = 0.5545$, $d = 5.276$, and $t = 0.1$. Unit: mm).

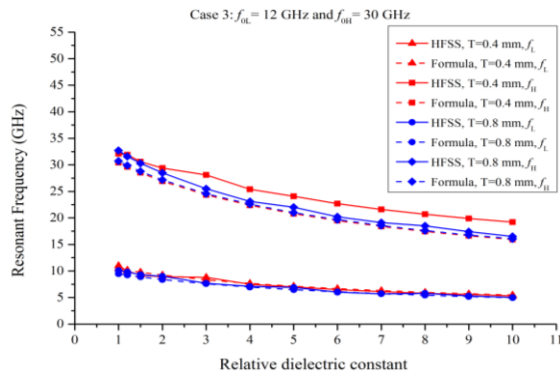


Fig. 15. Comparisons of shifted resonant frequencies calculated by the HFSS simulator and the empirical formula for case 3. The conductivity of the substrate is $\sigma = 1.3 \times 10^{-3}$ S/m ($p = 7.265$, $w = 0.7234$, $s = 0.7829$, $h = 0.5545$, $d = 5.276$, and $t = 0.1$. Unit: mm).

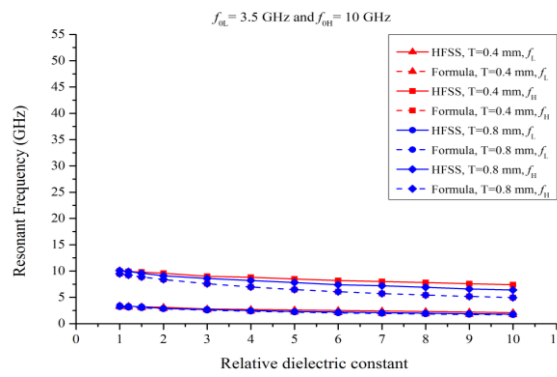


Fig. 18. Comparisons of shifted resonant frequencies calculated by the HFSS simulator and the empirical formula for case 4. The conductivity of the substrate is $\sigma = 1.3 \times 10^{-3}$ S/m ($p = 22.77$, $w = 2.212$, $s = 1.414$, $h = 1.524$, $d = 16.4$, and $t = 0.1$. Unit: mm).

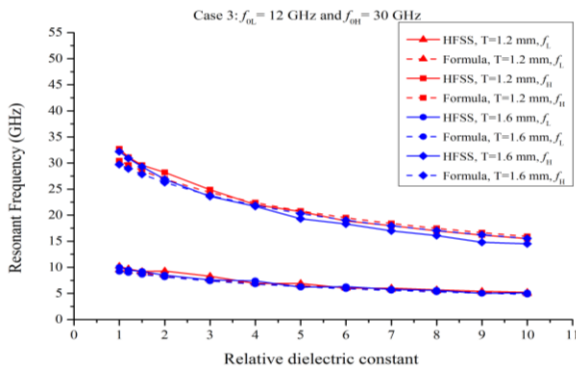


Fig. 16. Comparisons of shifted resonant frequencies calculated by the HFSS simulator and the empirical formula for case 3. The conductivity of the substrate is $\sigma = 1.3 \times 10^{-3}$ S/m ($p = 7.265$, $w = 0.7234$, $s = 0.7829$, $h = 0.5545$, $d = 5.276$, and $t = 0.1$. Unit: mm).

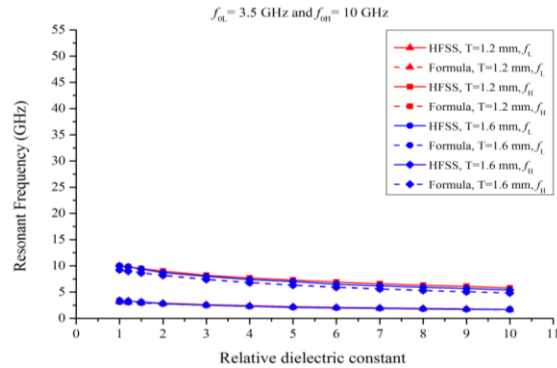


Fig. 19. Comparisons of shifted resonant frequencies calculated by the HFSS simulator and the empirical formula for case 4. The conductivity of the substrate is $\sigma = 1.3 \times 10^{-3}$ S/m ($p = 22.77$, $w = 2.212$, $s = 1.414$, $h = 1.524$, $d = 16.4$, and $t = 0.1$. Unit: mm).

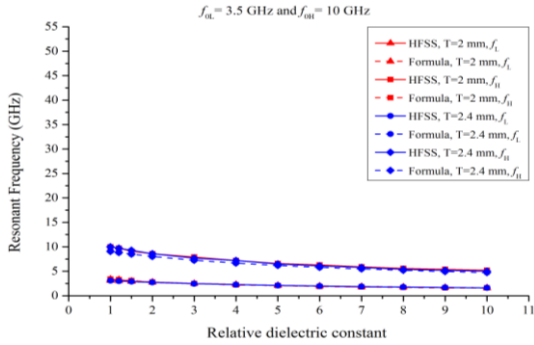


Fig. 20. Comparisons of shifted resonant frequencies calculated by the HFSS simulator and the empirical formula for case 4. The conductivity of the substrate is $\sigma = 1.3 \times 10^{-3}$ S/m ($p = 22.77$, $w = 2.212$, $s = 1.414$, $h = 1.524$, $d = 16.4$, and $t = 0.1$. Unit: mm).

Optimum geometrical parameters of a dual-band Jerusalem-cross FSS with a substrate at arbitrarily specifying two resonant frequencies can be easily and quickly obtained. With Rogers RO4003 substrate as an example, the relative dielectric constant is $\epsilon_r = 3.31$, dielectric loss tangent = 0.0027, and thickness of substrate is $T = 0.8$ mm. The dual operating frequencies are arbitrarily given at $f_1 = 5.8$ GHz and $f_2 = 24.0$ GHz. The lower resonant frequency $f_{0L} = 8.1$ GHz and the higher resonant frequency $f_{0H} = 33.5$ GHz are directly calculated by putting the two specific frequencies of f_1 and f_2 , relative dielectric constant, and thickness of substrate in the empirical formula (1), respectively. It takes 20.66 seconds to obtain the optimum geometrical parameters of the dual-band Jerusalem-cross FSS without substrates at the operating frequencies $f_{0L} = 8.1$ GHz and $f_{0H} = 33.5$ GHz by the technique presented in [55]. The obtained optimum geometrical parameters are $p = 7.577$ mm, $w = 0.6059$ mm, $s = 0.1294$ mm, $h = 0.3793$ mm, and $d = 4.931$ mm. The resonant frequencies of this dual-band Jerusalem-cross FSS without substrate obtained by the HFSS simulator are founded to be $f_{0L} = 8.1$ GHz and $f_{0H} = 31.1$ GHz as shown in Fig. 21. There are 0% and 7.1% differences in the lower and higher resonant frequencies calculated by the HFSS simulator and the technique presented in [55], respectively.

The optimum geometrical parameters of the dual-band Jerusalem-cross FSS with substrates at operating frequencies of f_1 and f_2 will be the same as those obtained for the dual-band Jerusalem-cross FSS without substrates at operating frequencies of $f_{0L} = 8.1$ GHz and $f_{0H} = 31.1$ GHz. The frequency response of this dual-band Jerusalem-cross FSS with substrate calculated by the HFSS simulator is shown in Fig. 21. The optimum geometrical parameters of the dual-band Jerusalem-cross FSS with substrates are $p = 7.577$ mm, $w = 0.6059$ mm, $s = 0.1294$ mm, $h = 0.3793$ mm, $d = 4.931$ mm, $t = 0.035$ and $T = 0.8$ mm.

mm, and $T = 0.8$ mm. From Fig. 21, the dual resonant frequencies of this dual-band Jerusalem-cross FSS with substrate are found to be $f_L = 5.6$ GHz and $f_H = 23.3$ GHz, respectively. Compared with the arbitrarily given frequencies $f_1 = 5.8$ GHz and $f_2 = 24.0$ GHz, there are 3.4% and 2.9% differences in the lower and higher resonant frequencies, respectively. In order to compare with simulation results, the prototype of this dual-band Jerusalem-cross FSS with substrate is fabricated as shown in Fig. 22 and measurements are conducted. Measurement setup is shown in Fig. 23. Comparison of frequency response of this FSS with substrate between simulation results and measurement data is also made as shown in Fig. 21. Good agreement between the simulation results and measurement data has been shown in Fig. 21. From measurement data shown in Fig. 21, it is clear that the lower and higher resonant frequencies are found to be $f_L = 5.9$ GHz and $f_H = 23.4$ GHz, respectively. Compared with the arbitrarily given frequencies $f_1 = 5.8$ GHz and $f_2 = 24.0$ GHz, there are 1.7% and 2.5% differences in the lower and higher resonant frequencies, respectively.

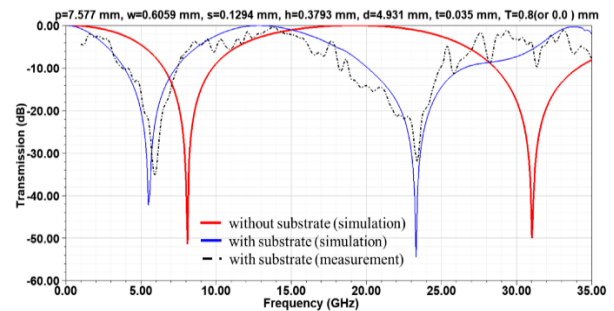


Fig. 21. Frequency responses of a dual-band Jerusalem-cross FSS with and without substrate obtained by HFSS simulator. The geometrical parameters of the FSS are $p = 7.577$, $w = 0.6059$, $s = 0.1294$, $h = 0.3793$, $d = 4.931$, $t = 0.035$, and $T = 0.8$ (or 0.0). Unit: mm.

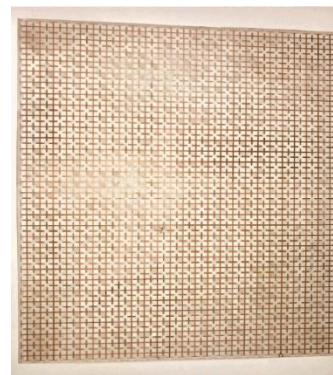


Fig. 22. The prototype of the dual-band Jerusalem-cross FSS with substrate. The geometrical parameters of the FSS are $p = 7.577$, $w = 0.6059$, $s = 0.1294$, $h = 0.3793$, $d = 4.931$, $t = 0.035$, and $T = 0.8$. Unit: mm.

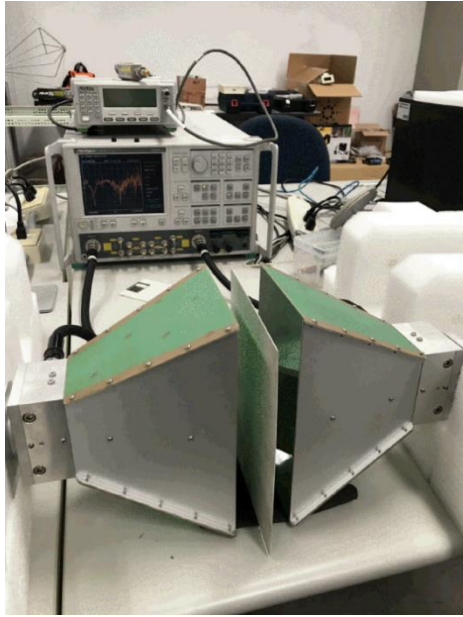


Fig. 23. Measurement setup.

VI. CONCLUSIONS

Based on equivalent circuit models, we proposed a technique to quickly obtain optimum geometrical parameters of a dual-band Jerusalem-cross FSS without substrate for arbitrarily specifying any dual resonant frequencies in the Applied Computational Electromagnetics Society Journal in June, 2015. The drawback of this proposed technique is that it is only available for a dual-band Jerusalem-cross FSS without substrate. In order to overcome the drawback of the proposed technique, firstly, the shifted effects of dual resonant frequencies of Jerusalem-cross FSS with different substrates on one side were extensively studied. After curve-fitting 672 sets of shifted resonant frequencies calculated by the HFSS simulator, we derived an empirical formula for calculating the optimum geometrical parameters of a dual-band Jerusalem-cross FSS with a substrate at arbitrarily specifying two resonant frequencies. The empirical formula is in terms of relative dielectric constant and thickness of substrate. It takes a few seconds to obtain the optimum geometrical parameters of a dual-band Jerusalem-cross FSS with substrates by applying the empirical formula combined with our previous technique. The validity of this empirical formula is checked by comparing simulation results and measurement data of frequency response. The accuracy of the empirical formula is better than 5%. The empirical formula provides a very simple, inexpensive, and quick method for obtaining optimum geometrical parameters of a dual-band Jerusalem-cross FSS with substrate for arbitrarily specifying any dual resonant frequencies. The accuracy of this empirical formula may be within a reasonable error of 5% for substrates with

relative dielectric constants in the range from 1.0 to 10, thickness in the range from 0.0 to 3.0 mm, conductivities in the range from 1.0×10^{-5} to 1.0×10^{-1} S/m, and operating frequencies below 50 GHz.

REFERENCES

- [1] B. A. Munk, R. J. Luebbers, and R. D. Fulton, "Transmission through a 2-layer array of loaded slots," *IEEE Trans. Antennas Propagat.*, vol. AP22, no. 6, pp. 804-809, Nov. 1974.
- [2] M. A. Hiranandani, A. B. Yakovlev, and A. A. Kishk, "Artificial magnetic conductors realized by frequency-selective surfaces on a grounded dielectric slab for antenna applications," *IEE Pro.-Microw. Antennas Propagat.*, vol. 153, no. 5, pp. 487-493, Oct. 2006.
- [3] F. Yang and Y. Rahmat-Samii, "Reflection phase characterizations of the EBG ground plane for low profile wire antenna applications," *IEEE Trans. Antennas Propagat.*, vol. 51, no. 10, pp. 2691-2703, Oct. 2003.
- [4] J. Liang and H. Y. David Yang, "Radiation characteristics of a microstrip patch over an electromagnetic bandgap surface," *IEEE Trans. Antennas Propagat.*, vol. 55, no. 6, pp. 1691-1697, June 2007.
- [5] D. Sievenpiper, L. Zhang, R. F. Jimenez Broas, N. G. Alex'opolous, and E. Yablonovitch, "High-impedance electromagnetic surfaces with a forbidden frequency band," *IEEE Trans. Microwave Theory Tech.*, vol. 47, no. 11, pp. 2059-2074, Nov. 1999.
- [6] Y. Zhang, J. von Hagen, M. Younis, C. Fischer, and W. Wiesbeck, "Planar artificial magnetic conductors and patch antennas," *IEEE Trans. Antennas Propagat.*, vol. 51, no. 10, pp. 2704-2712, Oct. 2003.
- [7] X. L. Bao, G. Ruvio, M. J. Ammann, and M. John, "A novel GPS patch antenna on a fractal high-impedance surface substrate," *IEEE Antennas Wireless Propagat. Lett.*, vol. 5, pp. 323-326, 2006.
- [8] H. Mosallaei and K. Sarabandi, "Antenna miniaturization and bandwidth enhancement using a reactive impedance substrate," *IEEE Trans. Antennas Propagat.*, vol. 52, no. 9, pp. 2403-2414, Sep. 2004.
- [9] R. F. J. Broas, D. F. Sievenpiper, and E. Yablonovitch, "A high-impedance ground plane applied to a cellphone handset geometry," *IEEE Trans. Microw. Theory Tech.*, vol. 49, no. 7, pp. 1262-1265, July 2001.
- [10] A. P. Feresidis, G. Goussetis, S. Wang, and J. C. Vardaxoglou, "Artificial magnetic conductor surfaces and their application to low-profile high-gain planar antennas," *IEEE Trans. Antennas Propagat.*, vol. 53, no. 1, pp. 209-215, Jan. 2005.
- [11] H. Li, S. Khan, J. Liu, and S. He, "Parametric

- analysis of Sierpinski-like fractal patch antenna for compact and dual band WLAN applications,” *Microw. Opt. Technol. Lett.*, vol. 51, no. 1, pp. 36-40, Jan. 2009.
- [12] M. Hosseini and S. Bashir, “A novel circularly polarized antenna based on an artificial ground plane,” *Progress Electromagn. Research Lett.*, vol. 5, pp. 13-22, 2008.
- [13] H.Y. Chen and Y. Tao, “Bandwidth enhancement of a U-Slot patch antenna using dual-band frequency selective surface with double rectangular ring elements,” *Microw. Opt. Technol. Lett.*, vol. 53, no. 7, pp. 1547-1553, July 2011.
- [14] H. Y. Chen and Y. Tao, “Performance improvement of a U-slot patch antenna using a dual-band frequency selective surface with modified Jerusalem cross elements,” *IEEE Trans. Antennas Propagat.*, vol. 59, no. 9, pp. 3482-3486, Sep. 2011.
- [15] R. Ulrich, “Far-infrared properties of metallic mesh and its complementary structure,” *Infrared Phys.*, vol. 7, no. 1, pp. 37-50, 1967.
- [16] M. Philippakis, C. Martel, D. Kemp, M. C. S. M. R. Allan, S. Appleton, W. Damerell, C. Burton, and E. A. Parker, “Application of FSS structures to selectively control the propagation of signals into and out of buildings,” ERA Technology, Leatherhead, Surrey, U.K., Tech. Rep., 2004.
- [17] M. Gustafsson, A. Karlsson, A. P. P. Rebelo, and B. Widenberg, “Design of frequency selective windows for improved indoor outdoor communication,” *IEEE Trans. Antennas Propagat.*, vol. 54, no. 6, pp. 1897-1900, June 2006.
- [18] G. I. Kiani, L. G. Osslon, A. Karlsson, and K. P. Esselle, “Transmission of infrared and visible wavelengths through energy-saving glass due to etching of frequency-selective surfaces,” *IET Microw. Antennas Propagat.*, vol. 4, pp. 955-961, 2010.
- [19] G. I. Kiani, L. G. Osslon, A. Karlsson, K. P. Esselle, and M. Nilsson, “Cross-dipole bandpass frequency selective surface for energy-saving glass used in building,” *IEEE Trans. Antennas Propagat.*, vol. 59, no. 2, pp. 520-525, Feb. 2011.
- [20] D. J. Kern, D. H. Werner, A. Monorchio, L. Lanuzza, and M. J. Wilhelm, “The design synthesis of multiband artificial magnetic conductors using high impedance frequency selective surfaces,” *IEEE Trans. Antennas Propagat.*, vol. 53, no. 1, pp. 8-17, Jan. 2005.
- [21] J. McVay, N. Engheta, and A. Hoorfar, “High impedance metamaterial surfaces using Hilbert-curve inclusions,” *IEEE Microw. Wireless Compon. Lett.*, vol. 14, pp. 130-132, 2004.
- [22] J. Bell and M. Iskander, “A low-profile archimedean spiral antenna using an EBG ground plane,” *IEEE Antennas Wireless Propagat. Lett.*, vol. 3, pp. 223-226, 2004.
- [23] F. Costa, S. Genovesi, and A. Monorchio, “On the bandwidth of high-impedance frequency selective surfaces,” *IEEE Antennas Wireless Propagat. Lett.*, vol. 8, pp. 1341-1344, 2009.
- [24] R. Mittra, C. H. Chan, and T. Cwik, “Techniques for analyzing frequency selective surfaces - A review,” *Pro. IEEE*, vol. 76, no. 12, pp. 1593-1615, Dec. 1988.
- [25] B. A. Munk, *Frequency Selective Surfaces - Theory and Design*. John Wiley & Sons, Inc., New York, 2000.
- [26] R. Dickie, R. Cahill, H. Gamble, V. Fusco, M. Henry, M. Oldfield, P. Huggard, P. Howard, N. Grant, Y. Munro, and P. de Maagt, “Submillimeter wave frequency selective surface with polarization independent spectral responses,” *IEEE Trans. Antennas Propagat.*, vol. 57, no. 7, pp. 1985-1994, July 2009.
- [27] F. R. Yang, K. P. Ma, Y. Qian, and T. Itoh, “A uniplanar compact photonic-bandgap (UC-PBG) structure and its applications for microwave circuits,” *IEEE Trans. Microw. Theory Tech.*, vol. 47, no. 8, pp. 1509-1514, Aug. 1999.
- [28] C. N. Chiu, C. H. Kuo, and M. S. Lin, “Bandpass shielding enclosure design using multipole-slot arrays for modern portable digital devices,” *IEEE Trans. Electromagn. Compat.*, vol. 50, no. 4, pp. 895-904, Nov. 2008.
- [29] M. S. Zhang, Y. S. Li, C. Jia, and L. P. Li, “Signal integrity analysis of the traces in electromagnetic-bandgap structure in high-speed printed circuit boards and packages,” *IEEE Trans. Microw. Theory Tech.*, vol. 55, no. 5, pp. 1054-1062, Nov. 2007.
- [30] K. Sarabandi and N. Behdad, “A frequency selective surface with miniaturized elements,” *IEEE Trans. Antennas Propagat.*, vol. 55, no. 5, pp. 1239-1245, May 2007.
- [31] T. Kamgaing and O. M. Ramahi, “Design and modeling of high-impedance electromagnetic surfaces for switching noise suppression in power planes,” *IEEE Trans. Electromagn. Compat.*, vol. 47, no. 3, pp. 479-489, Aug. 2005.
- [32] T. K. Wu and S. W. Lee, “Multiband frequency selective surface with multiring patch elements,” *IEEE Trans. Antennas Propagat.*, vol. 42, no. 11, pp. 1484-1490, Nov. 1994.
- [33] T. K. Wu, “Four-band frequency selective surface with double-square-loop patch elements,” *IEEE Trans. Antennas Propagat.*, vol. 42, no. 12, pp. 1659-1663, Dec. 1994.
- [34] H. L. Liu, K. L. Ford, and R. J. Langley, “Design methodology for a miniaturized frequency selective surface using lumped reactive components,” *IEEE Trans. Antennas Propagat.*, vol. 57, no. 9, pp.

- 2732-2738, Sep. 2009.
- [35] R. R. Xu, H. C. Zhao, Z. Y. Zong, and W. Wu, "Dual-Band capacitive loaded frequency selective surfaces with close band spacing," *IEEE Microw. Wireless Compon. Lett.*, vol. 18, no. 12, Dec. 2008.
- [36] G. I. Kiani, K. L. Ford, K. P. Esselle, A. R. Weily, C. Panagamuwa, and J. C. Batchelor, "Single-layer bandpass active frequency selective surface," *Microw. Opt. Technol. Lett.*, vol. 50, no. 8, pp. 2149-2151 Aug. 2008.
- [37] G. I. Kiani, K. L. Ford, K. P. Esselle, A. R. Weily, and C. J. Panagamuwa, "Oblique incidence performance of a novel frequency selective surface absorber," *IEEE Trans. Antennas Propagat.*, vol. 55, no. 10, pp. 2931-2934, Oct. 2007.
- [38] B. A. Munk, P. Munk, and J. Pryor, "On designing Jaumann and circuit analog absorbers (CA absorbers) for oblique angle of incidence," *IEEE Trans. Antennas Propagat.*, vol. 55, no. 1, pp. 186-193, Jan. 2007.
- [39] A. K. Zadeh and A. Karlsson, "Capacitive circuit method for fast and efficient design of wideband radar absorbers," *IEEE Trans. Antennas Propagat.*, vol. 57, no. 8, pp. 2307-2314, Aug. 2009.
- [40] A. Itou, O. Hashimoto, H. Yokokawa, and K. Sumi, "A fundamental study of a thin wave absorber using FSS technology," *Electron. Commun. Jpn.*, vol. 87, pt. 1, pp. 77-86, 2004.
- [41] A. Itou, H. Ebara, H. Nakajima, K. Wada, and O. Hashimoto, "An experimental study of a wave absorber using a frequency-selective surface," *Microw. Opt. Technol. Lett.*, vol. 28, pp. 321-323, 2001.
- [42] G. I. Kiani, A. R. Weily, and K. P. Esselle, "A novel absorb/transmit FSS for secure indoor wireless networks with reduced multipath fading," *IEEE Microw. Wireless Compon. Lett.*, vol. 16, no. 6, pp. 378-380, 2006.
- [43] N. Engheta and R. W. Ziolkowski, *Metamaterials: Physics and Engineering Explorations*. Hoboken/Piscataway, NJ: Wiley-IEEE Press, 2006.
- [44] R. Baggen, M. Martinez-Vazquez, J. Leiss, and S. Holzwarth, "Comparison of EBG substrates with and without vias for GALILEO/GPS applications," In *Proc. EuCAP 2007, 2nd European Conf. Antennas Propagat.*, Edinburgh, UK, 2007.
- [45] Y. Fan, B. L. Ooi, H. D. Hriston, and M. S. Leong, "Compound diffractive lens consisting of Fresnel zone plate and frequency selective screen," *IEEE Trans. Antennas Propagat.*, vol. 58, no. 6, pp. 1842-1847, June 2010.
- [46] P. Harms, R. Mittra, and W. Ko, "Implementation of the periodic boundary-condition in the finite-difference time-domain algorithm for FSS structures," *IEEE Trans. Antennas Propagat.*, vol. 42, no. 9, pp. 1317-1324, Sep. 1994.
- [47] J. L. Volakis, T. Ozdemir, and J. Gong, "Hybrid finite-element methodologies for antennas and scattering," *IEEE Trans. Antennas Propagat.*, vol. 45, no. 3, pp. 493-507, Mar. 1997.
- [48] T. W. Leonard and J. W. Cofer, "A new equivalent circuit representation for the Jerusalem cross," in *Proc. IEE Int. Conf. Antennas Propagat.*, London, England, vol. 2, pp. 65-69, 1978.
- [49] R. J. Langley and A. J. Drinkwater, "Improved empirical model for the Jerusalem cross," *IEE Proc.*, vol. 129, Pt. H., no.1, pp. 1-6, Feb. 1982.
- [50] M. Hosseinipناه and Q Wu, "Equivalent circuit model for designing of Jerusalem cross-based artificial magnetic conductors," *Radioeng.*, vol. 18, no. 4, pp. 544-550, Dec. 2009.
- [51] T. Cwik, R. Mittra, K. Lang, and T. K. Wu, "Frequency selective screens," *IEEE Antennas Propagat. Soc. Newslett.*, vol. 29, no. 2, pp. 5-10, Apr. 1987.
- [52] T. K. Wu, "Dielectric properties measurement of substrate and support materials," *Microw. Opt. Technol. Lett.*, vol. 3, no. 8, pp. 283-286, Aug. 1990.
- [53] L. B. Wang, K. Y. See, J. W. Zhang, B. Salam, and A. C. W. Lu, "Ultrathin and flexible screen-printed metasurfaces for EMI shielding application," *IEEE Trans. Electromagn. Compat.*, vol. 53, no. 3, pp. 700-705, Aug. 2011.
- [54] L. H. Lafara, *Computer Method for Science and Engineering*. New York: Hayden, 1973, pp. 148-157.
- [55] H. Y. Chen, T. H. Lin, and P. K. Li, "Fast design of Jerusalem-cross parameters by equivalent circuit model and least-square curve fitting technique," *Appl. Comput. Electromagn. Soc. J.*, vol. 30, no. 7, pp. 717-730, July 2015.



Hsing-Yi Chen was born in Taiwan, in 1954. He received the B.S. and M.S. degrees in Electrical Engineering in 1978 and 1981 from Chung Yuan Christian University and National Tsing Hua University, respectively. He received the Ph.D. degree in Electrical Engineering from University of Utah, Salt Lake City, Utah in 1989. He joined the faculty of the Department of Electrical Engineering, Yuan Ze University, Taiwan, in September 1989. He was the Chairman of Electrical Engineering from 1996 to 2002, the Chairman of Communications Engineering from 2001 to 2002, the Dean of Engineering College from 2002 to 2006, the Dean of Electrical and Communication Engineering College from 2006 to 2012, and the Dean of Research and Development Office from

2012 to 2013. Currently, he is the Dean of General Affairs Office, Yuan Ze University. His current interests include electrostatic discharge, electromagnetic scattering and absorption, waveguide design, radar systems, electromagnetic compatibility and interference, bioelectromagnetics, electromagnetic radiation hazard protection, and applications of frequency selective surface.

He is a member of Phi Tau Phi. He was also a member of the editorial board of the *Journal of Occupational Safety and Health* from 1996 to 1997. He was elected an Outstanding Alumnus of the Tainan Second High School in 1995. He has been the recipient of numerous awards including the 1990 Distinguished Research, Service, and Teaching Award presented by the Yuan Ze University, the 1999 and 2002 YZU Outstanding Research Award, and the 2005 Y. Z. Hsu

Outstanding Professor Award for Science, Technology & Humanity Category. He was awarded Chair Professor by Far Eastern Y. Z. Hsu Science and Technology Memorial Foundation in 2008. His name is listed in *Who's Who in the World* in 1998.



Shu-Huan Wen was born in Taiwan, in 1991. He received the B.S. degree in Electronic Engineering from Oriental Institute of Technology in 2013. He is currently working toward the Ph.D. degree in Communications Engineering at Yuan Ze University, Taiwan. His research interests include patch antenna design, frequency selective surfaces, EM field measurement, and computational electromagnetics.

The Human Body Modelled by Canonical Geometric Shapes for the Analysis of Scattered E-fields

G. Manfredi^{1,2}, V. Di Mattia³, P. Russo³, A. De Leo³, and G. Cerri³

¹Department of Electromagnetism and Radar (DEMR)
ONERA, Université Paris Saclay, Palaiseau Cedex, F-91123
France giovanni.manfredi@onera.fr

²SONDRA
CentraleSupélec, Gif-sur-Yvette, 91190
France giovanni.manfredi@supelec.fr

³Department of Information Engineering
Università Politecnica delle Marche, Ancona, 60131, Italy
v.dimattia@univpm.it, paola.russo@staff.univpm.it, a.deleo@univpm.it, g.cerri@staff.univpm.it

Abstract — The objective of this paper is to propose a simplified model of a human body to be used in electromagnetic problems involving high frequency field scattering. Canonical geometric shapes, analytically described, represent the body. The accuracy of the model was tested comparing the field scattered by the simplified body representation with the one scattered by a more realistic phantom. At first, the influence of anatomical details of the body was analysed, comparing the electromagnetic field reflected by a realistic human head with the backscattering of spheres and of an ellipsoid. A second test concerns the human body, modelled by sphere, parallelepiped and cylinders. In this case, the possibility of reconstructing a wideband pulse scattered by the whole body with the superposition of pulses scattered by its separated parts was demonstrated. Both analyses were carried out in the frequency range 3-5 GHz using a full wave numerical simulator.

Index Terms — Computationally body model, on body model, scattering.

I. INTRODUCTION

The optimal design of contact-less monitoring systems of the main human physical and physiological activities involves analysis of the interactions between the human body and electromagnetic (EM) waves [1,2]. These studies are widely carried out by means of computer simulations, which are well suited for a careful study, but involve the use of detailed human body models [3-5]. Most EM solvers perform an automatic meshing on the simulated objects, choosing an arbitrary number of cells per wavelength.

Starting from the S-band, the human body becomes

an electrically large structure, and several cells per wavelength are required to model the target and to decrease the numerical dispersion error [6-8].

This implies simulations that are highly memory and time intensive, depending on the body model and the frequency of interest [9-11].

Several research works have focused on modelling simplified human body mannequins to reduce the computational burden. Perfectly electric conductor cylinders were employed to reproduce the body [12] or to predict the effect of people on indoor propagation channel [13]. The validation of the models was carried out with experimental investigations, comparing the signal attenuation between the transmitting and the receiving units and antennas located on the simplified human model and on a real target. Nevertheless, to our knowledge, very few studies have been done to assess the characteristics of a body model to be used in scattering problems, guaranteeing accuracy and computational efficiency at the same time. This issue is dealt with in the paper, and an efficient simplified human model is accurately analysed.

In detail, a human body represented by canonical geometrical shapes is proposed. It exhibits many advantages: 1) all the elements are analytically described; 2) it is simple and easy to implement; 3) it is very flexible, because all postures can be represented; 4) movements and animations are possible; 5) it is effective in a wide frequency range.

The accuracy of the model was tested by comparing the waveforms of EM pulse, reflected by a realistic human body and by the proposed model.

A human head and the effect of anatomical details such as nose, mouth and ears were evaluated. A further

investigation was extended to the whole body, analysing the possibility of retrieving the field backscattered by the whole body as superposition of the field reflected by separated body parts.

II. HUMAN FACE REPRESENTED BY CANONICAL GEOMETRIC SHAPES

A previous work [2] pointed out that the most proper frequency range to detect the breathing rate or body activities during real-time monitoring is 2-6 GHz. In this frequency range, approximate skin depth is lower than 1.5 cm. Therefore, a body representation with an accurate knowledge of internal tissues is useless, because only a thin external layer is involved in the evaluation of the scattered field.

Another aspect concerns the representation of external details of the body, such as the nose, mouth and ears. The great variability of such anatomical details from one individual to another makes an excessively accurate modelling ineffective.

In this section, the relevance of the anatomical details for the evaluation of EM backscattering was analysed, both in time and in frequency domain. The EM field reflected by the head of a Specific Anthropomorphic Mannequin (SAM) was compared with the backscattering of canonical geometric shapes, using a full wave numerical tool (CST Microwave Studio [14]). The chosen targets are shown in Fig. 1.

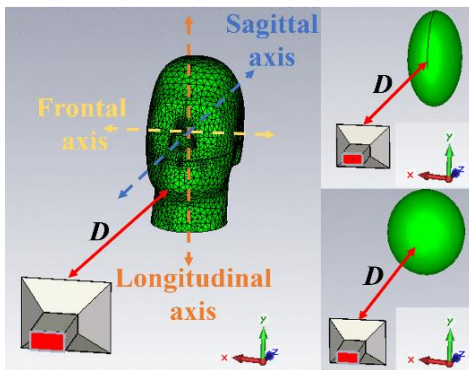


Fig. 1. Geometric configurations implemented in CST Microwave Studio: head on the left side; spheres of different radii and an ellipsoid on the right side.

More precisely, four spheres and one ellipsoid were analysed. The first sphere has a radius $r = 109$ mm, providing a volume equivalent to SAM's head. The other spheres have a radius of 80 mm, 126 mm and 132 mm, which correspond to the dimensions of the head, along the frontal, sagittal and longitudinal axes respectively. The ellipsoid has dimensions of 80 mm x 126 mm x 132 mm. The head and solids were filled with a homogeneous dielectric material with the same properties as the skin

(relative permittivity $\epsilon_r = 42$, and conductivity $\sigma = 3.6$ S/m [15]). Both targets were placed at a distance of $D = 1.5$ m from a horn antenna along the z-direction. The excitation signal is a modulated Gaussian pulse, generated by the CST Microwave Studio's time domain solver, whose spectrum is in the range 3-5 GHz. The wave travels in free space along the z-direction and the electric E-field is polarized in the y-direction. Figure 2 and Fig. 3 show the E-fields reflected by the solids and by the head, observed at 1 m along the z-axis, in time (TD) and frequency (FD) domain respectively. For a better comparison among the waveforms, the cross-correlation r_{xy} was evaluated between the E-fields diffracted by each solid (y) and by the head (x). Table 1 reports the absolute value of the maximum amplitude of the backscattered electric fields, and the results of the corresponding r_{xy} in both TD and FD.

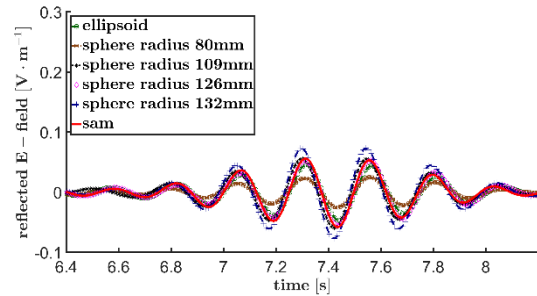


Fig. 2. E-fields backscattered by the head and the solids, observed in time domain.

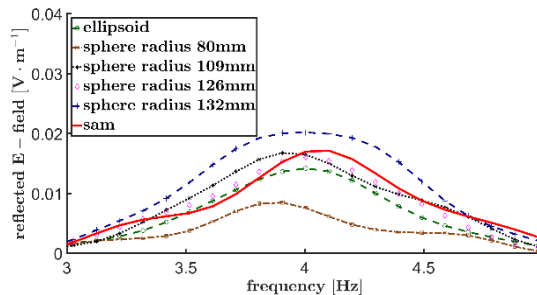


Fig. 3. E-fields backscattered by the head and the solids, observed in frequency domain.

We may appreciate that the sphere ($r = 109$ mm) with equivalent volume to the head provides a response that best fits the realistic situation.

Moreover, the reflected waves were normalized to the maximum peak value and correlated, in order to observe how their distortion depends on the scattering surface. All the chosen geometric shapes present a correlation of 0.99. The result proves that the representation of the anatomical details can be neglected in the range of a few GHz.

Table 1: Maximum field intensity and cross-correlation between the E-field waveforms diffracted by the spheres, the ellipsoid and the head

Target	E-field [V/m]	TD: r_{xy}	FD: r_{xy}
SAM	0.058	1	1
Sphere ($r = 80\text{mm}$)	0.025	0.44	0.46
Sphere ($r = 109\text{mm}$)	0.059	0.99	0.98
Sphere ($r = 126\text{mm}$)	0.055	0.95	0.95
Sphere ($r = 132\text{mm}$)	0.077	0.74	0.74
Ellipsoid	0.047	0.82	0.83

III. NUMERICAL RESULTS OF THE E-FIELDS SCATTERED BY THE HUMAN BODY PARTS

The results achieved in the preceding section were extended to the whole body, analysing the possibility to retrieve the electric field backscattered by the whole body as superposition of the electric fields backscattered by separated body parts. The error due to the approximation of neglecting mutual electromagnetic coupling between body parts was estimated to quantify the trade-off between accuracy and computational efficiency.

The human body was modelled as a collection of sphere, cylinders and parallelepiped to reproduce head, chest, arms and legs, whose dimensions are defined according to those of a realistic body. The height of the human model is 1.68 m and each part is characterized by the dielectric properties of the skin. Furthermore, the mutual coupling among body parts was neglected.

The analysis was carried out with the same simulation set-up described in the previous section. Figure 4 shows the E-fields scattered by each body parts and observed at the distance D of 1.5 m in the time domain. As expected, at this position, the E-field reflected by the chest is greater than any other E-fields, because of its dimension and flat surface.

The comparison between the E-fields reflected by the total body E_{r1} (mutual coupling considered) and by its individual parts E_{r2} (mutual coupling neglected) was examined both in time and in frequency domain.

The results are shown in Fig. 5 and Fig. 6, respectively. The cross-correlation pointed out a similarity between the two curves equal to 0.85 in both domains. Since the waveforms are quite similar, we can infer that the different field contributions due to each body part are combined with the proper time delay; the peak amplitude difference is due to the numerical accuracy, and is not significantly affected by the assumption of negligible mutual coupling among body parts.

To highlight this aspect, further simulations were performed to evaluate the influence of spatial discretization.

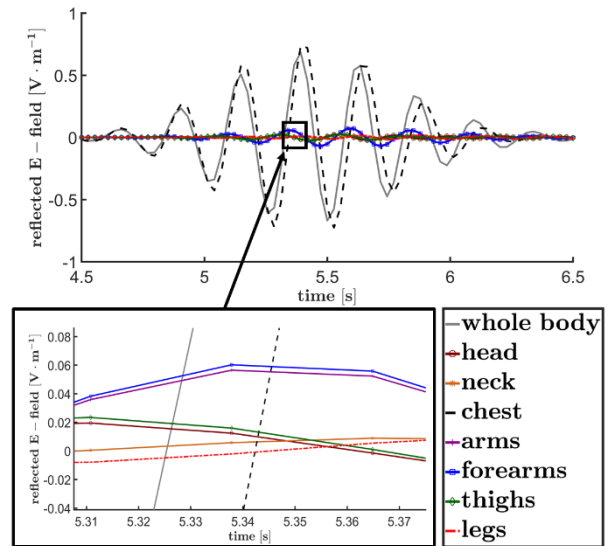


Fig. 4. Electric fields backscattered by individual elements of the human body (time domain).

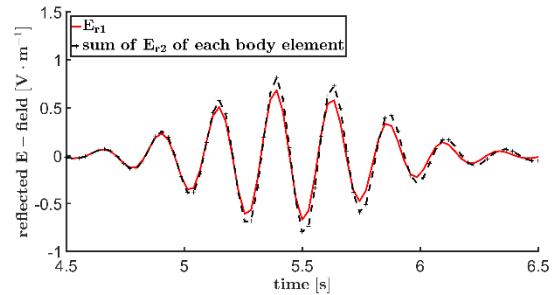


Fig. 5. E-field scattered by the whole body phantom and the sum of the E-fields scattered by each body part (time domain).

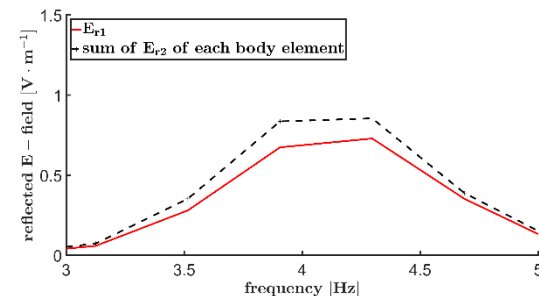


Fig. 6. E-field scattered by the whole body phantom and the sum of the E-fields scattered by each body part (frequency domain).

The total calculation times required to simulate separately the body parts as a function of the spatial resolution, and the cross-correlation coefficient r_{xy} between the resulting curves mentioned above, are shown in Table 2.

The computer employed for the simulations has the following characteristics: processor Intel(R) Core(TM) i5-5200 CPU, 8GB RAM DDR4, graphics card NVIDIA GEFORCE 820M 1800MHz.

Table 2: Analysis of the numerical accuracy as a function of spatial discretization

Resolution (Cells per Wavelength)	Calculation Time	Cross-Correlation
$\lambda/8$	26 h, 14 m, 28 s	0.83
$\lambda/10$	45 h, 34 m, 25 s	0.85
$\lambda/12$	87 h, 50 m, 39 s	0.89

As expected, a finer grid provides better accuracy in the computation of the peak values and improves the correlation coefficient, but the waveform is not significantly affected by this parameter and no distortion can be appreciated.

IV. CONCLUSION

In this paper, we have demonstrated that in the S and C bands a simplified model of a human body compared to realistic model can be efficiently employed to evaluate the reflected electric fields. The correlation coefficients were analysed to compare in time and in frequency domain the realistic and the approximate solutions. The results outline that from a computational point of view, the body elements can be replaced with homogeneous geometric solids, and the anatomical details, as well as the mutual coupling among body parts, can be neglected. The simplified model proves to be efficient, light in terms of computational burden, and sufficiently accurate to analyse the interactions between the human body and the EM fields.

REFERENCES

[1] A. Rahman, Y. Ishii, and V. Lubecke, "UAV-radar system for vital sign monitoring," *ACES Journal*, vol. 1, no. 5, 2016.

[2] V. Petrini, V. Di Mattia, A. De Leo, P. Russo, V. P. Mariani, G. Manfredi, G. Cerri, and L. Scalise, *Domestic Monitoring of Respiration and Movement by an Electromagnetic Sensor*. Ambient Assisted Living (Springer International Publishing), Basel, 2014.

[3] 3D CAD Browser. <http://www.3dcadbrowser.com/3dmodels.aspx?category=1182>, accessed May 2018.

[4] REMCOM - VariPose. <https://www.remcom.com/varipose-biological-mesh-repositioning-software>, accessed May 2018.

[5] Makehuman - open source tool for making 3d

characters. <http://www.makehuman.org/404.php>, accessed May 2018.

- [6] R. K. Najm, "Simplified 3-D mesh generator," *ACES Journal*, vol. 6, no. 2, pp. 86-98, 1991.
- [7] S. Kashyap and A. Louie, "Surface modelling for EM interaction analysis," *ACES Journal*, vol. 6, no. 2, pp. 38-53, 1991.
- [8] C. J. Roy, "Grid convergence error analysis for mixed-order numerical schemes," *AIAA Journal*, vol. 41, no. 4, pp. 595-604, 2003.
- [9] H. B. Lim, D. Baumann, and E. P. Li, "A human body model for efficient numerical characterization of UWB signal propagation in wireless body area networks," *IEEE Transactions on Biomedical Engineering*, vol. 58, no. 3, pp. 689-697, 2011.
- [10] L. Roelens, S. Van den Bulcke, W. Joseph, G. Vermeeren, and L. Martens, "Path loss model for wireless narrowband communication above flat phantom," *Electronics Letters*, vol. 42, no. 1, pp. 10-11, 2006.
- [11] L. Roelens, W. Joseph, E. Reusens, G. Vermeeren, and L. Martens, "Characterization of scattering parameters near a flat phantom for wireless body area networks," *IEEE Transactions on Electromagnetic Compatibility*, vol. 50, no. 1, pp. 185-193, 2008.
- [12] Ł. Januszkiewicz and S. Hausman, "Simplified human phantoms for wireless body area network modelling," *9th European Conference on Antennas and Propagation (EuCAP)*, Lisbon, Portugal, pp. 1-4, April 2015.
- [13] M. Ghaddar, L. Talbi, and T. A. Denidni, "Human body modelling for prediction of effect of people on indoor propagation channel," *Electronics Letters*, vol. 40, no. 25, pp. 1592-1594, 2004.
- [14] CST Microwave Studio, ver. 2017, Computer Simulation Technology, Darmstadt, Germany, 2017.
- [15] IFAC - Dielectric properties of body tissues. <http://niremf.ifac.cnr.it/tissprop/htmlclie/htmlclie.php>, accessed May 2018.



Giovanni Manfredi was born in Messina, Italy, in 1987. He received his B.S. degree in Electronic Engineering from the University of Messina in 2010, his M.S. degree in Electronic Engineering at "Sapienza," University of Rome in 2013, and his Ph.D. in Information Engineering

from the Università Politecnica delle Marche, Ancona, in 2017.

He currently works as a Research Fellow at the French Aerospace Lab in Paris, ONERA. His recent activities have included developing an electromagnetic model, based on physical optics, to characterize the field reflected by a human body, and utilizing this system for the Doppler analysis of the signature of human motion. Manfredi is a Member of the Italian Electromagnetic Society (SIEm).



Valentina Di Mattia was born in Teramo, Italy, in 1984. She received her M.S. degree (cum laude) in Clinical and Biomedical Engineering at “Sapienza” University of Rome in 2009 and her Ph.D. in “Bio-engineering and Electromagnetism” at Università Politecnica delle Marche, Ancona, in 2014. Currently, she is a Research Fellow at the Department of Information Engineering of the same University, and her main research activities focus on the design of: electromagnetic devices for the contactless monitoring of human vital signs, indoor localization and tracking; small systems to support the autonomous walking or running of visually impaired people and athletes.

In particular, her expertise concerns the simulation, optimization and testing of small antennas working at high frequencies. She is a Member of Italian Electromagnetic Society (SIEm).



Paola Russo received her Ph.D. degree in Electronic Engineering from the Polytechnic of Bari, in Bari, Italy, in 1999. During 1999, she worked under a research contract at the Motorola Florida Research Laboratory. From 2000 to 2004 she worked, under a research contract at University of Ancona, Italy, (now Università Politecnica delle Marche), on the development of numerical tools applied to different electromagnetic problems. Since January 2005, she has held a tenured position as Researcher at Università Politecnica delle Marche. She teaches EMC, antenna design and fundamentals of electromagnetics.

Her current research interests include the application of numerical modelling to EMC problems, reverberation chamber, and new antenna design such as plasma antennas.

Russo is a Member of IEEE EMC Society and the Italian Electromagnetic Society (SIEm).



Alfredo De Leo was born in Bari, Italy in 1975. He graduated in Electronic Engineering in 1999 from the University of Ancona (currently Università Politecnica delle Marche), and received his Ph.D. degree in Electromagnetism and Bioengineering in 2014 from Università Politecnica delle Marche where he currently heads the Antenna and EMC laboratories.

His research activities concern the development of electromagnetic models, laboratory experiments and numerical simulation techniques related to interactions between electromagnetic fields and biological beings, the design of electromagnetic travel aids for visually impaired people, remote sensing of physiological activities, and reverberation chambers.

De Leo is a Member of IEEE EMC Society and the Italian Electromagnetic Society (SIEm).



Graziano Cerri is currently Full Professor of Electromagnetic Fields at the Department of Electromagnetics and Bioengineering at Università Politecnica delle Marche.

His research is mainly devoted to EMC problems, to the analysis of the interaction between EM fields and biological bodies, and to plasma antennas. From 2006 to 2014, he was Director of the Ph.D. programme in Engineering Sciences in the Engineering Faculty at Università Politecnica delle Marche. Since 2004, he has been Director of ICEmB (Interuniversity Italian Center for the study of the interactions between Electromagnetic Fields and Biosystems).

He is also Member of the Administrative and Scientific Board of CIRCE (Interuniversity Italian Research Centre for Electromagnetic Compatibility), and Member of the Scientific Board of SIEm (Italian Association of Electromagnetics). From 2006 to 2014, he was also Member of the steering committee of EMC-Europe – International Symposium on Electromagnetic Compatibility.

Cerri is a Member of IEEE and of AEI (Italian Electrotechnical and Electronic Association).

Design and Implementation of Dual Band Microstrip Patch Antenna for WLAN Energy Harvesting System

Osama Amjad¹, Syeda W. Munir¹, Şehabeddin T. İmeci², and Ali Ö. Ercan¹

¹Department of Electrical and Electronics Engineering
Ozyegin University, Istanbul 34794, Turkey
osama.amjad@ozu.edu.tr, wajiha.munir@ozu.edu.tr, ali.ercan@ozyegin.edu.tr

²Department of Electrical and Electronics Engineering
International University of Sarajevo, 71210, Bosnia and Herzegovina
simeci@ius.edu.ba

Abstract — Since the demand for self-sustained wireless systems is increasing, there is a trend towards RF energy harvesting. It is a key solution to energize the low power systems such as the Internet of Things (IoT) devices without replacing the batteries periodically. This paper presents the design and analysis of RF energy harvesting system that consists of dual-band microstrip patch antenna operating at 2.4 GHz and 5.8 GHz, an impedance matching network, 4-stage voltage doubler and a storing circuit. The antenna is designed using ADS Agilent and sonnet suites software that provides a directivity of 5.5 dBi and 6.3 dBi at 2.4 GHz and 5.8 GHz respectively. The measured results of the fabricated antenna are well agreement with the simulated results. Simulated results show that for an input received power of 10 mW, the proposed system can provide 4.5 mW power at the output of 4-stage voltage rectifier with an overall efficiency of 45%.

Index Terms — Dual-band, impedance matching, microstrip patch antenna, RF energy harvesting and voltage rectifier.

I. INTRODUCTION

With the rapid growth of low power wireless devices, the last few years have witnessed enhanced research trends towards energy efficient wireless systems. Conventionally, these devices were powered by batteries, which have limited life time and were needed to be replaced/recharged manually once the energy is consumed. This challenge leads to an upsurge of research interests in wireless energy harvesting technique from ambient green sources (e.g., solar, thermal, vibrational, RF). Among other sources, RF source is a potential

candidate for energy harvesting due to continuous availability of RF signals irrespective of geographical area and weather conditions. Moreover, RF energy harvesting is considered as a revolutionary technology that helps to develop the energy efficient wireless networks. It converts the received RF ambient signals into usable form i.e. electricity and enables the efficient use of available spectrum and provides an efficient solution to empower low-power wireless devices [1], [2]. Energy can be harvested from several digital and analog RF sources such as analog/digital TV broadcasting stations, FM/AM radio towers, WLAN access points, and cellular base stations [3]. Although a limited amount of energy can be harvested from these RF sources, it can still be used to energize the low power devices, which may solve the problem of replacing the batteries [1], [2]. Despite certain critical challenges in design and implementation of RF energy harvesting system, it is still preferred due to the high availability of free RF signals.

The concept of RF energy harvesting is shown in Fig. 1. It constitutes of receiving antenna that captures the RF signal of a certain frequency from the transmitter, matching network, RF-DC converter, and load circuitry [4]. The proposed work details the design, implementation, and analysis of energy harvesting system with dual-band microstrip patch antenna operating at WLAN frequencies. The designed antenna is integrated with the energy harvester and DC voltage has been measured at the output.

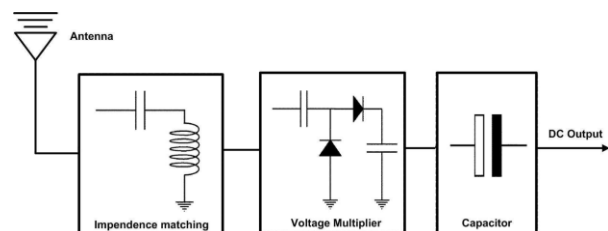


Fig. 1. General architecture of RF energy harvesting system.

This work has been partially supported by the Scientific and Technological Research Council of Turkey (TÜBİTAK) under BİDEB-2215 graduate scholarship programme for international students and under Grant No. 114E739.

The amount of harvested energy depends on the type of source, transmitted power, environment, path loss exponent and distance between the source and receiving antenna, etc. [2]. Moreover, it is significantly affected by the characteristics of the antenna; therefore suitable receiving antenna is very important in this regard. In past few years, different types of antennas have been proposed for RF energy harvesting, for example, dipoles, Yagi-Uda, microstrip, monopole, loop, spiral, and coplanar patch antennas [5]. The design of RF energy harvesting system generally utilized microstrip patch antennas because of their low profile, lightweight and planar structure.

In today's wireless communication systems, development of multiple frequency bands has provided the multi-band antennas structures for RF energy harvesting, which is quite useful. The design and implementation of energy harvesting antennas from 3G/4G cellular base stations and WLAN RF sources are presented in [6]. In [7], a 2.45/5.8 GHz simultaneously operating dual-band rectenna for an integrated wireless energy harvesting system has been implemented and analyzed. A dual-frequency circular patch antenna with a gain of 8.3 and 7.8 dBi at 1.95 and 2.45 GHz, respectively has been shown in [8]. A microstrip patch antenna with novel slot resonator for compact RF energy harvesting modules operating at 2.4 GHz is proposed in [9]. The energy harvesting system presented in [10], has been integrated with dual-core wireless multimedia sensor networks to enhance the capability of the system. Within short distances, limited amount of energy can be harvested from a typical WLAN router with transmitting power of 50-100 mW. It is an omnipresent source of renewable energy in an indoor environment and size of resonating antennas is in the order of 10-50 cm² [11].

In comparison to the past research that only considered the single band for RF energy harvesting this paper focuses on dual-band RF energy harvesting system that operates at Wi-Fi frequencies of 2.4 GHz and 5.8 GHz. In the simulation setup, we have used our designed dual-band microstrip patch antenna published in [3]. Moreover, the antenna is fabricated on FR4 substrate and the measured and simulated results are compared. In Section II, the design consideration of energy harvesting systems is explained including antenna design, impedance matching, and voltage rectification. Section III presents the results of the designed antenna and overall RF energy harvesting system. Section IV concludes our findings and analysis.

II. DESIGN CONSIDERATION IN RF ENERGY HARVESTING

In RF energy harvesting the most important component is the receiving antenna, which captures the ambient RF signals of a particular frequency band from transmitting source via wireless channel and converts

these signals to AC voltages. The matching network, composed of capacitive and inductive elements ensures the maximum power delivery from receiving antenna to the voltage rectifier by reducing the transmission loss. The matching network has AC type voltage at the output; therefore the voltage rectifier is used to convert this voltage into usable DC power. The obtained power is either directly supplied to energize the low power device or stored in the energy storage unit. The storage circuit allows uninterrupted power delivery to the load and serves as a backup reserve when external energy is not available.

A. Proposed antenna design

The antenna can be designed to operate on either single frequency or multiple frequency bands, in which the device can simultaneously harvest from single or multiple sources. Previously, research motivation on RF energy harvesting was restricted to a single band which was not much efficient. However, recently there has been more focus towards design and implementation of dual-band and antenna arrays for RF energy scavenging. In this regard, the design of high directive dual-band microstrip patch antennas for wireless applications also received much importance [5], [6].

The proposed antenna in this paper is microstrip-fed patch antenna with a rectangular slot to operate at WLAN dual frequencies, i.e., 2.4 GHz and 5.8 GHz. The antenna has been designed on ADS Agilent software and Sonnet Suites. An FR4 epoxy substrate with a thickness of 1.6 mm and dielectric constant $\epsilon_r = 4.4$ is used. Figure 2 shows the front and back view of the designed antenna. The dimensions of the antenna are given in Table 1. A prototype of the fabricated antenna is shown in Fig. 3. The feed line for excitation is provided having an impedance of 50 Ω . The slot dimensions are optimized such that maximum efficiency can be achieved in terms of return loss.

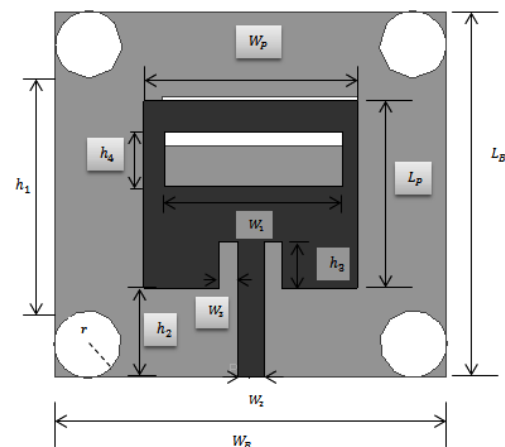


Fig. 2. Front and back view of the proposed dual-band antenna.

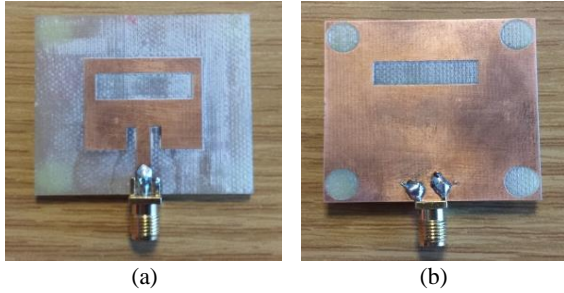


Fig. 3. Prototype of the designed antenna: (a) front view and (b) back view.

B. Impedance matching network

Impedance matching decreases the transmission loss and ensures the maximum power transfer from antenna to the rectifier circuit such that the output voltage of rectifier circuit is increased [12]. The input impedance of the rectifier at each frequency is calculated using the modular block provided in the ADS schematic design. Further, ADS Smith chart utility has been used to match the input impedance of the rectifier to the antenna impedance of 50Ω . Two separate LC matching networks with a capacitor $C1 = 6.8 \text{ pF}$ and an inductor $L1 = 5.35 \text{ nH}$ for 2.4 GHz and a capacitor $C1 = 1.3 \text{ pF}$ and an inductor $L1 = 0.68 \text{ nH}$ for 5.8 GHz are obtained. However, in a practical scenario two separate band pass filters can be deployed at the output of matching networks. The each band pass filter allows the frequency band to pass, whose power transfer is being maximized by the respective impedance matching network and rejects the high-frequency components which consequently results in the undesired harmonic re-radiation and electromagnetic interferences [13].

Table 1: Physical parameters of the proposed antenna

Parameters	Dimensions (mm)
Rectangular patch	Length $L_p = 21$ Width $W_p = 24$
Ground plane	Length $L_B = 41$ Width $W_B = 44$
Rectangular slot	Length $h_4 = 5.98$ Width $W_1 = 20$
Microstrip feed line	Width $W_2 = 3$
Inset gap	Length $h_3 = 5.2$ Width $W_3 = 2$
Circle	Radius $r = 3$
Remaining parameters	$h_1 = 26$ $h_2 = 10$

C. Voltage rectifier circuit

RF signals are converted into DC voltage at the given frequency band to energize the low power devices/circuits. The main elements of the voltage rectifier are diodes; we have used the silicon-based HSMS-2850 Schottky diodes with a threshold voltage of 250 mV and

diode capacitance of 0.18 pF. It provides low forward voltage, low substrate leakage and has a unidirectional flow of current [14]. Figure 4 shows the proposed RF energy harvesting system. A coupler is used to combine the antenna model with the rest of circuit. Selection of the number of stages is very crucial so that output voltage can be maximized. An optimal number of stages should be added to the system because parasitic losses of nonlinear devices also increase by increasing the number of stages.

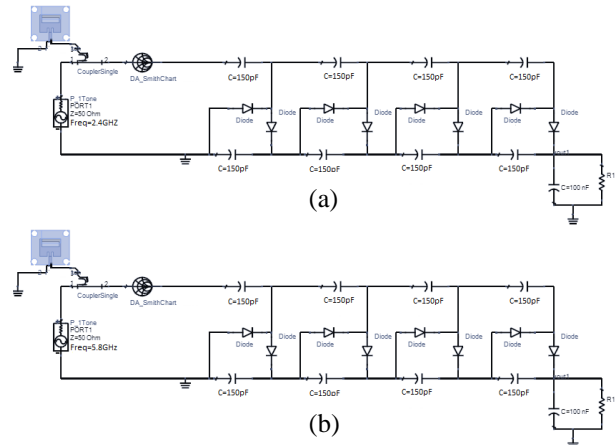


Fig. 4. Schematic diagram of 4-stage RF energy harvesting system for: (a) 2.4 GHz and (b) 5.8 GHz.

III. SIMULATION RESULTS

The proposed antenna is designed and simulated using ADS software. It can be seen in Fig. 5 that, the antenna has two operating bands around the center frequencies of 2.4 GHz and 5.8 GHz with sharp resonance. In a low band, the simulated 10 dB bandwidth is between 2.39-2.52 GHz, and similarly, at 5.8 GHz, the bandwidth is between 5.65-5.85 GHz. Moreover, it can be noticed that measured and simulated results agree well.

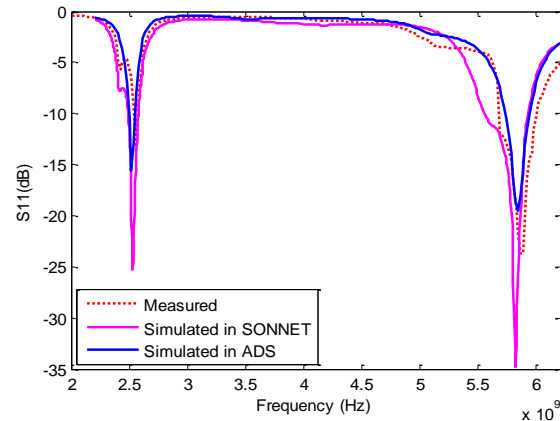


Fig. 5. Input reflection coefficients (S11) of the proposed antenna.

In order to analyze the complete energy harvesting system the designed antenna model that contains the S11 information and retains its resonant frequencies after impedance matching is exported to the schematic for co-simulation with rest of the energy harvesting circuit as shown in Fig. 4. The S-parameter and harmonic balance methods are used to interpret the relation between RF source parameters with output power. It is clearly seen in Fig. 5 that the two resonant frequencies at 2.4 GHz and 5.8 GHz are excited with good impedance matching. Best possible values of matching network are obtained using smith chart tools, which ultimately provides minimum input return loss (S11). Our results mainly focus the output power obtained versus input power, a gain of the proposed antenna, maximum power transfer from source to load and antenna efficiency in terms of its radiation pattern.

A. Effect of input power on output

The parameter sweep for an input power of -15 dBm to 0 dBm is plotted against the output power. Figure 6 shows that the output power increases with the increase of input power. Moreover, it can also be inferred that, at high resonating frequency power obtained is low as the higher frequencies are more vulnerable to path-loss and attenuation.

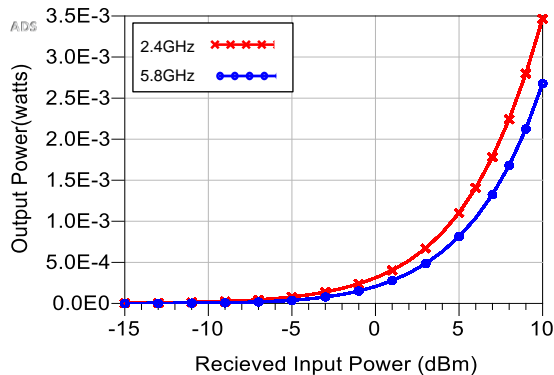


Fig. 6. Output power versus input received power at 2.4 GHz and 5.8 GHz.

B. Antenna directivity and radiation intensity

Directivity describes the direction in which the antenna has maximum gain. Radiation pattern shows the variation of the power radiated by an antenna as a function of the direction. From Fig. 7, it can be observed that antenna’s maximum gain (directivity) at 2.4 GHz is 5.53 dBi in $\theta=0^\circ$ direction (and at 5.8 GHz, the directivity is 6.3 dBi. It can also be noticed that the simulated and measured results of radiation patterns are in well agreement with each other. At both the frequencies, the radiation patterns are almost the same, thus they maintain the same polarization. Moreover, the graph shows clear deterioration at $\theta = 90^\circ$ when operates at 2.4 GHz. Similarly, when the antenna operates at

5.8 GHz, deterioration appears at $\theta = 90^\circ$.

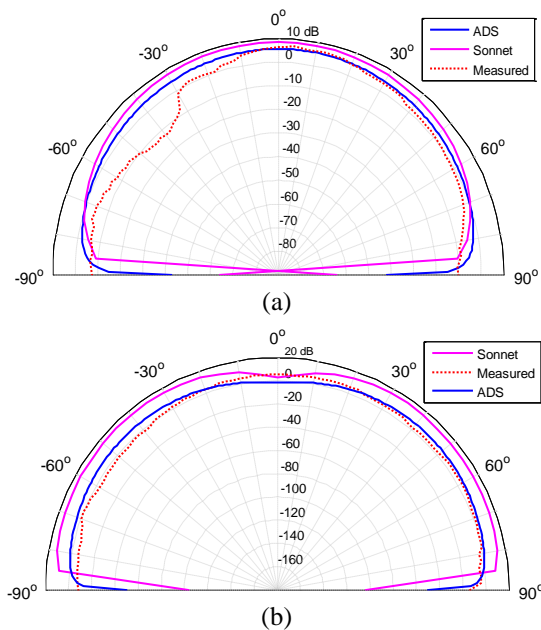


Fig. 7. Directivity of the antenna: (a) at 2.4 GHz and (b) at 5.8 GHz.

D. Effect of number of stages of rectifier

The output voltage at the first stage of the rectifier is usually too low for energizing a low power device and the conversion efficiency is also not very high. Therefore, for designing RF energy harvesting system multiple stages of voltage rectifier are connected in series one after the other stage, so as to achieve sufficient amount of voltage at the output to power the particular device. Figure 8 shows the effect of number of stages on the output voltage versus input power. It can be seen that voltage is directly proportional to the stages. Four stages have been used in the designed circuit which provides enough voltage at the output that can be used to power the required WSN applications.

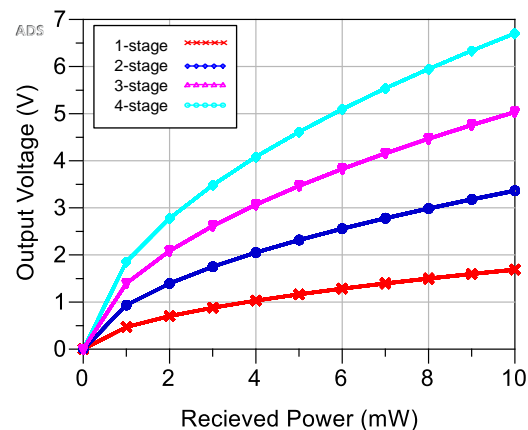


Fig. 8. Effect of number of stages on the output voltage.

IV. EFFICIENCY OF PROPOSED SYSTEM

In the proposed system two separate circuits for dual resonating frequencies are designed with different LC matching networks as shown in Fig. 4. HSMS-2850 Schottky diodes are used which provide higher conversion efficiency as they have low built-in voltage [12]. The overall efficiency of the energy harvesting system is defined as the ratio of DC power at the output to the input received power on the receiving antenna. The graph that measures the efficiency of the system against the input received power is called efficiency curve. It is of paramount importance to measure the efficiency of the designed system. Figure 9 shows the system response, when the input received power is varied between 1 mW to 10 mW. The proposed system can provide maximum output power of 4.5 mW for an input received power of 10 mW with an efficiency of 45%. The efficiency of RF energy harvesting system depends on accurate matching, efficient antenna and the power efficiency of the voltage rectifier that converts the received RF signals to DC voltage.

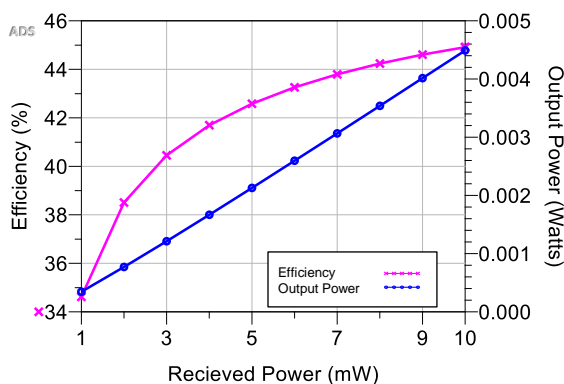


Fig. 9. Effect of incident RF power on efficiency of the proposed system.

V. CONCLUSION

In this paper, energy harvesting from WLAN source with dual-band antenna is designed in ADS Agilent and Sonnet Software. The designed antenna is fabricated on FR4 substrate and S-parameter and radiation pattern are measured. The results show that the simulated and measured results are in well agreement. Furthermore, the designed antenna is integrated with the rest of energy harvesting circuit that includes an impedance matching network, 4-stage voltage rectifier and a storing circuit. Our proposed network is designed to be used for RF energy harvesting from Wi-Fi frequency bands. The results show a reflection coefficient of almost -22 dB and maximum gain of 5.5 dBi at 2.4 GHz. Similarly, at 5.8 GHz reflection coefficient of -48 dB and maximum gain of 6.3 dBi is obtained. Moreover, result shows that 10 mW of RF incident power on antenna can generate 4.5 mW power at output resistance of 10 k Ω with an

overall efficiency of 45%.

REFERENCES

- [1] X. Lu, P. Wang, D. Niyato, D. Kim, and Z. Han, "Wireless networks with RF energy harvesting: A contemporary survey," *IEEE Communication Survey & Tutorials*, vol. 17, no. 2, May 2015.
- [2] T. Soyata, L. Copeland, and W. Heinzelman, "RF energy harvesting for embedded systems: A survey of tradeoffs and methodology," *IEEE Circuits and Systems Magazine*, Feb. 2016.
- [3] S. W. Munir, O. Amjad, E. Zeydan, and A. Ö. Ercan, "Optimization and analysis of WLAN RF energy harvesting system architecture," *International Symposium on Wireless Communication Systems (ISWCS)*, pp. 429-433, Oct. 2016.
- [4] Y. Uzun, "Design of an efficient triple band RF energy harvester," *ACES Journal*, vol. 30, no. 12, Dec. 2015.
- [5] S. Shrestha, S. Noh, and D. Choi, "Comparative study of antenna designs for RF energy harvesting," *International Journal of Antennas and Propagation*, Jan. 2013.
- [6] M. Hoang, H. Phan, T. Q. V. Hoang, and T. P. Vuong, "Efficient compact dual-band antennas for GSM and Wi-Fi energy harvesting," *IEEE International Conference on Advanced Technologies for Communications*, Oct. 2014.
- [7] X. Li, J. Wang, X. Wu, and H. Zaho, "A dual-band integrated wireless energy harvesting system," *International Applied Computational Electromagnetics Society Symposium (ACES)*, Sept. 2017.
- [8] M. Aboulalaa, A. B. Abdel-Rahman, A. Allam, H. Elsadek, and R. K. Pokharel, "Design of a dual-band microstrip antenna with enhanced gain for energy harvesting applications," *IEEE Antennas and Wireless Propagation Letters*, vol. 16, pp. 1622-1626, Jan. 2017.
- [9] M. Palandoken, "Microstrip antenna with compact anti-spiral slot resonator for 2.4 GHz energy harvesting applications," *Microwave and Optical Letters*, vol. 58, no. 6, Mar. 2016.
- [10] M. A. Jamshed and O. Amjad, "Multicore energy efficient scheduling with energy harvesting for wireless multimedia sensor networks," *International Multi-topic Conference (INMIC)*, Feb. 2018.
- [11] M. Arrawaita, M. S. Baghini, and G. Kumar, "RF energy harvesting systems from cell towers in 900 MHz band," *IEEE-Conference In Communications*, pp. 1-5, Jan. 2011.
- [12] P. Nintanavongsa, U. Muncuk, D. R. Lewis, and K. R. Chowdhury, "Design optimization and implementation for RF energy harvesting circuits," *IEEE Journal on Emerging and Selected Topics in Circuits and Systems*, vol. 2, no. 1, pp. 24-33, Mar.

2012.

- [13] B. Schauwecker, "Design of processing circuitry for an RF energy harvester," *University of Arkansas, Fayettevill*, May 2016.
- [14] K. K. A. Devi, N. Md. Din, and C. K. Chakrabarty, "Optimization of the voltage doubler stages in an RF-DC convertor module for energy harvesting," *Circuits and Systems*, vol. 3, no. 3, July 2012.



Osama Amjad has received his B.S. degree in Electrical Engineering from COMSATS Institute of Information Technology (CIIT), Islamabad, Pakistan, in 2014 and his M.S. degree in Electrical and Electronics Engineering from Özyegin University in 2017. He is currently a Ph.D.

student and a graduate assistant at Lakehead University, Canada since September 2017. His research interests are in the areas of wireless communications and wireless networks.



Syeda Wajiha Munir has completed her B.S. Electrical Engineering with Gold Medal from COMSATS Institute of Information Technology (CIIT), Islamabad, Pakistan, in 2014 and her M.S. degree in Electrical and Electronics Engineering from Özyegin University in 2017. Her

research interests are in the areas of wireless communications and wireless networks.



Şhabeddin Taha İmeci received the B.Sc. degree in Electronics and Communications Engineering from Yildiz Technical University, Istanbul, Turkey in 1993, and the M.S.E.E. and Ph.D. Degrees from Syracuse University, Syracuse, NY in 2001 and 2007, and Associate

Professorship degree from Istanbul Commerce University, Istanbul Turkey in 2014, respectively. İmeci was

appointed as Full Professor in Int. Univ. of Sarajevo in Nov. 2017. He is working as the Dean of FENS (Faculty of Engineering and Natural Sciences) in Sarajevo. He was with Anaren Microwave Inc., East Syracuse, NY from 2000 to 2002, and Herley Farmingdale, New York from 2002 to 2003, and PPC, Syracuse, NY from 2003 to 2005, and Sonnet Software Inc., Liverpool, NY from 2006 to 2007. He was a Teaching Assistant in the Department of Electrical Engineering and Computer Science at Syracuse University from 2005 to 2006. His current research areas are microwave antennas and electromagnetic theory.



Ali Özer Ercan received his B.S. degree in Electrical and Electronics Engineering from Bilkent University, Ankara, Turkey in 2000, and his M.S. and Ph.D. degrees in Electrical Engineering from Stanford University, CA, USA in 2002 and 2007 respectively. From 2007

until 2009, he was with the Berkeley Wireless Research Center of University of California, Berkeley, CA, USA, for post-doctoral studies. He joined Özyegin University, Istanbul, Turkey, in September 2009 as an Assistant Professor. He is the recipient of FP7 Marie Curie International Reintegration Grant and TUBITAK Career (3501) Award. He served as the Publications Chair of IEEE 3DTV Conference (3DTV-CON) in 2011, and Technical Program Co-chair and Publications Chair of IEEE Signal Processing and Communication Applications Conference (SIU) in 2012. His research interests are in the areas of signal and image processing, and wireless communication networks. Ercan is a Senior Member of the IEEE.

A Compact Tunable Triple Stop-Band Filter Based on Different Defected Microstrip Structures

Yingsong Li^{1,2}, Shengyuan Luo¹, and Wenhua Yu³

¹ College of Information and Communications Engineering
Harbin Engineering University, Harbin, Heilongjiang 150001, China
liyingsong@ieee.org

² National Space Science Center
Chinese Academy Sciences, Beijing 100190, China

³ 2COMU, Inc.,
4031 University Drive, Suite 100, Fairfax, VA 22030, USA
wenyu@2comu.com

Abstract — A compact triple stop-band filter based on different defected microstrip structures is proposed, fabricated and measured to filter out the undesired narrowband signal interferences against UWB systems. A meander line slot (MLS), a U-shaped slot (USS) and a spur line (SL) are etched on a 50-Ohm microstrip line to achieve the expected triple stop-band function and to provide a good tunable characteristic by selecting the proper dimensions of the MLS, USS and SL. The equivalent circuit model and its simulations are presented to evaluate the designed triple stop-band filter. Simulated and measured results are given to demonstrate that the proposed triple stop-band filter has controllable center frequencies and compact size.

Index Terms — Defected microstrip structure, meander line slot, spur line, triple stop-band filter, U-shaped slot.

I. INTRODUCTION

Recently, high data rate wireless communication systems have achieved much more attention such as ultra-wideband (UWB) system [1-3]. However, there are several narrowband systems overlap with the UWB system and these narrowband systems have been used for a long time, and hence, they may give potential interferences to the UWB system [3]. To give resistant to these interferences, stop-band filters are necessary to suppress these unexpected interference signals. Then, many filters have been reported in recent years. On the other hand, defected ground structure (DGS) has been widely used to design low-pass and stop-band filters [4-9]. However, the DGS may leak electromagnetic wave and might give harmful radiation from the defected ground plane.

To overcome this drawback of the DGSs, defected

microstrip structures (DMSs) have been presented and used to develop stop-band and low pass-band filters [9-13]. The DMSs are carried out by cutting various slots in the microstrip line rather than etching slots in the ground planes. These DMSs can effectively reject unwanted electromagnetic waves in special frequencies and directions, which is similar to the DGSs. Moreover, The DMS is easy to integrate with the planar microwave circuits owing to its simpler circuit model and less electromagnetic radiation noise interferences. In addition, the DMS has smaller size because it has higher effective inductance in comparison with the DGSs. A basic DMS has been realized by a T-shaped or L-shaped slot which consists of a horizontal slot and a vertical slot in [10-21]. The horizontal slot and vertical slot can control the equivalent inductance and capacitance of the DMS [10], respectively. Based on the advantages of the DMSs, they have been widely studied and utilized for filter designs and crosstalk reductions. Although many DMS-based filters have been reported, most of them can only provide single or dual filtering bands.

In this paper, a compact triple stop-band filter is proposed, fabricated and measured to suppress the undesired narrowband signal interferences, which is implemented by using different defected microstrip structures (DMSs). The DMSs are etched on a 50-Ohm microstrip line to achieve the expected triple stop-band function and each stop-band can be controlled by the corresponding DMS. The proposed tri-stop-band filter is optimized by using the HFSS, and its equivalent circuit model and electromagnetic simulations are presented to evaluate the designed triple stop-band filter. Also, the proposed filter is fabricated and measured to verify the simulations. Simulated and measured results demonstrate that the proposed triple stop-band filter has controllable

center frequencies and good stop-band characteristics.

II. TRIPLE STOP-BAND FILTER DESIGN

The configuration of the proposed triple stop-band filter is well designed and described in Fig. 1. The proposed filter consists of a meander line slot (MLS), a U-shaped slot (USS) and a spur line (SL) which are etched on a 50Ω microstrip line. Each DMS cell controls a stop-band, and hence, these three stop bands can be designed independently. The three stop bands are first designed based on the DMS theory presented in [10]. The proposed triple band-stop filter is printed on a Rogers RT/Duroid 5880 substrate with a relative dielectric of 2.2 and a thickness of 0.784mm. The stop-band characteristic of the DMS is controlled by changing the effective capacitance and inductance of the DMS because of the variable electric length, which can be implemented by adjusting the dimensions of the DMSs. In fact, the MLS controls the lower stop-band operating at 3.5GHz, while the USS controls the middle stop-band which operates at 5.8GHz. The upper band operating at 8.5GHz is controlled by the SL and the high-order mode of DMS-1. Then, the HFSS is used to analyze the effects of the dimensions on the stopband characteristics to get the desired stop bands. The proposed filter is optimized by using the high-frequency structure simulator (HFSS) based on finite element method (FEM) and the optimized parameters are $X=32$, $Y=2.5$, $x_1=7$, $x_2=5$, $x_3=10.5$, $x_4=5.8$, $s_1=0.1$, $s_2=0.1$, $s_3=0.55$, $s_4=0.25$, $s_5=0.6$, $s_6=0.2$, $h_1=0.3$, $h_2=0.4$, $h_3=0.35$ (All units: mm).

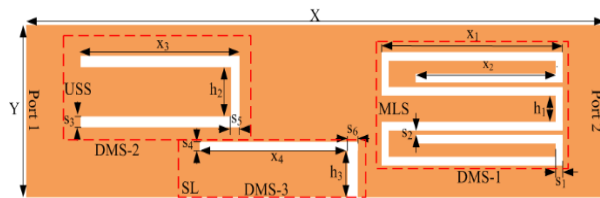


Fig. 1. Geometry of the proposed triple stop-band filter.

III. RESULTS AND DISCUSSIONS

To study the performance of the proposed triple stop-band filter, parameters x_1 , x_3 , and x_4 are selected in this section to analyze their effects. Herein, to well understand the effects of the key parameters, only one parameter is investigated by using the HFSS with different values while all the other parameters are fixed as the optimized values. The effects of S_{11} and S_{21} are shown in Figs. 2, 3 and 4, respectively, where the S_{11} is to analyze the impedance characteristics and the S_{21} is to depict the transmission characteristics.

With an increment of x_1 , the center frequency of the lower stop-band operating at 3.5GHz moves to the low frequency, which is shown in Fig. 2. In this case,

the increased length of x_1 increases the value of the equivalent inductance of DMS-1 and, hence, the center resonance frequency of lower stop-band changes. Additionally, the upper stop-band is affected since it is controlled by both the high-order resonance of the DMS-1 and the resonance of DMS-3. As x_3 increases from 9.4mm to 9.9mm, the center frequency of the middle stop-band shifts toward low frequency and the simulation results are given in Fig. 3. This means that the prolonged length of x_3 increases the equivalent inductance of the DMS-2. In this case, the lower and upper stop-bands keep constant. Since the upper stop-band is generated by the high-order mode of the DMS-1 and the DMS-3, the bandwidth and the center frequency of the upper stop-band can be controlled by the dimensions of both DMS-1 and DMS-3. The effects of the x_4 on the S_{11} and S_{21} are given in Fig. 4. It can be seen that the bandwidth of upper stop-band has obvious effects and x_4 also affects the lower resonance because of the coupling between the SL and the USS.

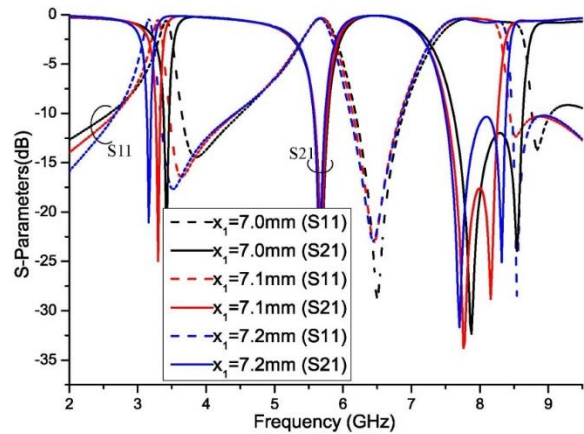


Fig. 2. Effects of x_1 on the S_{11} and S_{21} .

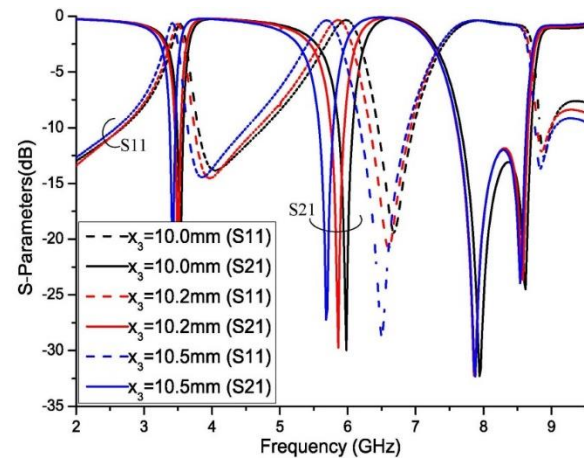


Fig. 3. Effects of x_3 on the S_{11} and S_{21} .

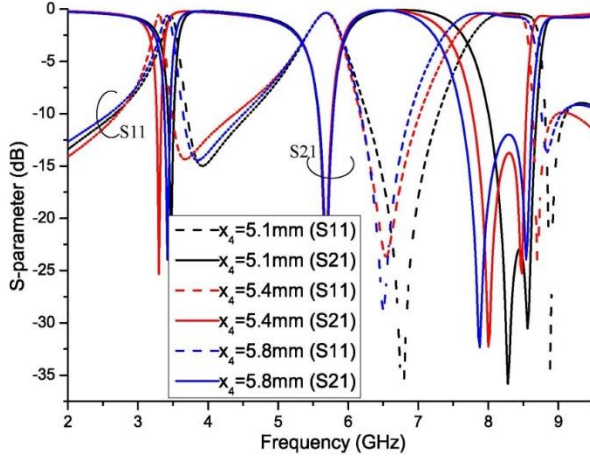


Fig. 4. Effects of x_4 on the S11 and S21.

In order to analyze the proposed triple stop-band filter, its equivalent circuit model is extracted and presented to confirm the effectiveness of the simulation, which is obtained based on the Butterworth low-pass filter theory. Based on the defected grounded structure circuit analysis theory, the DMS cell can be analyzed herein. The basis circuit model of the DMS is given in Fig. 5 in comparison with the Butterworth low-pass filter model.

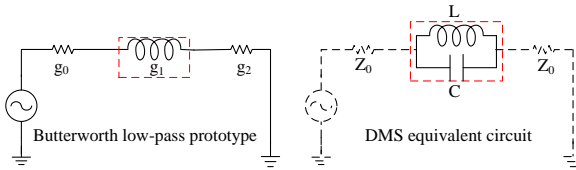


Fig. 5. Equivalent circuit models.

From the previous studies, we know that the impedance of the 1st Butterworth low-pass filter can be modeled as:

$$X_L = \omega Z_0 g_1, \quad (1)$$

where ω is the normalized angular frequency that the filter operates, g_1 represents the normalized 1st

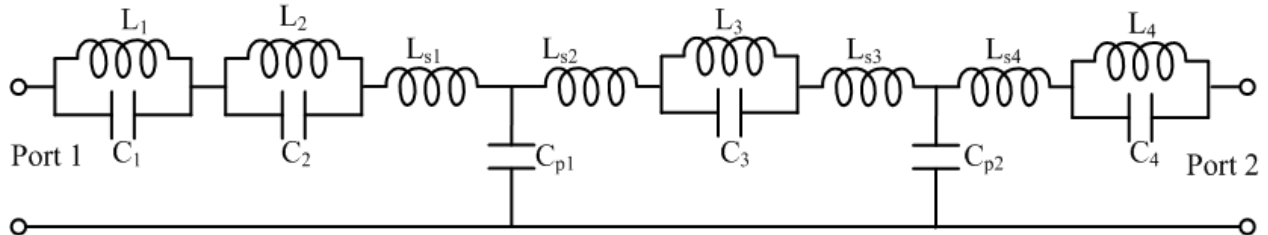


Fig. 6. Equivalent circuit of the proposed tri-stop-band filter.

To verify the performance of the proposed triple stop-band filter, the optimized filter is fabricated and

its performance is measured by using Agilent N5224A vector network analyzer. It can be seen from Fig. 7 that

$$X_{LC} = [\omega_0 C (\frac{\omega_0}{\omega}) + \frac{\omega}{\omega_0}]^{-1}, \quad (2)$$

where ω_0 is the desired resonance frequency given by the modeled parallel inductance and capacitance. In order to simplify the analysis of the proposed triple band-stop band filter, the mentioned Equations (1) and (2) are equal when $\omega = \omega_c$, where ω_c denotes the cut-off frequency of the parallel LC resonator illustrated in the Fig. 5. Thus, we can get:

$$X_{LC} /_{\omega=\omega_c} = X_L /_{\omega=1}. \quad (3)$$

According to the Equations (1)-(3), the capacitance and inductance can be obtained by using the following equation:

$$C = (\frac{\omega_c}{Z_0 g_1}) \frac{1}{\omega_0^2 - \omega_c^2}, \quad (4)$$

$$L = \frac{1}{4\pi^2 f_0^2 C}. \quad (5)$$

By using the formulas (1)-(5) presented above, the capacitance and inductance of single DMS based stop-band filter parameters can be obtained.

Then, the all the DMS cells have been analyzed to get an integration analysis of the proposed triple band-stop filter. Here, the couplings between the DMS cells have been included in the circuit of the proposed filter to get the effects of the different DMS cells. According to the equivalent circuit model and the analysis of the basic DMS cell in [9-10], the equivalent circuit model of the proposed triple stop-band filter is extracted and is given in Fig. 6. The circuit parameters are obtained by using the formulas given above and the circuit parameters are optimized by using the Advanced Design System (ADS) produced by the Keysight. The parameters are $L_1=0.344\text{nH}$, $L_2=0.316\text{nH}$, $L_3=0.306\text{nH}$, $L_4=0.372\text{nH}$, $C_1=6.291\text{pF}$, $C_2=1.098\text{pF}$, $C_3=2.567\text{pF}$, $C_4=1.098\text{pF}$, $L_{s1}=-0.4776\text{nH}$, $L_{s2}=-0.65\text{nH}$, $L_{s3}=0.6021\text{nH}$, $L_{s4}=-0.6264\text{nH}$, $C_{p1}=-0.2596\text{pF}$, $C_{p2}=0.01532\text{pF}$.

the measurement approaches well to both the circuit and HFSS simulations. The proposed filter has good frequency selectivity. These transmission zeros are obtained by the coupling of the DMSs and are tunable by adjusting the coupling strength which is implemented by changing the distances between the DMSs. It is worth noting that there are some differences between the measured and simulated results, which may be caused by fabrication tolerances and inaccuracies introduced by manual welding. The measured bandwidths of the designed triple stop-band are 3%, 3.5% and 12.3%, respectively, while the insertion losses at the center frequency are -0.54dB, -0.32dB and -0.43dB, respectively. The triple stop-band filter has a small size of 32mm×2.5mm. Compared with the previously proposed filters [15,20], the proposed triple stop-band filter has a size reduction of 55% and 92%, respectively.

Furthermore, it has a size reduction of 60% in comparison with the DMS filter in [14]. Additively, the proposed filter is flexible in design because of its independently controllable center frequencies and tunable bandwidth, and it has simple structure and compact size, which render it suitable for integrating into a UWB system to mitigate the unexpected interferences.

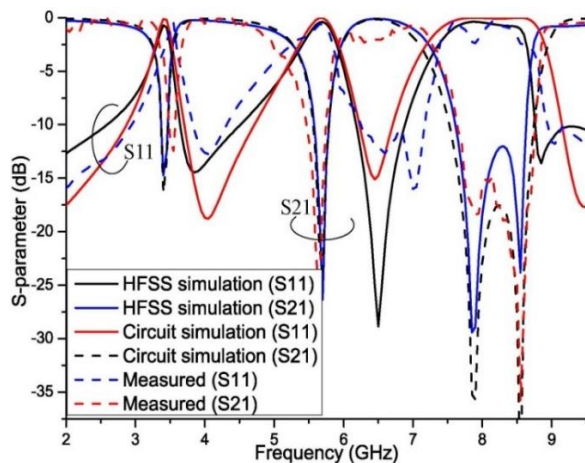


Fig. 7. Comparisons of S11 and S21 of the proposed triple stop-band filter.

IV. CONCLUSION

A compact triple stop-band filter by using DMSs has been proposed and its performance has been investigated by HFSS, circuit simulations and measurement. The proposed tri-stop-band filter with simple and compact structure highly reduced the size in comparison with the previously designed filters. Additionally, the proposed tri-stop-band filter is easy to design, and its center frequencies and bandwidth of the stop-band can be controlled individually, which gives a high flexibility and wide application. The equivalent circuit and HFSS simulations are presented to evaluate the designed triple

stop-band filter. The filter has been fabricated and measured, and the experiment result agrees well with the circuit and HFSS simulations.

ACKNOWLEDGMENT

This paper is supported by the National Key Research and Development Program of China (2016YFE0111100), Key Research and Development Program of Heilongjiang (GX17A016), the Science and Technology innovative Talents Foundation of Harbin (2016RAXXJ044), the Natural Science Foundation of Beijing (4182077), China Postdoctoral Science Foundation (2017M620918), the Natural Science Foundation of China (61701366) and the Fundamental Research Funds for the Central Universities (HEUCFM180806).

REFERENCES

- [1] Federal Communications Commission, First Report and Order, Revision of Part 15 of Commission's Rule Regarding UWB Transmission System FCC 02-48, Washington, DC, USA, 2002.
- [2] Y. Li, W. Li, and W. Yu, "A switchable UWB slot antenna using SIS-HSIR and SIS-SIR for multi-mode wireless communications applications," *Applied Computational Electromagnetics Society Journal*, vol. 27, no. 4, pp. 340-351, 2012.
- [3] Y. Li, W. Li, and Q. Ye, "A reconfigurable triple-notch-band antenna integrated with defected micro-strip structure band-stop filter for ultra-wideband cognitive radio applications," *International Journal of Antennas and Propagation*, vol. 2013, Article ID: 472645, pp. 1-13, 2013.
- [4] D. J. Woo, T. K. Lee, J. W. Lee, C. S. Pyo, and W. K. Choi, "Novel U-slot and V-slot DGSs for band-stop filter with improved Q factor," *IEEE Transactions on Microwave Theory and Techniques*, vol. 54, no. 6, pp. 2840-2847, 2006.
- [5] Q. Chen and J. Xu, "DGS resonator with two transmission zeros and its application to lowpass filter design," *Electronics Letters*, vol. 46, no. 21, pp. 1447-1449, 2010.
- [6] A. Nouri and G. R. Dadashzadeh, "A compact UWB band-notched printed monopole antenna with defected ground structure," *IEEE Antennas and Wireless Propagation Letters*, vol. 10, pp. 1178-1181, 2011.
- [7] B. Wu, B. Li, and C. Liang, "Design of lowpass filter using a novel split-ring resonator defected ground structure," *Microwave and Optical Technology Letters*, vol. 49, no. 2, pp. 288-291, 2007.
- [8] X. Li, Z. Shao, and C. J. You, "X-band substrate integrated waveguide bandpass filter using novel defected ground structure cell," *Microwave and Optical Technology Letters*, vol. 57, no. 5, pp. 1156-1160, 2015.
- [9] D.-S. La, W.-H. Han, and J.-L. Zhang, "Compact

- band-stop filters using π -shape DGS and π -shape DMS,” *Microwave and Optical Technology Letters*, vol. 56, no. 11, pp. 2504-2507, 2014.
- [10] S. Zhang, J.-K. Xiao, Z.-H. Wang, and Y. Li, “Novel low pass filters using a defected microstrip structure,” *Microwave Journal*, vol. 49, no. 9, pp. 118-128, 2006.
- [11] J.-K. Xiao, W.-J. Zhu, and J. S. Fu, “New bandstop filter using simple defected microstrip structure,” *Microwave Journal*, vol. 54, no. 9, pp. 134-144, 2011.
- [12] M. Naser-Moghadasi, M. Alamolhoda, and B. Rahmati, “Spurious-response suppression in microstrip parallel-coupled bandpass filters by using defected microstrip structures,” *IEICE Electronics Express*, vol. 8, no. 2, pp. 70-75, 2011.
- [13] N. Ojaroudi, H. Ojaroudi, and Y. Ojaroudi, “Very low profile ultrawideband microstrip band-stop filter,” *Microwave and Optical Technology Letters*, vol. 56, no. 3, pp. 709-711, 2014.
- [14] D. La, Y. Lu, S. Sun, N. Liu, and J. Zhang, “A novel compact bandstop filter using defected microstrip structure,” *Microwave and Optical Technology Letters*, vol. 53, no. 2, pp. 433-435, 2011.
- [15] S. Zhang and L. Zhu, “Compact tri-band bandpass filter based on $\lambda/4$ resonators with U-folded coupled-line,” *IEEE Microw. Wirel. Compon. Lett.*, vol. 23, no. 5, pp. 258-260, 2013.
- [16] Z. Jiang, Z. Sun, Y. Li, and Y. Zhao, “A wide dual band stop-band filter with two different defected microstrip structures,” *The 39th Progress In Electromagnetics Research Symposium*, Singapore, Nov. 19-22, 2017.
- [17] Y. Wang, T. Jiang, and Y. Li, “A miniaturized dual stop-band filter using meander defected microstrip structures,” *IEEE International Conference on Wireless Information Technology and Systems (ICWITS) and Applied Computational Electromagnetics (ACES)*, Mar. 13-17, Hawaii, USA, 2016.
- [18] Y. Wang, T. Jiang, and Y. Li, “Development of a microstrip-fed multi-band antenna by means of defected microstrip structures,” *Progress In Electromagnetics Research Symposium*, Shanghai, China, Aug. 8-11, 2016.
- [19] T. Jiang, Y. Wang, and Y. Li, “Design and analysis of a triple stop-band filter using ratioed periodical defected microstrip structure,” *Frequenz*, vol. 71, no. 7-8, pp. 341-347, 2017.
- [20] C. F. Chen, T. Y. Huang, and R. B. Wu, “Design of dual- and triple-passband filters using alternately cascaded multiband resonators,” *IEEE Trans. Microw. Theory Tech.*, vol. 54, no. 9, pp. 3550-3558, 2006.
- [21] Y. Li, W. Zhang, and W. Yu, “A circular slot UWB antenna with independently tunable quad-band filtering characteristics,” *Applied Computational*

Electromagnetics Society Journal, vol. 30, no. 10, pp. 1089-1095, 2015.

Yingsong Li received his B.S. degree in Electrical and Information Engineering, and M.S. degree in Electromagnetic Field and Microwave Technology from Harbin Engineering University, 2006 and 2011, respectively. He received his Ph.D from Harbin Engineering University, China and Kochi University of Technology, Japan in 2014. Now, he is Full Professor in College of Information and Communication Engineering, Harbin Engineering University, China. He is a Senior Member of Chinese Institute of Electronics (CIE), a Member of IEEE and The Applied Computational Electromagnetics Society (ACES). He is an Area Editor of *AEÜ - International Journal of Electronics and Communications and Wireless Personal Communications*. He serves as reviewers for the journals *IEEE Antennas and Wireless Propagation Letters*, *International Journal of Electronics*, *Progress In Electromagnetics Research Series*, *Journal of Electromagnetic Waves and Applications*, *COMPEL: The International Journal for Computation and Mathematics in Electrical and Electronic Engineering* and *Applied Computational Electromagnetics Society Journal*. He is also a Session Chair and TPC Chair for many international conferences. His recent research interests are mainly in microwave theory, microwave filters, small antenna technologies and computational electromagnetic.

Shengyuan Luo received his B.S. degree in Electrical and Information Engineering in 2014. Now, he is positing his master in Information and Communication Engineering, Harbin Engineering University. His recent research interests are mainly in microwave theory, microwave filters, small antenna technologies.

Wenhua Yu joined the Department of Electrical Engineering of the Pennsylvania State University, and has been a Group Leader of the Electromagnetic Communication Lab since 1996. He received his Ph.D. in Electrical Engineering from the Southwest Jiaotong University in 1994. He worked at Beijing Institute of Technology as a Postdoctoral Research Associate from February 1995 to August 1996. He has published one book on CFDTD software and two FDTD books: *Conformal Finite-Difference Time-Domain Maxwell's Equations Solver: Software and User's Guide* (Artech House, 2003), *Parallel Finite-Difference Time-Domain* (CUC Press of China, 2005, in Chinese), and *Parallel Finite-Difference Time-Domain Method* (Artech House, 2006). He has published over 100 technical papers and four book chapters. He developed the Computer and Communication Unlimited [Http://www.2comu.com](http://www.2comu.com), and

serves as its President. He is a Senior Member of the IEEE. He was included in Who's Who in America, Who's Who in Science and Engineering, and Who's Who in Education. He is also a Visiting Professor and Ph.D.

Advisor of the Communication University of China. Yu's research interests include computational electromagnetic, numerical techniques, parallel computational techniques, and the theory and design of parallel computing systems.

Mutual Coupling Reduction of a MIMO Antenna Array Using 3-D Novel Meta-material Structures

Kai Yu¹, Yingsong Li^{1,2,*}, and Xiaoguang Liu³

¹ College of Information and Communication Engineering
Harbin Engineering University, Harbin, 150001, China
*liyingsong@ieee.org

² Key Laboratory of National Microwave Remote Sensing
National Space Science Center, Chinese Academy of Sciences, Beijing 100190, China

³ Electrical and Computer Engineering Department
University of California, Davis, CA 95616, USA

Abstract — A 3-D metamaterial structure (3DMMS) is proposed and is used to reduce mutual coupling of a two-element patch antenna array. The 3DMMS consists of an upper M-shaped patch and two lower U-shaped patches, which are connected by two shorted pins. The proposed 3DMMS has a negative permeability at 2.35-2.45 GHz band, which covers the operation band of the patch antenna array with an edge-to-edge array-element distance of $0.13\lambda_0$. Five designed 3DMMS cells are embedded into the substrate between two antenna elements, which has a 0.1mm vertical distance to the patch antennas. The proposed antenna is optimized, fabricated and measured. The results show that about 18 dB mutual coupling reduction is achieved by using the 3DMMS without affecting the operating bandwidth and radiation characteristics.

Index Terms — Metamaterial structure, microstrip patch antenna array, mutual coupling reduction.

I. INTRODUCTION

Recently, planar antennas have been extensively studied and integrated into various portable and compact mobile terminals [1, 2]. To improve the spectrum efficiency of a wireless communication system, one of the effective methods is to use the multiple-input multiple output (MIMO) technology [3-4]. As a MIMO system, multiple antennas are used for both the transmitters and receivers to improve the channel capacities. Thus, small and broadband MIMO antennas are required to construct desired high-capacity next-generation mobile communication systems.

Moreover, smaller and higher data transmission devices are needed to install a MIMO antenna in a limited space. As a result, the distance between the antenna elements are becoming narrower, which will not

only result in a strong mutual coupling between the array elements but also increase the spatial correlation. Additionally, the mutual coupling between antenna elements is an urgent problem, because the inter-coupling will affect wireless system performance, antenna efficiency, as well as amplitude and phase errors [5-19].

In order to reduce the mutual coupling of planar antenna array, various decoupling methods have been presented. Defected ground structure (DGS) is proved to be an effective method to reduce the mutual coupling and enhance the isolation, which is etched various slots in the common ground plane. Then, an S-shaped periodic DGS is utilized to obtain more than 40 dB mutual coupling reduction between antenna elements. After that, a novel fractal DGS (FDGS) is designed to enhance the isolation of a dual elements antenna array [6-7]. Then, the stub technologies have been investigated to reduce the mutual coupling in MIMO array [8-11]. Moreover, electromagnetic band gap (EBG) structure has been utilized to reduce the mutual coupling in a two-element antenna array [12-15]. Then, several EBG structures have been reported to improve the isolation between the antenna elements [12-15]. However, some of the EBG structures are complex and others have high profile, which is difficult in the practical terminal applications. Furthermore, many other solutions have been presented to reduce the strong mutual coupling, including conducting wall [16], neutralization line [17], parasitic structures and meta-material based decoupling structures [18-19]. However, the mutual coupling is reduced only 6 dB by the wave-guided meta-material given in [19].

In this paper, a 3-D meta-material structure developed and integrated into a two-element MIMO antenna array to reduce the mutual coupling. The designed meta-material unit is comprised of an upper M-shaped patch

and two lower U-shaped patches, and which are connected by two shorted pins. Then, five 3-D meta-material cells are embedded into the substrate into the substrate between two antenna elements, which has a vertical distance of 0.1mm from 3-D meta-material cells to the top surface of the substrate. By using the proposed meta-material structures, more than 18 dB mutual coupling reduction is achieved, which greatly enhances the isolation without affecting the operating bandwidth and radiation characteristics. The proposed structure is embedding in the FR4 substrate, which effectively reduce the profile of the MIMO array and give small effects on the bandwidth and the radiation patterns. Also, the proposed structure provides better isolation.

II. METAMATERIAL UNIT AND ANTENNA CONFIGURATION

The configuration of the proposed two-element MIMO antenna with developed 3-D meta-material structure is depicted in Fig. 1, which is fabricated on a FR-4 substrate with a relative permittivity of 4.4, a loss tangent of 0.02, and a thickness of 1.6mm. The total size of the MIMO antenna is $60 \times 60\text{mm}^2$. Two rectangle patch antennas with 50-Ohm coaxial feeding are utilized to construct the two-element MIMO antenna array whose edge-to-edge antenna element distance is $0.13\lambda_0$. To reduce the mutual coupling, a 3-D meta-material is developed and incorporated into the MIMO antenna. It is found that the MIMO antenna consists of two identical rectangle patch antennas fed by coaxial lines, five 3-D meta-material cells are embedded in the FR-4 substrate to improve the isolation of the MIMO antenna. The vertical distance from the upper M-shaped patch of the designed 3-D meta-material to the top surface of the FR-4 substrate is very small. The 3-D meta-material cell is shown in Fig. 1 (b). It is noted that the proposed meta-material is a non-planar structure, which is composed of an upper M-shaped patch and two lower U-shaped patches. Both of the upper and lower patches are connected via two shorted pins, which is a 3-D meta-material structure. The proposed MIMO antenna and the 3-D meta-material are optimized by using the HFSS and the optimal parameters are: $W=60$, $L=60$, $W1=15$, $L1=30$, $d1=7$, $d2=15$, $m=11$, $n=7.5$, $s=0.8$, $a1=6.3$, $a2=3$, $a3=2.5$, $a4=2.5$, $a5=5.2$, $a6=6.3$, $h=1.6$, $h1=0.8$, $h2=0.1$, (unit:mm).

III. PERFORMANCE OF THE PROPOSED 3-D META-MATERIAL AND THE MIMO ANTENNA

In order to master the electromagnetic properties of proposed 3-D meta-material cell, S-parameters retrieval method is utilized to retrieve the electromagnetic parameters of the cell. The reflection coefficient (S_{11}) and transmission coefficient (S_{12}) are obtained by the HFSS, which are shown in Fig. 2 (In order to write well,

S_{11} and S_{12} are also denoted as S11 and S12, respectively). It is observed that a band-gap characteristic appears around 2.4 GHz, where the electromagnetic waves are almost reflected. Moreover, the retrieved permeability of developed 3-D meta-material cell is given in Fig. 2. We can see that the real of permeability of the 3-D meta-material cell is negative from 2.35 GHz to 2.45 GHz, which can be used to block the surface wave propagation.

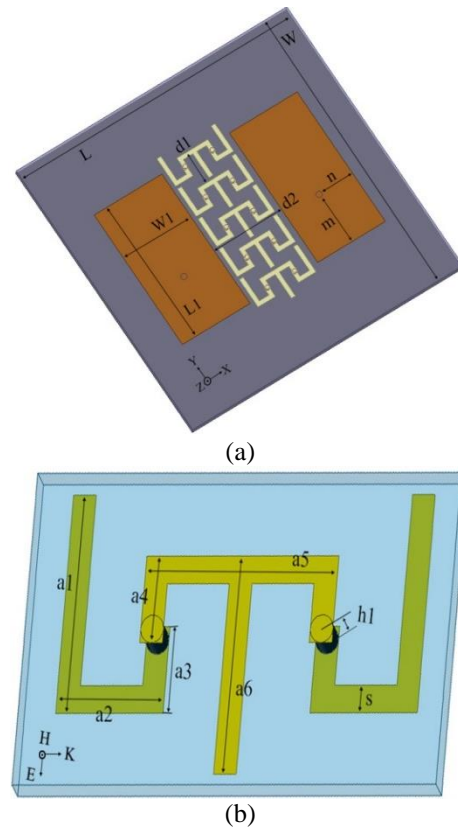


Fig. 1. Geometry structure of the proposed MIMO antenna: (a) MIMO antenna and (b) meta-material cell.

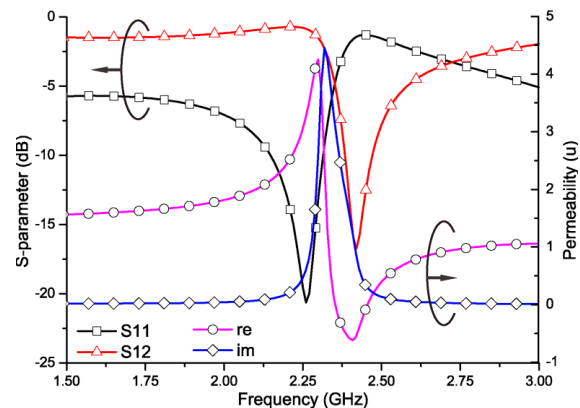


Fig. 2. Characteristics of the proposed 3-D meta-material cell.

Then, five proposed 3-D meta-material cells are integrated into the designed two-element MIMO antenna. The performance of the MIMO antenna with and without the proposed 3-D meta-material is investigated by using the HFSS, and the simulation results are compared in Fig. 3. It can be seen that the proposed MIMO antenna provide about 100MHz bandwidth. The resonance frequency of the MIMO antenna is almost same. However, the mutual coupling of the MIMO antenna with the proposed 3-D meta-material cells drops more than 18 dB in comparison with the MIMO antenna without the meta-material structure. That is to say that the proposed MIMO antenna with proposed 3-D meta-material cells provides a significant improvement with respect to the isolation.

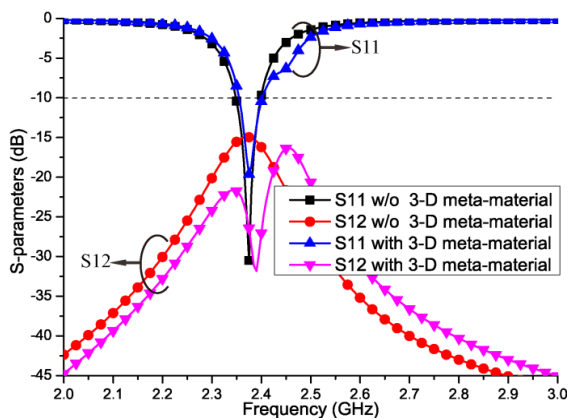


Fig. 3. Impedance bandwidth and mutual coupling of the MIMO antenna.

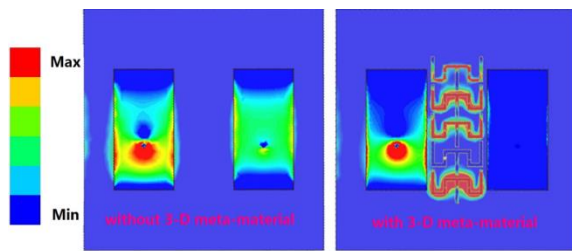


Fig. 4. Current distribution of the proposed MIMO antenna array at 2.38 GHz.

To further understand the effects of proposed 3-D meta-material cells in the MIMO antenna, the current distributions on the MIMO antenna are investigated and shown in Fig. 4 at the 2.38 GHz operation band. Obviously, without the proposed 3-D meta-material structure, strong currents are coupled from one antenna to another patch antenna, whereas only weak surface currents are induced on another patch when the proposed 3-D meta-material structure is loaded. In this case, a large current appears on the proposed 3-D meta-material structure, which blocks the surface current and reduces the mutual

coupling of the closed assignment MIMO antenna array.

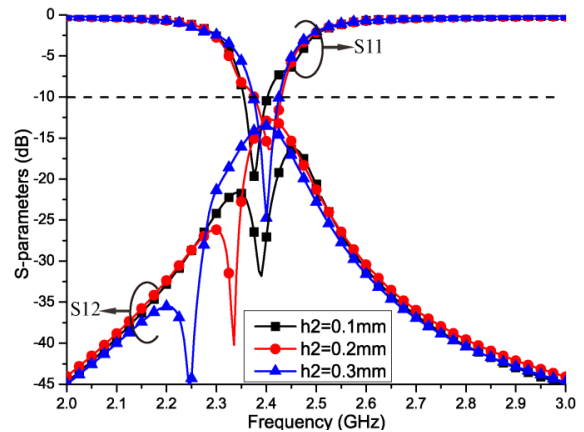
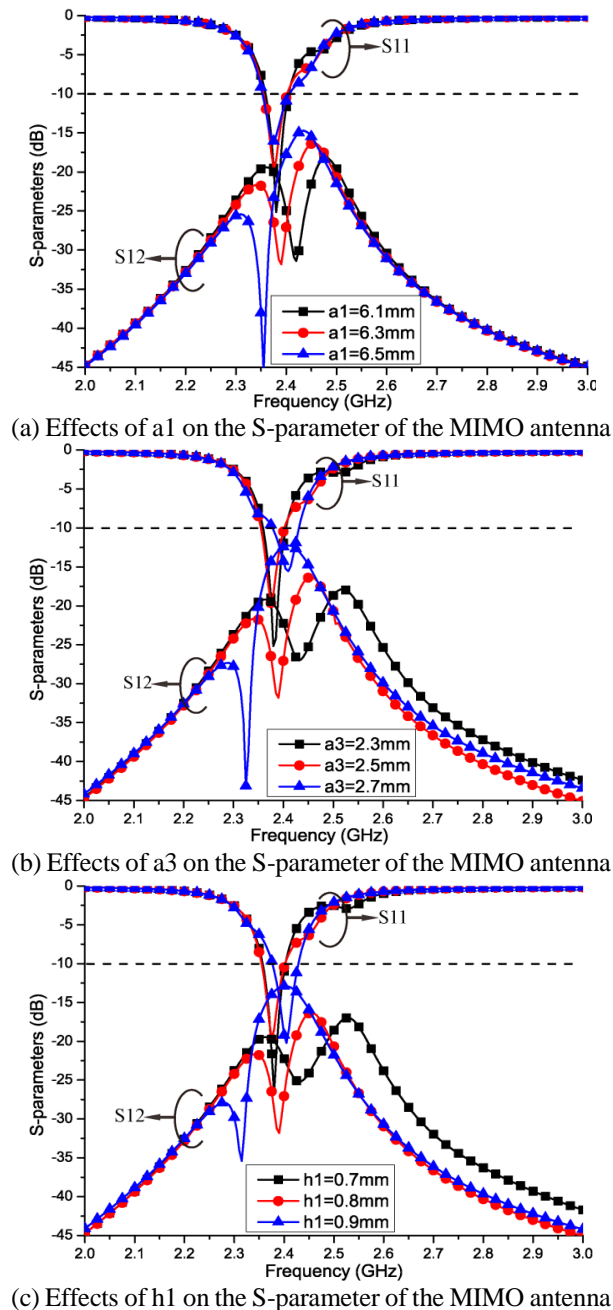
Next, the key parameter effects on the impedance bandwidth and isolation of the MIMO antenna with respect to S11 and S21 are presented by considering a_1 , a_3 , h_1 and h_2 . Figure 5 (a) gives the effects of a_1 on the S-parameter of the MIMO antenna. It is found that the operating band of the MIMO antenna is almost constant, while the isolation is improved in terms of S12.

Moreover, the S12 moves from high frequency to low frequency when a_1 ranges from 6.1mm to 6.5mm. Parameter a_3 has an important effect on both the bandwidth and the isolation and the simulation results are illustrated in Fig. 5 (b). It can be seen that the mutual coupling is reduce when a_3 increases from 2.3mm to 2.5mm. When a_3 continues to increase, both the isolation is deteriorated since the a_3 changes the dimensions of the M-shaped patch and the U-shaped patch of the 3-D meta-material cells, which alters the resonance characteristics of the meta-material. The parameter h_1 and h_2 affect the impedance bandwidth and the mutual coupling and their performance is shown in Figs. 5 (c) and (d), respectively. When h_1 increases from 0.8mm to 0.9mm, the shorted pins are increased, which increase the inductance of the 3-D meta-material. Thus, the center resonance frequency of the 3-D meta-material shifts to the high frequency, and hence, the mutual coupling is also increased. The parameter h_2 control the distance between the top of the 3-D meta-material and the top surface of the FR-4 substrate. With the increment of h_1 and h_2 , the 3-D meta-material is pushed to the direction of the ground plane of the MIMO antenna, which also increases its equivalent capacitance. Thus, the center frequency and the isolation of the MIMO antenna are affected. Thus, we can optimize the parameters of the 3-D meta-material to select the proper dimensions to obtain an optimal performance.

The optimized antenna is fabricated and measured in an anechoic chamber. The fabricated prototype of the MIMO antenna with the proposed embedded 3-D meta-material is shown in Fig. 6 and the measured results are given in Fig. 7. It can be seen that the measured results agree well with the simulated ones. The proposed MIMO antenna operates at 2.4 GHz band, and it also shows a low mutual coupling of -35 dB. Thus, the proposed MIMO antenna with 3-D meta-material achieves an isolation improvement of 18 dB in comparison of the simulated MIMO antenna without the proposed meta-material structure. The differences between the measured and simulated results may be caused by the fabrication errors. The Envelope correlation coefficient (ECC) is also given in Fig. 7 to discuss the mutual coupling of the MIMO antenna. Herein, the ECC of a two-port MIMO antenna in a uniform propagation environment is given by [12]:

$$\rho_e = \frac{|S_{11}^* S_{12} + S_{21}^* S_{22}|}{\left(1 - (|S_{11}|^2 + |S_{21}|^2)\right) \left(1 - (|S_{22}|^2 + |S_{12}|^2)\right)}$$

We find that the ECC is almost zero at 2.35 GHz to 2.42 GHz, which means that the two antennas are irrelevant. Thus, our proposed 3-D meta-material structure effectively reduces the mutual coupling and helps to improve the isolation between the two antenna elements. The measured radiation patterns at center operating frequency are shown in Figs. 8 (a) and (b). It is found that the MIMO antenna has directional radiation patterns in both XOZ- and YOZ-planes. Some deviations from the measured and simulated radiation patterns arise from the errors in fabrication and experiment. The gain of the MIMO antenna array is 5 dBi in the center of the operation band.



(d) Effects of h_2 on the S-parameter of the MIMO antenna

Fig. 5. Parameter effects on the MIMO antenna.

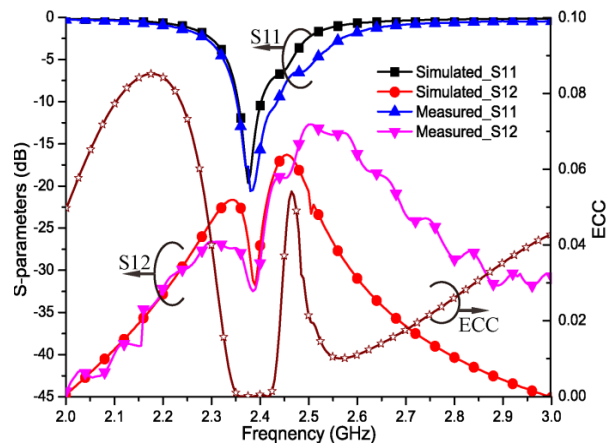
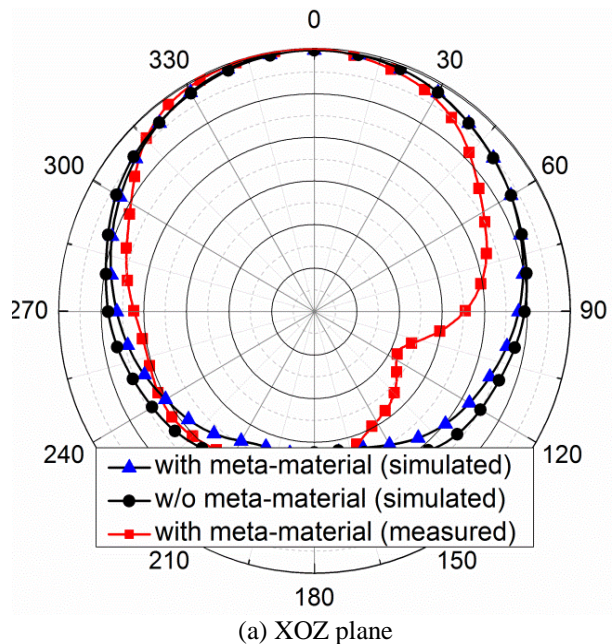


Fig. 7. Performance of the fabricated antenna.



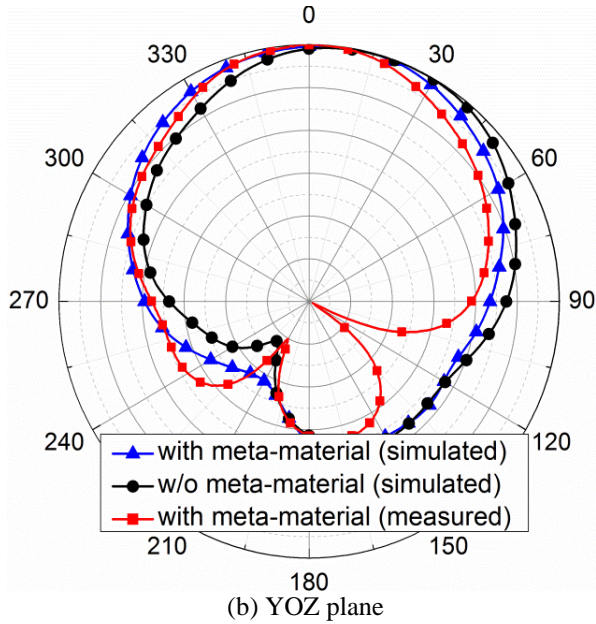


Fig. 8. Radiation patterns of fabricated antenna.

IV. CONCLUSION

A 3-D meta-material structure has been proposed and it has been integrated into a MIMO antenna to reduce the mutual coupling between two rectangle patch antennas. The proposed 3-D meta-material cell is a two-layer connected by the shorted pins. The 3-D meta-material cell has been investigated to catch its characteristics. Then, five 3-D meta-material cells have been incorporated into a MIMO antenna with a distance of $0.13\lambda_0$ to improve the isolation. Both the numerical and experimental results showed that more than 18 dB mutual coupling reduction has been obtained without affecting the operating bandwidth and radiation characteristics. Furthermore, the proposed 3-D meta-material structure has a flexible and adjustable characteristic, which can easily integrate into antenna array to improve the isolation.

ACKNOWLEDGMENT

This paper is supported by the National Key Research and Development Program of China (2016YFE0111100), Key Research and Development Program of Heilongjiang (GX17A016), the Science and Technology innovative Talents Foundation of Harbin (2016RAXXJ044), the Natural Science Foundation of Beijing (4182077), China Postdoctoral Science Foundation (2017M620918), the Fundamental Research Funds for the Central Universities (HEUCFM180806).

REFERENCES

- [1] Y. Li, W. Li, and R. Mittra, "Miniaturized CPW-fed UWB antenna with dual frequency rejection bands using stepped impedance stub and arc-

shaped parasitic element," *Microwave and Optical Technology Letters*, vol. 56, pp. 783-787, 2014.

- [2] Y. Li, W. Li, and W. Yu, "A switchable UWB slot antenna using SIS-HSIR and SIS-SIR for multi-mode wireless communications applications," *Applied Computational Electromagnetics Society Journal*, vol. 27, no. 4, pp. 340-351, 2012.
- [3] H. Yu, G. Yang, F. Meng, and Y. Li, "Performance analysis of MIMO system with single RF link based on switched parasitic antenna," *Symmetry*, vol. 9, no. 12, ID: 304, 2017.
- [4] Y. Yang, Q. Chu, and C. Mao, "Multiband MIMO antenna for GSM, DCS, and LTE indoor application," *IEEE Antennas and Wireless Propagation Letters*, vol. 15, pp. 1573-1576, 2016.
- [5] E. Rajo-Iglesias, Ó. Quevedo-Teruel, and L. Inclán-Sánchez, "Mutual coupling reduction in patch antenna arrays by using a planar EBG structure and a multilayer dielectric substrate," *IEEE Transactions on Antennas and Propagation*, vol. 56, pp. 1648-1655, 2008.
- [6] K. Wei, J. Li, L. Wang, Z. Xing, and R. Xu, "S-shaped periodic defected ground structures to reduce microstrip antenna array mutual coupling," *Electronics Letters*, vol. 52, pp. 1288-1290, 2016.
- [7] K. Wei, J. Li, L. Wang, Z. Xing, and R. Xu, "Mutual coupling reduction by novel fractal defected ground structure bandgap filter," *IEEE Transactions on Antennas and Propagation*, vol. 64, pp. 4328-4335, 2016.
- [8] Y. Li, W. Li, and W. Yu, "A multi-band/UWB MIMO/diversity antenna with an enhance isolation using radial stub loaded resonator," *Applied Computational Electromagnetics Society Journal*, vol. 28, no. 1, pp. 8-20, 2013.
- [9] S. Zhang, Z. Ying, J. Xiong, and S. He, "Ultra wideband MIMO/diversity antennas with a tree-like structure to enhance wideband isolation," *IEEE Antennas and Wireless Propagation Letters*, vol. 8, pp. 110-114, 2009.
- [10] Y. Kong, Y. Li, and W. Yu, "A minimized MIMO-UWB antenna with high isolation and triple band-notched functions," *Frequenz*, vol. 70, no. 11-12, pp. 463-471, 2016.
- [11] Y. Li, W. X. Li, C. Y. Liu, and T. Jiang, "Two UWB-MIMO antennas with high isolation using sleeve coupled stepped impedance resonators," *2012 Asia-Pacific Conference on Antennas and Propagation (APCAP 2012)*, Singapore, August 27-29, 2012.
- [12] T. Jiang, T. Jiao, and Y. Li, "Array mutual coupling reduction using L-loading e-shaped electromagnetic band gap structures," *International Journal of Antennas and Propagation*, vol. 2016, Article ID 6731014, 2016.
- [13] T. Jiao, T. Jiang, and Y. Li, "A low mutual

- coupling MIMO antenna using 3-D electromagnetic isolation wall structures,” *6th Asia-Pacific Conference on Antennas and Propagation*, Xi’an, China, Oct. 16-19, 2017.
- [14] T. Jiang, T. Jiao, Y. Li, and W. Yu, “A low mutual coupling MIMO antenna using periodic multi-layered electromagnetic band gap structures,” *Applied Computational Electromagnetics Society Journal*, vol. 33, no. 3, pp. 305-311, 2018.
- [15] H. Farahani, M. Veysi, M. Kamyab, and A. Tadjalli, “Mutual coupling reduction in patch antenna arrays using a UC-EBG superstrate,” *IEEE Antennas and Wireless Propagation Letters*, vol. 9, pp. 57-59, 2010.
- [16] C. Park and H. Son, “Mutual coupling reduction between closely spaced microstrip antennas by means of H-shaped conducting wall,” *Electronics Letters*, vol. 52, pp. 1093-1094, 2016.
- [17] S. Zhang and G. Pedersen, “Mutual coupling reduction for UWB MIMO antennas with a wideband neutralization line,” *IEEE Antennas and Wireless Propagation Letters*, vol. 15, pp. 166-169, 2016.
- [18] R. Hafezifard, M. Naser-Moghadasi, J. Rashed Mohassel, and R. Sadeghzadeh, “Mutual coupling reduction for two closely spaced meander line antennas using metamaterial substrate,” *IEEE Antennas and Wireless Propagation Letters*, vol. 15, pp. 40-43, 2015.
- [19] X. Yang, X. Liu, X. Zhou, and T. Cui, “Reduction of mutual coupling between closely packed patch antennas using waveguided metamaterials,” *IEEE Antennas and Wireless Propagation Letters*, vol. 11, pp. 389-391, 2012.

Wideband Multi-Port Network Integrated by 3-dB Branch-Line Couplers

Nor Azimah Mohd Shukor, Norhudah Seman, and Tharek Abd Rahman

Wireless Communication Centre
University Teknologi Malaysia, 81310 UTM Johor Bahru, Johor, Malaysia
azimahshukor@fkegraduate.utm.my, huda@fke.utm.my, tharek@fke.utm.my

Abstract — The design of a multi-port network integrated by symmetrical alignment of four 3-dB branch-line couplers (BLCs) for wideband communication applications is presented. The BLC is designed with the implementation of stub impedance at each port's transmission line and defect ground structure (DGS) underneath the shunt branches of BLC to improve bandwidth. The designs of the BLC and the multi-port network are performed by using CST Microwave Studio, a three-dimensional (3D) electromagnetic wave simulator. The designed wideband BLC and multi-port are fabricated, and their wideband performances of 2.3 to 5.3 GHz are verified.

Index Terms — Branch line coupler, defect ground structure, multi-port, stub impedance, wideband.

I. INTRODUCTION

The rapid development of wireless communication demands high-performance devices for future 5th Generation (5G) technologies considering spectrum below 6 GHz and higher than 6 GHz, which yet to be finalized. This future 5G-communication system is envisioned as the possibility of boundless and continuous communication and connection among any devices and machines at anywhere and anytime [1]. This vision prompts an enormous challenge to design and plan a network and front-end system that include antenna and RF/microwave components.

The multi-port network is one of the RF/microwave components that have been growing steadily, owing to its outstanding potential for the future technology of 5G. The multi-port network can be used in various wireless communication applications, such as a modulator or demodulator for modulation and demodulation purposes [2-4]. The common modulator is basically built up based on the mixer-based approach, which involves active devices that require biasing voltage, resulting in design complexity [2-3]. Therefore, in favor of reducing the complexity of the design, the multi-port network integrated by passive devices such as the quadrature coupler and power divider is proposed as an alternative to the common modulator.

An impressive bandwidth of a multi-port network has

been demonstrated by [5], which implements the design technique of the multilayer microstrip-slot. It consists of two substrates, which are sandwiched by three layers of conductive copper. The microstrip patches on the top and bottom layer are broadside-coupled through slotlines that are placed at the middle layer. In contrast to its wide bandwidth, the design faces the production of an air gap and misalignment between the two substrates. Furthermore, it may encounter a connection problem to other components since the ports are located at both top and bottom layers.

Consequently, to deal with these drawbacks in [5], the branch line coupler (BLC) is an alternative that can be used in the multi-port network configuration. However, the conventional BLC is only capable of offering limited bandwidth. Accordingly, various studies have been conducted, specifically to improve the bandwidth performance of BLC. As reported in [6], a technique of implementing the defect ground structure (DGS) onto the single-section BLC is used. The purpose of implementing the DGS is to increase the phase velocity delay [6, 7, 8] of the design that contributes to bandwidth improvement. Another technique in improving the bandwidth is by implementing the stub impedance onto the single-section BLC as proposed in [9]. The implementation of stub allows the design to have wideband operation with very flat coupling [9].

However, the bandwidth of the proposed single-section BLC reported in [6, 9] is still inadequate. Therefore, to overcome the limited bandwidth in [6, 9], another technique can be used to broaden the bandwidth, which is by increasing the sections of BLC [10]. Thus by considering the design techniques in [6, 9, 10], it is worth applying the stub impedance and DGS to the two-section BLC, whereby well-tuning the stub impedance, matching can be improved and, consequently, bandwidth is enhanced. In addition, the DGS also contributes to improving the bandwidth.

In this article, a multi-port network integrated by four two-section 3-dB BLCs is proposed. The BLC is designed with the implementation of DGS underneath the shunt branches at the ground plane and stub impedance at each port's transmission line, which can operate across 2.3 to

5.3 GHz. The designs of the two-section 3-dB BLC and multi-port network are executed in an electromagnetic simulator known as CST Microwave Studio. The performance of the scattering parameters and phase characteristics of the proposed multi-port network and BLC are studied and verified experimentally.

II. DESIGN OF MULTI-PORT NETWORK

The proposed multi-port network is formed by integrating four BLCs that are denoted as blocks of ‘Q’, which are placed symmetrically as in Fig. 1 (a). Its CST generated layout is shown in Figs. 1 (b) and (c) and is integrated by the enhanced BLCs. As shown in Fig. 1, the input ports are depicted by Ports 1 and 2, while other corresponding ports are labelled as Ports 4 to 7. The other two remaining unused ports (Ports 3 and 8) are terminated by 50Ω to maintain well-matching operation of the multi-port network.

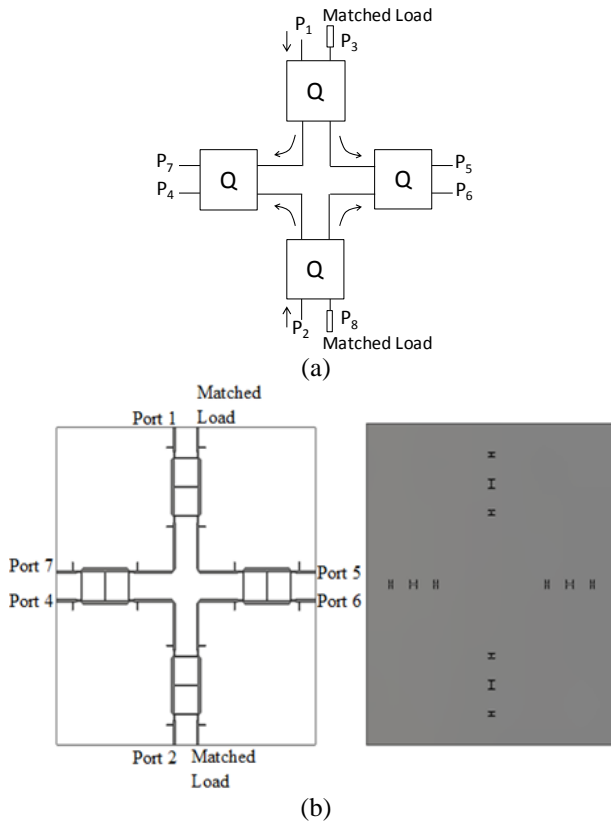


Fig. 1. (a) The configuration of the proposed multi-port network, and the CST generated layout of proposed multi-port network; (b) top and (c) bottom view.

The proposed design is initially utilizing two-section BLC with step impedance at four ports as presented in the following Fig. 2. The implemented step impedance is functioning as one of the matching techniques in this proposed design to reduce the reflections occurred at the transition between ports' transmission lines and BLC's

branches. Referring to [10], the initial characteristic impedances of a and d are set to 157Ω, while, b and c are set to 29Ω. These initial values are determined through the deliberation on the correlation of cascade parameters, transmission and reflection coefficients, perfect matching isolation at design frequency with $S_{11} = S_{41} = 0$, the equal power ratio between output ports (Port 2 and 3) and the assumption of the characteristic impedance, $Z_0 = 50\Omega$. Afterward, the optimization is performed to improve bandwidth in which the finalized impedances are $a = c = d = 121\Omega$ and $b = 35\Omega$.

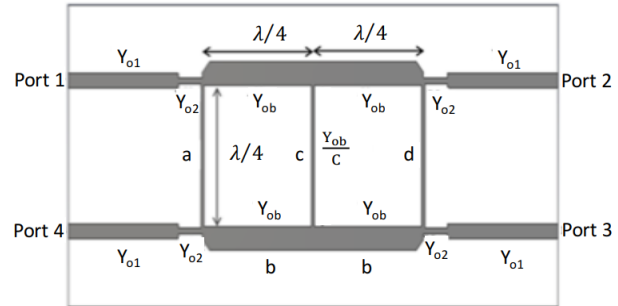


Fig. 2. The CST generated layout of the two-section branch-line coupler with step0 impedance at ports.

The step impedance at four ports is denoted by width, W_1 and length, L_1 , which has admittance of Y_{02} . This Y_{02} can be determined from the following relation of (1) [11]:

$$\left[\left(1 + \frac{Y_{01}}{Y_{02}} \right) \cos^2 \Delta - \left(1 + \frac{Y_{01}}{Y_{02}} \right) \sin^2 \Delta \right] Y_{01}^2 + \left[\frac{1}{\cos \Delta} \right] \frac{1+C}{1-C} Y_{01} - \left[\left(1 + \frac{Y_{01}}{Y_{02}} \right) \cos^2 \Delta - \left(1 + \frac{Y_{01}}{Y_{02}} \right) \sin^2 \Delta \right] = 0 \tag{1}$$

where Y_{01} , Δ and C are the admittance of the port transmission line, load impedance and numerical coupling coefficient, accordingly. In this design, Y_{01} is fixed at $1/Z_0 = 0.02$ S. Meanwhile, to obtain equal power division at Ports 2 and 3, C is set to 0.707. Thus, admittance of Y_{02} is 0.0083 S, which corresponds to 120Ω. Whereas, the Δ is set to 0 to have maximally flat solution with a perfect matching at center frequency, which also enhanced the bandwidth performance. Whilst, the initial dimension of step impedance length, L_1 is $\lambda/4$. However, transmission loss has occurred, which degrades the performance of the coupler. Hence, the length is varied and optimized, where the optimal length of $\lambda/73$ is accomplished.

Afterward, stub impedance is placed at 0.07λ from the branch that determined through the conducted parameter sweep to avoid junction discontinuities and improve matching, which corresponds to 3.7mm as shown in Fig. 3. Theoretically, the half-wavelength stub impedance with higher impedance is required in order to achieve optimal performance [11]. However, the half-wavelength of stub impedance in this design has

contributed to mismatch problems. Thus, the length of stub impedance, L_{s1} is varied and optimized that resulting the optimal length of $50\lambda/657$. While, its optimized impedance is 121Ω . Next, the H-shaped DGS is employed at the ground plane of the BLC, where the DGS employment can improve the bandwidth performance due to its slow-wave characteristic [16]. The implementation of DGS is only suitable on the microstrip line with higher impedance. Therefore, it is placed underneath each of parallel branches that having impedance of 121Ω as shown in Fig. 3. The DGS characteristic impedance, Z_D , is expressed as in (2) [6]:

$$Z_D = Z_0 Z_{in}, \quad (2)$$

where Z_{in} is the input impedance towards DGS section that can be determined by the following Equation (3):

$$Z_{in} = Z_0 \sqrt{\frac{1+|\Gamma|}{1-|\Gamma|}}, \quad (3)$$

where Γ is the reflection coefficient prior to the addition of DGS in the design. Hence, Z_D for this design is 122Ω . Whilst, the initial length of the DGS, L_m is computed by referring to [13]. In order to improve the performance of S_{21} , the size of DGS at the center is designed to be slightly larger, which also influences the flatness of the phase difference performance.

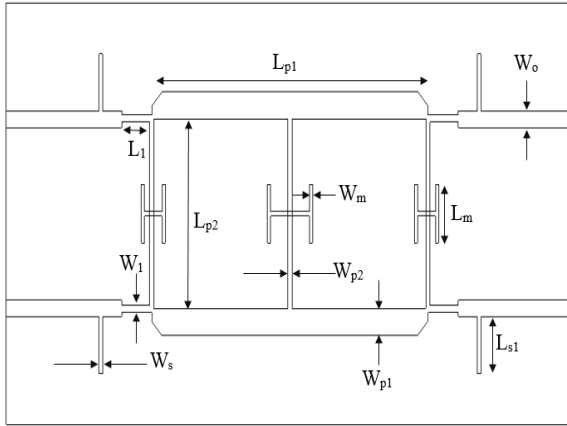


Fig. 3. The CST generated layout of the proposed design with its dimensions.

As shown in Fig. 3, the width dimensions of W_o , W_1 , W_{p1} and W_{p2} that correspond to the respective impedances of 50Ω , 120Ω , 35Ω and 121Ω are determined by the microstrip line equation as expressed in the following (4) [12]:

$$\frac{W}{h} = \frac{2}{\Pi} \left[\frac{377\Pi}{2Z_0\sqrt{\epsilon_r}} - 1 - \ln \left(\frac{377\Pi}{Z_0\sqrt{\epsilon_r}} - 1 \right) + \frac{\epsilon_r - 1}{2\epsilon_r} \right] \left\{ \ln \left(\frac{377\Pi}{2Z_0\sqrt{\epsilon_r}} - 1 \right) + 0.39 - \frac{0.61}{\epsilon_r} \right\}, \quad (4)$$

where h and ϵ_r are the thickness of the substrate and dielectric constant, respectively. Meanwhile, the length dimensions of L_{p1} , L_{p2} , L_1 and L_{s1} are calculated to correspond to $\lambda/2$, $\lambda/4$, $\lambda/73$ and $50\lambda/657$, accordingly. The wavelength, λ is computed from (5) [12]:

$$\lambda = \frac{c}{f\sqrt{\epsilon_e}}, \quad (5)$$

where c , and f are the respective speed of light and design frequency. Meanwhile, ϵ_e is the effective dielectric constant that can be presented by (6) [12]:

$$\epsilon_e = \frac{\epsilon_r + 1}{2} + \frac{\epsilon_r - 1}{2} \frac{1}{\sqrt{1 + 12h/W}}. \quad (6)$$

The width dimension of DGS, W_m is determined from $Z_D = 122\Omega$ using the following Equation (7) [14-15]:

$$Z_D = 60 + 3.69 \sin \left[\frac{(\epsilon_r - 2,22)\Pi}{2.36} \right] + 133.5 \ln(10\epsilon_r) \sqrt{\frac{W_m}{\lambda_0}} + 2.81 \left[t - 0.11\epsilon_r (4.48 + \ln \epsilon_r) \right] \left(\frac{W_m}{h} \right) \ln \left(\frac{100h}{\lambda_0} \right) + 131.1 (1.028 - \ln \epsilon_r) \sqrt{\frac{h}{\lambda_0}} + 12.48 (1 + 0.181 \ln \epsilon_r) \frac{W_m/h}{\sqrt{\epsilon_r - 2.06 + 0.85(W_m/h)^2}}. \quad (7)$$

The proposed design of 3-dB BLC is realized utilizing a substrate of Rogers RO4003C. This substrate has 0.508 mm thickness with 0.017 mm copper cladding at both sides, a 3.38 dielectric constant and a very low loss tangent of 0.0027. The coupler, as shown in Fig. 3, has final optimized dimensions of $W_o = 1.15$ mm, $W_1 = 0.48$ mm, $W_{p1} = 1.85$ mm, $W_{p2} = 0.4$ mm, $W_m = 0.3$ mm, $W_s = 0.35$ mm, $L_1 = 2.2$ mm, $L_{p1} = 26.28$ mm, $L_{p2} = 13.14$ mm, $L_{s1} = 4.0$ mm. The BLC design occupies an area of 54 mm x 29 mm.

III. RESULTS AND DISCUSSION

The performance of the BLC and multi-port are evaluated based on the S-parameters and phase characteristics, which are split into two subsections. The initial design of the two-section BLC with step impedance at ports is assessed and presented, followed by the enhanced BLC design with DGS and stub impedance, and the multi-port network design. The proposed BLC and multi-port network designs are fabricated and verified through the measurement using a vector network analyzer (VNA) in the laboratory.

A. Analysis and verification of enhanced two-section branch-line coupler

The first concern involves the performance of the initial design of the two-section BLC with step impedance at ports, whose configuration is presented in Fig. 2. Figure 4 (a) shows the initial BLC's simulated performance of

the S-parameter. It can be observed that the good return loss and isolation performance of greater than 10 dB are both within 2.5 to 4 GHz. Furthermore, the transmission coefficient of S_{21} demonstrates the performance of -3 dB with oscillated deviation of -2 dB across the similar frequency range. Meanwhile, this initial design offers an oscillation of S_{31} between -4 dB and -5 dB.

The plotted response in Fig. 4 (b) shows the simulated performance of phase differences among output ports. It demonstrates that the simulated phase difference between Port 2 and 3 is at $90^\circ \pm 10^\circ$ between 2.5 and 4 GHz. The performance of this initial design of the proposed coupler is summarized in Table 1. This initial design offers a fractional bandwidth of 46% compared to a conventional single-section BLC and conventional two-section BLC presented in [10] with respective bandwidths of 32% and 34.4%.

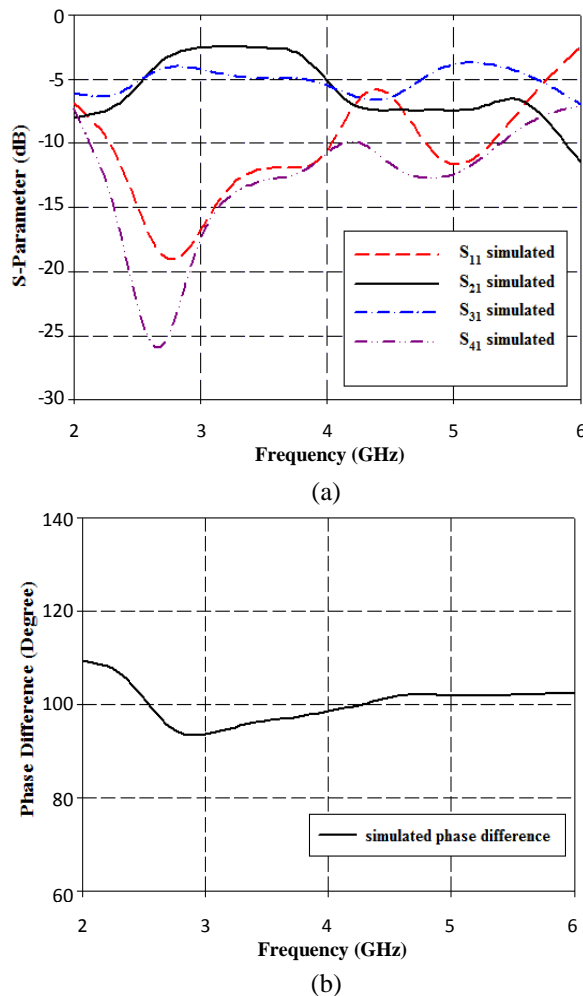


Fig. 4. The simulated (a) S-performance and (b) phase difference of the initial design of two-section BLC with step impedance at ports.

Following this, the proposed design of a two-section

BLC with stub impedance and DGS is fabricated. Figure 5 shows the fabricated prototype of the proposed two-section BLC, where each port is connected to subminiature A (SMA) connectors. Its wideband performance is then practically measured in the laboratory using a vector network analyzer (VNA). Afterward, the comparison is made in terms of the simulated and measured S-parameters and phase characteristic performances.

Table 1: The simulated performance of the initial design of two-section BLC with step impedance at ports

Parameters	Performance
S_{11} & S_{41}	≤ -10 dB
S_{21}	-3 dB ~ -5 dB
S_{31}	-4 dB ~ -5 dB
Phase Difference	$90^\circ \pm 10^\circ$
Operating Frequency	2.5 GHz – 4 GHz

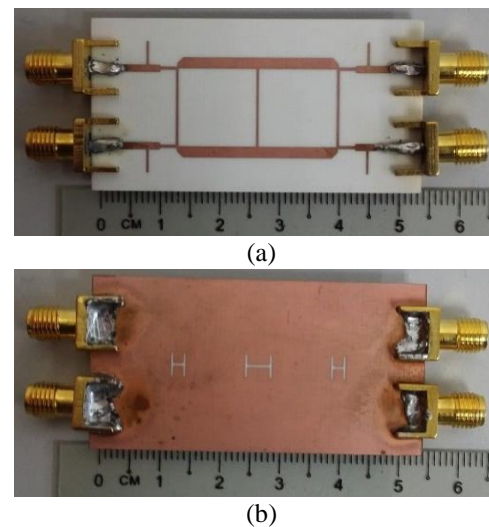


Fig. 5. The prototype of the two-section BLC design with DGS and stub impedance: (a) front and (b) bottom view.

Figure 6 and Fig. 7 depict the simulated and measured performances of the proposed BLC, which exhibits a good wideband operation of 2 GHz bandwidth, between 2.3 and 5.3 GHz. Within this frequency range, the simulated and measured reflection coefficient performances of S_{11} at Port 1 are lower than -10 dB. Meanwhile, the isolation performance is better than 11 dB.

The simulated and measured coupling coefficients show the respective performance between 2.2 dB to 5 dB and 4 dB to 5 dB, as plotted in Fig. 6 (b). Moreover, the simulated and measured transmission coefficients between the through port (Port 2) and the input port (Port 1), which are presented by S_{21} , are fluctuating within -2.4 dB to -5 dB and -3.2 dB to -4.5 dB, accordingly. Meanwhile, the plotted responses in Fig. 7 show that the simulated and measured phase difference between output ports are $90^\circ \pm 2^\circ$ and $90^\circ \pm 4^\circ$, accordingly. These S-parameter

and phase difference performances are then summarized in Table 2 for better comparison purposes. The analysis of the reflection coefficient, transmission coefficient, coupling coefficient, isolation and phase characteristic performance of the proposed coupler summarized in Table 2 shows that employing stub impedance improves the matching of the designed coupler.

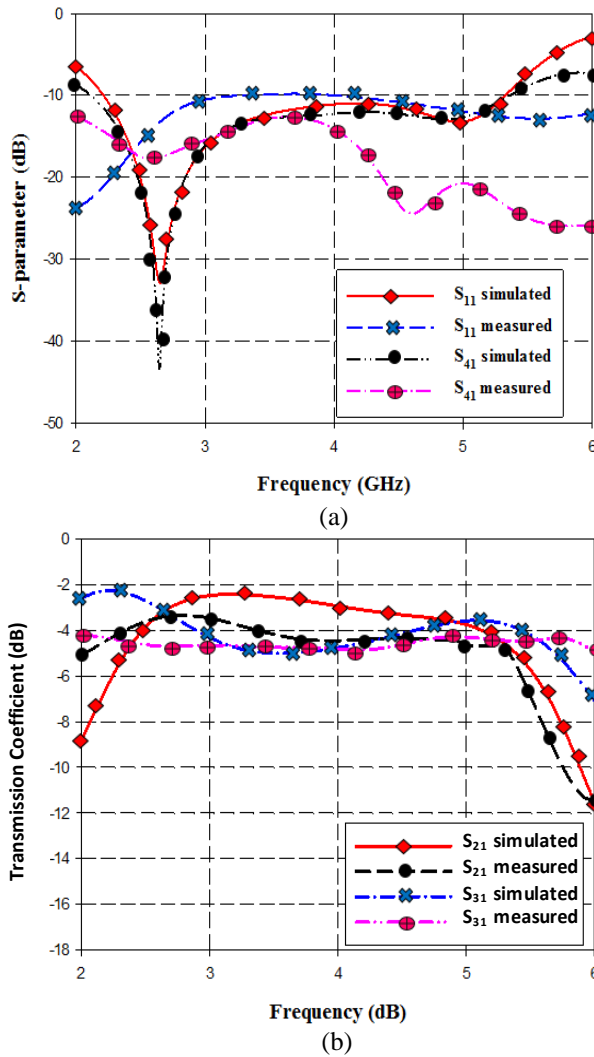


Fig. 6. The simulated and measured (a) S_{11} and S_{41} , and (b) transmission coefficients of S_{21} and S_{31} of the proposed BLC with stub impedance and DGS.

Consequently, stub impedance also improves the performance of phase characteristic with less deviation compared to the initial design. Meanwhile, the implementation of DGS enhances the bandwidth performance of the proposed coupler with a fractional bandwidth of 79% compared to the initial design, which exhibited a bandwidth of 46%. Following the wideband performance verification of the proposed BLC, the next

concern is to evaluate the performance of the multi-port network.

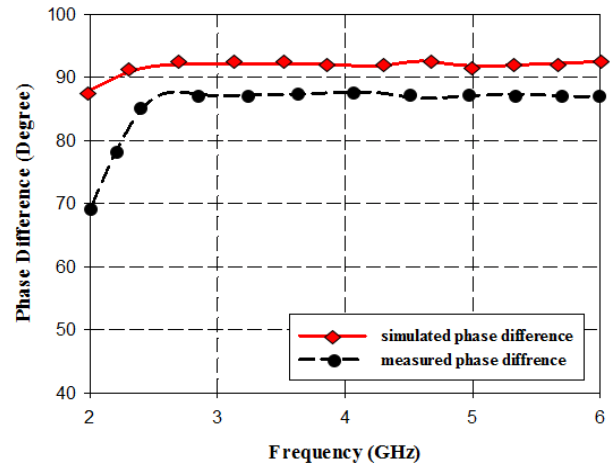


Fig. 7. The simulated and measured phase difference of the proposed BLC with stub impedance and DGS

Table 2: The performance of the designed BLC with stub impedance and DGS

Parameters	Performance	
	Simulation	Measurement
S_{11}	≤ -10 dB	
S_{21}	-2.4 dB ~ -5 dB	-3.2 dB ~ -4.5 dB
S_{31}	-2.2 dB ~ -5 dB	-4 dB ~ -5 dB
S_{41}	≤ -11 dB	
Phase Difference	$90^\circ \pm 2^\circ$	$90^\circ \pm 4^\circ$
Operating Frequency	2.3 GHz – 5.3 GHz	

B. The performance of multi-port network

The proposed multi-port network is fabricated using Rogers RO4003C substrate, where each port is connected to subminiature A (SMA) connectors for testing purposes, as shown in Fig. 8. The multi-port design has a total size of 144 mm x 144 mm.

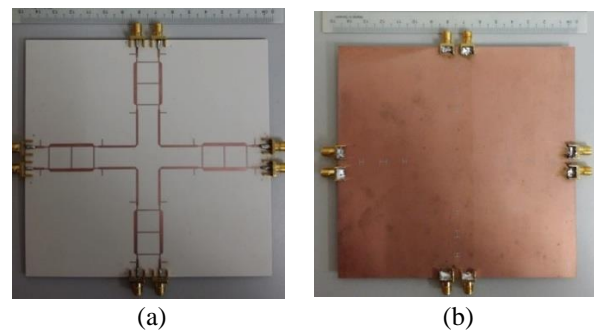


Fig. 8. The photography of the fabricated multi-port network: (a) top view and (b) bottom view.

As observed in Fig. 9 to Fig. 11, the proposed multi-port network has a good wideband performance of 2.3 to 5.3 GHz. The performances of simulated and measured reflection coefficients of S_{11} and S_{22} are less than -10 dB, as denoted by the plotted responses in Fig. 9. These indicate good return loss performance at the input ports of Port 1 and Port 2. The next concern involves the simulated and measured transmission coefficients referenced against Port 1 and Port 2, which are presented in Fig. 10.

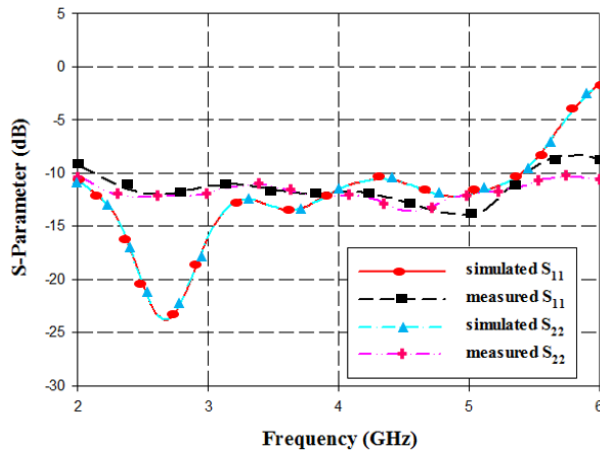


Fig. 9. Simulated and measured reflection coefficients of the proposed multi-port network.

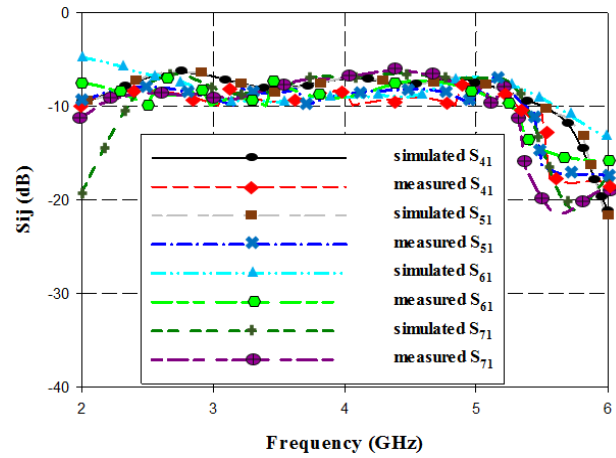
Referring to Fig. 10 (a), the simulated and measured transmission coefficients referenced to Port 1 oscillate in the range of $-8 \text{ dB} \pm 1.5 \text{ dB}$, and $-8 \text{ dB} \pm 2 \text{ dB}$ across 2.3 to 5.3 GHz, respectively. Meanwhile, Fig. 10 (b) presents the respective simulated and measured transmission coefficients referenced to Port 2, which fluctuate around $-8 \text{ dB} \pm 1.8 \text{ dB}$ and $-8 \text{ dB} \pm 2 \text{ dB}$ in a similar frequency range. As expected, the measured results exhibit more deviation compared to the simulation. This can be attributed by the inaccurate width of transmission lines that may occur during the fabrication process. The slight changes in the width of transmission lines can affect the performance of the overall design. However, the measurement results still demonstrate good performance across the designated frequency range.

Then, the analysis proceeds with performances of the phase characteristics. The phase characteristics can be analyzed based on Equation (8):

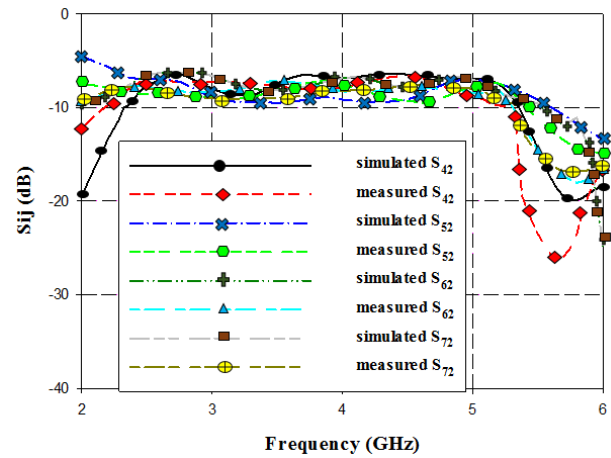
$$\angle S_{\Delta ij} (\text{deg ree}) = \angle S_{ij} (\text{deg ree}) - \angle S_{Ak} (\text{deg ree}), \quad (8)$$

where $i = 4, 5, 6, 7$, $j = 1, 2$, and $k = 1, 2$. Figure 11 (a) shows that the performances of the simulated and measured phase characteristics of $S_{\Delta 711}$ and $S_{\Delta 421}$ are $90^\circ \pm 10^\circ$ from 2.3 to 5.3 GHz, respectively. Meanwhile, the simulated and measured phase characteristics of $S_{\Delta 511}$, $S_{\Delta 621}$ and $S_{\Delta 721}$ are approximately 0° within the similar range

frequency. Next, the simulated and measured phases of transmission coefficients $S_{\Delta 611}$ and $S_{\Delta 521}$ are $-90^\circ \pm 10^\circ$.



(a)



(b)

Fig. 10. Simulated and measured transmission coefficients, S_{ij} ($i = 4, 5, 6, 7$ and $j = 1, 2$): (a) S_{i1} and (b) S_{i2} of the proposed multi-port network.

Figure 11 (b) depicts the simulated and measured phases of transmission coefficients that are plotted against the transmission coefficient phase of S_{42} . As seen in the plotted graph, the simulated and measured transmission coefficient phases of $S_{\Delta 412}$, $S_{\Delta 512}$, $S_{\Delta 622}$ and $S_{\Delta 722}$ are $-90^\circ \pm 10^\circ$ across 2.3 to 5.3 GHz. The simulated and measured transmission coefficients' phases of $S_{\Delta 612}$ and $S_{\Delta 522}$ show the worst deviation of 20° from 180° within the similar frequency range. Meanwhile, the phase of transmission coefficient of $S_{\Delta 71}$ is almost 0° . Based on Figs. 9 to 11, the multi-port network demonstrates comparable performance between simulation and measurement, which offers a good wideband operation with a fractional bandwidth of 79%, covering 2.3 to 5.3 GHz.

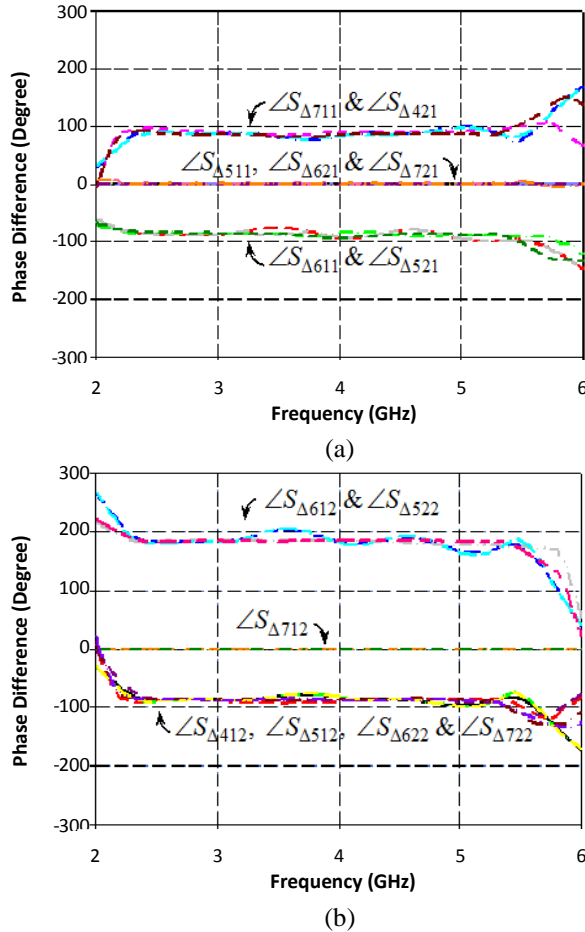


Fig. 11. Multi-port network's simulated and measured phase characteristics referenced to: (a) $\angle S_{\Delta 41}$ and (b) $\angle S_{\Delta 42}$.

IV. CONCLUSION

A wideband multi-port network integrated by four two-section BLCs implemented with DGS and stub impedance techniques with an overall size of 144 mm x 144 mm has been presented. The design and optimization have been executed using CST Microwave Studio, an electromagnetic (EM) simulator. The performances of transmission coefficients, reflection coefficients and phase characteristics of the designed couplers and multi-port network have been assessed and analyzed. The designed two-section BLC and multi-port network have been fabricated. Their wideband performances from 2.3 to 5.3 GHz are proven via measurement in the laboratory. This wideband multi-port can be employed in the front-end system of various wireless communication applications as a modulator or demodulator for modulation and demodulation purposes.

ACKNOWLEDGMENT

This work was supported by Ministry of Higher-Education Malaysia (MOHE) and Universiti Teknologi Malaysia (UTM) through Prototype Research Grant

Scheme (PRGS) [Vote Number of 4L684]; Flagship Grant [Vote Number of 03G41] and HiCoE Grant [Vote Number of 4J212].

REFERENCES

- [1] A. Gohil, H. Modi, and S. K. Patel, "5G technology of mobile communication: A survey," *International Conference on Intelligent Systems and Signal Processing (ISSP)*, pp. 228-292, 2013.
- [2] M. Dušek and J. Y. Šebesta, "Design of substrate integrated waveguide six-port for 3.2 GHz modulator," *International Conference on IEEE Telecommunications and Signal Processing (TSP)*, pp. 274-278, 2011.
- [3] Y. Y. Zhao, J. F. Frigon, K. Wu, and R. G. Bosisio, "RF front-end for impulse UWB communication systems," *IEEE MTT-S International Microwave Symposium Digest*, pp. 308-311, June 2006.
- [4] N. Seman, M. E. Bialkowski, S. Z. Ibrahim, and A. A. Bakar, "Design of an integrated correlator for application in ultra wideband six-port transceivers," *IEEE Antennas and Propagation Society International Symposium*, pp. 1-4, 2009.
- [5] N. Seman and S. N. A. M. Ghazali, "Quadrature phase shift keying (QPSK) modulator design using multi-port network in multilayer microstrip-slot technology for wireless communication applications," *Radioengineering*, vol. 24, pp. 527-534, 2015.
- [6] T. Moyra, A. Roy, S. K. Parui, and S. Das, "Design of 10 dB branch line coupler by using DGS," *Communications, Devices and Intelligent System International Conference (CODIS)*, pp. 516-519, 2012.
- [7] Y. M. Huang, Y. Peng, Y. Zhou, et al., "Size-reduced dual-band HMSIW cavity filters loaded with double-sided SICSRRs," *Electron. Lett.*, vol. 53, no. 10, pp. 689-691, 2017.
- [8] A. Boutejdar, A. A. Ibrahim, and W. A. E. Ali, "Design of compact size and tunable band pass filter for WLAN applications," *Electron. Lett.*, vol. 52, no. 24, pp. 1996-1997, 2016.
- [9] G. Prigent, E. Rius, H. Happy, K. Blary, and S. Lepilliet, "Design of wide-band branch line coupler in the G-Frequency band," *IEEE MTT-S International Microwave Symposium Digest*, pp. 986-989, 2006.
- [10] N. A. M. Shukor and N. Seman, "Enhanced design of two-section microstrip-slot branch line coupler with the overlapped $\lambda/4$ open circuited lines at ports," *Wireless Pers. Commun.*, vol. 88, pp. 467-478, 2016.
- [11] J. V. Ashforth, "Design equations to realise a broadband hybrid ring or a two-branch guide coupler of any coupling coefficient," *Electronic Letters*, vol. 24, pp. 1276-1277, 1988.

- [12] D. M. Pozar, *Microwave Engineering*. New York: Wiley, 2005.
- [13] P. Bhowmik, T. Moyra, and P. K. Deb, "Miniaturization and bandwidth enhancement of a loose coupler by DGS," *International Conference on Signal Processing and Integrated Networks (SPIN)*, pp. 638-641, 2015.
- [14] R. Gorg, I. Bahl, and M. Bozzi, *Microstrip Lines and Slotlines*. 3rd ed., Artech House, 2013.
- [15] K. H. Yusof, N. Seman, and M. H. Jamaluddin, "Design of U-shaped in-phase power divider employing ground-slotted technique for wideband applications," *Wireless Pers. Commun.*, vol. 81, pp. 359-371, 2015.
- [16] M. Shirazi, R. F. Shirazi, Gh. Moradi, and Mo. Shirazi, "Three new rat-race couplers with defected microstrip and ground structure (DMGS)," *Applied Computational Electromagnetics Society (ACES) Journal*, vol. 28, pp. 300-306, 2013.



Nor Azimah Mohd Shukor obtained her first degree from Universiti Teknologi Malaysia (UTM) in Electrical Engineering (Telecommunication) in 2013. She has completed her Master in Electrical Engineering from UTM in 2015. She currently pursues her Ph.D. in Electrical Engineering at UTM since 2016. Her research topic focusing on beam-forming network for 5G application.



Norhudah Seman received the B.Eng. in Electrical Engineering (Telecommunications) degree from the Universiti Teknologi Malaysia, Johor, Malaysia, in 2003 and M.Eng. degree in RF/Microwave Communications from The University of Queensland, Brisbane, St. Lucia, Qld., Australia, in 2005. In September 2009, she completed her Ph.D. degree at The University of Queensland. In 2003, she was an Engineer with Motorola Technology, Penang, Malaysia, where she was involved with the RF and microwave components design and testing. Currently, she is an Associate Professor in Wireless Communication Centre (WCC), Universiti Teknologi Malaysia. Her research interests concern the design of microwave circuits for biomedical and industrial applications, specific absorption rate (SAR), UWB technologies, and mobile communications.



Tharek Abd. Rahman is a Professor at Faculty of Electrical Engineering, Universiti Teknologi Malaysia (UTM). He obtained his B.Sc. in Electrical & Electronic Engineering from University of Strathclyde UK in 1979, M.Sc. in Communication Engineering from UMIST Manchester UK and Ph.D. in Mobile Radio Communication Engineering from University of Bristol, UK in 1988. He is the Director of Wireless Communication Centre (WCC) UTM. His research interests include radio propagation, antenna and RF design and indoors and outdoors wireless communication.

Efficient Design of Metamaterial Absorbers using Parametric Macromodels

Giulio Antonini¹, Maria Denise Astorino², Francesco Ferranti³,
Fabrizio Frezza², and Nicola Tedeschi²

¹UAq EMC Laboratory, Dipartimento di Ingegneria Industriale e dell'Informazione e di Economia
Università degli Studi dell'Aquila, 67100 L'Aquila, Italy
giulio.antonini@univaq.it

²Department of Information Engineering, Electronics and Telecommunications
La Sapienza University of Rome, 00184 Rome, Italy
mariadenise.astorino@uniroma1.it, nicola.tedeschi@uniroma1.it, fabrizio.frezza@uniroma1.it

³Microwave Department
Institut Mines-Télécom Atlantique, CNRS UMR 6285 Lab-STICC, 29238 Brest CEDEX 3, France
francesco.ferranti@imt-atlantique.fr

Abstract – Metamaterial absorbers have recently attracted a lot of interest for applications spanning from microwave to terahertz, near infrared and optical frequencies, such as electromagnetic compatibility, thermal emitters, solar cells and microbolometers. In this paper, a procedure for the efficient design of metamaterial absorbers based on parametric macromodels is presented. These models are used to describe the frequency-domain behaviour of complex systems as a function of frequency and design parameters (e.g., layout features). Parametric macromodels are very efficient and can be used to speed up the design flow in comparison with using electromagnetic simulators for design tasks. The use of quasi-random sequences for the sampling of the design space and of radial basis functions and polynomial functions for the model construction is proposed. Numerical results validate the efficiency and accuracy of the proposed technique for multiple optimizations.

Index Terms – Efficient Design, Metamaterial Absorbers, Optimization, Parametric Macromodeling.

I. INTRODUCTION

Recently, metamaterial absorbers (MMAs) have aroused a huge interest and a large amount of research has been dedicated to the design of such devices [1] with specific characteristics ranging from the wide-angular response [2–4], to the polarisation insensitivity [4–8] and the bandwidth enhancement [9, 10]. Moreover, their applications span from microwave [11] to terahertz (THz) [12], near infrared

and optical frequencies [13, 14], such as electromagnetic compatibility, thermal emitters [15], solar cells and micro-bolometers [16, 17].

The Salisbury screen was one of the first microwave absorbers [18], constituted of a resistive sheet and a dielectric layer backed by a metallic plate capable of achieving impedance matching with free space through quarter-wave antireflection interference, but with the disadvantage of a $\lambda/4$ thick dielectric spacer. Other examples, in the microwave range, are the Jaumann absorber [19] which exploits multiple resistive sheets to broaden the bandwidth and the high-impedance surfaces [20], i.e., periodic structures able to perform near-unity absorption at the desired frequency through the introduction of an amount of Ohmic or dielectric losses.

In the THz regime, instead, these absorbing devices are suitable for many applications in sensing, spectroscopy, monitoring, imaging and THz detectors, allowing to overcome the so-called “THz gap” [21, 22].

As pointed out in [23], it is not a challenging task to design an absorber working at a single frequency, at normal incidence, and with an arbitrary thickness. In the last decades, many efforts have been spent to reduce the absorbers thickness, and to improve the working bandwidth and the angular response. Moreover, another important property of an absorber is the polarisation insensitivity, i.e., the possibility to absorb the incident radiation independently of its polarisation. Several techniques have been implemented to achieve such requirements. Metamaterial absorbers, i.e., stratified

cations of metamaterial surfaces and dielectric slabs, usually allow to realize thin absorbers, at least for narrow-band applications. In order to obtain the polarisation insensitivity with a metamaterial absorber, it is enough to consider isotropic surfaces, i.e., isotropic unit cells in the directions transverse to the stratification one. In order to increase the bandwidth, the most common strategy is to superpose several layers, covering the upper layer with a dielectric superstrate [23–25].

Among the configurations of MMAs proposed in the literature, the most performable is composed of subwavelength frequency selective surfaces (FSSs) [24] printed on a grounded dielectric slab, i.e., a compact three-layer system in which the FSS is formed by electric ring resonators (ERRs) that allow controlling and independently tune the effective permittivity of the device.

While this setting has been found effective, to authors' knowledge its efficient optimization or design space exploration have never been addressed. These tasks are usually performed by multiple frequency-domain electromagnetic (EM) simulations for different design parameter values (e.g., layout features), trying to meet the desired requirements. It is also obvious that both design space exploration and optimization can be very time consuming since multiple EM simulations are needed, even for a single unit cell that is assumed to constitute a periodic structure.

In this paper, we focus on design optimization. In the literature, multiple optimization approaches have been proposed, e.g., based on particle swarm and genetic algorithms [26] and based on space mapping methods [27–31].

A different framework to efficiently and accurately perform design activities is based on parametric macromodels. These models [32–36] are able to accurately and efficiently model the behaviour of complex systems as a function of frequency (or time) and additional parameters (such as layout features). Once built, these models can be used to efficiently perform multiple design tasks such as design space exploration, optimization and variability analysis, which will otherwise result very computationally expensive if only based on EM simulations. We show that parametric macromodels are not only useful for a single design optimization, but they can be re-used to optimize the design to meet multiple sets of specifications. This is the main feature that distinguishes the proposed method from existing optimization methods proposed for EM systems. Also, the proposed technique leads to a model in a state-space form that provides an engineering interpretation: for example, poles and zeros of the system

transfer function can be computed and analyzed as a function of design parameters.

The paper is organised as follows. Section II briefly reviews the metamaterial absorbers with a special focus on the ultra-thin narrow-band MMA discussed in [37]. Then, the parametric macromodeling technique adopted to capture the dependence of the metamaterial absorber frequency-domain behaviour on the design parameters is presented in Section III. A design space composed of six design parameters has to be handled. We propose the use of quasi-random sequences for the sampling of the design space and of radial basis functions and polynomial functions for the model construction. Such a high-dimensional design space and model generation procedure have not been investigated in previous parametric macromodeling techniques. The effectiveness of the proposed approach is confirmed by the numerical results presented in Section IV. Finally, the conclusions are drawn in Section V.

II. METAMATERIAL ABSORBERS

The analysed ultra-thin narrow-band MMA with a four-fold rotational symmetry with respect to the incidence z -direction (see Fig. 1), follows a three-layer arrangement as discussed in [37, 38]. Its unit cell with a lattice constant $a = 80 \mu\text{m}$ consists of a top metallic ERR and a lower ground plane separated by a $5.8 \mu\text{m}$ thick dielectric layer of benzocyclobutane (BCB) with relative permittivity $\epsilon_r = 2.5$ and dielectric loss tangent $\tan\delta = 0.005$. Both the top and bottom layers are made up of lossy gold with a conductivity of $1 \times 10^7 \text{ S/m}$ and a thickness of 270 nm . In [37], an equivalent circuit is proposed in order to have a circuital (and more intuitive) interpretation of the EM phenomena related to the absorber. The numerical values of the circuit elements are identified only after the EM response of the absorber is obtained by an EM solver. Therefore, it is not a circuit model based on analytical equations, which can replace the EM solver to calculate the EM response of the absorber. It is to be noted that the equivalent circuit does not provide the same level of accuracy as the EM simulations.

In order to consider an infinitely periodic MMA, the unit cell has been simulated through the RF module of the EM solver of Comsol Multiphysics [39] based on the finite element method (FEM) applying Floquet periodic boundary conditions along the x and y axes and assuming an EM wave impinging at normal incidence along the z direction. We note that the use of a FEM solver is not mandatory for the proposed technique. Any EM solvers can be used. We employ perfectly matched layers (PMLs) on the top and bottom of the unit cell to absorb the excited

mode from the source port and any higher order modes generated by the periodic MMA along with port boundary conditions on the interior boundaries of the PMLs to retrieve the reflection and transmission coefficients in terms of scattering parameters. In fact, the absorbed power can be expressed as $A(\omega) = 1 - R(\omega) - T(\omega) = 1 - |S_{11}(\omega)|^2 - |S_{21}(\omega)|^2$, meaning that in a perfect MMA, the reflection and transmission need to be simultaneously minimised. Since, in this case, the backside is grounded by metallic plane thicker than the skin depth, the absorption equation reduced to $A(\omega) = 1 - R(\omega)$, and as the effective impedance is matched to the free space impedance, it is possible to obtain a perfect absorption at the resonant frequency on a wide angular spectrum. This behaviour can be reached by properly adjusting and selecting the geometric dimensions of the top ERR, the thickness and physical properties of the dielectric substrate, being these parameters responsible both for the electric and magnetic responses.

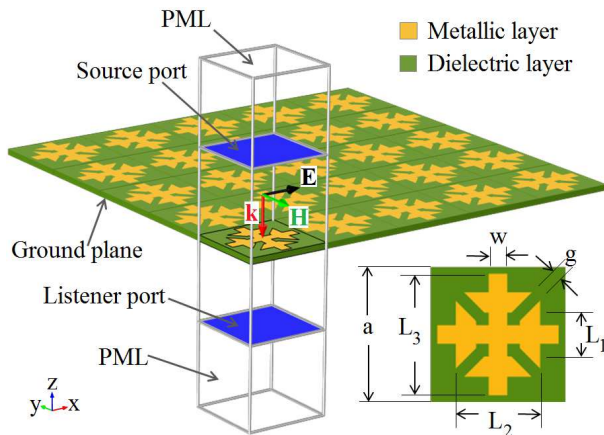


Fig. 1. Unit cell of the ultra-thin narrow-band MMA and virtual infinite 2D array.

In summary, the physical mechanism underlying this narrow-band MMA with a near unity absorption, is based on anti-parallel currents between the two metal layers that allow the coupling to the magnetic field, while the coupling to the incident electric field is due to the ERR that basically determines the absorption frequency. Indeed, when the electric field of the incident THz wave is parallel to one of the rods of the ERR, an electric dipole is excited on this rod, while no dipole exists on the orthogonal rod, but there is instead an electric-dipole resonance oscillating in anti-phase on the ground plane. Therefore, if the polarisation is not parallel to a particular rod, the electric dipoles of both rods will contribute to the absorption mechanism, giving results close to the case of parallel polarisation due to the symme-

try of the unit cell. In the following Section, we will determine the optimum set of geometric dimensions of the unit cell and the ERR able to guarantee the maximum absorption at a desired frequency.

III. PARAMETRIC MACROMODELING

In this Section, we describe the modeling method that will be used to generate parametric macromodels for efficient design. It aims to build a parametric macromodel $\mathbf{R}(s, \mathbf{g})$ that accurately describes the behaviour of a system as a function of the Laplace variable s and a set of design parameters $\mathbf{g} = (\mathbf{g}^{(m)})_{m=1}^M$, such as layout features. A parametric macromodel in the form:

$$\mathbf{R}(s, \mathbf{g}) = \mathbf{C}(\mathbf{g})(s\mathbf{I} - \mathbf{A}(\mathbf{g}))^{-1}\mathbf{B}(\mathbf{g}) + \mathbf{D}(\mathbf{g}), \quad (1)$$

is computed where $\mathbf{A}(\mathbf{g}) \in \mathbb{R}^{n_x \times n_x}$, $\mathbf{B}(\mathbf{g}) \in \mathbb{R}^{n_x \times n_u}$, $\mathbf{C}(\mathbf{g}) \in \mathbb{R}^{n_y \times n_x}$, $\mathbf{D}(\mathbf{g}) \in \mathbb{R}^{n_y \times n_u}$.

Let us consider a set of Q frequency-domain ($s = j\omega$) EM simulations at different values \mathbf{g}_q , $q = 1, \dots, Q$ of the design parameters. In this paper, each EM simulation corresponding at the \mathbf{g}_q sample provides the scattering parameters of the structure under study for a certain set of frequency samples $\mathbf{S}(j\omega_f, \mathbf{g}_q)$, $f = 1, \dots, F$. Based on these frequency-domain data sets, a set of local linear time-invariant (LTI) state-space models $\mathbf{A}(\mathbf{g}_q), \mathbf{B}(\mathbf{g}_q), \mathbf{C}(\mathbf{g}_q), \mathbf{D}(\mathbf{g}_q)$ can be identified using any system identification techniques for LTI systems [40–42]. The local LTI models $\mathbf{R}(s, \mathbf{g}_q) = \mathbf{C}(\mathbf{g}_q)(s\mathbf{I} - \mathbf{A}(\mathbf{g}_q))^{-1}\mathbf{B}(\mathbf{g}_q) + \mathbf{D}(\mathbf{g}_q)$ model the scattering parameters data $\mathbf{S}(j\omega_f, \mathbf{g}_q)$, $f = 1, \dots, F$. The state-space matrices of the local LTI models can be interpolated as a function of \mathbf{g} :

$$\begin{aligned} \mathbf{A}(\mathbf{g}) &= \sum_{q=1}^Q l_q(\mathbf{g})\mathbf{A}(\mathbf{g}_q), \mathbf{B}(\mathbf{g}) = \sum_{q=1}^Q l_q(\mathbf{g})\mathbf{B}(\mathbf{g}_q), \\ \mathbf{C}(\mathbf{g}) &= \sum_{q=1}^Q l_q(\mathbf{g})\mathbf{C}(\mathbf{g}_q), \mathbf{D}(\mathbf{g}) = \sum_{q=1}^Q l_q(\mathbf{g})\mathbf{D}(\mathbf{g}_q) \end{aligned} \quad (2)$$

to obtain a parametric macromodel. The interpolation models can use interpolation functions $l_q(\mathbf{g})$ whose value is based on the distribution of the design parameters values \mathbf{g}_q in the design space (e.g., multilinear interpolation [43]) and $\mathbf{A}(\mathbf{g}_q), \mathbf{B}(\mathbf{g}_q), \mathbf{C}(\mathbf{g}_q), \mathbf{D}(\mathbf{g}_q)$ are the state-space matrices estimated for the local LTI models identified at fixed design parameters values \mathbf{g}_q [44]. Other interpolation models select a set of interpolation functions $l_q(\mathbf{g})$ and compute the matrix coefficients $\mathbf{A}_q, \mathbf{B}_q, \mathbf{C}_q, \mathbf{D}_q$ of the functions $l_q(\mathbf{g})$ by means of the solution of a linear system of equations (e.g.,

polynomial interpolation) [45, 46]:

$$\begin{aligned} \mathbf{A}(\mathbf{g}) &= \sum_{q=1}^Q l_q(\mathbf{g}) \mathbf{A}_q, \mathbf{B}(\mathbf{g}) = \sum_{q=1}^Q l_q(\mathbf{g}) \mathbf{B}_q, \\ \mathbf{C}(\mathbf{g}) &= \sum_{q=1}^Q l_q(\mathbf{g}) \mathbf{C}_q, \mathbf{D}(\mathbf{g}) = \sum_{q=1}^Q l_q(\mathbf{g}) \mathbf{D}_q. \end{aligned} \quad (3)$$

We highlight that the matrix coefficients $\mathbf{A}_q, \mathbf{B}_q, \mathbf{C}_q, \mathbf{D}_q$ are different from $\mathbf{A}(\mathbf{g}_q), \mathbf{B}(\mathbf{g}_q), \mathbf{C}(\mathbf{g}_q), \mathbf{D}(\mathbf{g}_q)$.

In this work, we use an interpolation scheme based on radial basis functions and polynomial basis functions [47–49] where the interpolation for each entry of the state-space matrices can be written as:

$$\sum_{q=1}^Q w_q \phi(\mathbf{g} - \mathbf{g}_q) + \sum_{b=1}^B w_b p_b(\mathbf{g}). \quad (4)$$

Different radial basis functions $\phi(\mathbf{g} - \mathbf{g}_q)$ exist in the literature. In our work, we have chosen the multi-quadrics basis functions:

$$\phi(\mathbf{g} - \mathbf{g}_q) = \sqrt{r_q^2 + c^2}, \quad (5)$$

where r_q represents the euclidian distance between \mathbf{g} and \mathbf{g}_q and c is a positive parameter. The B polynomial functions have been chosen to be $[1, g^{(1)}, g^{(2)}, \dots, g^{(M)}]$ in our work.

The local LTI models are generated by independent system identification steps [40–42]. In this paper, we use the Vector Fitting (VF) technique [40] to first obtain pole-residue models for each design space samples \mathbf{g}_q :

$$\mathbf{S}(j\omega_f, \mathbf{g}_q) \simeq \mathbf{D}(\mathbf{g}_q) + \sum_{p=1}^P \frac{\text{Res}_p(\mathbf{g}_q)}{j\omega - \text{poles}_p(\mathbf{g}_q)}. \quad (6)$$

Then, different state-space realization techniques can be used to generate the state-space matrices of the local LTI models $\mathbf{A}(\mathbf{g}_q), \mathbf{B}(\mathbf{g}_q), \mathbf{C}(\mathbf{g}_q), \mathbf{D}(\mathbf{g}_q)$ starting from the pole-residue models (6). The state-space representation of LTI models is unique up to a similarity transformation. The state-space matrices of the local LTI models need to be represented in a common state-space form to avoid potentially large variations as a function of the design parameters due to underlying similarity transformations, which might degrade the accuracy of the interpolation significantly. In the literature, several approaches have been proposed to transform the local LTI models into a state-space representation suitable for interpolation [35, 45, 46]. In this paper, we have used the barycentric realization discussed in [35].

If using one specific state-space realization would not provide the desired accuracy, then the technique [50] could be used to compute similarity transformation matrices that transform the set of

local LTI models into a state-space form suitable to interpolation.

A. Design space sampling and model cross-validation

Multiple schemes can be used to choose the location of the Q samples in the \mathbf{g} space. For example, Latin hypercube design [51] and quasi-random sequences [52]. Sobol and Halton sequences [52] are famous among quasi-random sequences. In this work, we have chosen the Sobol quasi-random sequence scheme [52]. Simple sampling schemes such as a regular tensor-product sampling will immediately provide a high number of samples as soon as the number of dimensions of the design space increases. Let us imagine to have M design parameters and to sample each design parameters interval with L samples. By taking the combination of all these samples (tensor-product), the total number of samples is equal to L^M . This is clearly not an efficient sampling scheme.

To estimate the accuracy of a parametric macromodel, of all Q simulations (then of all Q samples in the design space), a part of it is used to build the parametric macromodel (estimation) and another part is used to validate the model (validation). A scheme inspired by k -fold cross validation is used to subdivide estimation and validation samples in the design space [53]. The set of Q simulations is randomly partitioned into k sets of approximately equal size. Then, for $i = 1, \dots, k$, a parametric macromodel is built considering all but the i -th data partition and the excluded dataset is used to evaluate the corresponding validation model error. An average validation model error based on the validation model errors of all the k iterations is used to estimate the average error over the design space for the parametric macromodel built by using all the data samples [53]. A 10-fold ($k = 10$) cross validation has been used in this work. An illustration of the 10-fold cross validation is provided in Fig. 2.

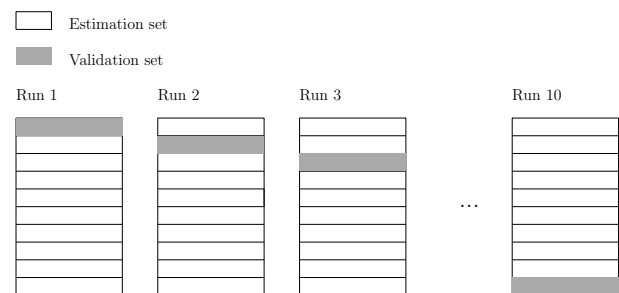


Fig. 2. 10-fold cross validation process.

Once the parametric macromodel is built, it can be used for design tasks, such as design optimization. The same model can be reused for different optimization tasks.

Concerning some computational considerations:

- if an EM solver-based approach is used, each iteration of a design optimization task leads to an EM simulation. Since each EM simulation can be computationally expensive, such an approach is very inefficient.
- Instead, in the case of the proposed technique, there is an initial computational cost needed to generate the parametric macromodel (the Q EM simulations previously mentioned). This initial computational effort becomes negligible when the model is used in multiple optimization cases. The parametric macromodel is an analytical model and therefore its evaluation is extremely fast. The same model is reused in multiple optimization tasks with different optimization objectives. This allows obtaining a very significant computational speed-up with respect to optimizations directly based on EM simulations. The proposed technique is based on system identification tools, interpolation schemes and cross-validation algorithms.

These computational considerations will be fully supported by numerical results in Section IV.

Figure 3 summarises the main steps of the proposed modeling techniques.

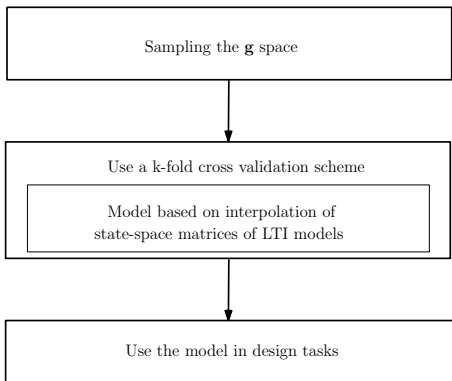


Fig. 3. Main steps of the proposed modeling techniques.

IV. NUMERICAL RESULTS

A narrow-band MMA structure is used to validate the proposed modeling technique. The design parameters of the narrow-band MMA are: the lattice constant a , the gap g , the width w and the

lengths L_1, L_2, L_3 which vary over the ranges [77-90] μm , [3-7] μm , [5-15] μm , [22-35] μm , [40-55] μm and [60-75] μm , respectively, as shown in Fig. 1. The 6D design space (a, g, w, L_1, L_2, L_3) includes 150 samples (Sobol sampling scheme) and each sample has required an EM simulation, examined over the frequency range [0.9-1.4] THz with a frequency resolution of 10 GHz (i.e., 51 frequency points for each simulation). In order to obtain the frequency-domain data samples of the reflection spectra for all 150 design space samples, it is necessary an overall CPU time equal to 237 h 30 m with an average CPU time for one EM simulation of about 1 h 35 m. Considering the 150 simulations, the VF technique [40] has been used to obtain pole-residue models (6) with $P = 6$ as number of poles. Figure 4 shows the location of the poles in the Laplace domain corresponding to the 150 pole-residue models.

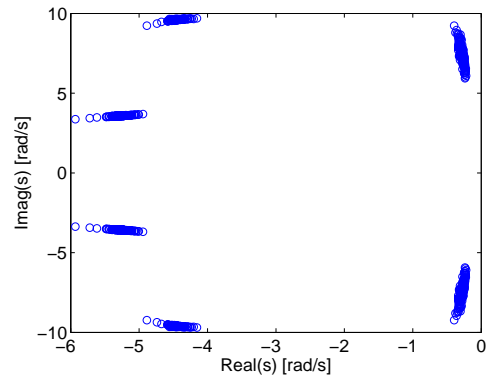


Fig. 4. Location of the poles in the Laplace domain corresponding to the 150 pole-residue models.

Then, the barycentric realization [35] has been used to generate the state-space matrices of the local LTI models $\mathbf{A}(\mathbf{g}_q), \mathbf{B}(\mathbf{g}_q), \mathbf{C}(\mathbf{g}_q), \mathbf{D}(\mathbf{g}_q)$ starting from the pole-residue models. Finally, an interpolation scheme based on multiquadratics radial basis functions and polynomial basis functions [47] has been used to construct the parametric macromodel.

A 10-fold cross validation has been used to estimate the average absolute error of the final parametric macromodel in the design space. This estimated error is equal to 0.0208. The CPU time needed to perform the 10-fold cross-validation and to build the final parametric macromodel using all data samples is equal to 58 s and 8.6 s, respectively. Then, the parametric macromodel has been used for three multiobjective optimizations whose objective is to achieve a maximum absorption at three different frequencies, namely $freq_{optim} = 1.1$ THz (Case I), $freq_{optim} = 1.2$ THz (Case II) and

Table 1: Optimal design parameters values (μm)

Case	a	g	w	L_1	L_2	L_3
I	78.68	4.61	12.67	27.59	52.89	73.13
II	82.66	5.67	12.60	27.09	49.66	69.87
III	84.99	5.06	12.75	26.78	45.57	66.76

Table 2: CPU time comparison

	Model Generation
EM FEM solver	
Proposed	$150 \times 1 \text{ h } 35 \text{ m} + 58 \text{ s} + 8.6 \text{ s}$
	Optimization 1
EM FEM solver	$9811 \times 1 \text{ h } 35 \text{ m}$
Proposed	84 s
	Optimization 2
EM FEM solver	$10081 \times 1 \text{ h } 35 \text{ m}$
Proposed	88 s
	Optimization 3
EM FEM solver	$9451 \times 1 \text{ h } 35 \text{ m}$
Proposed	82 s
	Speed-up
EM FEM solver	
Proposed	195x

$freq_{optim} = 1.3 \text{ THz}$ (Case III). Therefore, we have three optimization tasks. The function gamultiobj in Matlab[®] (R2014) has been used to run the three multiobjective optimizations with the default Matlab settings. The parametric macromodel has provided the value of S_{11} over a dense frequency grid of 501 points and for each design parameters value required by the optimizer. The obtained optimal values of the design parameters are shown in Table 1 for the three optimization cases.

To achieve these optimal values, the routine gamultiobj has required 9811, 10081 and 9451 function evaluations and a CPU time equal to 84 s, 88 s and 82 s using the parametric macromodel, respectively.

Three additional EM simulations have been performed to confirm the accuracy of the optimization results provided by the parametric macromodel. Figure 5 shows the absorbance response obtained by the parametric macromodel and the EM solver at the three optimal points. A very good agreement is achieved.

Table 2 summarizes the computational cost re-

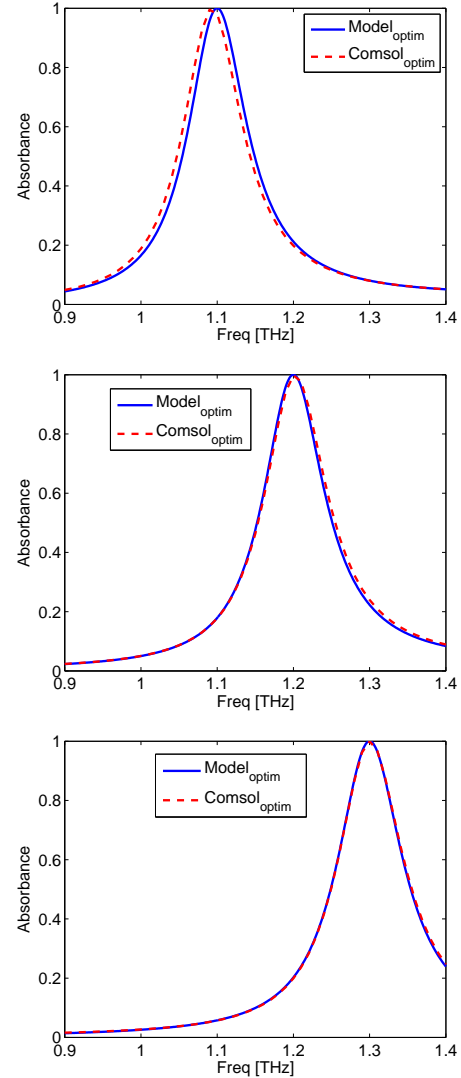


Fig. 5. Optimization results: cases I-II-III (from top to bottom).

lated to 1) using Cmsol and 2) using the proposed parametric macromodeling technique for the three optimization tasks. The speed-up obtained by using the proposed technique for the three optimizations is mentioned. It becomes evident that the initial computational effort for the parametric macromodel construction is justified by the very significant computational saving obtained for multiple design optimizations.

V. CONCLUSIONS

We have proposed an approach for the efficient design of metamaterial absorbers based on a parametric macromodeling technique. The interpolation of the state-space matrices of a set of LTI models is used to generate a parametric macromodel. This

is then used for different optimizations of an ultrathin narrow-band metamaterial absorber. The numerical results confirm the efficiency and accuracy of the proposed technique, which allows computing optimal design values in a reduced amount of time.

REFERENCES

- [1] Q. Wu, K. Zhang, and G. H. Yang, "Manipulation of electromagnetic waves based on new unique metamaterials: theory and applications," *ACES Journal*, vol. 12, pp. 977–989, December 2014.
- [2] O. Luukkonen, F. Costa, C. R. Simovski, A. Monorchio, and S. A. Tretyakov, "A thin electromagnetic absorber for wide incidence angles and both polarizations," *IEEE Trans. Antennas Propag.*, vol. 57, no. 10, pp. 3119–3125, 2009.
- [3] M. Diem, T. Koschny, and C. M. Soukoulis, "Wide-angle perfect absorber/thermal emitter in the terahertz regime," *Phys. Rev. B*, vol. 79, no. 3, p. 033101, 2009.
- [4] S. Ghosh, S. Bhattacharyya, D. Chaurasiya, and K. V. Srivastava, "Polarisation-insensitive and wide-angle multi-layer metamaterial absorber with variable bandwidths," *Electronics Letters*, vol. 51, no. 14, pp. 1050–1052, 2015.
- [5] H. Cheng, S. Chen, H. Yang, J. Li, X. An, C. Gu, and J. Tian, "A polarization insensitive and wide-angle dual-band nearly perfect absorber in the infrared regime," *J. Opt.*, vol. 14, no. 8, p. 085102, 2012.
- [6] N. I. Landy, C. Bingham, T. Tyler, N. Jokerst, D. R. Smith, and W. J. Padilla, "Design, theory, and measurement of a polarization-insensitive absorber for terahertz imaging," *Phys. Rev. B*, vol. 79, no. 12, p. 125104, 2009.
- [7] L. Lu, S. Qu, H. Ma, F. Yu, S. Xia, Z. Xu, and P. Bai, "A polarization-independent wide-angle dual directional absorption metamaterial absorber," *Prog. Electromagn. Res. M*, vol. 27, pp. 191–201, 2012.
- [8] D. Chaurasiya, S. Ghosh, S. Bhattacharyya, A. Bhattacharyya, and K. V. Srivastava, "Compact multi-band polarisation-insensitive metamaterial absorber," *IET Microwaves, Antennas & Propagation*, vol. 10, pp. 94–101, 2016.
- [9] J. Sun, L. Liu, G. Dong, and J. Zhou, "An extremely broad band metamaterial absorber based on destructive interference," *Opt. Express*, vol. 19, no. 22, p. 21155, 2011.
- [10] S. Gu, J. P. Barrett, T. H. Hand, B. I. Popa, and S. A. Cummer, "A broadband low-reflection metamaterial absorber," *J. Appl. Phys.*, vol. 108, no. 6, p. 064913, 2010.
- [11] N. I. Landy, S. Sajuyigbe, J. J. Mock, D. R. Smith, and W. J. Padilla, "Perfect metamaterial absorber," *Phys. Rev. Lett.*, vol. 100, no. 20, p. 207402, 2008.
- [12] J. Grant, S. S. Y. Ma, L. B. Lok, A. Khalid, and D. R. S. Cumming, "Polarization insensitive terahertz metamaterial absorber," *Opt. Lett.*, vol. 36, no. 8, pp. 1524–1526, 2011.
- [13] G. Dayal and S. A. Ramakrishna, "Design of highly absorbing metamaterials for infrared frequencies," *Opt. Express*, vol. 20, no. 16, pp. 17503–17508, 2012.
- [14] N. Liu, M. Mesch, T. Weiss, M. Hentschel, and H. Giessen, "Infrared perfect absorber and its application as plasmonic sensor," *Nano Lett.*, vol. 10, no. 7, p. 2342, 2010.
- [15] X. Liu, T. Tyler, T. Starr, A. F. Starr, N. Jokerst, and W. J. Padilla, "Taming the blackbody with infrared metamaterials as selective thermal emitters," *Phys. Rev. Lett.*, vol. 107, no. 4, p. 045901, 2011.
- [16] M. Laroche, R. Carminati, and J. J. Greffet, "Near-field thermophotovoltaic energy conversion," *J. Appl. Phys.*, vol. 100, no. 6, p. 063704, 2006.
- [17] T. Maier and H. Bruckl, "Wavelength-tunable microbolometers with metamaterial absorbers," *Opt. Lett.*, vol. 34, no. 19, pp. 3012–3014, 2009.
- [18] R. L. Fante and M. T. McCormack, "Reflection properties of the Salisbury screen," *IEEE Trans. Antennas Propag.*, vol. 36, no. 10, pp. 1443–1454, 1988.
- [19] E. F. Knott and C. D. Lunden, "The two-sheet capacitive Jaumann absorber," *IEEE Trans. Antennas Propag.*, vol. 43, no. 11, pp. 1339–1343, 1995.
- [20] S. A. Tretyakov and S. I. Maslovski, "Thin absorbing structure for all incident angles based on the use of a high-impedance surface," *Microwave Opt. Technol. Lett.*, vol. 38, no. 3, pp. 175–178, 2003.
- [21] V. T. Pham, J. Park, D. L. Vu, H. Y. Zheng, J. Y. Rhee, K. Kim, and Y. P. Lee, "THz-metamaterial absorbers," *Adv. Nat. Sci. Nanosci. Nanotechnol.*, vol. 4, no. 1, p. 015001, 2013.
- [22] C. Debus and P. Bolivar, "Frequency selective surfaces for high sensitivity terahertz sensing," *Appl. Phys. Lett.*, vol. 91, no. 18, p. 184102, 2007.
- [23] C. S. Y. Ra'di and S. Tretyakov, "Thin perfect absorbers for electromagnetic waves: the-

- ory, design, and realization,” *Phys. Rev. Appl.*, vol. 3, p. 037001, 2015.
- [24] B. A. Munk, *Frequency Selective Surfaces: Theory and Design*, Wiley, 2000.
- [25] M. D. Astorino, F. Frezza, and N. Tedeschi, “Broad-band terahertz metamaterial absorber with stacked electric ring resonators,” *J. Electrom. Waves Appl.*, vol. 31, no. 7, pp. 727–739, 2017.
- [26] D.-H. Kwon, Z. Bayraktar, J. A. Bossard, D. H. Werner, and P. L. Werner, “Nature-inspired optimization of metamaterials,” in *24th Annual Review of Progress in Applied Computational Electromagnetics*, April 2008.
- [27] S. Koziel, “Multi-fidelity optimization of microwave structures using response surface approximation and space mapping,” *ACES Journal*, vol. 24, pp. 600–608, December 2009.
- [28] S. Koziel, J. Bandler, and Q. Cheng, “Robust trust-region space-mapping algorithms for microwave design optimization,” *IEEE Transactions on Microwave Theory and Techniques*, vol. 58, no. 8, pp. 2166–2174, August 2010.
- [29] S. Koziel and J. Bandler, “Fast design optimization of microwave structures using co-simulation-based tuning space mapping,” *ACES Journal*, vol. 26, pp. 631–639, August 2011.
- [30] S. Koziel, “Space mapping: Performance, reliability, open problems and perspectives,” in *2017 IEEE MTT-S International Microwave Symposium (IMS)*, pp. 1512–1514, June 2017.
- [31] S. Koziel and A. Bekasiewicz, “Reliable low-cost surrogate modeling and design optimisation of antennas using implicit space mapping with substrate segmentation,” *IET Microwaves, Antennas and Propagation*, vol. 11, no. 14, pp. 2066–2070, 2017.
- [32] F. Ferranti, L. Knockaert, and T. Dhaene, “Parameterized S-parameter based macromodeling with guaranteed passivity,” *IEEE Microw. Wireless Compon. Lett.*, vol. 19, no. 10, pp. 608–610, October 2009.
- [33] P. Triverio, S. Grivet-Talocia, and M. S. Nakhla, “A parameterized macromodeling strategy with uniform stability test,” *IEEE Transactions on Advanced Packaging*, vol. 32, no. 1, pp. 205–215, February 2009.
- [34] F. Ferranti, L. Knockaert, and T. Dhaene, “Passivity-preserving parametric macromodeling by means of scaled and shifted state-space systems,” *IEEE Transactions on Microwave Theory and Techniques*, vol. 59, no. 10, pp. 2394–2403, October 2011.
- [35] E. R. Samuel, L. Knockaert, F. Ferranti, and T. Dhaene, “Guaranteed passive parameterized macromodeling by using Sylvester state-space realizations,” *IEEE Transactions on Microwave Theory and Techniques*, vol. 61, no. 4, pp. 1444–1454, April 2013.
- [36] M. Kabir and R. Khazaka, “Parametric macromodeling of high-speed modules from frequency-domain data using Loewner matrix based method,” in *IEEE MTT-S International Microwave Symposium*, pp. 1–4, June 2013.
- [37] M. D. Astorino, F. Frezza, and N. Tedeschi, “Ultra-thin narrow-band, complementary narrow-band, and dual-band metamaterial absorbers for applications in the THz regime,” *J. Appl. Phys.*, vol. 121, no. 6, p. 063103, 2017.
- [38] M. D. Astorino, R. Fastampa, F. Frezza, L. Maiolo, M. Marrani, M. Missori, M. Muzi, N. Tedeschi, and A. Veroli, “Polarization-maintaining reflection-mode THz time-domain spectroscopy of a polyimide based ultra-thin narrow-band metamaterial absorber,” *Scientific Reports*, vol. 8, no. 1, p. 1985, 2018.
- [39] *COMSOL Multiphysics 4.4*, <http://www.comsol.com/products>.
- [40] B. Gustavsen, “Improving the pole relocating properties of vector fitting,” *IEEE Transactions on Power Delivery*, vol. 21, no. 3, pp. 1587–1592, 2006.
- [41] L. Ljung, *System Identification: Theory for the User (2nd Edition)*, Prentice Hall, 1999.
- [42] R. Pintelon and J. Schoukens, *System Identification: A Frequency Domain Approach*, Wiley-IEEE Press, 2012.
- [43] W. A. Weiser and S. E. Zarantonello, “A note on piecewise linear and multilinear table interpolation in many dimensions,” *Mathematics of Computation*, vol. 50, no. 181, pp. 253–264, January 1988.
- [44] F. Ferranti, L. Knockaert, and T. Dhaene, “Guaranteed passive parameterized admittance-based macromodeling,” *IEEE Trans. Advanced Packaging*, vol. 33, no. 3, pp. 623–629, August 2010.
- [45] J. De Caigny, J. Camino, and J. Swevers, “Interpolation-based modeling of MIMO LPV systems,” *IEEE Transactions on Control Systems Technology*, vol. 19, no. 1, pp. 46–63, 2011.
- [46] J. De Caigny, R. Pintelon, J. Camino, and J. Swevers, “Interpolated modeling of LPV systems,” *IEEE Transactions on Control Systems Technology*, vol. 22, no. 6, pp. 2232–2246, November 2014.

- [47] M. D. Buhmann, *Radial Basis Functions*, Cambridge University Press, New York, NY, USA, 2003.
- [48] G. Liu and Y. Gu, *An Introduction to Mesh-free Methods and Their Programming*, Springer, 2005.
- [49] G. R. Liu, *Meshfree Methods: Moving Beyond the Finite Element Method. Second Edition.*, CRC Press, 2010.
- [50] F. Ferranti and Y. Rolain, "A local identification method for linear parameter-varying systems based on interpolation of state-space matrices and least-squares approximation," *Mechanical Systems and Signal Processing*, vol. 82, pp. 478–489, 2017.
- [51] W.-L. Loh, "On Latin hypercube sampling," *Ann. Statist.*, vol. 24, no. 5, pp. 2058–2080, 1996.
- [52] P. Brandimarte, *Low-Discrepancy Sequences*, pp. 379–401, John Wiley and Sons, Inc., 2014.
- [53] T. Hastie, R. Tibshirani, and J. Friedman, *The Elements of Statistical Learning: Data Mining, Inference, and Prediction, Second Edition (Springer Series in Statistics)*, Springer, 2009.



Giulio Antonini received the Laurea degree (*cum laude*) in Electrical Engineering from the University of L'Aquila, L'Aquila, Italy, in 1994 and the Ph.D. degree in Electrical Engineering from University of Rome "La Sapienza" in 1998. Since 1998, he has been with the UAq EMC Laboratory, University of L'Aquila, where he is currently a Professor. His scientific interests are in the field of computational electromagnetics. He has coauthored the book "*Circuit Oriented Electromagnetic Modeling Using the PEEC Techniques*", (Wiley-IEEE Press, 2017).



Maria Denise Astorino received the B.S. and M.S. degrees in Electronic Engineering in 2012 and 2015, respectively, from the University of Rome "La Sapienza" where she is currently employed in the Ph.D. course in Mathematical Models for Engineering, Electromagnetics and Nanosciences. Her research interests include the study of microwave/THz periodic structures such as frequency selective surfaces and metamaterial absorbers through equivalent-circuit models, and the

analysis of anisotropic media for applications in the electromagnetic cloaking effect.



Francesco Ferranti received the Ph.D. degree in Electrical Engineering from Ghent University, Ghent, Belgium, in 2011. He is currently an Associate Professor at the Microwave Department at Institut Mines-Télécom (IMT) Atlantique, Brest, France. His research interests include parameterized macromodeling and model order reduction, sampling techniques, design space exploration, uncertainty quantification, optimization, applied electromagnetics, behavioural modelling, microwave design and characterization, and multiphysics modeling.



Fabrizio Frezza received the Laurea degree (*cum laude*) in Electronic Engineering in 1986 and the Doctorate degree in Applied Electromagnetics and Electrophysical Sciences in 1991, both from "La Sapienza" University of Rome. In 1986, he joined the Department of Electronics of the same University, where he was Researcher from 1990 to 1998, temporary Professor of Electromagnetic Fields from 1994 to 1998, Associate Professor from 1998 to 2004, and he has been Full Professor of Electromagnetic Fields since 2005. His research activity has concerned guiding structures, antennas and resonators for microwaves and millimeter waves, numerical methods, scattering, optical propagation, plasma heating, anisotropic media, artificial materials and metamaterials, cultural-heritage applications. Dr. Frezza is a Member of Sigma Xi and Senior Member of IEEE and OSA.



Nicola Tedeschi received the Master degree in Electronic Engineering, from "La Sapienza" University of Rome in 2009. He received the Ph.D. in Electromagnetics from the same University in 2013. He was visiting student in the Department of Radio Science and Engineering of the Aalto University, Espoo, Finland, in 2012. His research interests concern microwave amplifiers, electromagnetic scattering by objects near to interfaces, propagation of inhomogeneous waves in dissipative media, and the characterization of dispersive properties of natural and artificial materials.

Optimization of T-shaped Suspension Magnetic Ring for Vertical Axis Wind Turbine

Zhu Jun¹, Song Dandan¹, Han Qiaoli², Wang Jinmei¹, Guanghua Li¹, and Li Shaolong¹

¹ Department of Electrical Engineering
School of Electrical Engineering and Automation, Henan Polytechnic University, Jiaozuo, 454000, China
zhujunnd@163.com, 18625876973@163.com

² Department of Electrical Engineering
School of Energy and Transportation Engineering, Inner Mongolia Agricultural University
Hohehot Municipality, 010018, China
nmgtynxh@hotmail.com

Abstract — Aiming at realizing breeze startup, light wind power generation, a novel T-shaped group of passive magnetic bearing (PMB) with three rings high suspension characteristics was proposed to increase the utilization of wind energy and improve the suspension characteristics of passive bearings. The inner magnetic ring of the T-shaped magnetic ring group adopts an oblique 45° polarization method, which can simultaneously balance radial force and axial force with high suspension characteristics. The static characteristics of the T-shaped magnetic ring group are compared with the traditional double rings which dynamic disturbance characteristics were analyzed in three degrees of freedom (DOF) and the parameters are optimized to achieve the optimal suspension characteristics through methods of Taguchi, response surface with mathematical model. The study shows that the capacity of T-shaped magnetic ring group is 2.5 times which can balance axial force and radial force simultaneously with 40% increase in volume than the double ring. The capacity of T-shaped magnetic ring group is increased by 33.6% and the stiffness is increased by 33.7% after optimized, which meets the requirements of suspension characteristics. When the bearing is disturbed in 3 DOF operation, the stable running state of the bearing can still be maintained due to its self-stabilizing system. It provides a reference for the suspension characteristics of the vertical axis wind turbine suspension system.

Index Terms — 3 DOF, magnetic bearing, stability, T-shaped magnetic ring group.

I. INTRODUCTION

The performance of shafting components and the whole system are affected by bearing performance directly. Magnetic suspension bearings have the advantages of no friction, no wear and long service life which have broad

application prospects [1-3]. At present, magnetic suspension technology has made achievements in flywheel energy storage, pump, Hydropower Synchronous Generator, hard disk drive, maglev train, medical [4-10] and so on. The introduction of suspension technology to the wind power generation system can reduce the starting torque and expand the utilization rate of wind energy.

In order to improve the suspension characteristics of PMB, the domestic and foreign scholars have done a lot of research on their polarization direction, geometry structure and dynamic characteristics. The rotor is suspended by a repulsive force to replace the mechanical bearings and can generate anti-disturbance suspension characteristics with the parallel magnetized permanent magnets installed on the rotor and stator respectively [11-12]. In view of the greater force of the change polarization method than the single polarization [13], the literature [14-15] proposed the continuous Halbach structure with high rigidity, but with high processing cost. A comparative study was made on the suspension characteristics of four different polarized directions in different geometric structure, in which the suspension characteristics of the rotating 90 degree polarization are the best, but the installation is difficult [16-17].

The structure of three-ring was presented with high stiffness and bearing capacity, but its system stability is poor [18-22]. In order to keep the balance of the suspension system in every degree of freedom, the axial force is balanced by the radial magnetic ring group and the axial magnetic ring group, but the cost increased [23].

For its dynamic characteristics, the physical mathematical model was established for a passive magnetic and the danger were studied arising from possible resonances when the natural frequencies of the device were near to the excitation frequencies [24]. Two novel nonlinear controllers were studied in reference

23 for single-biasing freedom with anti-interference performance. But only one degree of freedom control can be realized [25].

In order to realize the goal of "light wind start, breeze wind power generation" and solve the above problems, a novel T-shaped group of PMB with three rings which can balance axial and radial forces simultaneously and is suitable for vertical axis is proposed; which high-suspension features can reduce the starting torque of wind turbines and increase wind energy utilization. Compared with the traditional double ring bearing, the bearing capacity of the new three-ring T-shaped magnetic ring group is increased by 2.5 times and has sufficient self-stability.

II. STRUCTURE OF SUSPENSION SYSTEM

Magnetic suspension bearing is a kind of bearing that uses a magnetic field force to suspend the shaft. According to its working principle, it can be divided into active magnetic bearing, passive magnetic bearing and mixed magnetic bearing. The passive magnetic bearing can be divided into the whole passive magnetic bearing (superconductor, diamagnetic body) and the permanent magnetic bearing (PMB). In passive magnetic bearings, permanent magnetic bearings are commonly used.

According to the Earnshaw theorem, it is impossible to maintain a stable suspension in 6 degrees of freedom. The Laplace equation of static magnetic field is as follows:

$$\partial^2 W = 0, \quad (1)$$

$$\frac{\partial^2 W}{\partial x^2} + \frac{\partial^2 W}{\partial y^2} + \frac{\partial^2 W}{\partial z^2} = 0. \quad (2)$$

Where W is the magnetostatic energy of the system. To make the system in a stable balance, the second-order derivative of the magnetostatic energy must be greater than zero:

$$\frac{\partial^2 W}{\partial x^2} > 0, \frac{\partial^2 W}{\partial y^2} > 0, \frac{\partial^2 W}{\partial z^2} > 0. \quad (3)$$

Obviously, the two formulae of (2) and (3) cannot be satisfied at the same time. This means that in an external magnetic field with only permanent magnets, it cannot be stable in all the degrees. In the best case, stability can only be obtained in two degrees of freedom. In the other degree of freedom, electromagnetic force and other controllable forces, such as hydraulic pressure and friction must be introduced to achieve a stable balance T-shaped magnetic ring group.

The vertical axis suspension system with T-shaped magnetic ring group instead of traditional mechanical bearings is shown in Fig. 1. The lower magnetic ring balances the gravity of the system, the outer magnetic ring balances the radial force of the system, and the upper T-type magnetic ring group serves as a backup magnetic ring group to prevent the system from going up

so as to ensure the stability of the system fundamentally.

When the inner magnetic ring is shifted to the left side, the left air gap decreases, but the magnetic density increases, and the inner magnetic ring is repelled to the right and restored to the equilibrium position. In order to make the kr/V reach the maximum, the square cross-section or square cross-section of the permanent magnet is selected usually.

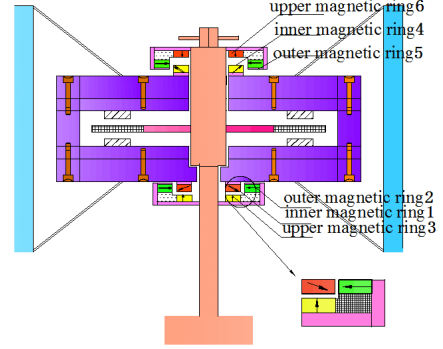


Fig. 1. Schematic diagram of vertical axis wind power generation system.

III. ANALYSIS AND CALCULATION OF MAGNETIC BEARINGS

A. Basic dimensions

The permanent magnetic material of the article is selected from NdFeB, whose Fe65%, Nd33%, B1.2%, and the maximum energy product can be as high as 400kJ/m³. Its outstanding performance makes it widely used. In order to ensure the maximum working capacity of the permanent magnet, the static analysis working point of the permanent magnet is stabilized near the maximum energy product and the proper bearing size is calculated by analyzing the demagnetization curve and the anti-magnetic curve of the NdFeB material.

The radial magnetization length of the permanent magnet is:

$$L_m = fkH_g L_g \sqrt{\frac{B_r}{H_c (BH)_{\max}}}. \quad (4)$$

f stands for magnetic resistance, usually between 1.1-1.5, k is the correction factor of the length of magnetic circuit in air which is equivalent to the length of air gap magnetic circuit, L_g is working air gap length, this paper takes 0.5mm, H_g is the air-gap magnetic field intensity, B_r is remanent magnetization, H_c is the coercive force, BH is the maximum magnetic energy product.

After the above calculation, the L_m is 10mm and the height of the magnetic ring is 10mm to ensure the maximum of kr/V .

B. Displacement in axial

The geometrical parameters of bearing have great

influence on the stiffness and capacity of passive magnetic bearing. The bearing capacity is an important parameter to measure the bearing, and the bearing capacity is proportional to the square of the magnetic density of the air gap and the air gap area between the magnetic rings. Reasonable magnetic circuit and geometric parameters play a key role in bearing capacity. Its size parameters are shown in Fig. 2.

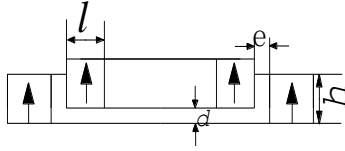


Fig. 2. The basic size of the magnetic ring.

Since the inner and outer magnetic rings are concentric magnetic rings and axially symmetrical. So the permanent magnet bearing radial force is 0, the axial force is:

$$F_x = \frac{-J_0^2}{2\pi\mu_0} p \{2\phi(d) - \phi(d+h) - \phi(d-h)\}. \quad (5)$$

In the formula:

$$\phi(z) = \left\{ (2l+e) \text{Arctg} \frac{2l+e}{z} - 2(l+e) \text{Arctg} \frac{2l+e}{z} + e \text{Arctg} \frac{e}{z} - \frac{z}{2} \left[\ln(2l+e)^2 + z^2 - 2\ln(l+e)^2 + \ln(e^2 + z^2) \right] \right\}. \quad (6)$$

Where p is the average perimeter of the magnetic bearing, h and l are the height and width of the permanent magnet, e is the gap, d is the axial offset distance, and J_0 is the magnetic polarization of the surface of the permanent magnet.

The stiffness may change the natural frequency and other dynamic characteristics of the system which is related to the bearing geometry, working environment and other factors. According to the Enshaow theorem, the higher the stiffness is, the higher the stability of the bearing is. The radial stiffness is half of the axial stiffness, so the magnitude of the axial stiffness represents the support characteristics of the magnetic bearing. The formula is as follows:

$$K_r = \frac{-J_0^2}{8\pi\mu_0} p [2\rho(d) - \rho(d+h) - \rho(d-h)]. \quad (7)$$

In the formula:

$$\rho(z) = \ln \frac{[(2l+e)^2 + z^2][e^2 + z^2]}{[(l+e)^2 + z^2]^2}. \quad (8)$$

Axial stiffness:

$$K_x = -2K_r. \quad (9)$$

In the center position ($d=0$):

$$K_r = \frac{J_0^2}{4\pi\mu_0} p [\rho(h) - \rho(0)]. \quad (10)$$

C. T-shaped magnetic ring group

Traditional magnetic rings use one pair of radial magnetic rings for generating radial force or one pair of axial magnetic rings for generating axial force. Considering the economics of permanent magnets, a T-shaped magnetic ring group was proposed. Compared with the traditional radial superposed double-ring magnetic bearing, the three-ring T-shaped magnetic ring group adds a magnetic ring that is in conformity with the inner magnetic ring specification and uses an oblique downward 45° polarization direction below the original double-ring magnetic ring group. It increases the magnetic density and area near the inner ring with greater capacity and stiffness.

Figure 3 (a) is the overall diagram of its structure and Fig. 3 (b) is a polarization section; the lower magnetic ring is polarized upward, the outer magnetic ring is inward polarization, the inner magnetic ring is inclined downward 45 degrees, the inner ring is suspended in the axial and radial force of the two magnetic rings. Figure 3 (c) is the cross section of the magnetic force line with the trend of its magnetic force line can be seen.

The bearing capacity of the new magnetic ring group is 2.5 times higher than the double ring with its unique structure, as shown in Fig. 4. The g_2 of the upper standly magnetic ring is 14mm which generates 80N force in a stable state. The bearing capacity of the new T-shaped magnetic ring group can provide 267N bearing capacity in the static state, but the actual operation of the need to provide the wind turbine system and its components and the gravity of the upper magnetic gravity repulsion is 280N, so the structural parameters need to be optimized.

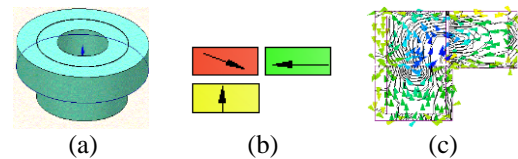


Fig. 3. Schematic diagram of T type magnetic ring. (a) Structure of T-shaped magnetic ring, (b) polarized section, and (c) section of magnetic line.

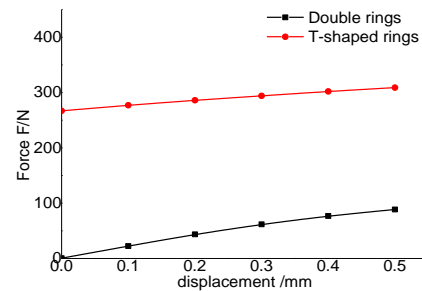


Fig. 4. Comparison of the bearing capacity of the two magnetic rings.

IV. OPTIMIZATION OF BEARING

A. Optimization of magnetic ring thickness l and air gap g_1

The suspension characteristic of the magnetic bearing is related to its geometric parameters. In this paper, four parameters of magnetic ring thickness A (l), magnetic ring height B (h) and air gap C (g_1) and D (g_2) between rings are taken as the factors and the multi-objective optimization design of magnetic bearing is carried out.

The influence of the four parameters on the bearing capacity F and the stiffness K of the passive magnetic bearing is studied and the quality characteristic of the magnetic bearing is optimized through optimization. That is to say, it has high bearing capacity and high stiffness. In the orthogonal test, the optimized target is called the quality characteristic, the condition that affects the quality characteristic is called factor and the value of the factor is called the level of the factor. The factor and the level of the factor are as shown in Table 1.

Table 1: The factors and the value of its level

Variables	A/mm	B/mm	C/mm	D/mm
Factorlevel1	9	9	0.4	0.8
Factorlevel2	10	10	0.5	1
Factorlevel3	11	11	0.6	1.2
Factorlevel4	12	12	0.7	1.4

Each optimization variable takes 4 factor levels and combination of the orthogonal experiment was carried out. Traditional analysis variables need to do $4^4 = 256$ times experiments, while Taguchi method establishes the experimental analysis matrix, which requires only 16 times finite element analysis and its specific orthogonal table is shown in Table 2.

Table 2: The actual value and result of the orthogonal table of 4 variables

N	A/mm	B/mm	C/mm	D/mm	F/N	K/(N/mm)
1	9	9	0.4	0.8	289.6	413.8
2	9	10	0.5	1	303.5	337.2
3	9	11	0.6	1.2	314.7	286.1
4	9	12	0.7	1.4	322.8	248.3
5	10	9	0.5	1.2	325.5	295.9
6	10	10	0.4	1.4	357.1	274.7
7	10	11	0.7	0.8	328.0	468.5
8	10	12	0.6	1	358.1	397.9
9	11	9	0.6	1.4	351.9	270.7
10	11	10	0.7	1.2	358.3	325.8
11	11	11	0.4	1	396.1	440.2
12	11	12	0.5	0.8	394.4	563.5
13	12	9	0.7	1	357.5	397.2
14	12	10	0.6	0.8	388.1	554.5
15	12	11	0.5	1.4	436.2	335.5
16	12	12	0.4	1.2	360.0	327.3

B. The proportion of factor level on quality characteristics

Analyzing the influence of 4 factors on quality characteristics of proportion, such as factor A in level factor 2 effect on the F can be solved as follow:

$$F_{A2} = \frac{1}{4} \times (F_{A25} + F_{A26} + F_{A27} + F_{A28}). \quad (11)$$

The effect of each factor level on factors A, B, C and D are shown in the following Tables 3, 4.

Table 3: Bearing capacity under different level factors

Factor Level	Force F/N			
	A/mm	B/mm	C/mm	D/mm
1	307.6	331.2	350.7	350.0
2	342.2	351.8	364.9	353.8
3	375.2	368.7	353.2	339.7
4	385.5	358.8	341.6	367.0

Table 4: Bearing stiffness under different level factors

Factor Level	Stiffness K/(N/mm)			
	A/mm	B/mm	C/mm	D/mm
1	321.3	344.4	364.0	500.1
2	359.3	373.0	383.0	393.1
3	400.0	382.6	377.3	308.8
4	403.6	384.3	360.0	282.3

C. The proportion of factors affecting the quality characteristics

The average values of bearing capacity \bar{F} and stiffness \bar{K} can be obtained from the results of 16 groups of orthogonal experiments in Table 2. The effects of four variables, A, B, C and D on multi-objective optimization are analyzed, as shown in Table 4.

The influence of four factors A, B, C, D on the bearing capacity F and stiffness K is analyzed, such as the influence of factor A on the bearing capacity F, and the formula is as follows:

$$S_{SB} = 4 \sum_{i=1}^4 (F_{Ai} - \bar{F})^2. \quad (12)$$

Where F_{Ai} is the average of the bearing capacity F under the influence factor A and the Factor level i ; \bar{F} is the average value of the bearing capacity.

Table 5: The influence of four variables on two quality characteristics

Factor	F/N		K/(N/mm)	
	S_{SB}	Percentage	S_{SB}	Percentage
A	14881	72%	18046	13%
B	3040	15%	4081	3%
C	1101	5%	1423	1%
D	1533	7%	115546	83%
SUM	20556	1.00	139097	1.00

D. Analysis of results

In order to know the influence of each level factor on the bearing capacity F and the stiffness K intuitively, Tables 3, 4 is used for graphic processing which is shown in Fig. 5.

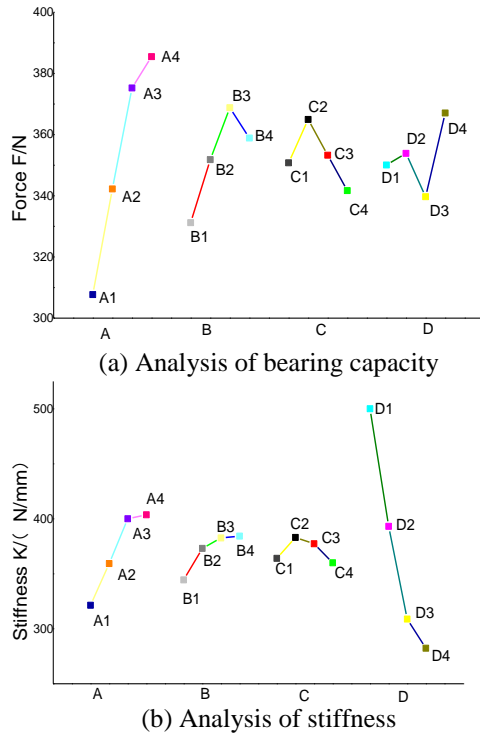


Fig. 5. Influence of each factor level on bearing capacity F and stiffness K.

It can be seen from Fig. 5 that the maximum combination of the bearing capacity is $A_4B_3C_2D_4$, while the maximum combination of the stiffness K is $A_4B_4C_2D_1$. It can be seen from Table 5 that the influence factor A has the most influence and factor C has the least influence on the force, while the influence factor D has the most influence and factor C has the least influence on the stiffness.

To achieve multi-objective optimization, the final value of A_4C_2 can be determined by Taguchi algorithm. Since the choice of B or D has a greater impact on the bearing capacity F and the stiffness K. The specific values of B and D are verified and analyzed by the following optimization methods.

E. Optimization of magnetic ring height h and magnetic ring gap g₂

The second order model of the response output and the variable response factor were proposed by selecting the experimental design scheme which using Graphical method and analysis method to find out the optimization

setting of independent variables. This method is a traditional statistical method to solve multivariate problems. An appropriate mathematical model is firstly established by experimental data, the function between objective function and variable is usually established by using second order function:

$$y = \beta_0 + \beta_1x_1 + \beta_2x_2 + \beta_{11}x_1^2 + \beta_{22}x_2^2 + \beta_{12}x_1x_2 + \varepsilon. \quad (13)$$

Where y is the response function of magnetic bearing capacity F or stiffness K, β is the undetermined coefficient, ε is fitting error, x_1 and x_2 are the height of magnetic ring B(h), the upper and lower magnetic loop D (g_2), respectively.

The size of the magnetic ring height B(h) affects the magnetic flux density of the magnetic ring. In the unsaturated zone, the magnetic density increases as the material increases. The size of the air gap D(g_2) affects the magnetic flux density and magnetic flux leakage. In a suitable air gap, the magnetic density increases as the air gap decreases. Outside the reasonable range, the magnetic flux leakage increases and the magnetic flux density decreases as the air gap increases [26]. The magnetic density and air gap area plays a decisive role in the bearing capacity of the passive suspension bearing, so the optimal solution can be obtained through scientific and rigorous optimization. From the above optimization analysis, it can be seen that when B belongs to $B_1 - B_3$ and D belongs to $D_1 - D_3$ can achieve the optimal target, the range of independent variables are:

$$\begin{aligned} 11\text{mm} < B(h) < 12\text{mm}, \\ 0.8\text{mm} < D(g_2) < 1.4\text{mm}. \end{aligned}$$

By using the central group design method, the values of independent variables are encoded separately. The center point is set to ensure the uniform accuracy of the predicted values of the entire experimental area. The experimental scheme and results are obtained as follows in Table 6.

Table 6: Design and results of experimental

N	Variables		Encod		F/N	K/(N/mm)
	B(h)	D(g_2)	X1	X2		
1	12.0	1.1	1	0	443.5	443.5
2	12.0	0.8	1	-1	429.1	613.1
3	11.0	0.8	-1	-1	410.7	586.7
4	11.0	1.4	-1	1	436.2	335.5
5	11.5	0.8	0	-1	420.0	600.0
6	11.5	1.1	0	0	434.0	434.0
7	12.0	1.4	1	1	454.8	349.8
8	11.5	1.4	0	1	445.1	342.4
9	11.0	1.1	-1	0	425.0	425.0

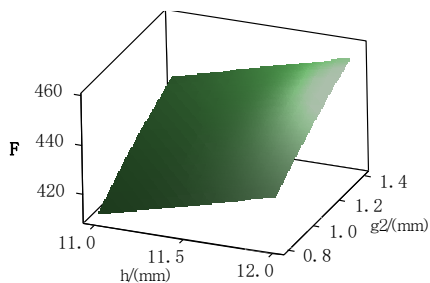
The 9 groups of orthogonal experimental results are obtained through the analysis of the finite element. The mathematical model of stiffness K and capacity F are estimated by the least square method as follows:

$$y_1 = 263.958 - 0.186197x_1 + 75.1742x_2 + 0.797271x_1^2 - 16.6519x_2^2 + 0.336581x_1x_2, \tag{14}$$

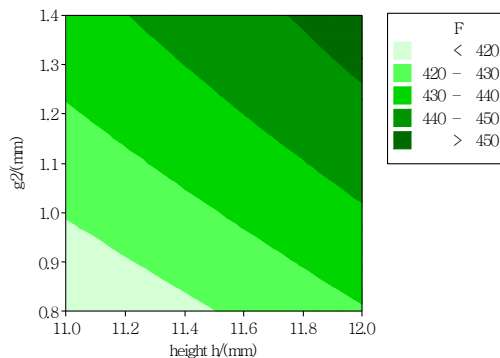
$$y_2 = 1010.59 + 26.7892x_1 - 1105.58x_2 + 0.6500724x_1^2 + 412.227x_2^2 - 20.0169x_1x_2. \tag{15}$$

Figure 6 is a curved surface map and a contour map that responds to the target and variable factor which can solve the best combination of factors. The slope size of response surface reflects the significant influence of interaction between two variables on the response value. The steeper the slope is, the more significant the interaction effects on the response value. On the contrary, it is not significant.

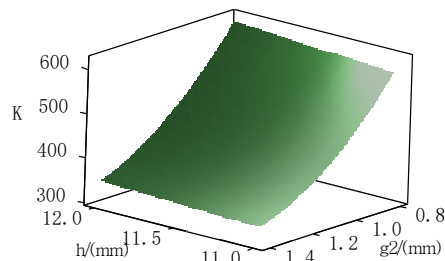
Figure 6 (a) is surface diagram formed by the force, magnetization height and air gap; 6 (b) is the contour map of the force, magnetization height and air gap. In Fig. 6 (b), the deepest part of the color indicates that the force is greater than 450N when H is between 11.75 and 12mm and the g_2 is between 12.5 and 1.4mm can reach the maximum capacity. Figure 6 (c) is surface diagram formed by the stiffness, magnetization height and air gap; 6 (d) is the contour map of the stiffness, magnetization height and air gap when the thickness belongs to 11.45-12mm and the gap belongs to 0.8-0.83mm, stiffness can reach the maximum. Through the analysis of Minitab, the overall solution of the response optimization is $(x_1, x_2) = (12, 0.94)$.



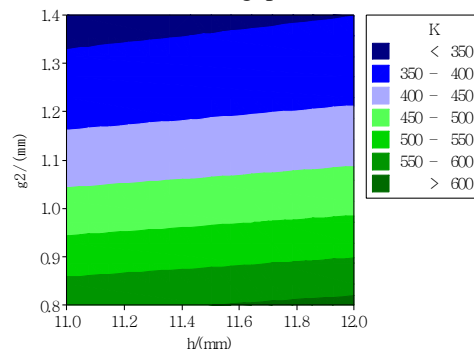
(a) Surface diagram formed by the force, height and air gap



(b) The contour map of the force, height and air gap



(c) Surface diagram formed by the stiffness, height and air gap

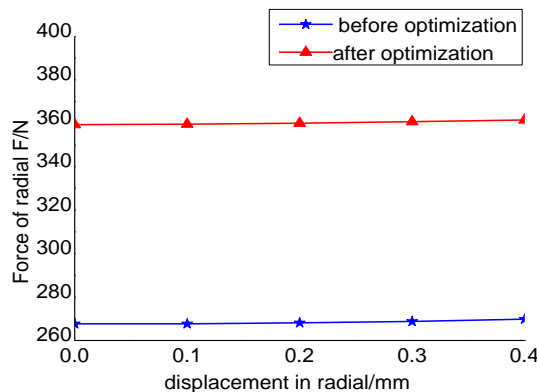


(d) The contour map of the force, height and air gap

Fig. 6. The surface and contour map of height and air gap and force and stiffness.

V. COMPARATIVE ANALYSIS

The parameters that affect the size of the magnet ring are optimized by two optimization methods. The geometric parameters are finally determined as follows: the thickness of the magnet ring A(l) is 12mm, the height of the magnet ring B(h) is 12mm, and the air gap C(g_1) is 0.5mm and D(g_2) is 0.93mm. The suspension characteristics before and after optimization are shown in Fig. 7. The direction of gravity acceleration is positive, and the displacement reference direction is set to negative direction when the inner magnetic ring is shifted upwards.



(a) Comparison of bearing capacity

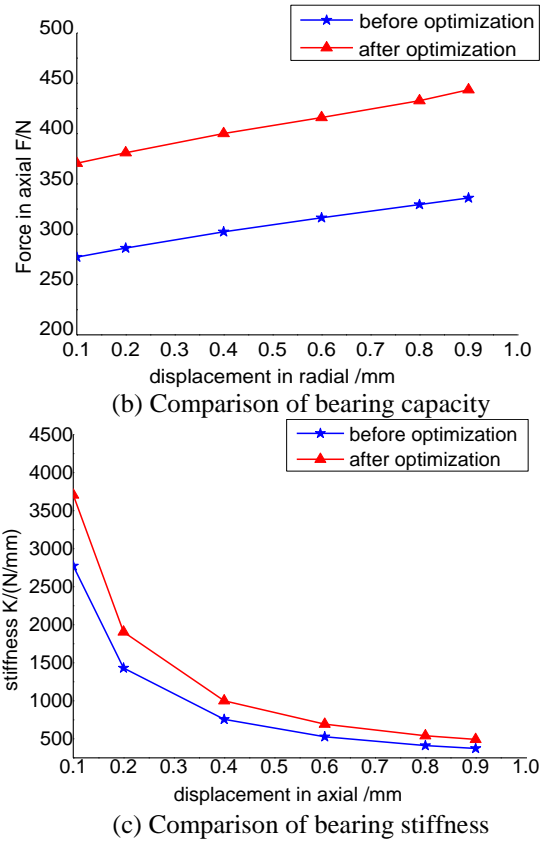


Fig. 7. Comparison of suspension characteristics.

According to the comparison and analysis of Fig. 7, the bearing capacity of the optimized passive bearing increased by 33.6% and the stiffness increased by 33.7%. Due to the need to provide a total of 280N for the gravity of the wind turbine system and its components and the repulsion of the upper magnetic ring, the optimization result meets the design requirements with a margin of 1.3 times.

VI. DYNAMIC CHARACTERISTICS

The dynamic characteristics of the bearing are derived from its equation of motion. Assuming that the bearing is balanced at z_0 and an interference is generated from the outside to cause a bearing disturbance $z_1(t)$. The equation of the bearing motion is:

$$z(t) = z_1(t) + z_0. \quad (16)$$

The bearing suspension force is F_1 and the bearing weight is mg . The motion equation of the bearing can be obtained in the vertical direction with interference:

$$m \frac{d^2 z_1}{dt^2} + c \frac{dz_1}{dt} + kz = F_1(z) - mg. \quad (17)$$

Where m is the bearing mass, c is the damping coefficient, and k is the stiffness factor. The maximum value of the damping condition is explained. The

maximum amplitude of the damping is 0.1mm, and the amplitude gradually decreases due to the stability of the magnetic field. The initial values are: $z_1(0)=h$, $z_1'(0)=0$. h is the maximum displacement of the bearing from the equilibrium point, and the speed is 0 at this time. The equation can be reduced to a differential equation group:

$$\begin{cases} z_1 = f_1 \\ df_1 / dt = f_2 \\ df_2 / dt = \frac{1}{m} F_1(z) - g. \\ f_1(0) = h \\ f_2(0) = 0 \end{cases} \quad (18)$$

The system can operate efficiently and make full use of wind energy with its self-stability. The passive T-shaped magnetic ring group has no power electronic control device and the immunity to external disturbances is worth studying. The self-stability of the disturbance was investigated when the system was operated at 3 DOF which refer to the left and right directions in the X axis direction, the up and down directions in the Y axis direction, and the Z axis rotation.

When the inner magnetic ring is disturbed by the Z axis, it will offset the equilibrium position and generate an amplitude in the axial direction. The reduction of the air gap between the inner magnetic ring and the lower magnetic ring will cause the lower magnetic ring to generate a repulsive force to reduce the amplitude of the inner magnetic ring and return to a stable position gradually. The curve of speed change is shown in Fig. 8.

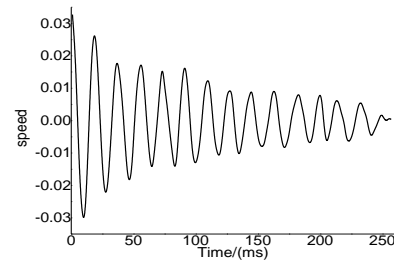


Fig. 8. Curve of speed (m/s).

VII. CONCLUSION

This paper presents a T-shaped group of PMB with three magnetic rings bearing for vertical axis wind power generation system. The structure has high suspension characteristics through the increase of magnetic flux density and section area and optimization of geometrical parameters. Research shows:

(1) The bearing capacity and stiffness of T-shaped group of PMB with three rings are 2.5 times of the double ring magnetic ring with better suspension characteristics, which is more suitable for adopting in the small wind turbine generator system.

(2) The geometric parameters of the magnetic ring have great influence on the suspension characteristics of the magnetic ring group. The thickness of the magnetic ring l has the greatest influence on the bearing capacity. The air gap g_2 between the upper and lower magnetic rings has the greatest influence on the stiffness. The capacity of T type magnetic ring group is increased by 33.6% and the stiffness is increased by 33.7% after optimized through methods of Taguchi, response surface with mathematical model, which meets the requirements of suspension characteristics.

(3) The T-shaped group of PMB with three magnetic rings provides enough axial repulsive force for the system with its novel structure and reasonable magnetization direction to balance the gravity and enough centripetal force of the system, so as to stabilize the system's disturbance in the radial direction. The upper T-shaped magnetic ring group is used as a spare magnetic ring group which ensures the stability of the system. When the bearing is disturbed in the three degree of freedom operation, the stable running state of the bearing can still be maintained due to its self-stabilizing system.

ACKNOWLEDGEMENTS

I would like to express my gratitude to all those who helped me during the writing of this thesis. My deepest gratitude goes first and foremost to Professor Zhujun, who has hosted many projects; key scientific and technological breakthrough projects in Henan Province: the research of low-speed direct-drive magnetic levitation axial flux wind turbine is conducted from September 2017 to September 2019 with its project number of 182102210052; Henan Colleges special funding for basic scientific research business expenses exploratory project: the vertical moving permanent magnet linear synchronous motor in meta information without sensing control key technology research is conducted from January 2015 to December 2018 with its project number of NSFRF140115. Key project of science and technology research of Henan Provincial Department of Education: the study on the theoretical study of the improved kalman filter permanent magnet synchronous motor without sensor control has been concluded from April 2014 to December 2014 with its project number of 12A470004. Also, my supervisor, for his constant encouragement and guidance; without his consistent and illuminating instruction, this thesis could not have reached its present form. Lastly my thanks would go to my beloved family for their loving considerations and great confidence in me all through these years. I also owe my sincere gratitude to my friends and my fellow classmates who gave me their help and time in listening to me and helping me work out my problems during the difficult course of the thesis.

REFERENCE

- [1] Z. Weiyu, "Study on key technologies and applications of magnetic bearings", Transactions of China Electrotechnical Society, vol. 30, no. 12, pp. 11-20, 2015.
- [2] Sunyang, "The design of flywheel energy storage system controller based on DSP+FPGA," *Hangzhou: Zhejiang University*, 2018.
- [3] Liusijia, "A rotor position control system of the vertical magnetic bearing based on linear induction motors," *Beijin: Beijing Jiaotong University*, 2017.
- [4] G. Goncalves Sotelo, "Magnetic bearing sets for a flywheel system," *IEEE Transactions on Applied Super-conductivity*, vol. 17, no. 2, pp. 2150-2153, 2007.
- [5] R. Moser, "Optimization of repulsive passive magnetic bearings," *IEEE Transactions on Magnetics*, vol. 42, no. 8, pp. 2038-2042, 2006.
- [6] G. H. Jang and J. S. Park, "Development of a highly efficient hard disk drive spindle motor with a passive magnetic thrust bearing and a hydrodynamic journal bearing," *Appl. Phys.*, vol. 97, no. 10, pp. 507-507, 2005.
- [7] X. Tang and Z. Yun, "The design of the magnetic and hydraulic suspension system on an axial blood pump and the analysis of its mechanical properties," *IEEE 2nd Advanced Information Technology, Electronic and Automation Control Conference (IAEAC), IEEE, Chongqing*, 2017.
- [8] H. Silu, C. Hu, and H. Lingduo, "Current loop analysis of magnetic suspension controller for magnetic suspension bearing," *Information Technology, Networking, Electronic and Automation Control Conference, IEEE, Chongqing*, 2016.
- [9] L. L. Zhang and J. H. Huang, "Stability analysis for a flywheel supported on magnetic bearings with delayed feedback control," *The Applied Computational Electromagnetics Society*, vol. 32, no. 8, pp. 642-649, 2017.
- [10] J. J. Pérez-Loya, C. J. D. Abrahamsson, F. Evestedt, and U. Lundin, "Performance tests of a permanent magnet thrust bearing for a hydropower synchronous generator test-rig," *The Applied Computational Electromagnetics Society*, vol. 32, no. 8, pp. 407-411, 2017.
- [11] P. Puentener, "Homopolar bearingless slice motor in temple design," *International Electric Machines and Drives Conference, IEEE, Miami*, 2017.
- [12] G. Wu and X. Wang, "Design and analysis of a novel axial actively regulated slotless skew winding bearingless motor," *International Conference on Mechatronics and Automation (ICMA), IEEE, Beijing*, 2015.
- [13] J.-P. Yonnet, G. Lemarquand, S. Hemmerlin, and

- E. Olivier-Rulliere, "Stacked structures of passive magnetic bearings," *Appl. Phys.*, vol. 70, pp. 6633, 1991.
- [14] D. Kevin, "Stable levitation of a passive magnetic bearing," *IEEE Transactions on Magnetics*, vol. 49, no. 1, pp. 609-617, 2013.
- [15] E. Marth, "A 2-D-based analytical method for calculating permanent magnetic ring bearings with arbitrary magnetization and its application to optimal bearing design," *IEEE Transactions on Magnetics*, vol. 50, no. 50, 7400308, 2014.
- [16] N. Tănase, "Passive magnetic bearings for flywheel energy storage - Numerical design, passive magnetic bearings design," *International Conference on Applied and Theoretical Electricity*, Craiova, IEEE, 2014.
- [17] J. Sun and D. Chen, "Stiffness measurement method of repulsive passive magnetic bearing in SGMSCMG," *IEEE Transactions on Instrumentation and Measurement*, vol. 62, no. 11, pp. 2960-2965, 2013.
- [18] G. Goncalves Sotelo, "Magnetic bearing sets for a flywheel system," *IEEE Transactions on Applied Superconductivity*, vol. 17, no. 2 pp. 2150-2153, 2007.
- [19] R. Ravaut, G. Lemarquand, and V. Lemarquand, "Halbach structures for permanent magnets bearings," *Prog. Electromagn.*, vol. 14, pp. 263-277, 2007.
- [20] R. Ravaut, "Force and stiffness of passive magnetic bearings using permanent magnets. Part 1: Axial magnetization," *IEEE Transactions on Magnetics*, vol. 45, no. 7, pp. 2996-3002, 2009.
- [21] M. Alizadeh Tir, "Design of a new structure passive magnetic bearing with radial magnetization using FEM," *The 22nd Iranian Conference on Electrical Engineering, IEEE*, Tehran, 2014.
- [22] M. Alizadeh Tir, "A novel structure of passive magnetic bearing with axial magnetization," *The 5th Power Electronics, Drive Systems and Technologies Conference, IEEE*, Tehran, 2014.
- [23] N. Tănase and A. M. Morega, "Radial-axial passive magnetic bearing system Numerical simulation aided design solutions," *The 9th International Symposium on Advanced Topics in Electrical Engineering (ATEE), IEEE*, Bucharest, 2015.
- [24] R. Muscia, "Magneto-mechanical model of passive magnetic axial bearings versus the eccentricity error, Part II: Application and results," *The Applied Computational Electromagnetics Society*, vol. 32, no. 8, pp. 678-684, 2017.
- [25] A. Mystkowski and E. Pawluszewicz, "Nonlinear position-flux zero-bias control for AMB system with disturbance," *The Applied Computational*

Electromagnetics Society, vol. 32, no. 8, pp. 650-656, 2017.

- [26] Liuhuijun, "Small axial flux vertical axis wind generators and characteristic research," *Jiaozuo: Henan Polytechnic University*, 2016.



Zhu Jun is engaged in the research of new energy wind power generation and sensorless control theory. Currently, the author has presided over more than 10 provincial projects, published more than 40 academic papers, including more than 20 SCI/EI, application for more than

10 patents. The current projects are: key scientific and technological breakthrough projects in Henan Province: the research of low-speed direct-drive magnetic levitation axial flux wind turbine is conducted from September 2017 to September 2019 with its project number of 182102210052; Henan Colleges special funding for basic scientific research business expenses exploratory project: the vertical moving permanent magnet linear synchronous motor in meta information without sensing control key technology research is conducted from January 2015 to December 2018 with its project number of NSFRF140115. Key project of science and technology research of Henan Provincial Department of Education: the study on the theoretical study of the improved kalman filter permanent magnet synchronous motor without sensor control has been concluded from April 2014 to December 2014 with its project number of 12A470004.



Songdandan is a graduate student, engaged in the design of the magnetic levitation new energy wind generator. There are 6 periodicals, including 2 SCI and EI, whose two patents have been granted.

Advanced Imaging for Down-Looking Contactless GPR Systems

D. Comite¹, F. Murgia¹, I. Catapano², F. Soldovieri², and A. Galli¹

¹Department of Information Engineering, Electronics and Telecommunications
Sapienza University of Rome, via Eudossiana 18, 00184, Rome, Italy
davide.comite, federica.murgia, alessandro.galli@uniroma1.it

²Institute for Electromagnetic Sensing of the Environment (IREA)
National Research Council of Italy (CNR), via Diocleziano 328, 80124, Naples, Italy
catapano.i, soldovieri.f@irea.cnr.it

Abstract — This paper investigates the performance of an advanced imaging procedure for ground penetrating radar (GPR) operating in contactless configuration, i.e., when data are collected at variable distances from the air-soil interface. A data processing procedure is presented, based on an advanced implementation of a microwave tomographic approach. This improved version, recently proposed by the authors, is able of accounting for the near-field distribution generated by a directional transmitting antenna. The effectiveness of the procedure is shown by processing numerical data, which are obtained by suitably implementing a realistic system on a full-wave commercial simulator. Metallic canonical objects are considered to compare the reconstruction capabilities of the proposed algorithm with respect to more conventional procedures, as well as to assess the role of the antenna distance from the air-soil interface.

Index Terms — Contactless configuration, GPR, inverse scattering, microwave imaging.

I. INTRODUCTION

Detection and reconstruction of shallow-buried targets by means of Ground Penetrating Radar (GPR) systems are highly desirable for several applications, such as demining and planetary exploration as well as for a wide class of non-destructing analyses [1], [2]. Several algorithms have been developed in the last two decades for an effective representation of the raw data collected by means of GPR systems [2]. As concerns the linear microwave tomography (MT), a number of approaches have been proposed [1], which have shown to be capable of providing effective 2-D and 3-D reconstructions (see, e.g., [3], [4], and references therein) in many real situations (e.g., archeology and structural diagnosis) and in different measurement configurations [1], [5]. Several nonlinear algorithms have also been designed [2], based on conventional regularization procedures as well as on *ad hoc* strategies able to deal with the occurrence of local

minima (i.e., false solutions), in the inversion process [6].

In standard implementations of the inversion and post-processing procedures, the source activating the scattering phenomenon is usually modeled as a filamentary electric current, or as an impinging plane wave, assuming, in this last case, the transmitter located in the far field with respect to the investigated region. In this context, several efforts have already been focused on the possibility of taking into account the pattern of the antenna that illuminates the considered object. A first insight into the role played by the antenna pattern for linear MT inversion algorithm has been provided in [7], whereas in [8] an extension of a migration algorithm, capable to account for the radiation pattern of an ideal antenna for multi-component GPR data, has been designed. A diffraction tomography algorithm accounting for the incident near-field distribution has also been proposed in [9]. For some applications, such as road prospecting [1] or planetary exploration [10], [11], the capability of collecting and elaborating data in contactless configuration, i.e., when the system is located at a distance from the air-soil interface at least comparable with the operating wavelengths, is highly desirable. In this frame, the theoretical solutions, which account for the presence of the interface, are based on a spectral decomposition of the Green's function of the problem (see, e.g., [4], [5]).

We investigate here the performance achievable by a linear MT approach, when the radiative features of a directional wide-band antenna, working in contactless configuration, are modeled in an *advanced* algorithm.

As a reference case, we focus our analysis on a directional system as that proposed for the WISDOM rover, in the framework of the ExoMars planetary mission [10], which requires a compact wide-band radiator to focus electromagnetic signals in the ground. A wide-band (0.5–3 GHz) printed Vivaldi antenna operating at a certain distance from the air-soil interface is thus considered as an effective and reliable solution for both *Tx* and *Rx* system [10]. We exploit here an efficient and reliable customized

numerical implementation based on *CST Microwave Studio*, widely tested by the authors to simulate actual GPR scenarios involving also commercial systems [11].

In this framework, the authors have already evaluated the radiative features of the Vivaldi antenna working in ground-coupled configurations [12], and including the near-field distribution of the antenna in the inversion algorithm. To this aim, various comparisons for the reconstructions, generated by modeling the scattering phenomenon as occurring in a homogeneous medium, were performed.

In the following, we propose a more general implementation of our advanced procedure, which removes the assumption of homogeneous medium and allows us to account for the presence of the air-soil discontinuity, positioning the antenna not in contact with the interface. In particular, we discuss the effects on the reconstruction results by considering different targets having canonical shape, with the directional antenna placed at variable distances from the interface. A frequency range from 0.5 to 3 GHz is considered.

II. IMAGING ALGORITHMS

We assume in our analysis a two half-space model with a GPR working in monostatic configuration placed at a distance D_g from the interface between air and a nonmagnetic and lossless dielectric medium (see Fig. 1), having permittivity $\epsilon_r = 3.2$, which effectively models a Martian-like sandy subsoil (see [11] and references therein). Similar values of the permittivity can also represent realistic wet soils having moisture content of about 5-10%. We consider here the direct solution of the scattering problem on a 2-D transverse plane (i.e., the xy plane in Fig. 1, half-cutting the buried object). Since the numerical scattering data are obtained by means of a 3D implementation and solution of the GPR scenario, to reduce the problem to a 2D scalar implementation, but preserving the directional features of the illumination, we consider the dominant component (i.e., the x -directed, for this case) of the field radiated by the Vivaldi antenna on the reference vertical plane. This allows for neglecting the dyadic nature of the wave/material interactions, and to deal with a simplified 2D scalar case.

The imaging procedure is formulated as a linear inverse scattering problem in the frequency domain [1] and the physical-optics (PO) approximation is adopted [13]. Accordingly, at each angular frequency ω and for each position of the antenna along the scanline, the scattered field at the receiver can be modeled as follows:

$$E_s(x_R, \omega) = -j\omega\mu_0 \int_{\Gamma} G(x_R; \mathbf{r}'; \omega) J_{PO}(x_T; \mathbf{r}'; \omega) d\Gamma', \quad (1)$$

where $E_s(x_R, \omega)$ denotes the complex scattered electric field for $f = \omega/(2\pi)$, probed at x_R (equal here to the source position x_T); k_b is the wavenumber in the background lower half-space, G is the scalar Green's function of the problem, Γ is the contour of the scattering object (unknown of the problem). J_{PO} is the physical-optics surface current density flowing on the metallic contour of the object,

related to the incident magnetic field in the lower half-space (in absence of scatterers) [2]. To account for the presence of the air-soil interface, we exploit the following spectral representation of the Green's function [1]:

$$G(x_R, \mathbf{r}') = \frac{-j}{2\pi} \int_{-\infty}^{\infty} \frac{e^{-jk_{yb}y'} e^{-jk_{y0}D_g} e^{-jk_y(x_R-x')}}{k_{y0} + k_{yb}} dk_x, \quad (2)$$

being $k_{y0} = \sqrt{k_0^2 - k_x^2}$ and $k_{yb} = \sqrt{k_b^2 - k_x^2}$.

To recover the unknown object contour, we follow the procedure outlined in [14]: thus (1) is discretized, inverted, and regularized through the truncated singular value decomposition (TSVD) approach [1], [7].

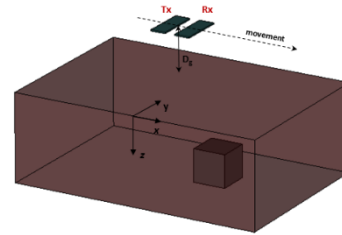


Fig. 1. 3D GPR reference scenario: a canonical object having dimension comparable with respect to the probing wavelengths is buried in the shallow region made by a dielectric half-space. The GPR is placed at a distance D_g from the air-soil interface.

In *standard* implementations, the evaluation of the scattered field is carried out by inserting (2) in (1). The impinging field on the object (that give rises to the currents J_{PO}) is assumed as that generated by a *line source*; due to reciprocity, the incident field is expressed by means of a spectral representation similar to (2). This can be accomplished by exploiting a simple point-matching procedure representing each pixel by means of a proper set of basis functions [3], [5].

To account for the actual near-field distribution radiated by the antenna we have generalized the *advanced* procedure outlined in [12]: the field radiated by a Vivaldi antenna and simulated with CST, as well as the Green's function of the problem, are exported and suitably inserted in (1), by considering both amplitude and phase of each sample in the frequency band of interest. Once that a linear discrete operator is obtained, the TSVD regularization scheme is adopted [1], [2] to retrieve the unknown Γ .

We mention that the proposed *advanced* procedure allows for sensibly mitigating the computational burden requested to deal with the frequency-domain spectral representation in (2). In fact, the wideband nature of the problem is alternatively faced here exploiting a time-domain solution of both incident field and Green's function of the problem. Thus, the FFT is applied to the impinging and scattered signals to generate the linear operator to be regularized and inverted.

III. RESULTS AND DISCUSSION

To assess and compare the capability of the

proposed advanced algorithm, which accounts for the actual field radiated by the antenna, we compare the imaging results with those provided by the MT approach as implemented in the standard way, i.e., by modeling the incident field as radiated by a filamentary current through the spectral representation of (2).

A. Canonical shapes for a fixed antenna height

The distance between the antenna and the interface has been fixed to $D_g = 20$ cm. The reconstruction capabilities of the algorithms are tested on four different metallic canonical configurations: *i*) a cube whose flat face is normal to the direction of illumination; *ii*) the inscribed sphere (diameter as the cube side); *iii*) a square-base pyramid; and *iv*) a cube rotated of 45° .

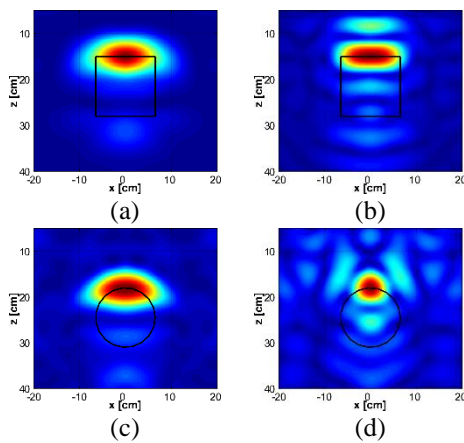


Fig. 2. Tomographic reconstructions of targets buried at a distance $d = 15$ cm from the air-sand interface, with the GPR antenna raised at $D_g = 20$ cm (cf. Fig. 1). (a) *Metallic cube* (side 13 cm) imaged with a *standard* implementation of the algorithm; (b) as in (a), with our *advanced* implementation, accounting for the actual near-field radiated by a Vivaldi antenna; (c) *metallic sphere* (diameter 13 cm) with the *standard* implementation; (d) as in (c), with our *advanced* implementation. $T = -25$ dB and the black-line profiles represent the zx section of the scatterers.

In Figs. 2 (a) and (b), the reconstruction obtained for the metallic cube (see caption for details) is reported for both the implementations. One can clearly recognize the signature relevant to the target. The upper side of the cube is better resolved by the advanced implementation, which provides also an improved focusing of the illuminated side of the object. The same observations apply to the profile presented in Figs. 2 (c) and (d), regarding the reconstruction of the metallic spherical object. However, the reconstruction improvements achievable in such contactless geometries are less evident with respect to the ground-coupled configuration (see also [12]). This is mainly due to the reduced synthetic aperture provided by the systems when $D_g \neq 0$. We mention that the advanced reconstruction shows

enhanced resolution but appears a bit more noisy around the central spot. This is due to the behavior of the singular values (similar to the one reported in [12]), which, for a fixed T , forces the advanced approach to deal with smaller, hence possibly noisier, values.

We note that, as also discussed in [12], the improvement in focusing the top side of the illuminated objects are not related to the total number of singular values comprised in the inversion scheme, but to the more accurate description of the directional features of the illuminating field. In fact, due to the smaller synthetic aperture provided by the Vivaldi antenna, even a smaller number of singular values are accounted for with the advanced scheme by thresholding the whole set to $T = -25$ dB with respect to maximum value.

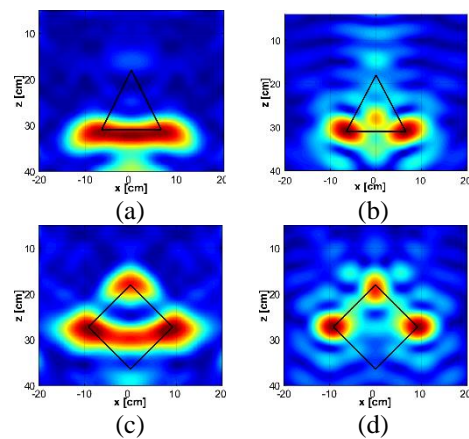


Fig. 3. As in Fig. 2, for other target shapes. (a) A *metallic pyramid* (base 13 cm, height 13 cm), buried at $d = 15$ cm, with the *standard* algorithm; (b) as in (a), with the *advanced* one; (c) a *metallic cube* ($d = 18$ cm) as in Figs. 2 (a,b), but *rotated of 45°* , with the *standard* implementation; (d) as in (c), with the *advanced* one; $T = -25$ dB.

In Figs. 3 (a) and (b) the same comparisons are presented for a metallic pyramid scatterer. Also in this case, the reconstruction capabilities of the advanced implementation are manifestly improved, since the two main edges giving the main contribution to the scattered field at the bottom of the pyramid are better resolved and reconstructed. Note that the bottom side of the pyramid is not illuminated and cannot give an appreciable contribution to the scattered field (the bottom profile in Fig. 3 (a) is fictitious and determined by the absence of adequate resolution). In addition, the spot visible at the bottom of the frame is determined by interference between two dominant scattering phenomena. It becomes weaker for a pyramid having a larger base. In Figs. 3 (c) and (d) the enhanced capabilities of the advanced procedure in locating and reconstructing the edges of the metallic rotated cube are also clearly visible. The presence of an elongated edge makes it visible with respect to vertex of the pyramid.

B. Effect of different antenna heights

Here we show the reconstructions for different values of D_g , in order to assess the informative contents provided by both the standard and advanced procedure as the antenna/interface distance gradually increases.

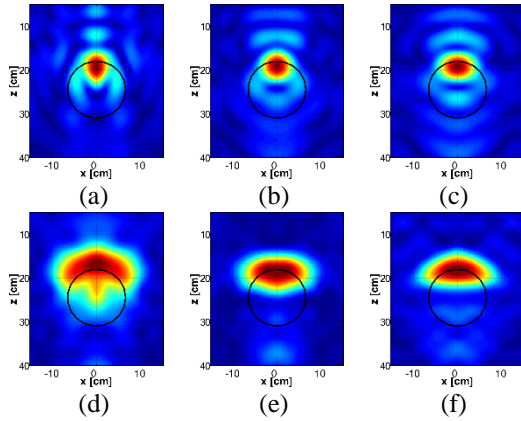


Fig. 4. Reconstructions of a metallic sphere buried at $d = 18$ cm from the interface, as in Figs. 2 (a, b), for different values of D_g : (a)-(c) advanced implementation for $D_g = 0, 10, 25$ cm, respectively; (d)-(f) as in (a)-(c) but with standard implementation; $T = -25$ dB.

In Figs. 4 (a)-(c) and (d)-(f), the reconstructions of a metallic sphere are presented for three different values of D_g (see captions) by considering both the implementations. From the analysis of Fig. 4, in conjunction with the results shown in Figs. 2 (a)-(b) and in Figs. 2 (c)-(d), one can clearly assess the improved imaging capabilities of the advanced algorithm, whose performance slightly degrades as D_g is increased. This can be related to the smaller synthetic aperture (i.e., the underlying angle-of-view) not compensated by an increasing dimension of the measurement line (kept constant for all the simulations to 75 cm).

IV. CONCLUSION

We have specifically discussed the performance of a microwave tomographic approach based on the PO approximation and accounting for the effective radiation behavior of a directional GPR antenna working in contactless configuration. The actual spatial distribution of the incident field and Green's functions, for variable distances between the antenna and the air/soil interface, has suitably been included in the numerical algorithm.

We have shown that, when a specific directive antenna is employed, the proposed advanced implementation can be beneficial to the quality of the reconstruction, especially for metallic objects with sharp edges.

The improvements in the spatial reconstructions of the targets have resulted to be generally significant. On the other hand, we have also shown that, when the antenna height from the interface gradually increases, the imaging becomes less informative on the target profiles,

even if correct detection and localization are achieved.

REFERENCES

- [1] R. Persico, *Ground Penetrating Radar: Inverse Scattering and Data Processing*. Wiley, 2014.
- [2] M. Pastorino, *Microwave Imaging*. Wiley, 2010.
- [3] G. Leone and F. Soldovieri, "Analysis of the distorted Born approximation for subsurface reconstruction: Truncation and uncertainties effects," *IEEE Trans. Geosci. Rem. Sens.*, vol. 41, no. 1, pp. 66-74, Jan. 2003.
- [4] T. B. Hansen and P. M. Johansen, "Inversion scheme for ground penetrating radar that takes into account the planar air-soil interface," *IEEE Trans. Geosci. Remote Sens.*, vol. 38, no. 1, pp. 496-506, Jan. 2000.
- [5] R. Persico, "On the role of measurement configuration in contactless GPR data processing by means of linear inverse scattering," *IEEE Trans. Antennas Propag.*, vol. 54, no. 7, pp. 2062-2071, July 2006.
- [6] M. Salucci, G. Olivieri, and A. Massa, "GPR prospecting through an inverse-scattering frequency-hopping multi-focusing approach," *IEEE Trans. Geosci. Remote Sens.*, vol. 53, no. 12, pp. 6573-6592, Jan. 2015.
- [7] F. Soldovieri, R. Persico, and G. Leone, "Effect of source and receiver radiation characteristics in subsurface prospecting within the distorted Born approximation," *Radio Sci.*, vol. 40, pp. 1-13, June 2005.
- [8] R. Streich and J. van der Kruck, "Accurate imaging of multicomponent GPR data based on exact radiation patterns," *IEEE Trans. Geosci. Remote Sens.*, vol. 45, pp. 93-103, Jan. 2007.
- [9] C. Dourthe, C. Pichot, J. Y. Dauvignac, and J. Cariou, "Inversion algorithm and measurement system for microwave tomography of buried object," *Radio Sci.*, vol. 35, pp. 1097-1108, Apr. 2000.
- [10] V. Ciarletti, et al., "WISDOM GPR designed for shallow and higher solution sounding of the martian subsurface," *Proc. IEEE*, vol. 99, pp. 825-836, May 2011.
- [11] G. Valerio, et al., "GPR detectability of rocks in a Martian-like shallow subsoil: A numerical approach," *Planet. Space Sci.*, vol. 62, pp. 31-44, 2012.
- [12] D. Comite, A. Galli, I. Catapano, and F. Soldovieri, "The role of the antenna radiation pattern in the performance of a microwave tomographic approach for GPR imaging," *IEEE J. Sel. Topics Appl. Earth Observ. Remote Sens.*, vol. 10, no. 10, pp. 4337-4347, Oct. 2017.
- [13] R. Pierri, A. Liseno, R. Solimene, and F. Soldovieri, "Beyond physical optics SVD shape reconstruction of metallic cylinders," *IEEE Trans. Antennas Propag.*, vol. 54, no. 2, pp. 655-665, Feb. 2006.
- [14] F. Soldovieri, et al., "GPR estimation of the geometrical features of buried metallic targets in testing conditions," *Prog. Electromagn. Res. B*, vol. 49, pp. 339-362, 2013.

A High Resolution Algorithm for Null Broadening Beamforming Based on Subspace Projection and Virtual Antenna Array

Wenxing Li, Hang Yang, and Yunlong Mao

College of Information and Communication Engineering
Harbin Engineering University, Harbin, 86 150001, People's Republic of China
liwenxing@hrbeu.edu.cn, hangyang1364@yahoo.com, mylharbin@outlook.com

Abstract — In this paper, we proposed a high resolution algorithm for null broadening beamforming. The algorithm is based on the property of subspace orthogonal principle between signal and noise, and on virtual antenna array. By utilizing Capon spectrum estimator, we construct the correlation matrix to obtain projection transformation matrix, the width of null increases when original covariance matrix is processed by projection transformation matrix. In order to improve the depth of null and increase array resolution, virtual antenna technique is introduced. Also diagonal loading technique is used to form robust beam pattern. With the theoretical analysis and computer simulation, it's demonstrated that the superiority of proposed algorithm corresponding other null broadening beamforming methods.

Index Terms — Array resolution, diagonal loading, null broadening beamforming, remove redundancy, subspace projection, virtual antenna array.

I. INTRODUCTION

Adaptive beamforming can suppress the interferences and noises by producing null at the direction of interferences, so it has been widely used in radar, sonar, mobile communications and many other fields [1-3]. One of the challenges of designing such a beamformer arises when the interference direction may be inaccurately known by Direction-of-Arrival (DOA) estimation. It's desired that interferences are suppressed within an angular region for enhancing fault tolerance. Thus many approaches of null broadening beamforming have been proposed [4-8].

Mailloux [4] and Zatman [5] have proposed pattern troughs techniques, respectively. Two methods are the same essentially and are unified by introducing the concept of covariance matrix tapers (CMT) [6]. However, the depth level of null degrades when a wide trough is obtained because of interference power dispersion. Amar [7] has proposed a new approach that called linear constraint sector suppressed (LCSS), by which the depth of null is improved, the performance of LCSS is degradation with high SNR, unfortunately. Recently,

a novel algorithm named projection and diagonal loading null broadening beamforming (PDNBB) was proposed [8], this method has excellent performance compared with previous algorithms, but depth of null is not enough in some certain cases and array resolution degrades when the null is broadened. In this paper, we construct the projection transformation matrix by PDNBB algorithm, and a high resolution algorithm for null broadening beamforming is proposed, in which covariance matrix is processed by projection transformation matrix to enhance the orthogonality of subspace and real antenna array is transformed into virtual antenna array by virtual antenna technique [9,10] to improve relative power distribution. Virtual antenna technique is an advanced array signal processing technique, array resolution could be improved by new virtual array elements. Compared with other algorithms, deeper null and higher array resolution can be got by proposed method when we broaden the null, and it's insensitive to snapshots.

II. THE SIGNAL MODEL

We consider a uniform linear array (ULA) with N omnidirectional antennas with spacing half a wave length uniformly. Assume that there are $M + 1$ narrowband far-field signals from the directions θ_p , $p=0,1,2,\dots, M$, where θ_0 represents the direction of desired signal and θ_q ($q=1,2,\dots, M$) are the direction of interference signal. The receive signal at the time index k could be expressed as follows:

$$\mathbf{X}(k) = \mathbf{A}\mathbf{S}(k) + \mathbf{N}(k), \quad (1)$$

where \mathbf{A} denotes array manifold matrix, $\mathbf{S}(k)$ is signal complex envelop vector, $\mathbf{N}(k)$ represents a vector modeled as zero-mean white Gaussian noise and complex vector $\mathbf{X}(k) = [x_1(k), x_2(k), \dots, x_N(k)]^T$ is an observation data vector at the sample snapshot k th. We assume that desired signal, interference signals and noise are statistically independent of each other. So output signal of beamformer at the receiving terminal can be denoted as:

$$y(k) = \mathbf{W}^H \mathbf{X}(k), \quad (2)$$

where \mathbf{W} is a complex weight vector with dimension

$N \times 1$ and $(\cdot)^H$ denotes Hermitian transpose.

According to the criterion of maximizing the output signal-to-interference-plus-noise ratio (SINR), the minimum variance distortionless response (MVDR) beamformer can be formulated as the following linearly constrained quadratic optimization problem [11,12]:

$$\begin{cases} \min_{\mathbf{W}} & \mathbf{W}^H \mathbf{R}_{i+n} \mathbf{W} \\ \text{subject to} & \mathbf{W}^H \mathbf{a}(\theta_0) = 1 \end{cases}, \quad (3)$$

where $\mathbf{a}(\theta_0)$ represents steering vector of desired signal and \mathbf{R}_{i+n} is the interference-plus-noise covariance matrix. The solution of optimal weight vector can be solved by lagrangian multiplier method and expressed as follows:

$$\mathbf{W}_{OPT} = \frac{\mathbf{R}_{i+n}^{-1} \mathbf{a}(\theta_0)}{\mathbf{a}^H(\theta_0) \mathbf{R}_{i+n}^{-1} \mathbf{a}(\theta_0)}, \quad (4)$$

In practice, we can't obtain the covariance matrix \mathbf{R}_{i+n} because of the existence of desired signal in the receive signal, so interference-plus-noise matrix is commonly replaced by the sample covariance matrix (SCM) with K snapshots, SCM can be described as:

$$\hat{\mathbf{R}} = \frac{1}{K} \sum_{i=1}^K \mathbf{X}(i) \mathbf{X}^H(i), \quad (5)$$

III. THE PDNBB APPROACH [8]

We construct correlation matrix \mathbf{R}_ω for the steering vector as follows:

$$\mathbf{R}_\omega = \int_{\omega} \mathbf{a}(\theta) \mathbf{a}^H(\theta) d\theta, \quad (6)$$

where ω is the angular sector that interference signals may appear. Because there is a high computational complexity in integral operation, we replace the integral with summation operation by selecting a series of discrete points within the desired null angular sector. Then \mathbf{R}_ω is decomposed with eigenvalue λ_i and eigenvector \mathbf{v}_i as:

$$\mathbf{R}_\omega = \sum_{i=1}^N \lambda_i \mathbf{v}_i \mathbf{v}_i^H \quad \lambda_1 \geq \lambda_2 \geq \dots \geq \lambda_N, \quad (7)$$

We assume there are Q larger eigenvalues which occupy the most energy of receiving signal and they are satisfied with inequality as follows:

$$\frac{\sum_{i=Q+1}^N \lambda_i}{\sum_{i=1}^N \lambda_i} \leq \varepsilon, \quad (8)$$

where parameter ε decides the depth of null. So projection transformation matrix can be obtained by \mathbf{T} :

$$\mathbf{T} = \text{span}(\mathbf{v}_1, \mathbf{v}_2, \dots, \mathbf{v}_Q), \quad (9)$$

where $\text{span}(\cdot)$ represents the generative vector space of selected based vector.

The original covariance matrix is replaced as follows:

$$\hat{\hat{\mathbf{R}}} = \hat{\mathbf{T}} \hat{\mathbf{R}} \hat{\mathbf{T}}^H + \gamma \mathbf{I}, \quad (10)$$

where γ is the diagonal loading factor and it can be selected in the range of $10^{-6} \leq \gamma \leq 10^{-4}$ by practical experience, and \mathbf{I} is identity matrix.

IV. THE PROPOSED METHOD

A. The proposed method

In this paper, the PDNBB algorithm is taken to obtain new covariance matrix which strengthens the orthogonality between signal subspace and noise subspace, but array resolution degrades when wider null is obtained. In order to get deeper null in some certain circumstances, we introduce the concept of Kronecker product [13], by which real array is transformed into virtual array and the number of antenna array increases, therefore, both covariance matrix and steering vectors are transformed as follows:

$$\hat{\hat{\mathbf{R}}} \stackrel{\cong}{=} \hat{\mathbf{R}} \otimes \hat{\mathbf{R}}^*, \quad (11)$$

$$\hat{\hat{\mathbf{a}}}(\theta) \stackrel{\cong}{=} \mathbf{a}(\theta) \otimes \mathbf{a}^*(\theta), \quad (12)$$

where \otimes operator denotes Kronecker product and $(\cdot)^*$ is conjugate operator.

B. Theoretical analysis

According to subspace decomposition theory, we write covariance matrix obtained by PDNBB algorithm as follows:

$$\begin{aligned} \hat{\hat{\mathbf{R}}} &\stackrel{\cong}{=} \mathbf{T} \mathbf{U} \Sigma \mathbf{U}^H \mathbf{T}^H \\ &= \mathbf{T} [\mathbf{U}_s \ \mathbf{U}_n] \begin{bmatrix} \Sigma_s & \\ & \Sigma_n \end{bmatrix} [\mathbf{U}_s \ \mathbf{U}_n]^H, \quad (13) \\ &= \mathbf{A}_s \Sigma_s \mathbf{A}_s^H + \mathbf{B}_n \Sigma_n \mathbf{B}_n^H \end{aligned}$$

where \mathbf{U}_s represents signal subspace and it can be written as $\mathbf{U}_s = [\mathbf{v}_1, \mathbf{v}_2, \dots, \mathbf{v}_{M+1}]$, \mathbf{U}_n represents noise subspace and it can be written as $\mathbf{U}_n = [\mathbf{v}_{M+2}, \mathbf{v}_{M+3}, \dots, \mathbf{v}_N]$, Σ_s and Σ_n are diagonal matrixes which could be expressed as $\Sigma_s = \text{diag}(\lambda_1, \lambda_2, \dots, \lambda_{M+1})$ and $\Sigma_n = \text{diag}(\lambda_{M+2}, \lambda_{M+3}, \dots, \lambda_N)$ corresponding eigenvalues of signal and noise subspace, respectively. In addition, let $\mathbf{A}_s = \mathbf{T} \mathbf{U}_s$, $\mathbf{B}_n = \mathbf{T} \mathbf{U}_n$, the latter tends to zero, ideally. Then covariance matrix of proposed method is expressed as:

$$\begin{aligned} \hat{\hat{\mathbf{R}}} &\stackrel{\cong}{=} (\mathbf{A}_s \Sigma_s \mathbf{A}_s^H) \otimes (\mathbf{A}_s \Sigma_s \mathbf{A}_s^H)^*, \quad (14) \\ &= \mathbf{V} (\Sigma_s \otimes \Sigma_s^*) \mathbf{V}^H \end{aligned}$$

where let $\mathbf{V} = \mathbf{A}_s \otimes \mathbf{A}_s^*$.

It can be seen from (14) that only signal subspace is retained, ideally. It is noteworthy that there are redundant items in covariance matrix and steering vector processed by Kronecker product, so it needs to be handled to remove

redundancy. The power of desired signal and interference components are enhanced furtherly so that the deeper null can be presented.

C. The method of removing redundancy

The dimension of covariance matrix increases after virtual transformation, which means there are more array antenna elements so that higher array resolution could be obtained, but many redundant items exist in covariance matrix processed by Kronecker product. According to the correspondence between steering vector and covariance matrix as follows:

$$\mathbf{a}(\theta) = [1, e^{-\frac{j2\pi d \sin \theta}{\lambda}}, \dots, e^{-\frac{j2\pi(N-1)d \sin \theta}{\lambda}}]^T, \quad (15)$$

$$\begin{aligned} \hat{\mathbf{R}} &= \mathbf{a}(\theta) \otimes \mathbf{a}^*(\theta) \\ &= [1, e^{\frac{j2\pi d \sin \theta}{\lambda}}, e^{\frac{j2\pi 2d \sin \theta}{\lambda}}, \dots, e^{\frac{j2\pi d(N-1) \sin \theta}{\lambda}}, \\ &\quad e^{-\frac{j2\pi d \sin \theta}{\lambda}}, 1, \dots, e^{-\frac{j2\pi(N-2)d \sin \theta}{\lambda}}, \dots, \\ &\quad e^{-\frac{j2\pi(N-1)d \sin \theta}{\lambda}}, \dots, 1]^T_{N^2 \times 1} \\ &\stackrel{\cong}{=} \hat{\mathbf{R}} \otimes \hat{\mathbf{R}}^* \end{aligned} \quad (16)$$

where d represents the spacing between elements and θ is signal incident direction. We can remove the redundant items from the covariance matrix and steering vector processed by Kronecker product. Figure 1 denotes covariance matrix after removing the redundancy.

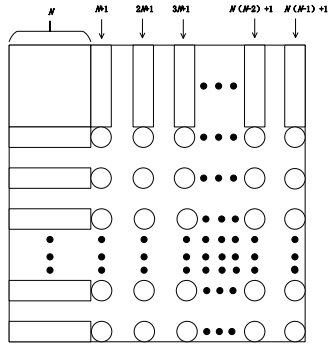


Fig. 1. Covariance matrix after removing the redundancy.

In the Fig. 1, large square box represents a matrix with dimension $N^2 \times N^2$, small square box denotes a matrix which dimension is $N \times N$, the rectangle boxes denote vector with dimension $N \times 1$, and circles are elements extracted from original covariance matrix. The original covariance matrix with dimension $N^2 \times N^2$ becomes a new covariance matrix with dimension $(2N-1) \times (2N-1)$ after using the method of removing redundancy.

In the proposed method, the main computational complexity lies in construction of \mathbf{R}_ω and matrix

inversion operation, the former is $O(PSN^2)$ where P denotes the number of null broadening and S is the number of samples taken in the summation with $S \gg N$, the latter is $O((2N-1)^3)$, so the overall computational complexity is $O(\max(PSN^2, (2N-1)^3))$. The PDNBB and LCSS have same computational complexity with $O(PSN^2, N^3)$. CMT has a lower complexity of $O(N^3)$. Although the proposed method has higher complexity than other algorithms, deeper null and higher array resolution can be got in practical application.

D. The summary of proposed method

The proposed algorithm can be implemented by several steps and summarized as follows:

- Step 1) Construct steering vector correlation matrix \mathbf{R}_ω as Equation (6);
- Step 2) Eigen decomposition of \mathbf{R}_ω as Equation (7);
- Step 3) Construct projection transformation matrix \mathbf{T} as Equation (8);
- Step 4) Projection and diagonal loading as Equation (10);
- Step 5) Kronecker product transforms as Equation (11) and Equation (12);
- Step 6) Removing the redundant items as Fig. 1;
- Step 7) Calculate optimal weight value as Equation (4).

V. SIMULATION RESULTS

We consider a uniform linear array (ULA) with 10 omnidirectional antennas spaced half a wave length uniformly. The direction-of-arrival of desired signal is 0° . The DOAs of the two interferences are -40° and 50° , respectively. The interference to noise ratio (INR) is 30 dB, SNR is 0 dB unless it's specified. The number of snapshot is 200. The width of null is 10° , so projection angular sector selects as $[-45^\circ, -35^\circ]$ and $[45^\circ, 55^\circ]$. The parameter ε decides the depth level of null, we select ε as 6×10^{-6} or 6×10^{-10} . The beam patterns of proposed method and other algorithms are compared in Fig. 2.

From the Fig. 2 (a) and Fig. 2 (b), it can be seen that there are deeper null and higher array resolution when null is broadened in proposed algorithm. In addition, there are different depth of null when parameter ε selected different values, the reason is that orthogonality between signal subspace and noise subspace increases when we select smaller ε . Figure 3 (a) demonstrates the output SINR performance versus SNR where the number of antenna array is 19, except from proposed method, it's consistent with what have been said before, the reason is that the proposed method has changed the number of array elements from N to $2N-1$ after Kronecker product transformation, where N takes 10. Figure 3 (b) shows beam patterns of proposed method when the number of snapshot takes different values, and $K=20$, $K=200$ and $K=500$ are used in the simulations. For each scenario,

there are Monte-Carlo simulations performed with the number of 200 and diagonal loading factor γ is 10^{-4} . We can see that the proposed method have deeper null, high resolution and good robustness which verifies the feasibility of the algorithm.

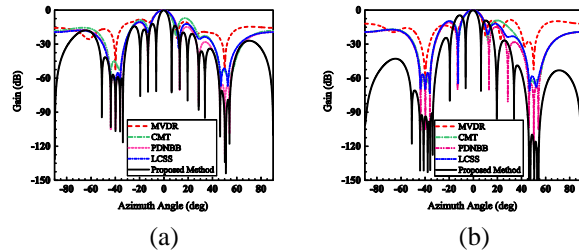


Fig. 2. (a) Normalized beampatterns of different algorithms when parameter ε is equal to 6×10^{-6} , and (b) normalized beampatterns of different algorithms when parameter ε is equal to 6×10^{-10} .

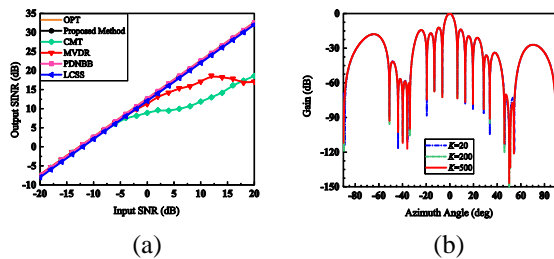


Fig. 3. (a) Output SINR versus the input SNR when parameter ε is equal to 6×10^{-10} , and (b) beam patterns of the proposed method when the number of snapshot takes different values and ε is equal to 6×10^{-6} .

VI. CONCLUSION

A high resolution algorithm for null broadening beamforming based on subspace projection and virtual antenna array is presented in this paper. The proposed method expands the direction of interference incidence through the projection transformation technique, deepens the depth of null, and improves the orthogonality between signal subspace and the noise subspace. At the same time, through the virtual antenna technology, the proposed method furtherly deepens the depth of null while achieving higher array resolution. Theoretical analysis and simulation results show that the proposed method has a good performance on null broadening, array resolution and robustness, it can still work steadily with a small number of snapshots, which enhances its practicality and saves the hardware storage resources.

ACKNOWLEDGMENT

The authors acknowledge all the anonymous reviewers for their constructive comments that helped to improve the quality of this paper.

REFERENCES

- [1] W. X. Li, X. J. Mao, W. H. Yu, Y. S. Li, and C. Y. Yue, "Robust adaptive array beamforming based on modified norm constraint algorithm," *Applied Computational Electromagnetics Society Journal*, vol. 29, pp. 1060-1066, 2014.
- [2] C. A. Valagiannopoulos and V. Kovanis, "Judicious distribution of laser emitters to shape the desired far-field patterns," *Phys. Rev. A*, 2017.
- [3] S. Delikarismanias and V. Pulkki, "Optimal directional pattern design utilizing arbitrary microphone arrays: A continuous-wave approach," *Audio Engineering Society Convention*, 2013.
- [4] R. J. Mailloux, "Covariance matrix augmentation to produce adaptive pattern troughs," *Electronics Letters*, vol. 31, pp. 771-772, 1995.
- [5] M. Zatman, "Production of adaptive array troughs by dispersion synthesis," *Electronics Letters*, vol. 31, pp. 2141-2142, 1995.
- [6] J. G. Guerci, "Theory and application of covariance matrix tapers for robust adaptive beamforming," *IEEE Transactions on Signal Processing*, vol. 47, pp. 977-985, 1999.
- [7] A. Amar and M. A. Doron, "A linearly constrained minimum variance beamformer with a pre-specified suppression level over a pre-defined broad null sector," *Signal Processing*, vol. 109, pp. 165-171, 2015.
- [8] W. X. Li, X. J. Mao, and Y. X. Sun, "A new algorithm for null broadening beamforming," *Journal of Electronics and Information Technology*, vol. 36, pp. 2882-2888, 2014.
- [9] W. Li, Y. Li, and L. Guo, "An effective technique for enhancing anti-interference performance of adaptive virtual antenna array," *Applied Computational Electromagnetics Society Journal*, vol. 26, pp. 234-240, 2011.
- [10] H. Deng, and B. Himed, "A virtual antenna beamforming (VAB) approach for radar systems by using orthogonal coding waveforms," *IEEE Transactions on Antennas and Propagation*, vol. 57, pp. 425-435, 2009.
- [11] W. X. Li, X. J. Mao, Z. Q. Zhai, and Y. S. Li, "High performance robust adaptive beamforming in the presence of array imperfections," *International Journal of Antennas and Propagation*, Article ID 3743509, 2016.
- [12] D. A. Pados and G. N. Karystinos, "An iterative algorithm for the computation of the MVDR filter," *Signal Processing IEEE Transactions on*, vol. 49, no. 2, pp. 290-300, 2001.
- [13] W. Li and Y. Hang, "A novel algorithm for null broadening beamforming based on subspace projection and virtual antenna array," *International Applied Computational Electromagnetics Society Symposium*, 2017.

On the Design and Simulation of Antennas on Ultra-thin Flexible Substrates

Ahmed Kashkool, Samer Yahya, Hussain Al-Rizzo, Abbas Al-Wahhamy, and Ayman A. Issac

Department of Systems Engineering, George W. Donaghey College of Engineering and Information Technology
University of Arkansas at Little Rock, Little Rock, AR 72204-1099, USA
asmahdi@ualr.edu

Abstract — Flexible wireless systems are rapidly evolving in a wide spectrum of applications such as medical, entertainment and sport facilities. The aim of this paper is to investigate whether the ultra-thin substrates along with their permittivity are essential for the initial design stage of a flexible antenna, which is a key element of any wireless system, or it is merely a supporting structure. Three state-of-the-art simulation tools are used to evaluate the scattering parameter, S_{11} which are then compared against precise measurements conducted inside an anechoic chamber. These methods are the Finite Integration Technique (FIT) based Time Domain Solver (TDS) and the Finite-Element Method (FEM) based Frequency Domain Solver (FDS) of CST Microwave Technology and the (FEM) based HFSS of ANSYS. This paper attempts to provide an answer as to whether the substrate and other geometrically small features such as the feeding structure should be sufficiently discretized or else conventional default adaptive meshing should be enough. Three different flexible antennas with two fabrication techniques and feed lines have been used in the simulations and measurements.

Index Terms — CST, flexible antenna, HFSS, substrate, ultra-thin.

I. INTRODUCTION

The past decade has witnessed an ever-growing demand for flexible wireless devices in medical, entertainment, military, sport and personal communications. Furthermore, the electronics market is moving towards flexible displays due to their low profile, low cost, portability and light weight [1-3]. However, literature lacks research on the role of the substrate during the initial design stage, commonly conducted by simulations and the associated challenges faced since commercially available flexible substrate exist in heights ranging from 25 μm up to 130 μm , to mention a few.

This paper mainly focuses on the role of the substrate on the operating frequency bands of flexible antennas, expressed in terms of the frequency spectrum

of S_{11} , with ultra-thin substrates. Three antennas are designed, fabricated and tested to benchmark the three simulation approaches used in this paper. It should be noted that the existing literature does not address this important issue in spite of the obvious discrepancies we observed between measured and simulated spectrum of S_{11} [1-8], to mention a few. Indeed, a close scrutiny of prestigious journals and flagship conferences revealed obvious discrepancies between measured and simulated values of S_{11} for antennas of widely different geometries, fed by different techniques. This motivated us to further investigate this important design issue and to aid researchers in the field of flexible antenna design. It should be emphasized that the dispersion caused by the variation of the real and imaginary parts of the permittivity of the substrate must have not been considered in the simulations reported in this paper due to the unavailability of the pertinent data from the manufacturer. However, it is expected that the effects of such dispersion as well as numerical dispersion caused by the finite-size of the mesh would not significantly alter the observation and conclusions reported in this paper.

II. THE FABRICATED PROTOTYPES

A printed trapezoidal monopole antenna has been chosen due to its wide bandwidth and geometrical symmetry which allows simulating only half the geometry. Photolithography microfabrication technique is used to fabricate this antenna.

The antenna geometry and prototype are shown in Fig. 1. The antenna consists of two parts: the radiating patch which is trapezoidal in shape and the coplanar feeding line. Copper is used for the conducting parts. The substrate is Rogers R03035 with a dielectric constant, $\epsilon_r=3.5$, $\tan\delta=0.05$, and thickness of 130 μm .

The second antenna is geometrically nonsymmetrical. It consists of a strip-loaded CPW-fed pentagonal antenna [9] prototyped using the 2831 Fujifilm material printer with silver nano-particles [10]. The antenna was printed on a polyimide substrate, $\epsilon_r=4.3$ and a thickness of 25 μm . The antenna geometry and prototype are shown in Fig. 2.

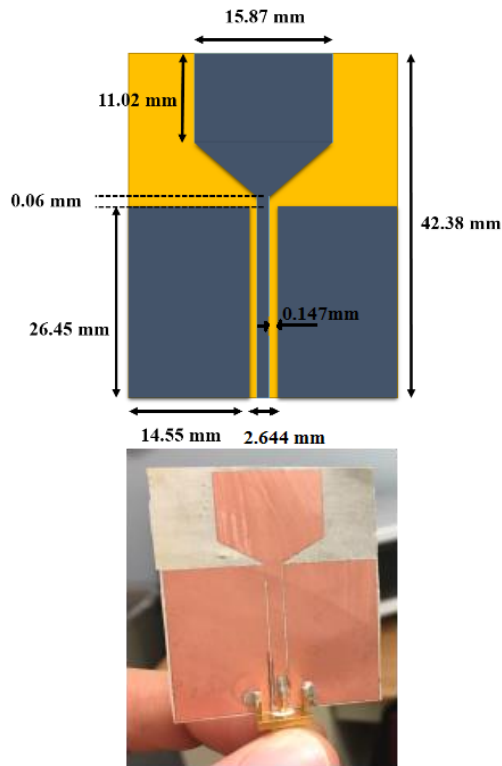


Fig. 1. Geometry and prototype of the trapezoidal flexible antenna.

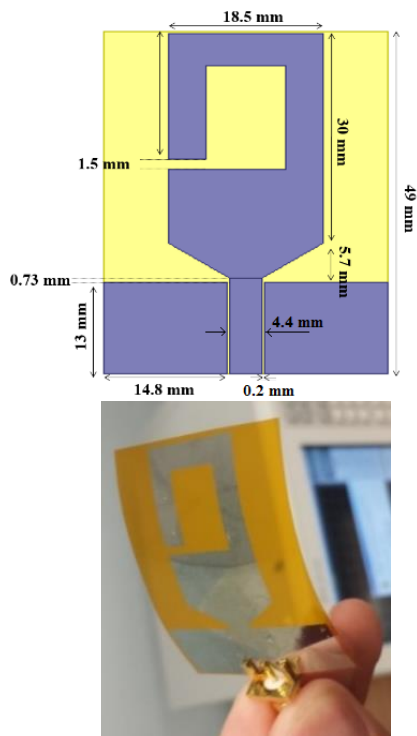


Fig. 2. Geometry and prototype of the strip-loaded CPW-fed pentagonal antenna.

The third antenna is a printed monopole fed by a microstrip line as shown in Fig. 3. This feeding technique has been chosen since the feed line lies partially above a grounded substrate which necessitates the role of the substrate. The substrate is Roger R03035, $\epsilon_r=3.5$, $\tan\delta=0.05$, and 50 μm thickness. The antenna is fabricated using photolithography technique with copper as conducting material. A perfect magnetic conductor boundary is used similar to the first antenna due to geometrical symmetry.

It should be emphasized that the three antennas considered in this paper are not optimized for large bandwidth, neither for a designated radiation pattern. Simple planar radiating and feeding geometries are chosen since our main focus is on the role of the substrate thickness.

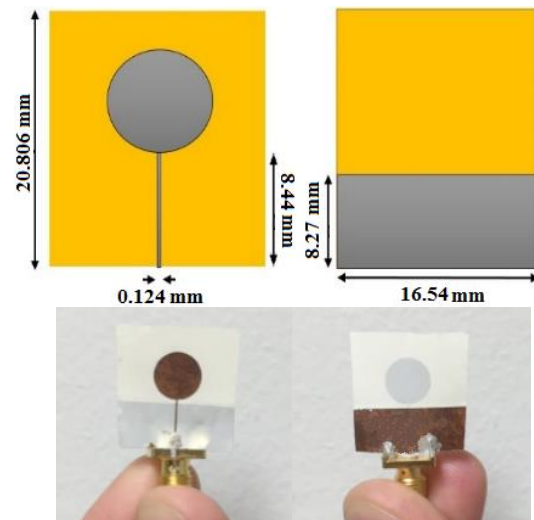


Fig. 3. Geometry and prototype of the circular monopole antenna with radius of 4.13 mm.

III. SIMULATION PROCEDURE

The first step is to find whether mesh seeding is critical in the simulation stage or not. Because of substrate and feeding width/gaps, a hexahedral mesh of at least four cells are taken along the height, length, and width of the substrate to capture the field in the TDS. For the FDS and HFSS, however, the tetrahedral mesh allows only a local mesh refinement along the substrate height of 10 μm due to limitations inherent by these two solvers. The mesh used to simulate this antenna in the time-domain solver of CST Microwave Studio will be elaborated in detail. The rest of the simulations are conducted using a similar meshing approach. In Fig. 4 we show the structure of the mesh used. A total of 37, 104,270 cells are used to provide sufficient representation of the geometry given the extremely large aspect ratio between the horizontal and vertical extent of the antenna. A hexahedral mesh in which Lines per wavelength=40,

Lower mesh limit=200, Mesh line ratio limit=200, and a PEC refinement factor of 6 has been adopted.

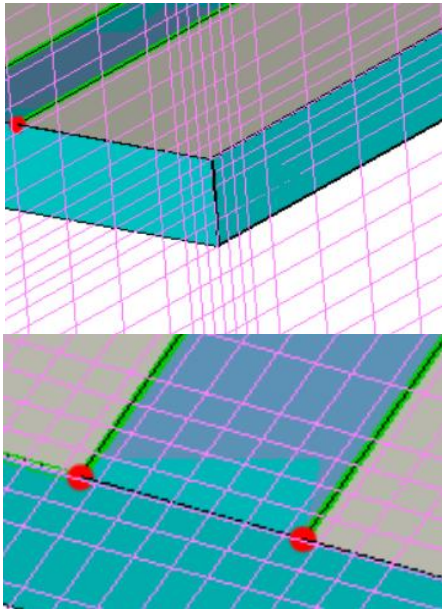


Fig. 4. Meshing scheme of the substrate and feed gaps of the trapezoidal antenna shown in Fig. 1.

The trapezoidal antenna shown in Fig. 1 is considered first. Results for S_{11} versus frequency obtained from measurements using the prototype are compared against simulated results as seen in Fig. 5. The measured results show two bands over which S_{11} is less than -10 dB. The first band extends from 2.93 GHz to 4.87 GHz; the second from 5.72 GHz to 6.71 GHz. With the exception of the TDS, the rest of the simulations reveal single band operation as seen in the figure caption. It is clear that TDS correctly predicts the existence of two separate bands albeit to the noticeable shift, particularly for the first band. Results obtained from the FDS and HFSS show a fair agreement with the measured value of the lower frequency of the first band, 2.93 GHz. However, both were unable to capture the higher end of the band, 4.87 GHz which the TDS predicted with 8% shift.

The second issue is whether the substrate is essential in the design stage or just acts as a supporting structure. As previously mentioned, we should emphasize that numerous papers ignore the presence of the substrate material in simulation and simply replace it by air or follow the default settings of CST and HFSS. If air is assigned as the substrate material, results shown in Fig. 5 obviously show unacceptable results. This observation should motivate researchers to consider the substrate dielectric constant when evaluating the operating frequency range of flexible antennas.

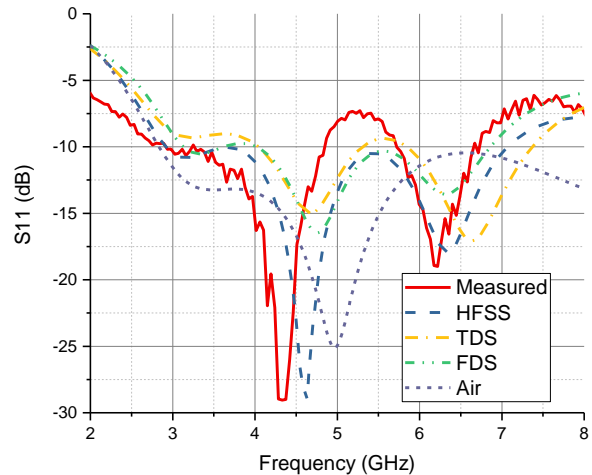


Fig. 5. Measured and simulated S_{11} for the trapezoidal antenna: measured bandwidths (2.93 GHz to 4.87 GHz) and (5.72 GHz to 6.71 GHz), TDS (4.04 GHz to 5.29 GHz) and (5.83 GHz to 7.36 GHz).

The second antenna was tested as well and the results are shown in Fig. 6. Results obtained from HFSS show better agreement than TDS and FDS for the first resonant band (1.36 GHz to 1.59 GHz) but significantly differs from the second measured resonant band (3.20 GHz to 6.04 GHz). However, the TDS and FDS provide excellent agreement for the second band. It is again noticed that air cannot replace the substrate to predict the measured performance.

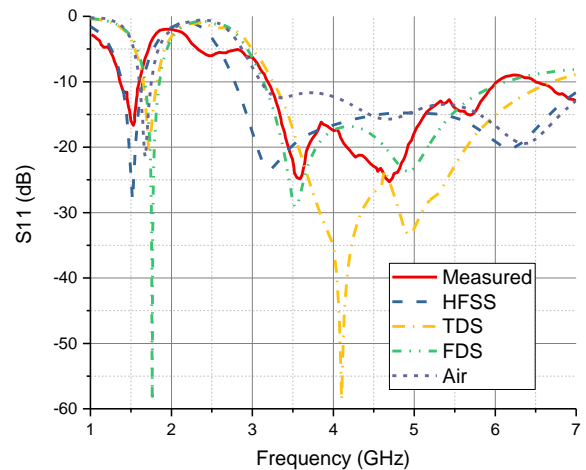


Fig. 6. Measured and simulated S_{11} for the strip-loaded CPW-fed pentagonal antenna: measured bandwidths (1.36 GHz to 1.59 GHz) and (3.20 GHz to 6.01 GHz), HFSS (1.40 GHz to 1.64 GHz), TDS (1.65 GHz to 1.82 GHz) and (3.25 GHz to 6.70 GHz), FDS (1.67 GHz to 1.85 GHz) and (3.13 GHz to 6.31 GHz).

The results of the third prototype are shown in Fig. 7. The first measured frequency at which S_{11} drops below -10 dB is at 5.44 GHz. HFSS yields a close value of 5.73 GHz while the values obtained from TDS and FDS are 6.26 GHz and 6.184 GHz, respectively. However, all simulations provided bandwidths well above the measured value of 8 GHz. Using air as a substrate provided erroneous results. It should be noted that the SMA for the prototype did not completely align within the 0.124 mm wide microstrip feed line. Another important issue is there is a common region in the substrate that is sandwiched between the partial ground and the microstrip line with a length of 8.27 mm may pose a challenge in the discretization and numerical simulations. This observation led us to conclude that microstrip-fed flexible antenna shown in Fig. 3 is more challenging to simulate as compared to the CPW-fed antennas in Figs. 1 and 2.

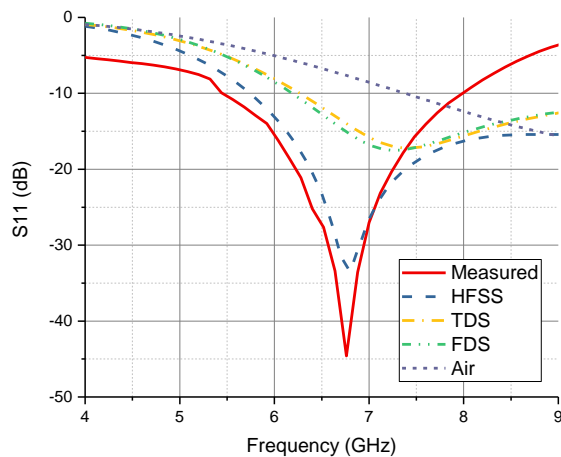


Fig. 7. Measured and simulated S_{11} for the circular monopole antenna: measured bandwidth (5.44 GHz to 7.96 GHz).

IV. CONCLUSION

The paper concludes that the substrate should be taken into consideration in the initial design of flexible antennas, at least for the feeding structure, and it is not merely a supporting structure. It was noticed through extensive simulations that appropriate manual meshing is essential to get the S_{11} spectrum closer to the measured values, and hence to reach the targeted design. Ignoring

the substrate or replacing it by air provides erroneous results.

REFERENCES

- [1] H. R. Raad, A. I. Abbosh, H. M. Al-Rizzo, and D. G. Rucker, "Flexible and compact AMC based antenna for telemedicine applications," *IEEE Trans. Antennas Propag.*, vol. 61, no. 2, pp. 524-531, 2013.
- [2] J. E. Ruyle, A. Moreno, and J. T. Bernhard, "Placement-insensitive flexible RFID antenna for 'peel-and-stick' applications," *IET Microw. Antennas & Propag.*, vol. 11, no. 3, pp. 433-441, 2017.
- [3] P. Rocca and A. F. Morabito, "Optimal synthesis of reconfigurable planar arrays with simplified architectures for monopulse radar applications," *IEEE Trans. Antennas Propag.*, vol. 63, no. 3, pp. 1048-1058, 2015.
- [4] S. Kumar, V. Bhat, K. J. Vinoy, and V. Santhanam, "Using an office inkjet printer to define the formation of copper films on paper," *IEEE Trans. Nanotechnol.*, vol. 13, no. 1, pp. 160-164, 2014.
- [5] H. R. Khaleel, H. M. Al-Rizzo, D. G. Rucker, and S. Mohan, "A compact polyimide-based UWB antenna for flexible electronics," *IEEE Antennas Wirel. Propag. Lett.*, vol. 11, pp. 564-567, 2012.
- [6] S. Hong, S. H. Kang, Y. Kim, and C. W. Jung, "Transparent and flexible antenna for wearable glasses applications," *IEEE Trans. Antennas Propag.*, vol. 64, no. 7, pp. 2797-2804, 2016.
- [7] Z. Hamouda, et al., "Dual-band elliptical planar conductive polymer antenna printed on a flexible substrate," *IEEE Trans. Antennas Propag.*, vol. 63, no. 12, pp. 5864-5867, 2015.
- [8] H. R. Khaleel, H. M. Al-Rizzo, and D. G. Rucker, "Compact polyimide-based antennas for flexible displays," *IEEE/OSA J. Disp. Technol.*, vol. 8, no. 2, pp. 91-96, 2012.
- [9] A. I. Hammodi, H. Al-Rizzo, A. A. Issac, A. S. Kashkool, K. Gamer, and H. Khaleel, "Studying the effect of bending of the performance of flexible dual band microstrip monopole antenna," *IEEE Conference on Antenna Measurements and Applications (CAMA)*, Syracuse, NY, pp. 1-3, 2016.
- [10] http://www.fujifilmusa.com/products/industrial_in_kjet_printheads/deposition-products/dmp-2800

Modelling of Electromagnetic Scattering from Large and General Intakes on Complex Platforms

Alessandro Mori, Stefano Bertini, Mirko Bercigli, Raffaele Scuderi, Paolo de Vita,
and Stefano Sensani

IDS Ingegneria dei Sistemi S.p.A.
Pisa, I-56121, Italy

{a.mori,s.bertini,m.bercigli,r.scuderi,p.devita,s.sensani}@idscorporation.com

Abstract — In the framework of the design of low observable aircraft, one of the most difficult problem is the numerical modelling of aeronautical air intakes with an – usually complex – arbitrary shape. Also the presence of radio absorbing material demands for accurate methods in evaluating the low level scattering for real life problems. This paper addresses the use of a full wave approach, based on the Multilevel Fast Multipole Approach (MLFMA), for a high fidelity modelling both of the whole (real life) aircraft, and of the intake scattering contribution, useful in the design and optimization stage of the intake itself.

Index Terms — Fast methods, Method of Moments (MoM), MLFMA, radar signature, scattering.

I. INTRODUCTION

One of the most demanding problems in computational electromagnetics is given by the low observable design of a modern aeronautical platform. This is due to the different scattering phenomena contributing to the global scattered field as well as to the electrical size of the platform at the typical impinging radar wave frequencies. The stealthness requirement in real life industrial problems requires computationally efficient and accurate electromagnetic computational tools able to assess low Radar Signatures.

In the nose on aspect angles, the jet intake is one of the major hot spots generating high level of radar signature for a large set of aspect angles. Particular design techniques are used to reduce the intakes' signature. For instance, line-of-sight blockage of the engine and usage of radar absorbing material / structure installation [1]. These techniques make usually intakes a complex – and electrically large – structure to be analyzed. In the design phase the capability to assess the scattering contribution of the only intake is a key point in order to optimize it in terms of shaping, materials, engine fan and air flow control structures. Other than the capability to aggregate the signature of the intake with the scattering contribution

of the whole aeronautical platform it is also mandatory since the electrical size of the EM problem makes a brute force application of a full wave approach strongly inefficient.

Several works have been published for the solution of the intake scattering, resorting to asymptotic [2] and hybrid numerical techniques [3-5]. In this contribution, we address the use of a frequency domain full wave (MoM) method for a high fidelity modelling of intakes and aircraft structures, with MLFMA to allow the analysis of the electrically large problems arising in real life cases. The used formulation and the main characteristics of the numerical solver are summarized in Section II, while Section III describes the evaluation of the scattering contribution of intake alone to the overall radar signature. Some results are described in Section IV and some conclusions are drawn in Section V.

II. HIGH FIDELITY AIRCRAFT SCATTERING MODEL

Real life aircrafts are very complicated structures. In order to accurately estimate their electromagnetic behavior, it is needed to finely model their geometry and structures (high fidelity modelling). This leads to a multi-scale object, composed by different materials (conducting, dielectric, radio absorbing). The Method of Moments is able to give very accurate results on an arbitrary geometry at the expenses of a high numerical complexity. Acceleration methods, like the MLFMA give the possibility to analyze electrically large structures.

The used electromagnetic solver is a Frequency Domain Method of Moments with Galerkin's discretization on a triangular mesh. It implements the Poggio-Miller-Chang-Harrington-Wu-Tsai (PMCHWT) formulation [6], and any combination and arrangement of lossy and lossless materials can be considered. In particular, such formulation is applied on the dielectric interfaces separating homogeneous dielectric materials; while the Electric Field Integral Equation (EFIE) and the Combined Field Integral Equation (CFIE) are applied on open

and closed conducting surfaces, respectively. The Multilevel Fast Multipole Approach (MLFMA) [7] is used to efficiently solve electrically large models. In such a case an iterative solver has to be employed (BiCGStab, GMRESR, etc.) and the MoM linear system has to be effectively preconditioned. Due to the multi-scale nature of the model (also determined by meshing the surface of dense materials), a MultiResolution (MR) preconditioning is adopted [8] to obtain a solver with high computational efficiency. By using such solver, it is possible to consider real life structures (Fig. 1, Fig. 2).

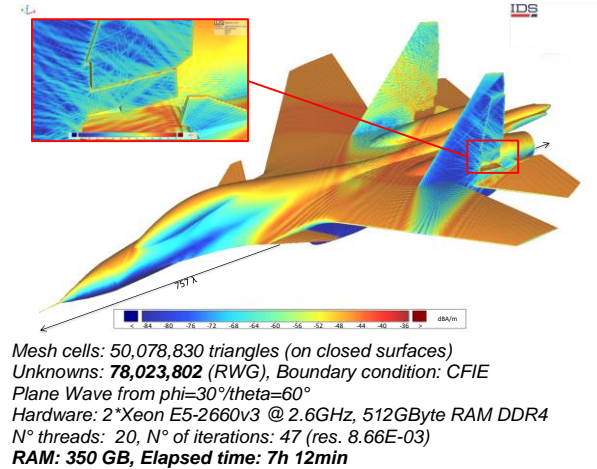


Fig. 1. Equivalent electric current on a Sukhoi, induced by an impinging plane wave @ 10 GHz.

Particular materials can be characterized by means of a general anisotropic Impedance Boundary Condition (IBC) [9], relating the tangential electric and magnetic field through a local Surface Impedance $\underline{\underline{Z}}_S$ described by a 3×3 dyad:

$$\vec{E} - (\hat{n} \cdot \vec{E})\hat{n} = \underline{\underline{Z}}_S \hat{n} \times \vec{H} \rightarrow \vec{M} = -\hat{n} \times \underline{\underline{Z}}_S \vec{J}, \quad (1)$$

where \hat{n} is the conducting surface normal. Equation (1) establishes a relation between the equivalent surface magnetic (\vec{M}) and electric (\vec{J}) currents on IBC surfaces (1, right). This allows to avoid magnetic unknowns on surface of IBC materials, but this has to be included carefully in the formulation, due to the fact that it defines a discontinuous distribution when RWG are used to expand the electric current \vec{J} .

Even if we can efficiently model whole aircrafts, it is important to consider the possibility of modelling the contribution of single parts (the intake in our case) for design and optimization purposes. A designer can model the aircraft platform once – also with techniques other than MoM (modelling the structure in Fig. 1 with the Iterative Physical Optics [10] we obtain the result shown in Fig. 3) – to be combined to the contribution of the intake, the last modelled every time a change is made by designers. The next section considers the evaluation of

the intakes contribution. All the results were obtained with the numerical code of IDS (IDS Method of Moment Multi-Port, IDS IPO), integrated in the Galileo-EME framework [11].

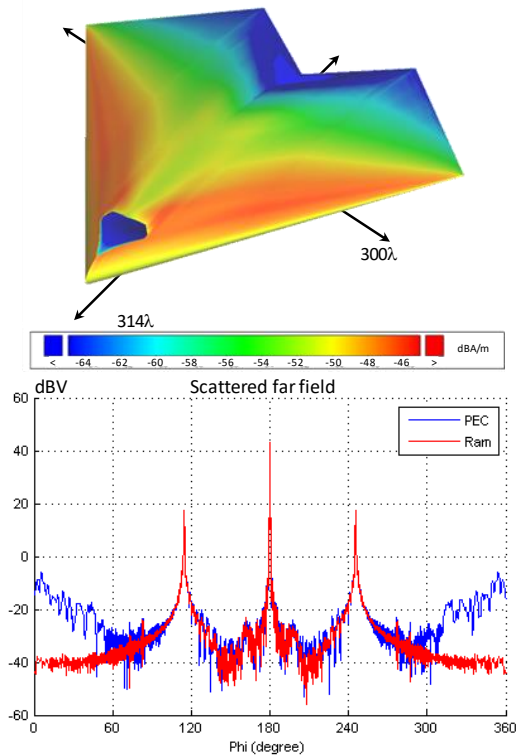


Fig. 2. Equivalent electric current (top) and scattered field (bottom) for a UCAV, induced by an impinging plane wave @ 10 GHz. Pec labels refers to an intake without a RAM covering.

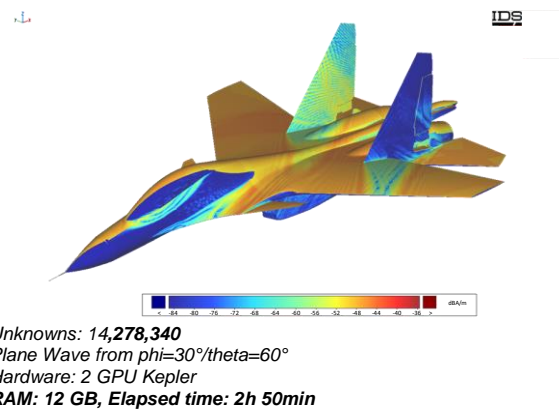


Fig. 3. Equivalent electric current on a Sukhoi, induced by an impinging plane wave @ 10 GHz, evaluated by using a fast IPO formulation.

III. INTAKE CONTRIBUTION TO RADAR SIGNATURE

In evaluation of the contribution of an air intake to the overall scattered field (obtained through a coherent sum of the different contributions), we could neglect some interactions (with the rest of the structure), and we could add other interactions (with the outer surface of the intake). We have different possibilities (Fig. 4):

- To model the intake walls as a thin surface. The walls contribute to the scattered field;
- To model the intake with both sides of the walls. Then, discard the scattering contribution of basis functions on the exterior side;
- To insert a dummy interface on the mouth. Then, discard the scattering contribution of basis functions on the exterior wall side. Only the mouth contributes to the scattered field, giving good results in the half space the mouth is looking to.
- To insert a dummy interface on the mouth and don't generate basis functions on the exterior wall side (halving the unknowns). Only the mouth contributes to the scattered field, giving good results in the half space the mouth is looking to.

The first choice can lead to inaccurate results. The other methods give almost the same results, but the last choice allows the halving the unknowns on the intake. This is the method we have adopted in this paper. In every case, the inclusion of a small part of the aircraft structure near the mouth (discarded in the evaluation of the overall scattered field) helps to increase the accuracy of the simulation.

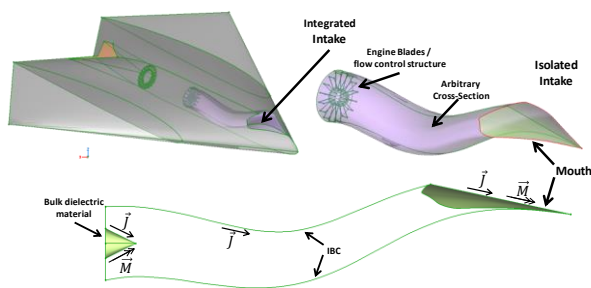


Fig. 4. Typical Air intake isolated problem.

IV. VALIDATION AND EXAMPLE OF APPLICATION

In this Section we report some validation data obtained on the 9 m × 9 m perfectly conducting UCAV shown in Fig. 4. The structure (60 λ × 60 λ @ 2 GHz) is discretized with 712365 triangles, and the validation is carried out in terms of monostatic scattered field on the +10 degrees elevation plane. The nose is heading 180 degrees azimuth. Figure 5 shows the Radar Cross Section of the Intake in Fig. 4, modelled with thin walls and with the proposed method. The scattered field from

the walls causes the beat visible at high angles. The platform contribution shows that the intake contributes significantly on the scattered field. The combination of intake and platform scattered field is compared to a simulation of the complete UCAV in Fig. 6. To the purpose of air intakes design, this result represents a good agreement, and by considering a small part of the fuselage in solving the intake allows to obtain a more accurate result (Fig. 6).

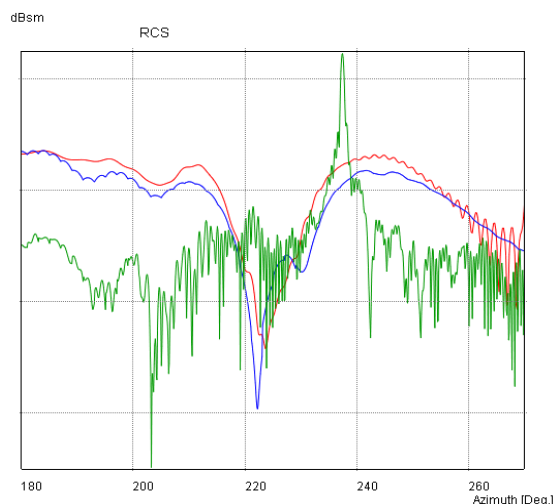


Fig. 5. VV monostatic scattered field of the intake in Fig. 4, modelled with thin walls (red) and with the proposed method (blue). The platform contribution (green) is also shown.

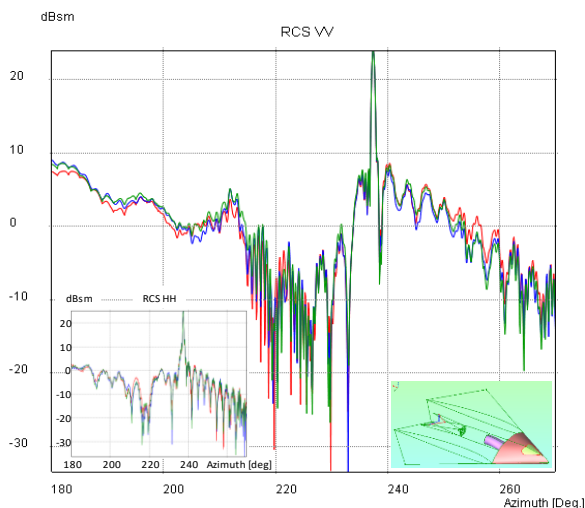


Fig. 6. VV monostatic scattered field of the UCAV in Fig. 4, considering the complete structure (blue), or combining separate contribution from the intake and the platform (red). Inclusion of a small part of the fuselage (inset) in solving the intake allows to obtain a more accurate result (green). Similar results are obtained for the HH polarization (inset).

Figure 7 shows some results on a more realistic case. Some details are given in the figure. The beat on the scattered field due to the walls is again visible in the graphs.

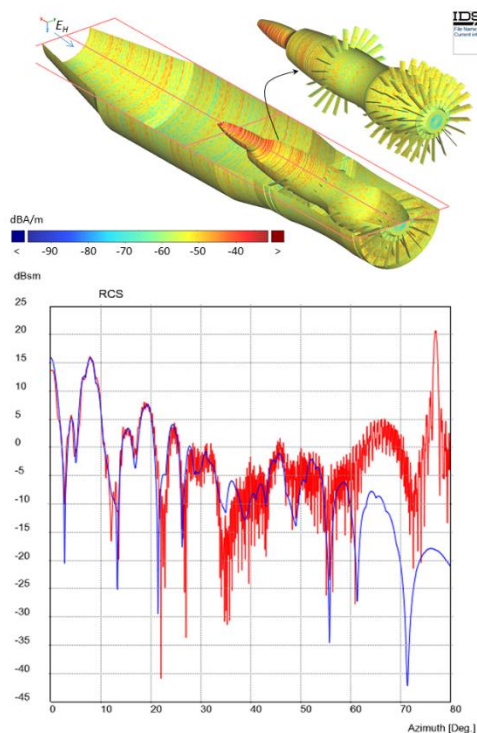


Fig. 7. Equivalent electric current (top) and monostatic Scattered field (bottom) for a $5.17 \text{ m} \times 1.19 \text{ m} \times 1.19 \text{ m}$ Intake @ 10 GHz (10,824,636 unknowns and CFIE+IBC formulation), modelled with thin walls (red) and with the proposed method (blue).

V. CONCLUSIONS

In this paper the modelling of real life, aeronautical air intakes with an arbitrary shape is addressed, with reference to the modeling of the intake alone and the combination of its response with the platform one to obtain the scattered field of the complete aircraft. Being able to maintain a sufficient accuracy, this allows an easier design and optimization of the intakes. Different ways to decouple intake and aircraft scattering

contribution was analysed, and the most efficient method is validated on a test case.

REFERENCES

- [1] B. S. Haisty, "Lockeed Martin's - Affordable Stealth," National Press Club, Washington DC, 15 Nov. 2000.
- [2] P. H. Pathak and R. J. Burkholder, "Modal, ray, and beam techniques for analyzing the EM scattering by open-ended waveguide cavities," *IEEE Trans. Antenna Propagat.*, vol. 37, pp. 635-647, May 1989.
- [3] P. R. Rousseau and R. J. Burkholder, "A hybrid approach for calculating the scattering from obstacles within large open cavities," *IEEE Trans. Antenna Propagat.*, vol. 43, pp. 1068-1075, Oct. 1995.
- [4] A. Barka, P. Soudais, and D. Volpert, "Scattering from 3-D cavities with a plug and play numerical scheme combining IE, PDE, and modal techniques," *IEEE Trans. Antenna Propagat.*, vol. 48, pp. 704-712, May 2000.
- [5] F. Hu, C. Wang, and Y. Gan, "Efficient calculation of interior scattering from large three-dimensional PEC cavities," *IEEE Trans. Antenna Propagat.*, vol. 55, pp. 167-177, Jan. 2007.
- [6] P. Yla-Oijala, M. Taskinen, and J. Sarvas, "Surface integral equation method for general composite metallic and dielectric structures with junctions," *Prog. Electromagn. Res.*, vol. 52, pp. 81-108, 2005.
- [7] W. C. Chew, J. Song, et al., *Fast and Efficient Algorithms in Computational Electromagnetics*. Boston, MA: Artech House, 2001.
- [8] F. Vipiana, G. Vecchi, and D. R. Wilton, "A multi-resolution moment method for wire-surface objects," *IEEE Trans. Antenna Propagat.*, vol. 58, no. 5, pp. 1807-1813, May 2010.
- [9] A. W. Glisson, et al., "Electromagnetic scattering by an arbitrarily shaped surface with an anisotropic impedance boundary condition," *App. Comp. Elec. Soc. Jour.*, vol. 10, no. 3, pp. 93-106, 1995.
- [10] P. De Vita, A. Mori, L. Pandolfo, M. Bercigli, M. Bandinelli, G. Carluccio, M. Albani, et al., "Analysis of scattering from electrically large objects using fast far field iterative physical optics," *2017 11th Euro. Conf. on Ant. and Prop. (EUCAP)*, Paris, pp. 509-512, 2017.
- [11] <https://www.idscorporation.com/pf/galileo-suite/>

A Finite Difference Frequency Domain Based Full Vectorial Transverse Modesolver for Anisotropic Waveguides with Arbitrary Permittivity and Permeability Tensors

Varun Singh

Department of Electrical Engineering
Indian Institute of Technology Madras, Chennai, Tamil Nadu, 600036, India
varunsingh316@gmail.com, ee11d025@ee.iitm.ac.in

Abstract — In this work a Yee's mesh based full vectorial transverse finite difference frequency (FDFD) modesolver has been derived from discretized Maxwell's equations in Matrix form for anisotropic waveguides with arbitrary permittivity and permeability tensors. This work incorporates arbitrary permittivity and permeability simultaneously into matrix equations of Yee's mesh based modesolver, which previous works have not done. For benchmarking the Python implementation of these matrix equations, cross section of Yitrium Iron Garnate (YIG) channel waveguide has been taken as first one of the three test structures. Numerical result from this work has been compared with that from previous work on YIG channel waveguide and is found to be in good agreement. Further, for benchmarking the effective index values of waveguides having both permittivity and permeability anisotropic simultaneously, a finite element based commercial software (COMSOL) has been used, the values of effective indexes from solver presented in this work and commercial software have been compared, and are also found to be in good agreement.

Index Terms — Anisotropic waveguides, finite difference frequency domain, full vectorial, modesolver.

I. INTRODUCTION

Despite finite difference time domain (FDTD) method being the most general purpose and robust method for simulation of Nanophotonic and Integrated Optic devices, finite difference frequency domain (FDFD) method is also very useful in solving some Nanophotonic and Integrated Optic problems such as single mode verification, coupling length calculations etc. Moreover the mode field solutions obtained from a Yee's mesh based FDFD modesolver are more compatible with Yee's mesh based propagation methods for the purpose of mode launching. The previous works on transverse FDFD modesolvers [1-5] have not incorporated arbitrary permittivity and permeability tensors simultaneously into their formulation but this work incorporates arbitrary

permittivity and permeability tensors simultaneously into formulation of FDFD based transverse modesolver.

In order to benchmark accuracy of the solver, numerically calculated effective index from the solver presented here has been compared with effective index given in [4] for Yttrium Iron Garnate (YIG) channel waveguide. Moreover effective indexes of waveguides having both permeability and permeability anisotropic simultaneously have also been calculated and compared with values given by finite element based commercial software [6].

II. THEORY AND MATRIX FORMULATIONS

While deriving the matrix equations for modesolver the convention for naming variables is same as in [5]. The Maxwell's equations are written assuming $e^{i(\beta z - \omega t)}$ dependence (where $\beta = 2\pi \frac{N_{eff}}{\lambda}$ and $k_0 = 2\pi/\lambda$, with λ being free space wavelength) which leads to $\frac{\partial}{\partial z} = i\beta$ and $\frac{\partial}{\partial t} = -i\omega$. N_{eff} contains both real and imaginary part of scaled eigen solution (scaled by $\lambda/2\pi$). The real part of this solution is denoted by n_{eff} (effective index), also electric fields are scaled by the impedance of free space. Further all permittivity and permeability values used here are relative.

The Maxwell's equations with above conditions applied are:

$$ik_0 \varepsilon_{xx} H_x + ik_0 \varepsilon_{xy} H_y + ik_0 \varepsilon_{xz} H_z = \frac{\partial E_z}{\partial y} - i\beta E_y, \quad (1)$$

$$ik_0 \mu_{yx} H_x + ik_0 \mu_{yy} H_y + ik_0 \mu_{yz} H_z = i\beta E_x - \frac{\partial E_z}{\partial x}, \quad (2)$$

$$ik_0 \mu_{zx} H_x + ik_0 \mu_{zy} H_y + ik_0 \mu_{zz} H_z = \frac{\partial E_y}{\partial x} - \frac{\partial E_x}{\partial y}, \quad (3)$$

$$-ik_0 \varepsilon_{xx} E_x - ik_0 \varepsilon_{xy} E_y - ik_0 \varepsilon_{xz} E_z = \frac{\partial H_z}{\partial y} - i\beta H_y, \quad (4)$$

$$-ik_0 \varepsilon_{yx} E_x - ik_0 \varepsilon_{yy} E_y - ik_0 \varepsilon_{yz} E_z = i\beta H_x - \frac{\partial H_z}{\partial x}, \quad (5)$$

$$-ik_0 \varepsilon_{zx} E_x - ik_0 \varepsilon_{zy} E_y - ik_0 \varepsilon_{zz} E_z = \frac{\partial H_y}{\partial x} - \frac{\partial H_x}{\partial y}, \quad (6)$$

Now discretizing the fields in above equations in accordance with Yee's meshing scheme, the fields can

be represented as, $E_x \rightarrow E_x(j+1/2, 1)$, $E_y \rightarrow E_y(j, 1+1/2)$, $E_z \rightarrow E_z(j, 1)$, $H_x \rightarrow H_x(j, 1+1/2)$, $H_y \rightarrow H_y(j+1/2, 1)$, $H_z \rightarrow H_z(j+1/2, 1+1/2)$. Now writing the discretized Maxwell's equations into matrix form (with bold symbols representing matrix variables) leads to:

$$ik_0 \begin{bmatrix} \boldsymbol{\mu}_{xx} & \boldsymbol{\mu}_{xy} & \boldsymbol{\mu}_{xz} \\ \boldsymbol{\mu}_{yx} & \boldsymbol{\mu}_{yy} & \boldsymbol{\mu}_{yz} \\ \boldsymbol{\mu}_{zx} & \boldsymbol{\mu}_{zy} & \boldsymbol{\mu}_{zz} \end{bmatrix} \begin{bmatrix} \mathbf{H}_x \\ \mathbf{H}_y \\ \mathbf{H}_z \end{bmatrix} = \begin{bmatrix} \mathbf{0} & -i\beta\mathbf{I} & \mathbf{U}_y \\ i\beta\mathbf{I} & \mathbf{0} & -\mathbf{U}_x \\ -\mathbf{U}_y & \mathbf{U}_x & \mathbf{0} \end{bmatrix} \begin{bmatrix} \mathbf{E}_x \\ \mathbf{E}_y \\ \mathbf{E}_z \end{bmatrix}, \quad (7)$$

$$-ik_0 \begin{bmatrix} \boldsymbol{\epsilon}_{xx} & \boldsymbol{\epsilon}_{xy} & \boldsymbol{\epsilon}_{xz} \\ \boldsymbol{\epsilon}_{yx} & \boldsymbol{\epsilon}_{yy} & \boldsymbol{\epsilon}_{yz} \\ \boldsymbol{\epsilon}_{zx} & \boldsymbol{\epsilon}_{zy} & \boldsymbol{\epsilon}_{zz} \end{bmatrix} \begin{bmatrix} \mathbf{E}_x \\ \mathbf{E}_y \\ \mathbf{E}_z \end{bmatrix} = \begin{bmatrix} \mathbf{0} & -i\beta\mathbf{I} & \mathbf{V}_y \\ i\beta\mathbf{I} & \mathbf{0} & -\mathbf{V}_x \\ -\mathbf{V}_y & \mathbf{V}_x & \mathbf{0} \end{bmatrix} \begin{bmatrix} \mathbf{H}_x \\ \mathbf{H}_y \\ \mathbf{H}_z \end{bmatrix}, \quad (8)$$

In the above matrix Eqs. (7) and (8), $\boldsymbol{\epsilon}_{xx}$, $\boldsymbol{\epsilon}_{yy}$, ... and $\boldsymbol{\mu}_{xx}$, $\boldsymbol{\mu}_{yy}$, ... are all diagonal square matrices with diagonal size equal to the number of field computation points in the simulation window. \mathbf{U}_x , \mathbf{U}_y , \mathbf{V}_x and \mathbf{V}_y are Yee's mesh based differential operators in sparse square matrix form, the size of these matrices is equal to square of the number of field computation points in the simulation window. For this work \mathbf{U}_x and \mathbf{U}_y are given by Eqs. (9) and (10) respectively, \mathbf{V}_x and \mathbf{V}_y can be derived from \mathbf{U}_x and \mathbf{U}_y respectively, by transferring the smaller diagonal to lower triangular region while keeping the offset from the main diagonal unchanged, followed by change of sign in both diagonals. Here the offset in \mathbf{U}_x is one and in \mathbf{U}_y , it is equal to number of field computation points along x direction. The above matrices have also been described in [6]:

$$\mathbf{U}_x = \frac{1}{\Delta x} \begin{bmatrix} -1 & 1 & & \\ & & -1 & \ddots \\ & & & \ddots \\ & & & & \ddots \end{bmatrix}, \quad (9)$$

$$\mathbf{U}_y = \frac{1}{\Delta y} \begin{bmatrix} -1 & & & & \\ & 1 & & & \\ & & -1 & & \\ & & & \ddots & \\ & & & & \ddots \end{bmatrix}, \quad (10)$$

\mathbf{E}_x , \mathbf{E}_y , \mathbf{E}_z and \mathbf{H}_x , \mathbf{H}_y , \mathbf{H}_z are field matrices which contain the mode field values and their size is equal to the number of field computation points in the simulation window. It is worth mentioning here that the number of field computation points will be dictated by discretizations Δx and Δy in x and y directions respectively. Further the field matrices have been stored in row-major order. After careful algebraic manipulations (substitutions &

eliminations) on matrix Eqs. (7) and (8), they get reduced to Eigen equation given by Eq. (11). It is worth mentioning here that Eqs:

$$\beta \begin{bmatrix} \mathbf{E}_x \\ \mathbf{E}_y \\ \mathbf{H}_x \\ \mathbf{H}_y \end{bmatrix} = \begin{bmatrix} \mathbf{F}_{11} & \mathbf{F}_{12} & \mathbf{F}_{13} & \mathbf{F}_{14} \\ \mathbf{F}_{21} & \mathbf{F}_{22} & \mathbf{F}_{23} & \mathbf{F}_{24} \\ \mathbf{F}_{31} & \mathbf{F}_{32} & \mathbf{F}_{33} & \mathbf{F}_{34} \\ \mathbf{F}_{41} & \mathbf{F}_{42} & \mathbf{F}_{43} & \mathbf{F}_{44} \end{bmatrix} \begin{bmatrix} \mathbf{E}_x \\ \mathbf{E}_y \\ \mathbf{H}_x \\ \mathbf{H}_y \end{bmatrix}, \quad (11)$$

where

$$\mathbf{F}_{11} = i\boldsymbol{\mu}_{yz}(\boldsymbol{\mu}_{zz})^{-1}\mathbf{U}_y + i\mathbf{U}_x(\boldsymbol{\epsilon}_{zz})^{-1}\boldsymbol{\epsilon}_{zx}, \quad (12)$$

$$\mathbf{F}_{12} = -i\boldsymbol{\mu}_{yz}(\boldsymbol{\mu}_{zz})^{-1}\mathbf{U}_x + i\mathbf{U}_x(\boldsymbol{\epsilon}_{zz})^{-1}\boldsymbol{\epsilon}_{zy}, \quad (13)$$

$$\mathbf{F}_{13} = k_0\boldsymbol{\mu}_{yx} - k_0\boldsymbol{\mu}_{yz}(\boldsymbol{\mu}_{zz})^{-1}\boldsymbol{\mu}_{zx} - (k_0)^{-1}\mathbf{U}_x(\boldsymbol{\epsilon}_{zz})^{-1}\mathbf{V}_y, \quad (14)$$

$$\mathbf{F}_{14} = k_0\boldsymbol{\mu}_{yy} - k_0\boldsymbol{\mu}_{yz}(\boldsymbol{\mu}_{zz})^{-1}\boldsymbol{\mu}_{zy} + (k_0)^{-1}\mathbf{U}_x(\boldsymbol{\epsilon}_{zz})^{-1}\mathbf{V}_x, \quad (15)$$

$$\mathbf{F}_{21} = -i\boldsymbol{\mu}_{xz}(\boldsymbol{\mu}_{zz})^{-1}\mathbf{U}_y + i\mathbf{U}_y(\boldsymbol{\epsilon}_{zz})^{-1}\boldsymbol{\epsilon}_{zx}, \quad (16)$$

$$\mathbf{F}_{22} = i\boldsymbol{\mu}_{xz}(\boldsymbol{\mu}_{zz})^{-1}\mathbf{U}_x + i\mathbf{U}_y(\boldsymbol{\epsilon}_{zz})^{-1}\boldsymbol{\epsilon}_{zy}, \quad (17)$$

$$\mathbf{F}_{23} = -k_0\boldsymbol{\mu}_{xx} + k_0\boldsymbol{\mu}_{xz}(\boldsymbol{\mu}_{zz})^{-1}\boldsymbol{\mu}_{zx} - (k_0)^{-1}\mathbf{U}_y(\boldsymbol{\epsilon}_{zz})^{-1}\mathbf{V}_y, \quad (18)$$

$$\mathbf{F}_{24} = -k_0\boldsymbol{\mu}_{xy} + k_0\boldsymbol{\mu}_{xz}(\boldsymbol{\mu}_{zz})^{-1}\boldsymbol{\mu}_{zy} + (k_0)^{-1}\mathbf{U}_y(\boldsymbol{\epsilon}_{zz})^{-1}\mathbf{V}_x, \quad (19)$$

$$\mathbf{F}_{31} = -k_0\boldsymbol{\epsilon}_{yx} + k_0\boldsymbol{\epsilon}_{yz}(\boldsymbol{\epsilon}_{zz})^{-1}\boldsymbol{\epsilon}_{zx} + (k_0)^{-1}\mathbf{V}_x(\boldsymbol{\mu}_{zz})^{-1}\mathbf{U}_y, \quad (20)$$

$$\mathbf{F}_{32} = -k_0\boldsymbol{\epsilon}_{yy} + k_0\boldsymbol{\epsilon}_{yz}(\boldsymbol{\epsilon}_{zz})^{-1}\boldsymbol{\epsilon}_{zy} - (k_0)^{-1}\mathbf{V}_x(\boldsymbol{\mu}_{zz})^{-1}\mathbf{U}_x, \quad (21)$$

$$\mathbf{F}_{33} = i\boldsymbol{\epsilon}_{yz}(\boldsymbol{\epsilon}_{zz})^{-1}\mathbf{V}_y + i\mathbf{V}_x(\boldsymbol{\mu}_{zz})^{-1}\boldsymbol{\mu}_{zx}, \quad (22)$$

$$\mathbf{F}_{34} = -i\boldsymbol{\epsilon}_{yz}(\boldsymbol{\epsilon}_{zz})^{-1}\mathbf{V}_x + i\mathbf{V}_x(\boldsymbol{\mu}_{zz})^{-1}\boldsymbol{\mu}_{zy}, \quad (23)$$

$$\mathbf{F}_{41} = k_0\boldsymbol{\epsilon}_{xx} - k_0\boldsymbol{\epsilon}_{xz}(\boldsymbol{\epsilon}_{zz})^{-1}\boldsymbol{\epsilon}_{zx} + (k_0)^{-1}\mathbf{V}_y(\boldsymbol{\mu}_{zz})^{-1}\mathbf{U}_y, \quad (24)$$

$$\mathbf{F}_{42} = k_0\boldsymbol{\epsilon}_{xy} - k_0\boldsymbol{\epsilon}_{xz}(\boldsymbol{\epsilon}_{zz})^{-1}\boldsymbol{\epsilon}_{zy} - (k_0)^{-1}\mathbf{V}_y(\boldsymbol{\mu}_{zz})^{-1}\mathbf{U}_x, \quad (25)$$

$$\mathbf{F}_{43} = -i\boldsymbol{\epsilon}_{xz}(\boldsymbol{\epsilon}_{zz})^{-1}\mathbf{V}_y + i\mathbf{V}_y(\boldsymbol{\mu}_{zz})^{-1}\boldsymbol{\mu}_{zx}, \quad (26)$$

$$\mathbf{F}_{44} = i\boldsymbol{\epsilon}_{xz}(\boldsymbol{\epsilon}_{zz})^{-1}\mathbf{V}_x + i\mathbf{V}_y(\boldsymbol{\mu}_{zz})^{-1}\boldsymbol{\mu}_{zy}, \quad (27)$$

(12)-(27) are much more generalized equations than previously published works[1-3, 5], as previous works on transverse FDFD Yee's mesh based modesolvers can only handle arbitrarily anisotropic permittivity but not arbitrarily anisotropic permeability. Moreover this solver is also capable of handling anisotropic permittivity and permeability simultaneously which previous Yee's mesh based modesolvers have not addressed. The boundary conditions currently used assume zero field values outside the simulation window. It is worth pointing out here that future works based on this work will explore incorporation of modern boundary conditions such as surface impedance absorbing boundary conditions (SIABC) [7] and subgridding [8] for reducing the memory requirements for this solver.

Further it is also worth pointing out here that all programs for this work have been written in Python by making use of Python-scipy's (Version - 0.13.3) sparse linear algebra eigen value and eigen vector finder (which uses ARPACK library) with shift invert mode enabled. The wavelength (λ) used in channel waveguide simulations

is $1.3 \mu\text{m}$, while the wavelength used in the other two test cases is $1.55 \mu\text{m}$.

III. RESULTS AND COMPARISONS

For comparisons and benchmarking the first test structure [4], which has been used here is cross section of a YIG (Yttrium Iron Garnate) channel waveguide placed in air/vacuum with anisotropic rectangular core as shown in Fig. 1.

The anisotropic rectangular core of channel waveguide has height of 607.6 nm and is 800 nm wide. It has isotropic permeability but its relative permittivity tensor has five terms which are $-\epsilon_{xx}=\epsilon_{yy}=\epsilon_{zz} = 2.302^2$, $\epsilon_{xy} = i\Delta$ and $\epsilon_{yx} = -i\Delta$. The magnitude (Δ) of non-diagonal terms is 0.005 . The substrate has isotropic refractive index of $1.95(n_1)$ for this waveguide. For effective index calculation a simulation window of $3.2 \mu\text{m} \times 2.9 \mu\text{m}$ with discretization of 7.5 nm in both x and y directions has been used as opposed to $6.25 \text{ nm} \times 4.9 \text{ nm}$ discretization in [4] due to memory constraints but future works based on this work will handle this problem by utilizing advanced subgridding algorithms such as mentioned in [8]. The effective index of fundamental mode as given in [4] for the YIG channel waveguide is 2.0488 . The effective index of the same fundamental mode as calculated by Yee's mesh based solver described in this work is 2.0483 .

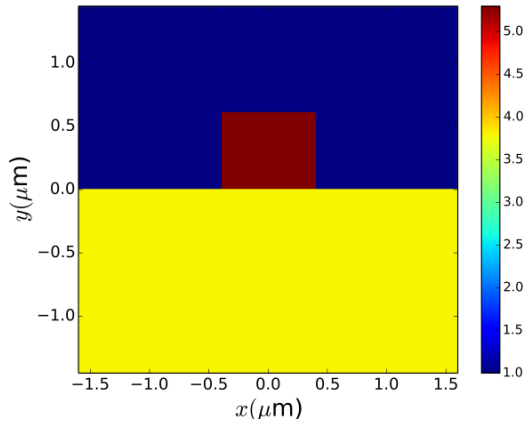


Fig. 1. Permittivity profile and structure of channel waveguide with anisotropic core (the central rectangular area).

The second test structure which has been used here for benchmarking is a rectangular waveguide with anisotropic core having a height of 180 nm and width of 300 nm . This waveguide is surrounded by an isotropic medium with relative permittivity equal to $2.0736(1.44^2)$ as shown in Fig. 2. This waveguide has both permittivity and permeability anisotropic simultaneously with $\mu_{xx} = \mu_{yy} = \mu_{zz} = 1.0$, $\mu_{xy} = i0.2$, $\mu_{yx} = -i0.2$ and $\epsilon_{xx} = \epsilon_{yy} = \epsilon_{zz} = 12.1104(3.48^2)$, $\epsilon_{xy} = i0.2$, $\epsilon_{yx} = -i0.2$,

rest of the terms in relative permittivity and relative permeability are zero.

The simulation window used in simulation of anisotropic rectangular waveguide of Fig. 2 with Yee's mesh based modesolver implemented for this work is $3 \mu\text{m} \times 3 \mu\text{m}$ with a discretization of 15 nm in both x and y directions. For benchmarking, commercial finite element based software [6] has been used, element size in the software has been set at 15 nm and the simulation window size has been kept at $3 \mu\text{m} \times 3 \mu\text{m}$. The effective index value of the fundamental mode as given by commercial software [6] is 1.7377 while its value given by solver implemented for this work in Python is 1.7415 .

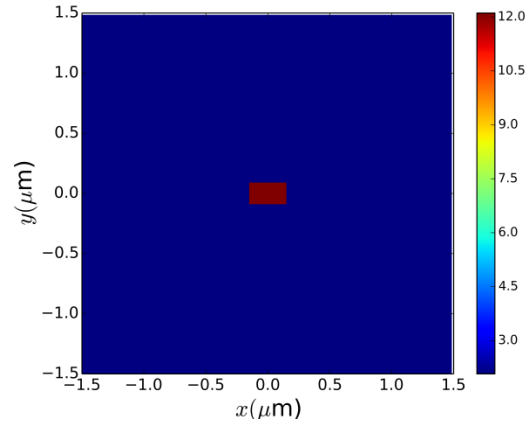


Fig. 2. Permittivity profile and structure of rectangular waveguide with anisotropic core (the central area).

The third test structure which has been used here for benchmarking is a square waveguide with anisotropic core having a height of 300 nm and width of 300 nm . This waveguide is also surrounded by an isotropic medium with relative permittivity equal to $2.0736(1.44^2)$ as shown in Fig. 3. This waveguide also has both permittivity and permeability anisotropic simultaneously with $\mu_{xx} = 1.5625(1.25^2)$, $\mu_{yy} = 1.44(1.2^2)$, $\mu_{zz} = 1.21(1.1^2)$, $\mu_{xy} = i0.3$, $\mu_{yx} = -i0.3$, $\mu_{xz} = 0.15$, $\mu_{zx} = 0.15$, $\mu_{zy} = -i0.25$, $\mu_{yz} = i0.25$ and $\epsilon_{xx} = 12.1104(3.48^2)$, $\epsilon_{yy} = 10.24(3.2^2)$, $\epsilon_{zz} = 9.0(3.0^2)$, $\epsilon_{xy} = i0.2$, $\epsilon_{yx} = -i0.2$, $\epsilon_{xz} = 0.1$, $\epsilon_{zx} = 0.1$, $\epsilon_{yz} = i0.1$, $\epsilon_{zy} = -i0.1$.

The simulation window used for Yee's mesh based simulation of the third structure with this solver as well as commercial software[6] is same as in the simulation of second test structure ($3 \mu\text{m} \times 3 \mu\text{m}$). The x and y discretizations for this solver as well as element size in commercial software [6] has been kept at 15 nm . The effective index value of the fundamental mode as given by commercial software [6] is 2.7980 , while its value as given by solver implemented for this work is 2.8124 . Its worth pointing out here that the values of terms in permittivity and permeability matrices in second and

third test cases above were chosen randomly for the purpose of comparison and benchmarking the waveguides with both permittivity and permeability anisotropic simultaneously. Table 1 sums up the benchmarking for this work.

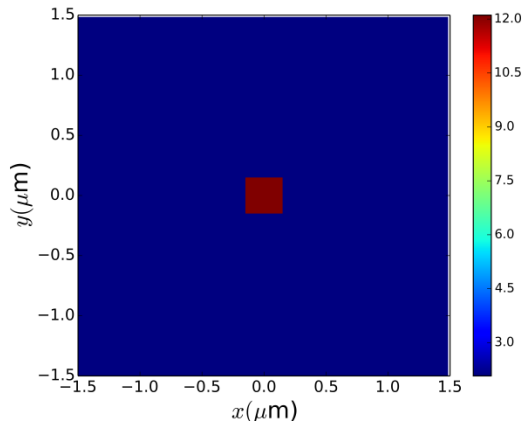


Fig. 3. Permittivity profile and structure of square waveguide with anisotropic core (the central area).

Table 1: Comparison of effective indexes of anisotropic waveguides taken from this work and other sources

Structure	n_{eff} (Other Sources)	n_{eff} (This Work)
Channel waveguide	2.0488 [4]	2.0483
Rectangular waveguide	1.7377 [6]	1.7415
Square waveguide	2.7980 [6]	2.8124

IV. CONCLUSION

In this work a transverse FDFD modesolver which can handle arbitrary permittivity as well as permeability simultaneously has been implemented in Python. Further waveguides with anisotropic core with both permittivity and permeability anisotropic simultaneously have also been analyzed which the previous works [1-5] on FDFD modesolver have not done. The capability to handle arbitrarily anisotropic permeability and permittivity simultaneously is unique and novel feature of this work. Future works based on this work will mainly focus on incorporating modern as well as advanced boundary conditions [7] and subgridding [8] algorithms in the

solver. Further combining this solver with modal expansion methods will also be explored in the future.

ACKNOWLEDGMENT

The author would like to thank Ministry of Human Resource Development (MHRD), Government of India, for funding this work.

REFERENCES

- [1] Z. Zhu and T. G. Brown, "Full-vectorial finite difference analysis of microstructured optical fibers," *Optics Express*, vol. 10, no. 17, pp. 853-864, August 2002.
- [2] C.-P. Yu and H.-C. Chang, "Yee's-mesh-based finite difference eigenmode solver with PML absorbing boundary conditions for optical waveguides and photonic crystal fibers," *Optics Express*, vol. 12, no. 25, pp. 6165-6177, December 2004.
- [3] M.-Y. Chen, S.-M. Hsu, and H.-C. Chang, "A finite-difference frequency domain method for full vectorial mode solutions of anisotropic optical waveguides with an arbitrary permittivity tensor," *Optics Express*, vol. 17, no. 8, pp. 5965-5979, April 2009.
- [4] A. B. Fallahkhair, K. S. Li, and T. E. Murphy, "Vector finite-difference modesolver for anisotropic dielectric waveguides," *Journal of Light-wave Technology*, vol. 26, no. 11, pp. 1423-1431, June 2008.
- [5] V. Singh, "A Yee's mesh based modesolver for anisotropic waveguides," *2016 IEEE/ACES International Conference on Wireless Information Technology and Systems (ICWITS) and Applied Computational Electromagnetics (ACES)*, pp. 1-2, March 2016.
- [6] <https://www.comsol.co.in/wave-optics-module>
- [7] Y. Mao, A. Z. Elsherbeni, S. Li, and T. Jiang, "Surface impedance absorbing boundary terminating FDTD simulations," *Applied Computational Electromagnetics Society Journal*, vol. 29, no. 12, pp. 1035-1046, December 2014.
- [8] G. Kim, E. Arvas, V. Demir, and A. Z. Elsherbeni, "A novel nonuniform subgridding scheme for FDTD using an optimal interpolation technique," *Progress in Electromagnetics Research*, vol. 44, pp. 137-161, September 2012.

Broadband Permittivity and Permeability Extraction of Ferrite Cores up to the GHz Range via Measurements and Simulations

Christian Reinhold^{1,2}, Peter Scholz¹, and Ulrich Jumar²

¹ Phoenix Contact Electronics GmbH
Dringenauer Str. 30, 31812 Bad Pyrmont, Germany
{creinhold,pscholz}@phoenixcontact.com

² ifak Magdeburg e.V.
Werner-Heisenberg-Straße 1, 39106 Magdeburg, Germany
ulrich.jumar@ifak.eu

Abstract — In this contribution a method is presented which allows for the characterization of the magnetic (μ' - $j\mu''$) as well as the dielectric (ϵ' - $j\epsilon''$) properties of ferrites in a broad frequency band (kHz to GHz). In order to determine the material properties at certain frequencies, the simulation model parameters of a particular test setup are tuned via optimization such that the simulated response of a sample to an electromagnetic excitation matches to the measured one. A loop and parallel plate setup support a low frequency parameter extraction of the sample while a coplanar line is used for high frequencies. The extracted material properties are fitted by a broadband causal fit in order to obtain a material model for the whole frequency range. The presented method is verified for a setup with a coil and a ferrite core. The results show that dielectric properties of the ferrite core cannot be neglected for microwave frequencies.

Index Terms — Broadband model, EM-simulation, ferrites, material characterization, wireless power.

I. INTRODUCTION

Wireless power transfer applications are emerging in the recent past. In many applications, additional to the power transmission data has to be transferred at the same time [1]. Moreover, often the power coils and data antennas have to be placed in close proximity to each other.

When designing and optimizing such a system containing closely coupled antennas and coils, numerical field simulation techniques are applied widely. For accurate simulation results, a good knowledge of the geometry and the material properties of the components are mandatory in the whole frequency range spanned by the power and data transmission links. The magnetic behavior in the GHz range as well as the dielectric material properties (i.e., the complex permittivity) in the

whole frequency range of the used ferrite cores are totally unknown in most cases.

In order to overcome this lack of information, we present an approach which allows for the determination of the complex permeability and the complex permittivity over a broad frequency range (kHz to GHz) for material samples composed of ferrite. In contrast to existing measurement techniques [2-4], the method proposed in this work does not demand for a special preparation or machining of the investigated core sample as long as a closed high permeable path and partially flat and parallel surfaces can be ensured. Examples of feasible samples are a ferrite plate with an arbitrary hole and a pot core investigated in this work.

In Section II, the determination of the material parameters at low frequencies up to a few MHz is focused on. Section III details the extraction of the material parameters at higher frequencies. In order to obtain a material model being feasible for both LF and HF simulations, in Section IV a broadband causal fit is introduced. The determined material parameters are validated in Section V with a typical test structure.

II. LF-PARAMETER EXTRACTION

In order to extract the electromagnetic material properties of simple sample geometries like toroidal cores or brick shaped samples, analytical methods are available [4, 5], which allow for directly computing the material properties from measurement data. Here, measurement equipment with special probe adapters is required. However, for arbitrary geometries, a more general determination procedure is of interest. For this purpose, in this section a material parameter extraction method for low frequency (LF) is described which is based on a comparison between measured and simulated data. LF measurements can be carried out with either impedance analyzers or network analyzers being suited for kHz and MHz frequencies. The procedure is detailed

with a ferrite pot core [6] with the material “N48” [7] as the material under test (MUT).

As presented in Fig. 1, two measurement setups are used in order to determine the complex permeability $\underline{\mu} = \mu_0(\mu_r' - j\mu_r'')$ and the complex permittivity $\underline{\varepsilon} = \varepsilon_0(\varepsilon_r' - j\varepsilon_r'')$ with μ_0 being the vacuum permeability and ε_0 the vacuum permittivity, respectively. The following iterative procedure similar to [8] was developed which enables the material parameter determination of samples with arbitrary shapes.

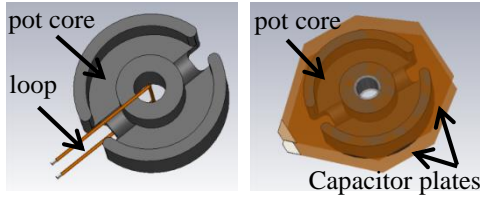


Fig. 1. Model of the LF measurement setups, left: loop setup for determining R and L ; right: parallel plate setup for determining G and C .

Initially, the magnetic and electric material parameters are guesses. A frequency f_i is selected from a given vector containing M frequencies at which the material parameters are sought. The series inductance L and resistance R of a loop enclosing the MUT as shown in Fig. 1 are computed at the selected frequency by using the finite element method simulation tool CST Microwave Studio. The simulation model contains 24.4k and 100k tetrahedron mesh cells for the inductive and capacitive setup respectively utilizing third order basis functions. Comparing the measured and computed impedances, a goal function can be determined:

$$\Delta = \left| \frac{\Delta A_S - \Delta A_M}{\Delta A_M} \right| + \left| \frac{\Delta B_S - \Delta B_M}{\Delta B_M} \right|. \quad (1)$$

In the above equation ΔA_S and ΔB_S represent the simulated series resistance and inductance change of the loop with respect to the setup without the MUT, whereas ΔA_M and ΔB_M are the measured counterparts.

In order to minimize (1) a trust region optimization alters the material parameters. If the goal function is lower than a predefined boundary, the optimization loop is aborted. The electric parameters are extracted in a similar way from the parallel plate setup. Equivalently to above, the goal function (1) is computed in this case with ΔA_M and ΔB_M representing the simulated change of the conductance and capacitance of the parallel plated setup respectively when the MUT is inserted into the parallel plate setup, and ΔA_M as well as ΔB_M are the measured quantities. As the permittivity of the MUT might influence the loop impedance, the magnetic parameters are optimized again with the found dielectric parameters. The whole procedure is repeated N times. In our

investigation three iterations proved feasible.

If for all given frequencies the material parameters are determined the task is finished. The material parameters of the previous frequency samples are used as starting values for optimizations at the next frequency. The number of simulations involved in the optimization can be reduced by this if the material parameters do not change significantly at two adjacent elements of the frequency vector. In [8] a sketch of a similar optimization sequence can be found.

It should be mentioned that the presented method can be applied to many other ferrite sample geometries like U-cores [8], E-cores, disks, and alike.

III. HF-PARAMETER EXTRACTION

In this section, the extraction method of the material parameters at high frequencies (HF) is focused on since the previous setups (closed loop and parallel plate capacitor) are motivated by mainly independent responses of the setups to magnetic and dielectric properties of the MUT which is no longer valid at high frequencies. Here, all electromagnetic properties must be taken into account simultaneously. For this reason, analog to [9] the MUT is placed on top of a coplanar transmission line and the two port scattering parameters are measured over a broad frequency range.

In a similar way as in the previous section simulations and measurements are compared in order to determine the material parameters. However, as presented in Fig. 2, in this case one single measurement and simulation setup is used in order to determine all four material parameters. Here, the FEM model consists of 41k mesh cells using third order basis functions.

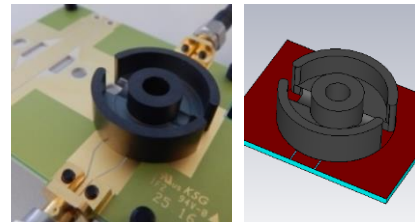


Fig. 2. Ferrite pot core on top of a transmission line, left: measurement setup; right: simulation model.

The complex scattering parameters of the coplanar line with the MUT are first measured and repeatedly simulated afterwards. As the structure is symmetric $\underline{S}_{11} = \underline{S}_{22}$ and reciprocal $\underline{S}_{12} = \underline{S}_{21}$ it is sufficient to consider only two of the four scattering parameters. A goal function is defined as:

$$\Delta_S = \left| \frac{\underline{S}_{11,S} - \underline{S}_{11,M}}{\underline{S}_{11,M}} \right| + \left| \frac{\underline{S}_{12,S} - \underline{S}_{12,M}}{\underline{S}_{12,M}} \right|. \quad (2)$$

In order to minimize the goal function (2) the complex permittivity and the complex permeability

are perturbed at the same time for each frequency $\{f_1, f_2, \dots, f_M\}$ given by the frequency vector. Again, a trust region optimization is applied for the minimization task. The influence of the connectors as well as the tapering section of the transmission line is removed as suggested in [10] by application of a through-reflect-line calibration.

In Fig. 3 it can be seen that the permeability curve gained with the HF-extraction technique in the range from 70 MHz to 100 MHz is in good agreement with the LF-extraction results. For lower frequencies the LF data with the closed magnetic path provide the most accurate results. Here, the extracted HF material parameters diverge due to a low sensitivity of the coplanar line setup at low frequencies. The relative permeability approaches the properties of vacuum at frequencies in the GHz range.

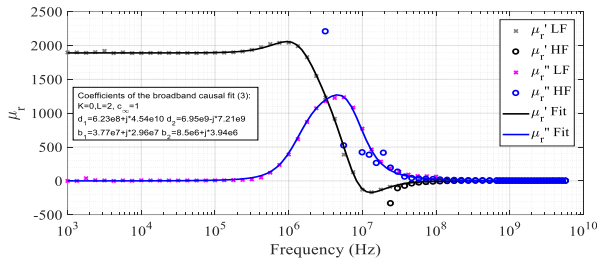


Fig. 3. Extracted relative permeability of the pot core from the LF-extraction (x markers), the HF-extraction method (circles) and the broadband causal model response (solid lines).

In Fig. 4 a steep drop in the real part of the relative permittivity gained from the LF approach is not present in the HF-data. Both, the real and the imaginary parts show material properties significant different from those of vacuum in the whole frequency range.

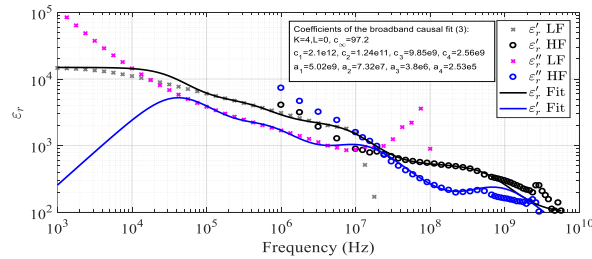


Fig. 4. Extracted relative permittivity of the pot core from the LF-extraction using Fig. 3 marker and line definitions.

IV. BROADBAND CAUSAL MODEL

Until now, two different approaches (LF and HF) with three different test scenarios (loop, capacitor, transmission line) have been set up in order to determine

the material properties of the MUT at certain individual frequency samples. However, for numerical field simulation in time domain like the FDTD method and transient models derived from field simulation data (e.g., SPICE models), a causal response of the material data [11] is important. Such a model is advantageous also for simulations in the frequency domain as it guarantees a smooth behavior across the frequency spectrum.

From the vector fitting technique it is known that any linear time invariant system response can be approximated by poles and residues of a rational function [12] which is causal by definition. Therefore in order to describe the material parameters with a causal model it is necessary to find the poles a_p , residues c_∞ , c_p and the complex conjugated pairs b_q, b_q^* and d_q, d_q^* giving the complex frequency response:

$$\{\underline{\mu}, \underline{\varepsilon}\} = c_\infty + \sum_{p=1}^K \frac{c_p}{a_p + j\omega} + \sum_{q=1}^L \left(\frac{d_q}{b_q + j\omega} + \frac{d_q^*}{b_q^* + j\omega} \right). \quad (3)$$

In (3), K represents the order of single poles and residues and L represents the complex conjugated order of the model. In Fig. 3 and Fig. 4 the determined parameters of the model of the investigated pot core model as well as the frequency response are displayed.

V. VALIDATION

In order to validate the determined material model for the MUT, a loop was designed. The loop is a preferable structure for wireless power and data transmission as it provides a rotation invariant coupling between a transmitter and a receiver. The loop structure realized on a printed circuit board (PCB) is inserted into the core as depicted in Fig. 5 and the impedance of the loop is measured in a broad frequency range via a network analyzer.

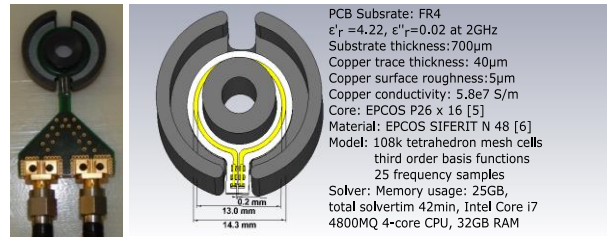


Fig. 5. Photo and model of the test loop antenna.

To determine the loop impedance, as shown in Fig. 5 the scattering parameters at the two coaxial terminals are measured. The impedance is computed from the differential scattering parameters which are gained from the nodal scattering parameters via:

$$\underline{S}_{dd} = 0.5(\underline{S}_{11} - \underline{S}_{21} - \underline{S}_{12} + \underline{S}_{22}). \quad (4)$$

The influence of the connectors as well as the feeding structure is removed with a differential open-short-load calibration.

In Fig. 6 and Fig. 7 it can be seen that measurement and simulation of the loop resistance as well as the loop inductance is in a good match when the causal model of the extracted material data is used. In the frequency range between 100 MHz and 1 GHz, a deviation between measurement and simulation with the extracted material data is visible which can be explained by an underestimated air gap in the HF-material parameter extraction [10] and an imperfect calibration of the loop. Nevertheless, the simulated loop impedance using the provided manufacturer data shows much larger deviations in the loop resistance as well as the loop inductance in the hole investigated frequency range showing that the permittivity of the ferrite core strongly influences the loop impedance in the whole investigated frequency range. Since no permittivity information is given by the manufacturer [7], $\epsilon_r = 1 - j0$ was assumed in this case.

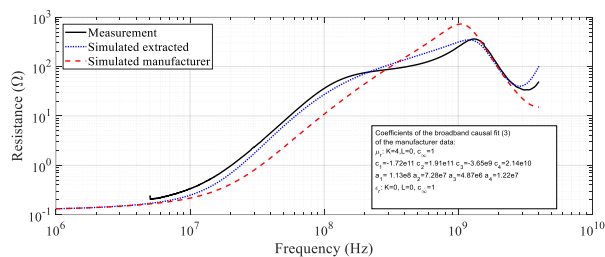


Fig. 6. Comparison of the loop resistance: Measured (solid line), simulated with causal fit of the extracted data (dotted line) and simulated with causal fit of the manufacturer provided data (dashed line).

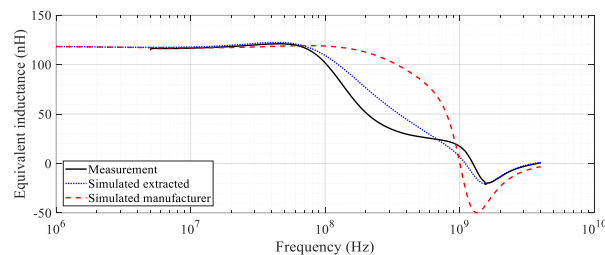


Fig. 7. Comparison of the loop inductance. The same line definitions as introduced in Fig. 6 are used.

VI. CONCLUSION

In this work a method was presented allowing for the broadband determination of the permeability and permittivity of ferrite cores typically applied in wireless power transfer systems. Two measurement setups for the low frequency parameter extraction as well as one setup for high frequency characterization were presented. A causal material model is described allowing for stable time domain simulations. The method is validated with a loop antenna inserted into the core showing a good agreement between the measurement and simulation

when the extracted material data is used. The ferrite core permittivity, in general not provided by the manufacturer, strongly influences the impedance of structures close to the investigated pot core.

REFERENCES

- [1] R. Trevisan and C. Alessandra, "A UHF near-field link for passive sensing in industrial wireless power transfer systems," *IEEE Trans. Microw. Theory Tech.*, vol. 64, no. 5, pp. 1634-1643, 2016.
- [2] V. Radonić, N. Blaž, and L. Živanov, "Measurement of complex permeability using short coaxial line reflection method," *Acta Phys.*, pol. A, vol. 117, no. 4, pp. 820-824, 2010.
- [3] J. Xu, et al., "Measurement of electromagnetic parameters and FDTD modeling of ferrite cores," *2009 IEEE Int. Symp. on Electromagn. Compat.*, pp. 83-88, 2009.
- [4] J. Baker-Jarvis, et al., "Measuring the permittivity and permeability of lossy materials: Solids, liquids, metals, building materials, and negative-index materials," *NIST Technical Note, National Institute of Standards and Technology*, 2005.
- [5] Agilent Technologies Inc., "Solutions for measuring permittivity and permeability with LCR meters and impedance analyzers," Application Note, Agilent Literature Number 5980-2862EN, 2014.
- [6] EPCOS AG, "Ferrites and accessories, P 26 x 16," 2015. <https://en.tdk.eu/tdk-en>
- [7] EPCOS AG, "Ferrites and accessories, SIFERIT material N48," 2015. <https://en.tdk.eu/tdk-en>
- [8] C. Reinhold, P. Scholz, and U. Jumar, "Electromagnetic material parameter extraction of ferrites up to the GHz range via measurements and simulations," *Applied Comp. Electromagn. Soc. (ACES) Symp., 2017 Int. IEEE*, Italy, 2017.
- [9] M. D. Deshpande, et al., "A new approach to estimate complex permittivity of dielectric materials at microwave frequencies using waveguide measurements," *IEEE Trans. Microw. Theory Tech.*, vol. 45, no. 3, pp. 359-366, 1997.
- [10] V. Shemelin and N. Valles, "Improved accuracy of measurements of complex permittivity and permeability using transmission lines," *Nuclear Instruments and Methods in Physics Research Section A*, 767, pp. 385-396, 2014.
- [11] M. Y. Koledintseva, et al., "Restoration of the Lorentzian and Debye curves of dielectrics and magnetics for FDTD modeling," *Int. Symp. 5th Electromagn. Compat.*, Europe, pp. 687-692, 2002.
- [12] K. P. Prokopoulos, et al., "Improved propagation modeling in ultra-wideband indoor communication systems utilizing vector fitting technique of the dielectric properties of building materials," *27th Annual Int. Symp. on Personal, Indoor, and Mobile Radio Comm. (PIMRC), IEEE*, pp. 1327-1332, 2016.

An HSS-Matrix-Based Fast Direct Solver with Randomized Algorithm

Weikang Yu, Hu Yang, Shengguo Li, and Yanlin Xu

College of Electronic Science and Engineering
National University of Defense Technology, Changsha, 410073, China
769280669@qq.com, yanghu90@163.com, shengguols@126.com, 13298656824@163.com

Abstract — Discretization of the electric field integral equation (EFIE) generally leads to dense impedance matrix. The resulting matrix, however, can be compressed in sparsity based on hierarchical structure and low rank approximation. In this paper, we propose an HSS-matrix-based fast direct solver for surface integral equation (SIE) that has a compression complexity of $O(rN^2)$ to analysis the large-scale electromagnetic problems, where r is a modest integer. The proposed solver efficiently compresses the dense matrices using a randomized algorithm and requires modest memory. Efficiency and accuracy is validated by numerical simulations. In addition, being an algebraic method, the HSS-matrix-based fast solver employs Green's kernels and hence is suitable for other integral equations in electromagnetism.

Index Terms — Electric field integral equation, HSS matrix, randomized algorithm.

I. INTRODUCTION

Method of Moment (MoM) is a powerful numerical method to obtain the electromagnetic characteristics based on the solution of integral equation (IE) on the surface of the object [1]. The discretization process usually generates dense impedance matrices with memory requirement of $O(N^2)$ and operation complexity of $O(N^3)$, where N represents the matrix size. In contrast, iterative methods often win the favor in many engineering applications with time complexity of $O(N_{iter}N^2)$, where N_{iter} is the number of iterations. Fast iterative algorithms, e.g., CG, GMRES and BiCGStab, generally being based on a Krylov subspace, take advantage of the rapid matrix-vector multiplication. The typical one is the multilevel fast multi-pole algorithm (MLFMA) which reduces the complexity to $O(N \log N)$ [2].

However, fast direct solvers have been rapidly developing in the recent years, and before proceeding any further, we would like to point out some relevant features of the direct methods. One of the most important advantages of the direct solver is that it works well with multiple right hand sides, which means once the matrix is efficiently compressed all right hand

sides can be considered with low computational cost [3]. Therefore, fast direct solvers offer great advantage especially in solving monostatic scattering problems. Besides, the direct method is robust while the iterative method is highly sensitive to the condition of the matrix itself. Finding a good preconditioner is difficult and imperative to avoid ill-conditioning.

In this paper, we introduce the rank-structured matrix to deal with the dense equation arising in MoM [4]. These theories all rely on the property that the off-diagonal blocks have low-rank properties and thus can be well-approximated. Such matrices are termed hierarchical matrices, which include H-matrix [5], H2-matrix [6], Hierarchically Semi-separable (HSS) [7,8], SSS [9], and so on. In some engineering applications, the given matrices are often rank-deficient or nearly so, which can be divided into a hierarchical structure and then compressed exactly or approximately using SVD or rank-revealing QR factorization. Due to this special structure, those dense matrices can be described as data sparse. The HSS method in this paper was first introduced by Chandrasekaran, Gu, Pals and others. Compare with earlier H-matrix, it develops a recursive relation between the generators appearing at different levels of recursions [6].

From a mathematical point of view, existing low-rank compression algorithm based on IE methods, although their exact methods could be different, utilizes the low-rank properties inherently in the impedance matrix [10]. HSS matrix-based solvers for Volume Integral Equation (VIE) and Surface Integral Equation (SIE) have been proposed in [11, 12]. In this work, we develop a new HSS-matrix-based fast direct solver based on randomized sampling algorithm. To be specific, ULV factorization method and Interpolative Decomposition (ID) method are adopted in this work which have not been seen in the existing literature [7]. Major advantages of this method are that the whole impedance matrix does not need to be explicitly formed and only requires the access to selected elements. Besides, a space grouping method for basis functions is also proposed to improve the low-rank properties of impedance matrices.

II. HSS MATRIX THEORY

Consider the electric field integral equation (EFIE):

$$n \times ik\eta \iint_S \left(\mathbf{J}(\mathbf{r}') g(\mathbf{r}, \mathbf{r}') + \frac{1}{k^2} \nabla' \cdot \mathbf{J}(\mathbf{r}') \nabla g(\mathbf{r}, \mathbf{r}') \right) dS' = n \times \mathbf{E}^{inc}, \quad (1)$$

in which $g(\mathbf{r}, \mathbf{r}') = \frac{e^{-jk|\mathbf{r}-\mathbf{r}'|}}{|\mathbf{r}-\mathbf{r}'|}$ represents Green's function

for free space. The Equation (1) can be compactly written as:

$$n \times L(J) = n \times \mathbf{E}^{inc}(\mathbf{r}), \quad r \in S, \quad (2)$$

where L represents a linear operator, J is the induced surface current density, and \mathbf{E}^{inc} is the imposed electric field. Discretizing J with a series of RWG (Rao-Wilton-Gilsson) basis functions results in the following linear system of equations:

$$Z\mathbf{I} = \mathbf{V}. \quad (3)$$

Here, we introduce the HSS matrix to show how to represent the matrix Z in data-sparse-form and underline the numbering rules of the RWG functions.

An HSS representation of matrix Z relies on a recursive clustering of the index set $I = \{1, \dots, n\}$. This partitioning is represented by a tree T , and there is no restriction on the shape of the tree, and usually a binary tree is used. Each node v of the tree is associated with a subset I_v of I . The subset associated with the root node is $I = \{1, \dots, n\}$, and for non-leaf node v with left child v_1 and right child v_2 :

$$I_\tau = I_{v_1} \cup I_{v_2}, \dots, I_{v_1} \cap I_{v_2} = \emptyset, \quad (4)$$

and $\bigcup_{v \in LN} I_v = I$ where LN denotes the set of all leaf nodes. We further assume T is postordered, i.e., the nodes are ordered so that a non-leaf node v satisfies $v_1 < v_2 < v$, as done in [13, 14]. Furthermore, for each node v , let I_v^L be the set of all indices less than those in I_v and I_v^R be the set of all indices greater than those in I_v . Thus, $I = I_v^L \cup I_v \cup I_v^R$ for each node v . Figure 1 illustrates these sets.

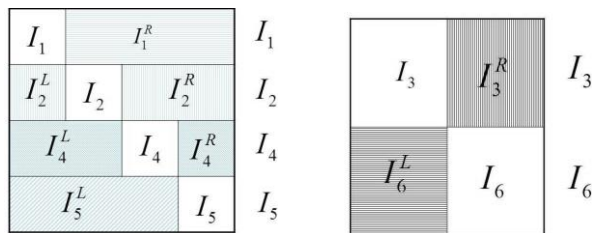


Fig. 1. Matrix partition and the corresponding index sets.

For each node v in T , there are matrices $D_v^{big}, U_v^{big}, V_v^{big}$ and Σ_v associated with it, called *generators*, such that:

$$D_v^{big} = Z(I_v, I_v) = \begin{bmatrix} D_{v_1}^{big} & U_{v_1}^{big} \Sigma_{v_1} (V_{v_2}^{big})^T \\ U_{v_2}^{big} \Sigma_{v_2} (V_{v_1}^{big})^T & D_{v_2}^{big} \end{bmatrix}, \quad (5)$$

$$U_v^{big} = \begin{bmatrix} U_{v_1}^{big} \\ U_{v_2}^{big} \end{bmatrix}, V_v^{big} = \begin{bmatrix} V_{v_1}^{big} \\ V_{v_2}^{big} \end{bmatrix}. \quad (6)$$

For a leaf node v , $D_v^{big} = Z_v, U_v^{big} = U_v, V_v^{big} = V_v$. Only the generators D_v, U_v, V_v and Σ_v are stored and the $(\bullet)^{big}$ matrices can be constructed recursively when needed. Z a 4×4 HSS matrix can be written as:

$$Z = \begin{bmatrix} \begin{bmatrix} Z_1 & U_1 \Sigma_1 V_2^T \\ U_2 \Sigma_2 V_1^T & Z_2 \end{bmatrix} & U_3^{big} \Sigma_3 (V_6^{big})^T \\ U_6^{big} \Sigma_6 (V_3^{big})^T & \begin{bmatrix} Z_4 & U_4 \Sigma_4 V_5^T \\ U_5 \Sigma_5 V_4^T & Z_5 \end{bmatrix} \end{bmatrix}. \quad (7)$$

There is a recursive relation between the generators appearing at different levels of recursion which is the essential difference between HSS and H^2 -matrix with other classes of H-matrix. The Equation (6) shows how the generators at different levels are nested.

In practice, the low-rank off-diagonal blocks arise because the associated Green's function is smooth with source point and field point fast decay away from the diagonal [14]. Thus, the order of the rows and columns of matrix Z matters. If Z is shuffled randomly [15], the low-rank property could be lost or not exactly. Therefore, it is necessary to renumber the RWG functions before the generation of the impedance matrix based on SIE. Referring to the idea in MLFMA, the RWG functions on the surface of the PEC model are divided into several groups as is shown in Fig. 2. The lowest cube unit contains the information of the number of RWGs, and it can find father cube according to tree structure. Once the new order of the RWGs is determined, we can use the traditional MoM method to generate the linear system.

III. GENERATION OF THE HSS MATRIX

In this section, we introduce the main step in the construction of HSS matrix and give the analysis of time complexity for each step. We are not going to introduce it in detail since all the mathematic details of theory can be found in [16].

Compression: the HSS compression method is based on the randomized sampling algorithm introduced by Martinsson and the major component is the Interpolative Decomposition (ID) [17]. The complexity of the compression operation is $O(rN^2)$ based on classical matrix-vector product, and r is the maximum rank found during the compression. The consequence of the algorithm is to construct the hierarchy form and special structure for generators U and V . One notable feature is that the original matrix could not be exact and only requires some selected elements and fast matrix-vector

product routine. Therefore, if fast multipole method (FMM) is used, the complexity can drop to $O(r^2N)$. We introduce the threshold ε which controls the size of generators and thus influence the memory-consuming in HSS representation, at the price of accuracy.

ULV factorization: in this factorization, orthogonal transformations are used to transform the problem of eliminating $O(r)$ unknowns [7]. These remaining unknowns are eliminated using a standard LU factorization. The complexity is $O(r^2N)$.

Solution: after ULV factorization, a linear system $ZI = V$ is solved using triangular solution, which involves two processes: forward elimination and backward substitution. The complexity is $O(rN)$. Furthermore, the accuracy of the solution can be improved by efficient iterative refinement (IR) method [16], which takes advantage of the fast matrix-vector product based on the HSS-matrix representation.

IV. NUMERICAL RESULTS

In this work, we illustrate the performance of the HSS-matrix-based solver in accelerating the direct solution of the EIEF-based analysis of electromagnetic problems. We validated the proposed solver on a conducting sphere ($r=1\text{m}$) grouped in three levels.

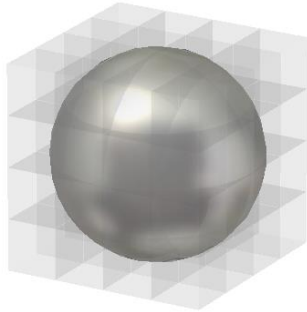


Fig. 2. Conducting sphere using space grouping.

Then the spherical surface was discretized into different number of RWGs by changing the frequency of incident wave. The matrix is built on complete binary trees with compression threshold $\varepsilon = 10^{-4}$ and iterative refinement in 5 times. We report time complexity for the HSS compression, the ULV factorization and the triangular solution. We tested the accuracy of the HSS-

matrix representation by $err = \frac{\|Z * I - V\|_F}{\|V\|_F}$, where “ $\|\bullet\|_F$ ”

denotes the Frobenius norm and compare with the run time for solving a system with direct solver in Armadillo. The results are reported in Table 1. We observe from the table that the efficiency improves significantly based on HSS compared with the traditional solver in Armadillo. The compression and ULV factorization occupy the major time and iterative refinement time increases as complexity in matrix product increases.

Thereby, balance must be found between the accuracy and the number of iterations.

Table 1: Time consumption in HSS-matrix based solver and in Armadillo

Unknowns	Compression (s)	ULV (s)	Solution +IR(s)	Total (s)	Armadillo (s)
2421	2.1	0.9	0.6	3.6	5.44
3624	9.3	1.8	0.7	11.8	20.3
4212	15.6	2.9	1.6	20.1	29.6
5808	23.8	5.7	2.8	32.3	78.8
6072	27.8	5.7	3.2	37.7	97.3
6612	29.9	5.9	3.7	39.6	124.5
7272	35.4	8.8	4.2	48.4	168.0

Next, we test the accuracy of HSS-based solver in each iterative refinement step as is shown in Fig. 3. The example also considers a conducting sphere illuminated by a normally incident plane wave. The sphere is discretized into 5808 unknowns. The compression threshold ε equals 10^{-4} and the max iteration is 9 times. Clearly good accuracy is obtained at the expense of matrix-vector product time. More importantly, the matrix-vector product process based on HSS matrix construction is more efficient than direct matrix-vector product.

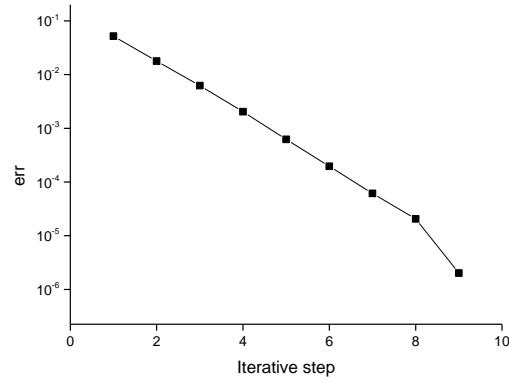


Fig. 3. HSS solution error in iterative refinement step.

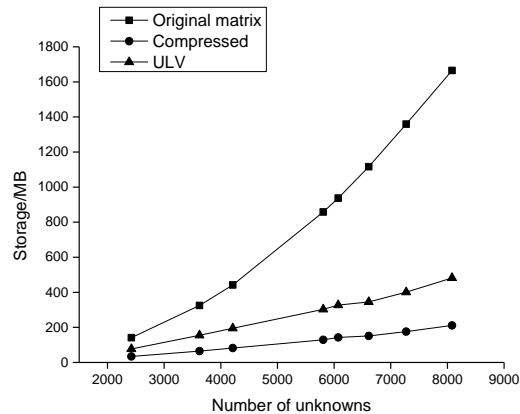


Fig. 4. Memory requirement for original matrix, compressed matrix and ULV factors.

In terms of memory, ignoring small temporary storage and communication buffers, the memory footprint for matrix Z in Armadillo is simply the storage of the matrix Z . In our new code, the matrix Z can be compressed in form of HSS binary tree together with ULV factors. In Fig. 4, the storage requirement in MB of the HSS-matrix-based solver was plotted with respect to the number of unknowns, from which the memory advantage of HSS structure can be clearly observed.

V. CONCLUSION

Integral-equation-based methods generally lead to dense systems of linear equation. In this paper, we introduce HSS matrix as a general algebraic framework to accelerate the solution of electromagnetic problem based on SIE and point out the importance of grouping the basic functions. Randomized sampling algorithm is introduced in compression process and the matrix in HSS form is factorized using classical ULV method. Numerical simulations have demonstrated the efficiency and accuracy of the HSS-matrix-based solver. We illustrate the memory cost before and after HSS compression and show the advantage in memory consumption. The HSS-matrix-based solver is also helpful in analyzing the field in actual radar systems because the characteristic of the impedance matrix will not change in radiation problem [18]. The randomized sampling algorithm in HSS is free of exact original matrix and high efficiency could be achieved with fast matrix-vector product, which is our future research topic.

ACKNOWLEDGMENTS

This work was supported by the Chinese National Science Foundation through Grant No. 11401580.

REFERENCES

- [1] R. F. Harrington, *Field Computation by Moment Methods*. New York: Macmillan, 1968.
- [2] R. Coifman, V. Rokhlin, and S. Wandzura, "The fast multipole method for the wave equation: A pedestrian prescription," *IEEE Antennas Propag. Mag.*, vol. 35, no. 3, pp. 7-12, June 1993.
- [3] S. Ambikasaran and E. Darve, "An $O(N \log N)$ fast direct solver for partial hierarchically semi-separable matrices," *Journal of Scientific Computing*, vol. 57, no. 3, pp. 477-501, 2013.
- [4] J. Xia, S. Chandrasekaran, M. Gu, et al., "Fast algorithms for hierarchically semiseparable matrices," *Numerical Linear Algebra with Applications*, vol. 17, no. 6, pp. 953-976, 2010.
- [5] W. Hackbusch, "A sparse matrix arithmetic based on H-matrix," *Computing*, vol. 62, no. 2, pp. 89-108, 1999.
- [6] W. Hackbusch, "Data-sparse approximation by adaptive H2-matrices," *Computing*, vol. 69, pp. 1-35, 2002.
- [7] S. Chandrasekaran, M. Gu, and T. Pals, "A fast ULV decomposition solver for hierarchically semi-separable representations," *Siam Journal on Matrix Analysis & Applications*, vol. 28, no. 3, pp. 603-622, 2006.
- [8] S. Chandrasekaran, M. Gu, and T. Pals, "Fast and stable algorithms for hierarchically semi-separable representations," *Technical Report, University of California: Berkeley, CA*, 2004.
- [9] S. Chandrasekaran, P. Dewilde, M. Gu, T. Pals, X. Sun, AJ van der Veen, and D. White, "Some fast algorithms for sequentially semiseparable representation," *SIAM Journal on Matrix Analysis and Applications*, vol. 27, pp. 341-364, 2005.
- [10] W. Chai and D. Jiao, "Fast-matrix-based direct integral equation solver with reduced computational cost for large-scale interconnect extraction," *IEEE Transactions on Components Packaging & Manufacturing Technology*, vol. 3, no. 2, pp. 289-298, 2013.
- [11] M. Ma and D. Jiao, "Exact-arithmetic HSS-inversion algorithm for fast direct solution of electrically large volume integral equations," *International Conference on Electromagnetics in Advanced Applications, IEEE*, pp. 597-599, 2016.
- [12] A. Manic, A. Smull, F. H. Rouet, et al., "Efficient scalable parallel higher order direct MoM-SIE method with hierarchically semiseparable structures for 3D scattering," *IEEE Transactions on Antennas & Propagation*, pp. 99:1-1, 2017.
- [13] J. Xia and M. Gu, "Robust approximate Cholesky factorization of rank-structured symmetric positive definite matrices," *SIAM Journal on Matrix Analysis and Applications*, vol. 31, pp. 2899-2920, 2010.
- [14] S. Li, M. Gu, L. Cheng, X. Chi, and M. Sun, "An accelerated divide-and-conquer algorithm for the bidiagonal SVD problem," *SIAM Journal on Matrix Analysis and Applications*, vol. 35, pp. 1038-1057, 2014.
- [15] A. Napov and X. S. Li, "An algebraic multifrontal preconditioner that exploits the low-rank property," *Numerical Linear Algebra with Applications*, vol. 23, no. 1, pp. 61-82, 2016.
- [16] F. H. Rouet and X. S. Li, et al., "A distributed-memory package for dense hierarchically semi-separable matrix computations using Randomization," vol. 42, no. 4, p. 27, 2015.
- [17] P. G. Martinsson, "A fast randomized algorithm for computing a hierarchically semiseparable representation of a matrix," *Siam Journal on Matrix Analysis & Applications*, vol. 32, no. 4, pp. 1251-1274, 2011.
- [18] P. Rocca and A. F. Morabito, "Optimal synthesis of reconfigurable planar arrays with simplified architectures for monopulse radar applications," *IEEE Transactions on Antennas & Propagation*, vol. 63, no. 3, pp. 1048-1058, 2015.

A Compact CPW-Fed MIMO Antenna with Band-Notched Characteristic for UWB System

Li-Yan Chen, Jing-Song Hong, and Muhammad Amin

Institute of Applied Physics, School of Physical
University of Electronic Science and Technology of China, 610054 Chengdu, China
727683316@qq.com, cemlab@uestc.edu.cn, aminssphysics@hotmail.com

Abstract — A compact coplanar waveguide (CPW)-fed multiple-input-multiple-output (MIMO) band-notched antenna with a small size of $20 \times 36 \times 0.8 \text{ mm}^3$ for ultra-wideband (UWB) system is proposed in this paper. The two rectangular monopole (RM) elements fed by CPW are printed on the FR4 substrate. To improve impedance bandwidth and the isolation, a T-shaped stub structure is positioned in the middle of two RM elements. The band-notched characteristic is achieved by etching a U-shaped loop resonator slot on each RM element. The S_{11} reflection coefficients, S_{12} coupling isolation, radiation pattern, peak gain and radiation efficiency of the MIMO antenna are measured. The MIMO performance of the proposed MIMO antenna is analyzed and evaluated by the envelope correlation coefficient (ECC) and total active reflection coefficient (TARC).

Index Terms — Band-notched, CPW, ECC, MIMO, TARC, UWB.

I. INTRODUCTION

Since the Federal Communication Commission (FCC) assigned an unlicensed 3.1-10.6 GHz bandwidth, ultra-wideband (UWB) devices have been one of the most rapidly developing technologies in wireless applications due to its numerous blessings, including low power, high transmission rate, and so on [1-2]. The multipath fading in UWB system has been becoming more and more serious because of the low power limited by FCC. Multiple-input-multiple-output (MIMO) generation has incomparable advantages in improving the wireless link transmission capacity and reliability [3]. Therefore, combining MIMO technology with UWB technology is an efficient way to decrease multipath fading in UWB system [4]. However, there is a strong mutual coupling among two close radiating elements, which result in the loss of antenna bandwidth and radiating efficiency and make it difficult to design MIMO antenna in a compact dimension. Besides, the UWB overlaps with other wireless frequency bands, especially the wireless local area network (WLAN) frequency band at 5.15-5.85 GHz, which can cause some potential interference and noisy to

the UWB system. Thus, it is inevitable to reduce both the mutual coupling among UWB MIMO antenna and the electromagnetic interference caused by WLAN system with some simple and effective methods.

Researchers have proposed various MIMO antennas [5-10]. Using electromagnetic band-gap (EBG) structure [5], or a tree-shaped parasitic structure [6], or a T-shaped protruded ground stub [7] to minimize the mutual coupling between radiating elements, or a complementary splitting resonator (CSRR) etching on the antenna ground [8]. The MIMO antenna in [9] don't use any decoupling structure, the high isolation performance is achieved by the asymmetrical and complementary structures of the quasi-self-complementary antenna (QSCA). The antenna in [10] has the smallest dimension in those UWB MIMO antennas, etching a T-shaped slot at the antenna ground to enhance the impedance bandwidth and reduce the mutual coupling. However, the antenna in [5] is not suitable for UWB system due to their narrow operation band. The operation band of antennas in [6], [8], [9] and [10] is UWB level, but it can't avoid the noise and interference in WLAN band.

In this paper, a compact CPW-fed UWB MIMO antenna with WLAN band-notched characteristic is proposed. The size of the proposed antenna is $20 \times 36 \times 0.8 \text{ mm}^3$, which is smaller than those in [5-10]. This UWB MIMO antenna consists of two identical RMs fed by CPW. The distance between two RM elements is only 8 mm to make the MIMO antenna a small dimension. A T-shaped ground stub which is protruded at the middle of two RM elements acts as a reflector to achieve UWB characteristic and high isolation between two ports. In order to obtain the band-rejected characteristic at WLAN band, a U-shaped loop resonator slot (about half wavelength at 5.5 GHz) is etched on each RM. Measured results show that the designed antenna exhibits an impedance match with $S_{11} < -10 \text{ dB}$, high isolation better than 15 dB, peak gain varies 2.4 dBi to 4.4 dBi, radiation efficiency are more than 85%, $\text{ECC} < 0.02$ and $\text{TARC} < -30 \text{ dB}$ over the UWB band except for a notched band at 5-6 GHz. Compared to the previous UWB MIMO antennas in [5-10], proposed UWB MIMO antenna has

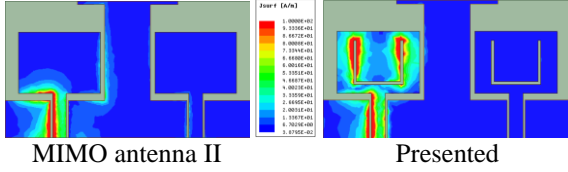


Fig. 5. Surface current distributions of the MIMO antenna II and the proposed MIMO antenna at 5.5 GHz.

III. MEASURED RESULTS

The prototype of the UWB MIMO antenna is shown in Fig. 6. The port 1 is measured and port 2 ceased with a 50 Ω load during the measurement.

A. S-parameters

The measured S-parameters tested with Agilent E5071C network analyzer are presented in Fig. 8. Some discrepancies can be seen between simulated and measured results, which is caused by the manufacture tolerance and SMA connector. Measured results show that the proposed MIMO antenna operates from about 2.9 GHz to 11 GHz with $S_{11} < -10$ dB and $S_{12} < -15$ dB except for a notched band from 5 GHz to 6 GHz.

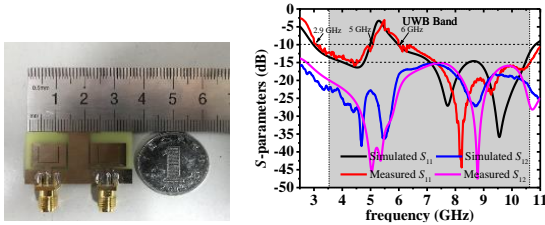


Fig. 6. The prototype and S-parameters of the UWB MIMO antenna

B. Radiation performance

Three frequency points (4 GHz, 7 GHz, 10 GHz) are selected to indicate the radiation pattern for low frequency, middle frequency, and high frequency in the UWB band, respectively. Figures 7 (a-d) illustrate the radiation pattern of UWB MIMO antenna at 4 GHz, 7 GHz, and 10 GHz. Besides, the peak gain and radiation efficiency cover the UWB range of the proposed MIMO antenna, when port 1 is measured are shown in Fig. 8. The peak gain varies from 2.4 dBi to 4.4 dBi and radiation efficiencies are higher than 85% over the UWB spectrum except for the notched band.

C. MIMO performance

The MIMO performance of the MIMO antenna is analyzed and figured out by the ECC and TARC. The value of ECC signifies how the two antennas are coupled to each other. For achieving good channel characteristics and antenna diversity, the ECC must be less than 0.05. The ECC between two elements can be calculated from

the S-parameters using the formula (2) when the radiation efficiency of the MIMO antenna is high [12]:

$$ECC = \frac{|S_{11}^* S_{12} + S_{21}^* S_{22}|^2}{(1 - |S_{11}|^2 - |S_{12}|^2)(1 - |S_{21}|^2 - |S_{22}|^2)} \quad (2)$$

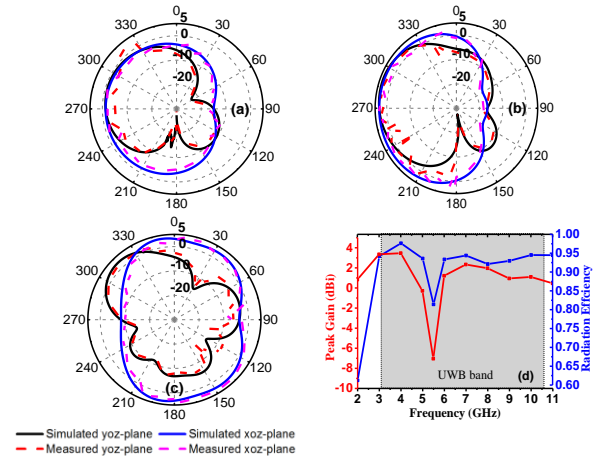


Fig. 7. Simulated and measured radiation pattern of UWB MIMO antenna at: (a) 4 GHz, (b) 7 GHz, (c) 10 GHz, and (d) measured peak gain and radiation efficiency of the proposed UWB MIMO antenna.

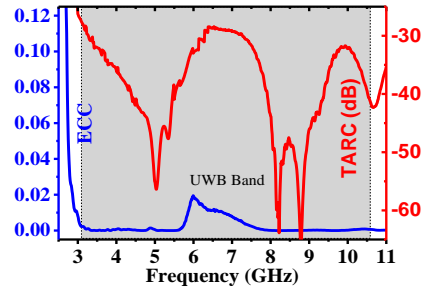


Fig. 8. Measured ECC and TARC of the proposed UWB MIMO antenna against frequency.

For MIMO antenna systems, traditional scattering matrixes are not sufficient to predict the real antenna performance. TARC which take coupling effect into account has been proposed. The TARC for the 2-port MIMO antenna could be described as [11]:

$$TARC = -\sqrt{\frac{(S_{11} + S_{12})^2 + (S_{21} + S_{22})^2}{2}} \quad (3)$$

As depicted in Fig. 8, the measured ECC is less than 0.02 and TARC is less than -30 dB for the UWB band.

IV. CONCLUSION

A compact CPW-fed UWB MIMO antenna with the band-notched characteristic in a small size of $20 \times 36 \times 0.8$ mm³ has been designed successfully. The available distance (0.19λ) between two RM elements is very small. A T-stub structure as a means to reduce mutual coupling between two RM elements of the MIMO antenna, and

a U-shaped loop resonator slot etching on each RM element to achieve a notching band at WLAN spectrum. In addition, the proposed scheme retains full planarity of the UWB MIMO antenna, involves simple and straightforward fabrication process. All the simulated, measured and calculated results indicate that the proposed UWB MIMO antenna is a good candidate for UWB system.

REFERENCES

- [1] Federal Communication Commission, "First report and order Revision of part 15 of the Commission's rules regarding ultra-wideband transmission system," FCC 02 48, 2002.
- [2] I. Oppermann, M. Hamalainen, and J. Iinatti, *UWB Theory and Applications*. New York: Wiley, ch. 1, pp. 3-4, 2004.
- [3] A. J. Paulraj, et al., "An overview of MIMO communications - A key to gigabit wireless," *Proceedings of the IEEE*, vol. 92, pp. 198-218, 2004.
- [4] T. Kaiser, F. Zheng, and E. Dimitrov, "An overview of ultrawide-band systems with MIMO," *Proceedings of the IEEE*, vol. 97, pp. 285-312, 2009.
- [5] Q. Li, A. P. Feresidis, M. Mavridou, and P. S. Hall, "Miniaturized double-layer EBG structures for broadband mutual coupling reduction between UWB monopoles," *IEEE Transactions on Antennas & Propagation*, vol. 63, no. 2, pp. 1168-1171, 2015.
- [6] S. Zhang, Z. Ying, J. Xiong, et al., "Ultra-wide-band MIMO/diversity antennas with a tree-like structure to enhance wideband isolation," *IEEE Antennas Wireless and Propagation Letters*, vol. 8, pp. 1279-1282, 2009.
- [7] L. Liu, S. W. Cheung, and T. I. Yuk, "Compact MIMO antenna for portable UWB applications with band-notched characteristic [J]," *IEEE Transactions on Antennas & Propagation*, vol. 63, no. 3, pp. 1917-1924, 2015.
- [8] M. S. Khan, et al., "A compact CSRR enabled UWB diversity antenna," *IEEE Antennas & Wireless Propagation Letters*, 2016.
- [9] X. L. Liu, Z. D. Wang, Y. Z. Yin, et al., "A compact ultra-wideband MIMO antenna using QSCA for high isolation [J]," *IEEE Antennas & Wireless Propagation Letters*, vol. 13, pp. 1497-1500, 2014.
- [10] C. M. Luo, J. S. Hong, and L. L. Zhong. "Isolation enhancement of a very compact UWB-MIMO slot antenna with two defected ground structures [J]," *IEEE Antennas & Wireless Propagation Letters*, vol. 14, pp. 1766-1769, 2015.
- [11] R. Chandel, A. K. Gautam, and K. Rambabu, "Tapered fed compact UWB MIMO-diversity antenna with dual band-notched characteristics," *IEEE Transactions on Antennas & Propagation*, vol. 1, no. 1, pp. 99-107, 2018.

- [12] S. Blanch, J. Romeu, and I. Corbella, "Exact representation of antenna system diversity performance from input parameter description," *Electron. Lett.*, vol. 39, no. 9, pp. 705-707, 2003.



Jing-song Hong received the B.Sc. degree in Electromagnetics from Lanzhou University, China, in 1991, and the M.Sc. and Ph.D. degrees in Electrical Engineering from the University of Electronic Science and Technology of China (UESTC), in 2000 and 2005, respectively. From 1999 to 2002, he was a Research Assistant with the City University of Hong Kong. He is now a Professor with UESTC. His research interest includes the use of numerical techniques in electromagnetics and the use of microwave methods for materials characterization and processing.



Li-yan Chen was born in Wuhan, China. He received his B.S. degree from Shanxi University in 2016. He is now working towards his M.S. degree in Radio Physics at the University of Electronic Science and Technology of China (UESTC). His interests include MIMO antenna and MIMO system.



Muhammad Amin was born in D.I.Khan, Pakistan. He received his Master degree from Gomal University D.I.Khan Pakistan in 2003. Since September 2014 he is a Ph.D student in the major of Radio Physics at the University of Electronic Science and Technology of China (UESTC). His interests include antenna technology and wireless communication technology.